University of Alberta

Origin and isotopic evolution of the Muskox Intrusion, Nunavut

by

Melanie Purves

A thesis submitted to the Faculty of Graduate Studies and Research
in partial fulfillment of the requirements for the degree of

Master of Science

Earth and Atmospheric Sciences

Edmonton, Alberta
Fall 2007

Your file Votre référence
ISBN: 978-0-494-33328-0
Our file Notre référence
ISBN: 978-0-494-33328-0

DEDICATION

In his hand are the depths of the earth,
And the mountain peaks belong to him.
The sea is his, for he made it,
and his hands formed the dry land.
Psalm 95: 4-5

Abstract

The 1.27 Ga Muskox Intrusion, Nunavut, is a layered mafic/ultramafic intrusion associated with Mackenzie Igneous Events. Eight samples from the intrusion and associated Keel Dyke were investigated for whole rock Hf, Nd, and Sr isotopes and *in situ* laser ablation MC-ICP-MS Pb and Sr isotopes in plagioclase. The *in situ* initial $^{87}Sr/^{86}Sr$ ratios vary between 0.70366 and 0.70692 and are consistently more primitive than Sr whole rock values for the same samples. *In situ* Pb isotope compositions define similar linear arrays with $^{206}Pb/^{204}Pb$ and $^{207}Pb/^{204}Pb$ ratios that vary between 15.79-16.41 and 14.73-15.63, respectively. The ε_{Nd} (1270 Ma) values vary between –3.2 and –0.2. Whole rock Hf isotopic data display a narrow range in ε_{Hf} (1270 Ma) between –0.3 and +3.2 with five of the samples tightly clustered at ε_{Hf} = +1.4±0.1. In general the Nd and Hf whole rock isotopic data indicate derivation from a chondritic-like mantle reservoir and do not display isotopic signatures of a depleted mantle source, such as those reported previously for the Coppermine River flood basalts.

ACKNOWLEDGMENTS

This work would not have been possible without my amazing teachers, the guidance and assistance of so many colleagues and staff, the support of my family and friends, and the financial support provided by NSERC, Alberta Ingenuity, and the University of Alberta.

I would like to thank the following people:

Firstly, my co-supervisors, Dr. Larry Heaman and Dr. Rob Creaser. Larry was especially integral in my decision to come to Alberta, as well providing the project, facilities to work in, much guidance along the way, and tremendous support. Rob's contributions to the isotope analyses of the study were vital, and his advice and instructions are of great value to me. As a committee member, Dr. Sarah Gleeson provided helpful reviews and well-sounded advice. Dr. Don Francis generously provided the rock samples for this study. Dr. Antonio Simonetti provided essential support for work on the ICP-MS, helpful reviews, and excellent teaching. Dr. Stefanie Schmidberger helped tremendously with the Lu-Hf analyses and interpretation. Judy Schultz helped immensely with the processing of samples. Dr. Sergei Matveev aided extensively with the electron microprobe analyses and interpretation. Kelly Nixon provided assistance and guidance in the isotope lab. Stacey Hagen assisted with the use of the mass-spectrometer. Dr. Tom Chacko and Dr. Robert Luth were excellent teachers to me. Dr. Mike Thomas, NRC, provided some maps for the use of the project. Don Resultay and Mark Labbe worked on the thin sections and taught me to safely process samples. Staff in the DIF lab, especially Randy Pakan and Michael Fisher helped in many aspects of my work, particularly with poster presentations. The following graduate students and friends helped me in many different ways during this project, their support is especially noted: Jason French, Trevor MacHattie, Russell Hartlaub, Rajeev Nair, Melissa Bowerman, Kendra Siemens, Ryan Morelli, Shannon Zurevinski, Rachel Day, Hilary Corlett, Roxanne McMillan, Sarah Burke, and Daniel Regehr. My office-mates and friends in the department helped to make the work more enjoyable. Finally, my friends and family have supported me tirelessly throughout this long journey.

I would like to sincerely thank everyone, as well as anyone I may have not mentioned, for their contributions to this project and their amazing support.

TABLE OF CONTENTS

Abbreviations used in this thesis

Mineral Abbreviations (most according to Kretz, 1983)

Ab	Albite
Amp	Amphibole
An	Anorthite
Ap	Apatite
Bd	Baddeleyite
Bt	Biotite
Chl	Chlorite
Chr	Chromite
Cp	Chalcopyrite
Cpx	Clinopyroxene
En	Enstatite
Ep	Epidote
Fa	Fayalite
Fsp	Feldspar
Fs	Ferrosilite
Fo	Forsterite
Hbl	Hornblende
Ilm	Ilmenite
Ksp	K - Feldspar
Ol	Olivine
Opaq	Opaque minerals
Ms	Muscovite
Mon	Monazite
Mag	Magnetite
Phl	Phlogopite
Plag	Plagioclase
Pn	Pentlandite
Px	Pyroxene (group)
Py	Pyrite
Qtz	Quartz
Rt	Rutile
Serp	Serpentine
Sph	Sphalerite
Ttn	Titanite
Wo	Wollastinite
Zr	Zircon
Znlt	Zirconolite

Rock Names (most as in Francis, 1994)

Cpxnite	Clinopyroxenite
GBN	Gabbronorite
GRPHYR	Granophyre

MIGMA	Migmatite
Ol-GBN	Olivine Gabbronorite
Opxnite	Orthopyroxenite
Perid	Peridotite
PIC	Picrite
Webst	Websterite

Other Abbreviations

BSe	Backscatter Electron
BSE	Bulk Silicate Earth
Byr	Billion years
CHUR	Chondritic uniform reservoir
CC	Copper Creek
CRB	Coppermine River Basalts
CU	Cyclic unit
DM	Depleted Mantle
EMP	Electron Microprobe
EMORB	Enriched-Mid ocean ridge basalt
FOV	Field of View
HC	Husky Creek
HREE	Heavy rare earth element
HFSE	High field strength element
IDTIMS	Isotope dilution thermal ionization mass spectrometry
LILE	Large ion lithophile element
LA-ICP-MS	Laser Ablation Intercoupled plasma mass spectrometry
LMI	Layered mafic intrusion
LREE	Light rare earth element
MD	Mackenzie Dykes
MIE	Mackenzie Igneous Events
Mag	Magnification
MC	Megacycle
MREE	Middle rare earth element
MORB	Mid-ocean Ridge Basalt
Ma	Million years ago
MI	Muskox Intrusion
NIST	National Institute of Standards and Technology
NMORB	Normal-Mid ocean ridge basalt
OIB	Ocean Island Basalt
Ppl	Plane polarized transmitted light
PM	Primitive mantle
REE	Rare earth element
SCLM	Sub-continental lithospheric mantle
UCC	Upper Continental Crust
Xn	Cross-polarized transmitted light

Notes: All errors reported are shown in the last decimal places of the reported value.

CHAPTER 1: INTRODUCTION

1.1 Introduction and Purpose

Layered Intrusions are large igneous bodies that primarily form by the fractional settling of crystals in a mafic magma chamber. They are arguably the best natural evidence for the processes of fractional crystallization and differentiation. Changes in the composition of the layers reflect changes over time as the magma chamber evolves. Processes such as the removal and addition of batches of magma, and assimilation of wall-rocks further complicate the idealized model. Layered intrusions host many of the worlds economic deposits of platinum, chromium, palladium, and nickel, thus they can be extremely important natural resources. Layered mafic intrusions are commonly associated with continental flood basalts, where large amounts of mafic magma are produced in a continental setting. The tectonic setting for many layered intrusions is unclear. Many are associated with rifting events and extensional settings, and as such have been attributed to mantle plumes (Ernst and Buchan, 2003). The ~15 Ma Columbia River Basalt Province in the NW United States (Washington, Oregon, Idaho), the ~65 Ma Deccan Traps of western India, and the ~130 Ma Parana large igneous province in Brazil are three relatively young examples of flood basalt provinces that have been linked to mantle plumes (e.g. Camp, 1995; Vandamme et al., 1991; Peate, 1990). Pre-Mesozoic examples are less easily identified, as the extrusive components are commonly eroded, leaving only dykes, sills, and layered intrusions. The Mackenzie igneous event in northern Canada is a unique magmatic province where all three components appear to be preserved. The scientific study of such ancient magmatic provinces is essential to our understanding of how mantle plumes may have operated through time, and will facilitate a better understanding of their role in tectonic processes.

The 1.27 Ga Muskox Intrusion (MI), located in Nunavut, Canada, is a layered mafic/ultramafic intrusion that is part of one of the world's major and best-preserved Proterozoic large igneous provinces (Fig. 1.1). The overlying flood basalts of the Coppermine Group and the associated Mackenzie dyke swarm are thought to be coeval and genetically related to the MI, and together are collectively referred to as Mackenzie Igneous Events (MIE; LeCheminant and Heaman 1989). The field and geochemical evidence for their association is well documented and undisputed in the literature (Fahrig and Jones, 1969; Irvine, 1977; Irvine and Smith, 1979; Dostal et al., 1983; Gibson et al., 1987; LeCheminant and Heaman, 1989; Stewart and DePaolo, 1992; Dupuy et al., 1992; Francis, 1994; Stewart and DePaolo, 1995; Baragar et al., 1996; Griselin et al., 1997). Principally tholeiitic magmas intruding the crust at this time are believed to have occurred above a large hotspot due to the presence of a mantle plume, possibly located below the west coast of Victoria Island (denoted by a star in Figure 1.1; LeCheminant and Heaman, 1989). Evidence for this includes the synchronicity of mafic magmatic events, the short duration of magmatism (<5 million years) and specific focus, the large volume of magma (>200,000 km^3), the radiating nature of the Mackenzie dykes, and the ~1 km of uplift recorded by the Dismal Lakes Group disconformity. LeCheminant and Heaman (1989) suggested that Mackenzie magmatism was caused by the melting of upwelling asthenosphere when rifting in the vicinity of a hot-spot occurred in a short-

lived, single-focus event. A summary of the current knowledge of each magmatic component is presented in section 2.1.2.

Although these three magmatic events are determined to be closely related in time, there are several interesting discrepancies noticeable in the geochemical and isotopic data, which are difficult to reconcile with any hypothesis that stipulates that all of this magmatism was derived from the same mantle source region. Firstly, the Nd isotopic signature of the 'uncontaminated' Coppermine River basalts (CRB; e.g. Dupuy et al. 1992; Griselin et al. 1997) is distinctly different than values reported for the MI (e.g. Stewart and DePaolo 1992; 1995). The Nd isotopic values reported for least contaminated CRB samples approach depleted mantle compositions ($\varepsilon_{Nd\ (1270)}$ = +3.0 to +4.7; Griselin et al., 1997), while the $\varepsilon_{Nd\ (1270)}$ values for least contaminated samples from the MI range from -3 to +1 and appear to be derived from an undepleted mantle source (Stewart and DePaolo, 1995). Previous researchers suggest that the mantle source for the CRB lavas was subject to long-term depletion, although not as extreme as MORB (Dupuy et al., 1992; Griselin et al., 1997). Also, the geochemical contamination reported for the entire MI documented by Francis (1994) is not reflected in the Nd or Sr isotope data to date. These discrepancies give strong cause to investigate the isotopic composition of the MI. As well, previous isotopic studies of the MI have been incomplete in the sense that they have largely focused on the margins of the intrusion, to study the effect of local crustal contamination and mineralization (e.g. Stewart and DePaolo, 1992; Mackie et al., 2005). This study will be unique in its focus on the isotopic composition of samples closer to the center of the intrusion, and also from the associated Keel Dyke. Also the Pb isotope systematics of the MI have not been previously explored, despite the fact that Pb is a very sensitive indicator of crustal contamination. The MI is the only exposed ultramafic intrusion associated with MIE. Field relationships indicate that some Mackenzie dykes cross-cut the Muskox intrusion (LeCheminant and Heaman 1989) so the MI represents one of the older recognized magma chambers within the Mackenzie large igneous province and therefore has the potential to preserve a detailed record of the earliest magma crystallization history, slightly before the injection of the Mackenzie dyke swarm (LeCheminant and Heaman, 1989). A study of the composition of the MI will add significantly to our understanding of this large igneous event.

The purpose of this study is to enhance our understanding of the origin of the Muskox Intrusion and its relationship to other Mackenzie Igneous Events. Specifically, the trace element, mineral chemistry and isotopic compositions (e.g. ^{176}Lu-^{176}Hf, ^{147}Sm-^{143}Nd, ^{87}Rb-^{87}Sr, ^{238}U-^{206}Pb and ^{235}U-^{207}Pb systems) of samples representing a complete transect through the Muskox intrusion were investigated in an attempt to evaluate the isotopic nature of the mantle source region, constrain its composition and depth of origin, assess the role of mantle lithosphere/crustal contamination processes, and assess whether magma from the Muskox intrusion directly fed the Coppermine River basalts and Mackenzie dykes (MD). The results from this study are used to evaluate and test previously proposed mantle plume models for the origin of Mackenzie Igneous Events (e.g. Dupuy et al. 1992: Griselin et al. 1997).

1.2 Objectives, Scope, and Organization

The main objectives of this study are:

(1) To further quantify the nature and source of mantle and crustal contamination in the Muskox Intrusion

(2) To apply the ^{176}Lu-^{176}Hf, ^{147}Sm-^{143}Nd and ^{87}Rb-^{87}Sr systems to samples of the MI, in order to better constrain the detailed Hf, Nd and Sr isotopic evolution of the MI magmas in an attempt to understand the isotopic nature of the mantle source region.

(3) To investigate the *in situ* (within mineral grain) Pb and Sr isotope characteristics of plagioclase in these samples, in order to evaluate in more detail the relationship between whole rock and individual mineral isotopic compositions, while preserving contextual information.

(4) Compare the new geochemical and isotopic data obtained in this study to results reported in previous studies to arrive at a more robust hypothesis for the origin and evolution of Mackenzie Igneous Events.

This thesis is divided into 6 chapters. Following this introductory chapter (Chapter 1), Chapter 2 provides a background of the regional geology of the study area, as well as summarizes previous research conducted on the MI and associated events. Chapter 3 introduces the petrology and geochemistry of the samples chosen for this study. Chapter 4 presents the isotopic results and interpretations of the data obtained. Chapter 5 discusses the results presented in the previous chapters. Chapter 6 is the conclusion chapter and summarizes the major findings of this study.

CHAPTER 2: REGIONAL GEOLOGY AND BACKGROUND

2.1 Regional Geology and Previous Work

2.1.1 The Wopmay Orogen

The Paleoproterozoic (1.92 - 1.84 Ga) Wopmay orogen (Hoffman and Bowring, 1984) lies between the Archean Slave craton (Fig. 2.1) and the Phanerozoic Canadian Cordillera. It represents a time of crustal growth in the area, as it comprises a series of north-south trending magmatic arcs and terranes which were accreted to the western margin of the Slave craton. Orogenic activity occurred during at least two major stages: (1) the accretion of the Hottah terrane (1.90 – 1.88 Ga), and (2) the accretion of the Nahanni-Fort Simpson terrane (~1.84 Ga) (Hoffman and Bowring, 1984; Cook et al. 1999). The orogen consists of several major tectonic zones. The eastern part of the orogen contains the Coronation Supergroup, deposited on a passive margin of the Slave craton (1.94 – 1.84 Ga) (Bowring and Podosek, 1989). These rocks have been thrust eastward, deformed, and intruded by syntectonic granitoid rocks (Hepburn metamorphic-plutonic belt) between 1.89 and 1.88 Ga (Bowring and Podosek, 1989). The eastern most part of the Coronation margin contains the Asiak Fold and Thrust Belt, which was active during the Calderan Orogeny (1.90 – 1.88 Ga; Cook et al., 1999). The western part of the orogen consists of the Hottah terrane, a magmatic arc with associated sedimentary rocks. This terrane is believed to be exotic and to have collided with the Coronation margin (Hildebrand et al. 1983; Hoffman and Bowring, 1984). The Hottah terrane is derived from old, 2.4 - 2.0 Ga basement (Bowring and Podosek, 1989) and is intruded by calc-alkaline plutons (1.914 – 1.902 Ga; Hildebrand et al., 1987). Between the Coronation Supergroup and the Hottah terrane is the Great Bear Magmatic Zone, a younger terrane which onlaps the Coronation and the Hottah terrane at its boundaries (1.875 - 1.84 Ga; Hildebrand et al., 1983; 1987). The Great Bear Magmatic Zone consists of volcanic-sedimentary sequences and plutonic rocks, and is believed to have formed as a result of subduction of oceanic lithosphere as the Hottah terrane collided with the Slave craton (Hildebrand, 1981). The Fort Simpson terrane occurs in the western most extent of the Wopmay orogen and is a second major terrane which collided with the western margin of the Hottah terrane and the craton, when Great Bear magmatism ceased, sometime after 1.84 Ga (Cook et al. 1999; Hildebrand et al. 1987). The Fort Simpson terrane is largely buried beneath the Western Canadian Sedimentary Basin.

The MI is located within the central portion of the Wopmay Orogen, and intrudes paragneisses of the Asiak fold and thrust belt to the east and granitic and volcanic rocks of the Hepburn plutonic belt to the west. It is intrusive into the sedimentary rocks of the Epworth and Recluse Groups. To the north, it intrudes metasediments of the Hornby Bay and Dismal Lakes groups (Irvine and Smith, 1967; 1969). A 1663 ± 8 Ma rhyolite porphyry from the Hornby Bay Group provides a maximum age constraint for the intrusion (Bowring and Ross, 1985).

2.1.2 Mackenzie Igneous Events

The emplacement of the MI is considered to be coeval with the Coppermine River volcanic rocks and the Mackenzie dyke swarm at about 1.27 Ga (LeCheminant and Heaman, 1989). Together they are collectively referred to as Mackenzie Igneous Events. These events are believed to have occurred above a large hotspot due to the presence of a mantle plume (LeCheminant and Heaman, 1989). Evidence that supports this hypothesis includes the similar age of events, the short period and specific focus, the large volume of magma, the radiating nature of the dykes, and the uplift recorded by the Dismal Lakes Group disconformity. LeCheminant and Heaman (1989) suggested that Mackenzie magmatism was caused by the melting of upwelling asthenosphere, due to rifting in the vicinity of a mantle plume, which occurred in a short-lived, single-focus event. Mackenzie Igneous Events (MIE) represent one of the world's major and best-preserved Proterozoic large igneous provinces. MIE largely intruded the crust between the Bear Province and the Epworth fold belt, along a zone of weakness, which likely controlled the emplacement of some mafic intrusions (Fraser et al. 1972). The area between the western edge of the MI and the eastern edge of the Hornby Bay Group is an area of intense structural complexity, which provided a conduit for magmas of the MI.

2.1.2.1 The Mackenzie Dykes

The Mackenzie dykes are one of the world's largest continental dyke swarms, radiating from a focal point located on northern Victoria Island, through an arc of ~100° (Baragar et al. 1996). The dykes extend for a maximum strike length of ~2400 km and cover a large part of the north-western Canadian Shield (Fig.1.1). Most dykes are about 30-m-wide and consist of gabbroic centres with chilled margins (LeCheminant and Heaman, 1989). U-Pb ages obtained on eight widely separated Mackenzie dykes lie in a narrow range from 1265 to 1272 Ma (LeCheminant and Heaman, 1989; Heaman and LeCheminant, 1993). Schwab et al. (2004) recently proposed that the Bear River dykes (1265 -1269 Ma), exposed in the northern Yukon, are a westward continuation of the Mackenzie dyke swarm, thus extending the total arc of dyke radiation to >150 °.

The field relationships and geochemical similarity of the dykes indicate that some acted as feeder dykes to the Coppermine River flood basalt flows (Gibson et al. 1987; LeCheminant and Heaman, 1989). There is field evidence that Mackenzie dykes both cross-cut the MI and are truncated by the intrusion and some are interpreted to be both feeders and outlets of crustal magma chambers (Baragar et al. 1996). Magnetic fabric studies of the swarm have shown that flow patterns within the dykes are vertical near the swarm focus, and horizontal at distances greater than 500 km (Ernst and Baragar, 1992), thus further supporting the mantle plume concept proposed by LeCheminant and Heaman (1989). The horizontal flow of the magma emanating from the focal region crossed many crustal-scale geological boundaries (Gibson et al. 1987).

The Mackenzie dykes are largely composed of plagioclase, orthopyroxene, clinopyroxene, and Fe-Ti oxides (largely magnetite). Olivine is rare, and quartz, K-feldspar, chlorite, amphibole, biotite, Fe-Ti oxides and apatite generally fill interstices in the rock. Chalcopyrite and other sulphide grains occur in small grains and veinlets. Plagioclase compositions range from An_{67-35}, and pyroxene compositions ($Wo_{39-40}En_{50-}$

$_{49}Fs_{11}$) are most similar to the lower flows of the Coppermine River Basalts, (Baragar et al. 1996).

The dykes have geochemical compositions matching typical continental tholeiites; they are quartz normative, with SiO_2 ranging from 48 to 54 weight percent, and MgO from 2.5 to 8.0 weight percent. The dykes show little effects from metamorphism or alteration, as only the concentrations of Ba, Rb, and Sr have undergone secondary modification (Gibson et al. 1996). Chondrite normalized rare earth element (REE) patterns show enrichment in the light rare earth elements (LREEs), with very few Eu anomalies, and is consistent with plume derived magmas (Gibson et al. 1987; Baragar et al., 1996). Dykes close to the swarm focus also show negative Nb and positive K and Rb anomalies. This, along with higher K/Ti ratios (below), is attributed to crustal contamination (Baragar et al. 1996). Pearce element ratio diagrams presented by Baragar et al. (1996) show that olivine is not a significant fractionating mineral in the main swarm; instead plagioclase, clinopyroxene, and orthopyroxene are the main fractionating phases.

The Mackenzie dyke swarm is very extensive and therefore lateral changes in the composition of the dykes can be expected as the magma travelled through many kilometres of varying rock formations. The composition of the dykes becomes more evolved outward along the swarm, matching those of the upper levels in the Coppermine River flood basalts (see section 2.1.2.2) (Baragar et al. 1996). In addition, many of the larger individual dykes are gradationally zoned, with more evolved centres, as compared to the margins (Gibson et al. 1987). Gibson et al. (1987) divided the Mackenzie dykes into two distinct groups, on the basis of trace element geochemistry. Type A dykes have a Zr/Y ratio < 5 and Ce/Yb ratio < 15, while Type B dykes have ratios greater than these values. Other differences between the two dyke types include varying trace element ratios and major element compositions (best viewed on plots of SiO_2 vs. P_2O_5 and TiO_2, and in concentrations of FeO and CaO). Baragar et al. (1996) also note that Type B dykes are generally more alkaline in nature and occur in a longitudinal, geographic group near the former district of Keewatin (now Nunavut). They are therefore regarded as a distinct subswarm (Keewatin Subswarm). The zoning in Type A dykes is well defined, the centres having enriched levels of P_2O_5, TiO_2, total Fe, incompatible trace elements, and the REEs, and depleted in MgO, CaO, Ni, and Cr. Locally, the cores of some Type A dykes show extreme enrichment of Th, Ba, Rb, and K_2O. As detailed in section 2.1.2.2, Dostal et al. (1983) notes similar enrichment in K, Rb, and Ba in the basal flows of the Coppermine River Basalts. This selective enrichment is thought to be due to contamination that occurred in high-level magma chambers before eruption of the flows and emplacement of the dykes (Gibson et al. 1987). Contamination in the MI is measured by K/Ti (Francis, 1994) (see section 2.1.2.3). If the same criterion can be applied to the Mackenzie dykes, contamination would be greatest in the dykes closest to the flows, and decreases to a constant level for dykes between 600 and 2100 km from the swarm focus. This is attributed to a higher ambient temperature near the focus, which would result in larger amounts of wall rock being assimilated locally, although significant wall rock contamination is generally not common (Baragar et al. 1996). Overall, crustal contamination is not believed to have played a major role in the compositional variations (Gibson et al. 1987).

According to Gibson et al. (1987), fractional crystallization models can account for the zoned margin and center compositional differences, although other explanations may be possible. Baragar et al. (1996) suggest instead that the zoning is due to *in situ* fractionation. Geochemical evolution outward along the swarm is accounted for by fractionation and crystal settling in transport. The fractionation is thought to have largely occurred before the emplacement of the dykes at low pressures, in multiple high-level magma chambers, such as the MI (Gibson et al. 1987). Baragar et al. (1996) suggest that the fractionation occurred in even larger chambers than the MI at the core of the uplift. These magma chambers are not exposed; however there are several large Bouguer anomalies arranged in a ring at the focus of the swarm, which are interpreted to indicate their presence (Goodacre et al., 1987). The MI would then be one of several smaller subsidiary magma chambers. The more alkaline nature of the Keewatin subswarm indicates that it may have had a deeper source, and was emplaced slightly before the mainstream of the Mackenzie dykes (Baragar et al. 1996).

Generally constant trace element ratios Zr/Y (5-6) and P/Ti (0.07-0.085) are interpreted to be primary characteristics of the plume magma (Baragar et al. 1996). Dudas and Peterson (1992) analysed 32 dyke samples for their Nd isotopic composition. The range of ε_{Nd} for dyke centers extends from +4.9 to –2.8. Values measured at dyke margins where contamination was clearly evident were approximately -9.8. Most values however, were between 0.0 and +2.0, with no geographic pattern or distinction between subswarms. These values, which are close to chondritic values, are more indicative of a plume source than any other reasonable source (Baragar et al. 1996). Nd isotope data for four of the Bear River dykes show considerable variation in ε_{Nd} (1270 Ma) values, from +1.4 to -7.2 (Schwab et al. 2004).

2.1.2.2 The Coppermine River Basalts

The Coppermine River Group is a large succession of flood basalt flows and interflow sediment that conformably overlie predominantly sedimentary sequences of the Dismal Lakes and Hornby Bay groups (Fig. 2.1). Together, these successions comprise the Coppermine homocline, a gently dipping succession resting unconformably on the Wopmay Orogen. The Coppermine River Group consists of about 150 flows, is approximately 2000- to 3500-m-thick, and extends for almost 300 km, although much of the formation underlies the interior platform between Great Bear Lake and the Beaufort Sea (Cook, 1988). The Coppermine River Group itself is divided into the Copper Creek (CC) and the Husky Creek (HC) formations. The lower Copper Creek formation is characterized by thick, continuous basalt flows (up to 100-m-thick), which are generally massive with amygdaloidal tops, with some exhibiting columnar jointing and pillows. The majority of flows erupted subaerially, with the exception of the first few (Baragar, 1969). The upper Husky Creek formation consists of basalt flows interbedded with fluvial sandstones, recording declining volcanic activity.

The Coppermine River basalts are considered, on the basis of field relations, paleomagnetic data, and K-Ar and Rb-Sr ages, to be coeval with the MD and the MI, at about 1270 Ma (Baragar, 1972, Fahrig, 1987, and LeCheminant and Heaman, 1989). The most precise age for the CRB, 1214±45 Ma, is based on a six-sample Rb-Sr whole rock

isochron from different flows from the Coppermine River Group (Baragar, 1972). The Dismal Lakes and Hornby Bay groups record uneven uplift and subsidence before the eruption of the basalts, which is attributed to the results of thermal effects from an underlying mantle plume (LeCheminant and Heaman, 1989).

Petrographically, the CRB are typically porphyritic with phenocrysts of augite being most common. However, less common and altered phenocrysts of olivine and orthopyroxene occur in the lower part of the sequence, and plagioclase phenocrysts occur mainly in the upper part of the sequence. The groundmass consists of altered glass, augite, plagioclase, and Fe-Ti oxides. The proportion of Fe-Ti oxides (largely magnetite) increases upwards in the succession. Copper exists as blebs and specks in the upper layers. The basalts have been metamorphosed at low grades, the expression of which is generally the replacement of plagioclase by saussurite or clays. Chemically, the Coppermine River Basalts are typical of continental tholeiites. Silica contents are less than 50%, and most lavas are quartz normative. Magnesium numbers vary between 62 and 37, and most are less than 50. Low Mg/Fe ratios and low abundances of Ni and Cr (<206 and 520 ppm, respectively) show that the lavas were fractionated before eruption (Dostal et al. 1983).

The chemical and isotopic compositions of the basalts change upwards in the sequence (Baragar, 1969; Dostal et al. 1983; Griselin et al. 1997). Secular geochemical changes are most evident in the Copper Creek Formation, where there is a decrease in SiO_2, K_2O, and MgO and an increase in Fe_2O_3 and TiO_2 up section. As well, Rb, Ba, Th, Cr and Ni decrease upwards in the sequence while Cu, Zn, V, and Sc all increase (Baragar, 1969). With the exception of K_2O, the behavior of these elements can be explained by crystal fractionation (Baragar, 1969). In contrast, incompatible elements such as the heavy rare earth elements (HREE), Ti, and Y increase upwards in the Copper Creek formation. LREE and Zr show more complex trends, decreasing upwards until the top of the middle member of the Copper Creek Formation, and then increasing upwards until the Husky Creek Formation (Griselin et al. 1997). Rocks of the Husky Creek Formation are similar in Mg number to the lowermost flows of the Copper Creek Formation, but lack the same enrichment in K_2O. The boundary between the Copper Creek and the Husky Creek formations is marked by significant changes in geochemistry, including decreases in TiO_2, Fe_2O_3 (total), Th, La, and Zr, and increases in MgO and Mg number. In summary, the compositions of the basalts evolve upwards in the Copper Creek Formation, but return to more mafic compositions in the Husky Creek formation.

Incompatible element contents decrease from the Copper Creek to the Husky Creek formations (Griselin et al. 1997). In the Copper Creek Formation, mantle-normalized patterns are steeply enriched, while in the Husky Creek Formation they are nearly flat (Griselin et al. 1997). Negative Nb anomalies occur in the Copper Creek lavas, and are especially well-defined in the lower member, while the Husky Creek lavas show positive Nb anomalies. Positive Pb anomalies are present in the Copper Creek lavas, while negative Pb anomalies are present in the Husky Creek lavas (Griselin et al., 1997). As well, negative Th-U anomalies occur in the Husky Creek lavas, but are absent in the Copper Creek lavas (Griselin et al. 1997). Incompatible elements that are relatively immobile (Zr, Hf, Nb, Th, Y, La, and Ce) show an overall increase upwards in the lavas, with increasing degrees of differentiation (Dostal et al. 1983). Rb, Ba, and K concentrations are higher in the lowermost flows of both sections, due to the high

proportion of granophyre in those layers. Both Ni and Cr correlate with Mg numbers, which decrease steadily until a sharp increase in the Husky Creek Formation. Cr decreases more significantly with differentiation. This observation, together with petrographic evidence (above), indicates that pyroxene fractionation was more dominant than olivine fractionation (Dostal et al., 1983). Rare earth element patterns of the lavas show enrichment in the LREE, and are divided into two groups according to their La/Yb ratios, by Dostal et al. (1983). The first group has low LREE contents, low La/Yb ratios (2.9 – 4.2), and slightly fractionated HREEs, and geochemically resemble E-MORBs. The second group has higher LREE contents, higher La/Yb (5.8 – 10.3), and fractionated HREEs, and is intermediate between OIBs and continental tholeiites (possibly more evolved and more contaminated). This variation between REE patterns cannot be explained by crystal fractionation, but by differential partial melting. Crustal contamination can account for enrichment of K and other incompatible elements, the observed negative Nb anomalies (Dostal et al. 1983), and possibly the positive Pb anomalies (Griselin et al., 1997). If the Coppermine lavas are viewed as the surface expression of the Muskox magmas, then contamination and fractionation processes should both have significant effects on the geochemistry (see section 2.1.2.3). Geochemical effects from crustal contamination decrease upwards in section. This is explained by Baragar et al. (1996) as resulting from an initial "flushing out" of the roof rock melt from the magma chamber (i.e. Muskox intrusion). As time passed, the magma chamber solidified, and the magmas of the Husky Creek formation came from a more primitive source.

The Nd-Sr-Pb isotope systematics were examined by Dupuy et al. (1992) for eight 'fresh' samples from the collection studied by Baragar (1969) and Dostal et al. (1983). The range of values for these samples are: ε_{Nd}: -4.82 to +4.10, $^{87}Sr/^{86}Sr_i$: 0.704222 to 0.715903, $^{206}Pb/^{204}Pb$: 18.449 to 19.203, $^{207}Pb/^{204}Pb$: 15.583 to 15.729, $^{208}Pb/^{204}Pb$: 38.268 to 39.180. Four of these samples appear to contain a crustal component, observable in the Nd and Sr isotopes, as well as some trace element ratios. The four samples that show a signature apparently devoid of crustal contamination have relatively constant $^{206}Pb/^{204}Pb$ ratios (19.1 – 19.2), $^{208}Pb/^{204}Pb$ ratios (39.0 – 39.2) and ε_{Nd} ranging from +3.03 to +4.10. These isotopic compositions are clearly different from primitive mantle, and consistent with a source that is less depleted than MORB. Dupuy et al. (1992) explain this source as a mixture between primitive mantle (from a plume) and the base of the continental lithosphere, which was well mixed prior to eruption.

The geochemical and Nd isotopic compositions of the basalts were examined in greater detail by Griselin et al. (1997). They examined 32 samples also from the collection of Baragar (1969) and Dostal et al. (1983). Griselin et al. (1997) also document geochemical change upwards in the stratigraphic section. The lower units have high SiO_2, incompatible elements, high fractionation of trace elements, negative Nb anomalies, and low ε_{Nd} (-5.5 to +1.7). These units are interpreted to have been produced by melting in the garnet stability field (>90km) in a mantle plume, which then became contaminated passing through magma chambers (such as the MI). The upper units however, have less pronounced enrichment and fractionation of incompatible elements, no Nb anomalies, and positive $\varepsilon_{Nd(T)}$ (+3.0 to +4.7) (Griselin et al. 1997). Griselin et al. (1997) suggest that this change is attributed to a shallower site of melting due to lithospheric thinning, along with minimal crustal contamination. The upper units were

used to infer the composition of the mantle source, because they were the least contaminated. The positive ε_{Nd} signature of these units suggests long-term depletion, although not as extreme as MORB. The Nd composition of the DM at 1.27 Ga is approximately ε_{Nd} +5.5. Although this information would seem to preclude the mantle plume hypothesis, Griselin et al. (1997) suggest that the magmas, similar to some studies from ocean island basalts, preferentially tap isotopically depleted material during shallower melting as the mantle plume evolved.

2.1.2.3 The Muskox Intrusion

The Muskox intrusion, located 500 km north of Yellowknife and 90 km south of Kugluktuk (formerly Coppermine) on the Coronation Gulf in Nunavut (Fig. 2.2), is a layered mafic intrusion that was emplaced at 1269.4 ± 1.1 Ma (LeCheminant and Heaman, 1989; French et al. 2002). It outcrops as an elongate, funnel-shaped body, with its feeder dyke exposed to the south and its layers dipping to the north. The intrusion is about 20-km-wide and more than 90-km-long at the surface, but a large gravity anomaly indicates that much of the intrusion continues north under the Coronation Gulf (Irvine and Smith, 1967). The main intrusion is divided into two zones: a layered series and a northern roof zone (Irvine and Smith, 1969).

The layered series is about 1800-m-thick and consists of layered ultramafic and gabbroic cumulates, split into 25 cyclic units (CU), each interpreted to represent a separate pulse of magma into the intrusion (Irvine and Smith, 1967). Francis (1994) regrouped these 25 units into 4 "Megacycles" (MC), each beginning with a large layer of olivine cumulate becoming interbedded with pyroxenite and gabbroic layers upsection (Fig. 2.3). Megacycles #1 and #2 are dominated by olivine cumulates. Pyroxenite units become more frequent and thicker upsection from MC #1 to MC #3. MC #4 is dominated by gabbro-norites interbedded with mostly pyroxenite units (such as websterites and orthopyoxenites). The parental magma of the MI is inferred to be picritic (Irvine, 1977). The layered series grade upward into the granophyric roof zone, which was partially generated by the assimilation of surrounding country rocks (Irvine and Smith, 1979). In general, the cumulates become less ultramafic with each successive cycle (Irvine, 1970). Extensive sulphide-rich zones occur along the marginal zone of the intrusion, consisting mainly of pyrrhotite (Francis, 1994). These sulphide zones are the targets for economic mining operations of Pd, Pt, Au, Cu, and Ni. Near the base of MC #4, in CU #21, a thin chromitite layer is exposed, overlying a 1-2 m thick layer of pegmatoidal, feldspathic websterite, and underlying an orthopyroxenite layer. The chromitite layer contains the highest platinum group element values recorded in the layered series. The layer and its associated pegmatoid are referred to as the Pt-bearing "reef", because of the similarities to the Merensky reef of the Bushveld Intrusion (Barnes and Francis, 1995). Irvine (1977) concluded that such chromitite layers can form as a result from an influx of chemically primitive magma intrudes into an existing chamber, mixing with a more evolved magma.

The Keel Dyke is exposed to the south of the MI and structurally underlies the main body of the MI. Recharging magma is thought to have flowed from a larger magma feeder from the north, while more differentiated magma was vented southward (Irvine

and Smith, 1967; Stewart and DePaolo, 1995). The Keel Dyke is thought to represent a lateral southward injection from this main conduit system in the north (Francis, 1994). The Keel Dyke is about 75-km-long and between 150- and 500-m-wide, consisting of olivine gabbronorite with an inner olivine-rich picrite zone and a chilled margin of fine grained gabbronorite. To the north, the inner picrite zone is further intruded by a central zone of olivine-gabbronorite (Francis, 1994). The core of the dyke also contains massive and disseminated PGM-rich Cu-Ni sulphides (Francis, 1994).

Francis (1994) performed a detailed geochemical analysis of the MI, documenting the levels of geochemical contamination within the marginal rocks of the intrusion. This study demonstrates that primitive magmas of the MI were actively assimilating the country rock, and that this assimilation increased at successively higher levels within the intrusion. Evidence for this contamination includes the presence of granophyric textures, elevated ratios of LIL/HFS elements, and enhanced orthopyroxene crystallization along the margins. Contamination however, was selective, and increased in the order: HFSE, HREE, LREE, U, Th, LILE, and chalcophile elements (Francis, 2004). The ratio of K/Ti is a particularly effective indicator of contamination in this case, because K in the host rock is approximately ten times more abundant than in the Muskox magmas and is very mobile compared to Ti. Based on geochemical arguments (Francis 1994), assimilation led to the formation of two hybrid magmas (one from the melted host rock, the other from the contaminated magma) which were buoyant and rose to the top of the intrusion during each megacycle. In the lower two megacycles, the hybrid magmas remained relatively isolated from the rest of the system until the crystallization of feldspar at the end of each megacycle. In the upper two megacycles there is evidence for episodic mixing of the hybrid magmas with the chamber magmas (Francis, 1994). This is somewhat contrary to the small amount of assimilation estimated by the studies of Stewart and DePaolo (1988, and 1989). Francis (1994) states that this could be due to: (1) the low sampling density for the isotopic studies, (2) the lower concentration contrast and extent of exchange of REE compared to LILE between the MI and the host paragneiss, and (3) the fact that feldspar acted as a restite phase in the paragneiss (i.e. retaining Sr).

Francis (1994) also shows that the estimated compositions for parental magmas for the MI show enriched incompatible trace element profiles. The parental magma composition is consistent with that of the CRB and the MD. Francis (1994) speculates that this enrichment was acquired from the subcontinental mantle source regions, or less likely, contamination from the lower crust. The MI is generally interpreted as part of a system of magma chambers that fed the flood basalts and the dykes. One model suggests that the separate layers of contaminated hybrid magmas were erupted from the MI chamber at the end of the first two megacycles, producing the lower members of the Coppermine River Group (Francis, 1994). Baragar et al. (1996) notes that although most MD cut the intrusion, some predate it, and therefore the MI may be regarded as both a reservoir and feeder to the Mackenzie magmatic system.

To date, the only isotopic studies on the MI are that of Stewart and DePaolo (1988, 1989, 1990a, 1992, and 1995), and Mackie et al. (2005, 2006). Stewart and DePaolo (1995) report Sr and Nd isotopic data for 27 samples across the intrusion, showing little isotopic variation until the upper most cyclic unit. The data suggest that very little assimilation (1% – 5%) of the country rock occurred. Stewart and DePaolo

(1992, 1995) examined the isotopic composition of the uppermost layers of the intrusion in detail. In cyclic unit (C.U.) 25, the Sr and Nd isotopic systems are decoupled. The ε_{Nd} remains relatively constant (at about -0.75), while the $^{87}Sr/^{86}Sr$ increases with stratigraphic height (from 0.7051 to 0.7097), indicating that the C.U. 25 magma was progressively enriched in radiogenic Sr. Their results demonstrate that isotopic mixing occurred between mafic and silicic magma layers within the magma chamber, and they use this information to model diffusive isotopic exchange between the two layers. These studies did not focus on the petrogenesis and isotopic composition of the source region of Mackenzie events. Mackie et al. (2005, 2006) report initial findings of a combined Hf and Nd isotope study which examines the crustal contamination and mineralization of the marginal zone of the MI. Mackie et al. (2006) report an age for the intrusion of 1268 ± 2 Ma (U-Pb on baddeleyite from peridotite and gabbronorite). They also report ε_{Hf} in the range of -15 to +2.0 and similar ε_{Nd} values reported by Stewart and DePaolo (1995), ranging from $\varepsilon_{Nd=}$ -13 to +0.5.

2.1.2.4 Summary of Previous Work

Previous studies of the MI have focused on structural and stratigraphic relations, origin of the chromitite layers, platinum group elements, and internal structure and composition. Isotopic studies of the MI have generally focussed on assimilation and fractional crystallization models, from marginal rocks, rather than on the primary source of the magma. The primary objective of this study is to fully characterize the least contaminated Muskox samples and evaluate the nature of the source region. Although the CRB are related to the MI, they are thought to be more evolved (e.g. Francis, 1994). It has been suggested that the lower two formations of the Coppermine River Basalts have formed from contaminated liquid expelled from the MI at the end of MC#1 and 2 (Francis, 1994).

Francis (1994) shows that the extent of chemical exchange between the MI and its wall rock increased in the order HFSE, HREE, LREE, U, Th, LILE, and chalcophile elements. Lu and Hf are HREE and HFS elements, respectively, while Sm and Nd are both LREE elements. Therefore, the Lu-Hf system has a greater chance of recording primary magma compositions (i.e. disturbed to a lesser extent by crustal contamination). The Lu-Hf system is also more likely to be more sensitive to the nature of the mantle source because there is greater fractionation between the parent/daughter during mantle melting compared to Sm-Nd (section 2.2.1).

2.2 Isotopic systems

2.2.1 $^{176}Lu - ^{176}Hf$

The $^{176}Lu - ^{176}Hf$ system is based on the radioactive decay of ^{176}Lu, a heavy rare earth element (HREE), to ^{176}Hf, a high field strength element (HFSE) (similar to Zr), with a half-life of 37 Byr (Scherer et al. 2001). The contrasting geochemical behavior of these two elements causes their fractionation during melting and the formation of crust,

and other metamorphic processes. This makes the $^{176}Lu - ^{176}Hf$ system useful not only as a geochronometer but also as a petrogenetic tool. Its potential as such has been made more popular in recent years, with the advent of plasma source mass spectrometers. Patchett and Tatsumoto (1981) conducted a study on the Hf isotopic composition of mantle-derived rocks; tracing their composition through time. More recent studies such as Vervoort et al. (1996) and Amelin et al. (1999) have used the $^{176}Lu - ^{176}Hf$ system to explore the nature of the Earth's early crust and mantle. Schmidberger et al. (2002) have explored the isotopic nature of the subcontinental mantle, an area that has yet to be investigated in detail with respect to Lu-Hf.

The Lu-Hf and the Sm-Nd systems are analogous to each other, as they fractionate in a similar fashion in terrestrial reservoirs. Because of this similarity, it has in the past been assumed that little extra information is to be gained from Lu-Hf studies; however, this is not the case (e.g. Vervoort et al. 1996; Vervoort and Toft, 1999). The most striking difference between the two systems is that Sm-Nd is a REE-REE pair of elements, while Lu-Hf is a HREE-HFSE pair. Lu-Hf therefore exhibits greater degrees of fractionation than Sm-Nd, and under some conditions, the two systems may be decoupled (e.g. Patchett et al. 1984; Salters and Hart, 1991; Vervoort and Patchett, 1996).

At higher temperatures, such at the ones in sub-continental mantle conditions, the Lu-Hf system has been shown to be more robust than the Sm-Nd system. The Sm-Nd system may be reset by metasomatic events, while Lu-Hf may not (e.g. Schmidberger et al. 2002). Also, because the Hf budget in some mafic rocks tends to reside in resistant minerals such as baddeleyite and zircon, while the Nd budget resides in various silicate minerals, the Hf composition of the rock may be less disturbed by alteration than Nd (e.g. Pearson and Nowell, 2003). This provides a strong rationale to investigate the Hf composition of the MI. Also, the combination of Hf and Nd isotopic data is a powerful tool, which would allow us to test for the presence of garnet in the source region (i.e. allow us to test for a deep source). In the shallow mantle, melting in the presence of garnet results in more extreme Lu/Hf fractionations (compared to Sm/Nd), and results in the decoupling of the two systems. As mentioned above, this is due to the different chemical behavior of Hf compared to the rare earth elements. The presence of garnet in the source region has been suggested for the lower flows of the CRB, but not the upper (Griselin et al. 1997).

If the MI is directly related to the CRB, then we should see this reflected in the Hf and Nd isotopes across the intrusion. According to Schmidberger et al. (2002), the shallow and deep subcontinental lithosphere beneath Somerset Island (north east of the Slave craton), are isotopically distinct domains. The shallow lithosphere stabilized in the Archean, has high Hf isotopic values (ε_{Hf} +53.3 - +8.5), suggesting mantle root formation in the presence of residual garnet (>80 km). While the deep lithosphere has lower Hf isotopic values (ε_{Hf} –3.3 - +21.8) is interpreted to represent younger mantle. Analysing Hf isotopes for the MI may allow us to better characterize the subcontinental lithosphere under the Slave craton, and determine if either the shallow or deep subcontinental lithosphere are involved in its genesis.

2.2.2 In situ Sr and Pb studies

With the advent of the laser-ablation multi-collector inductively coupled plasma mass spectrometer (LA-MC-ICPMS), it is now possible to measure variations in isotope compositions between and within individual mineral grains. This permits a new level of insight into the isotopic history of a region and magmatic processes, which were impossible to achieve using bulk dissolution. Use of the LA-MC-ICPMS is also a very rapid and less-destructive method of analysis compared to conventional techniques. It represents a significant advance in isotope geology.

In situ Sr-isotope analysis by LA-MC-ICPMS is a powerful tracer technique with widespread application to many fields of study. Examples of previous studies of magmatic-related systems include a study of feldspar phenocrysts in volcanic rocks by Davidson et al. (2001), and a study of clinopyroxene from peridotite xenoliths by Schmidberger et al. (2003). Davidson et al. (2001) used LA-MC-ICPMS to determine variations in $^{87}Sr/^{86}Sr$ across single plagioclase crystals from lavas of the El Chichon volcano, Mexico, to constrain timescales at which the crystals were held at magmatic temperatures. Schmidberger et al. (2003) analyzed Sr compositions of clinopyroxenes from peridotite xenoliths on Somerset Island, Canada, to examine the metasomatic history of the peridotites and the host kimberlites.

In situ Pb studies by LA-MC-ICPMS are still in the early stages of development. Mathez and Waight (2003) investigated the Pb isotope compositions of coexisting plagioclase and sulfide from the Bushveld layered intrusion by LA-MC-ICPMS. Their results show heterogeneity between layers of the intrusion, and require multiple sources of Pb during crystallization and/or soon after crystallization. Gagnevin et al. (2004) investigated the Pb isotopic composition of K-feldspar megacrysts from the Monte Capanne pluton in Italy, also using LA-MC-ICPMS. In addition, they investigated the Sr isotope composition of microdrilled samples from one megacryst using isotope dilution thermal ionization mass spectrometry (IDTIMS). Their results show strong zoning of Pb compositions within individual megacrysts, and show a decoupling between the two isotopic systems. The combination of Sr and Pb isotopes in a single feldspar grain is a virtually unexplored yet potentially powerful new technique.

CHAPTER 3: Petrology and Geochemistry

3.1 Sample Selection

A total of twenty-seven samples representative of the main rock types from the Muskox intrusion were investigated in this study and were selected from the same collection used in the geochemical study of Francis (1994) (Fig. 3.1). These samples were selected on the basis of: (1) level of geochemical contamination, (2) rock type, and (3) stratigraphic location within the intrusion, in order to obtain a varied sample collection.

The previous geochemical analyses of Francis (1994) were specifically used in the sample selection for this study. As shown in Francis (1994), a plot of K/Ti may be useful in identifying geochemically contaminated samples in this case, because K in the host rocks surrounding the MI is approximately ten times more abundant than in the Muskox magmas and is very mobile compared to Ti. Samples with a K/Ti ratio of ~1 or less are interpreted to be generally uncontaminated. We selected samples such that the majority had no or minimal evidence of major element modification by crustal contamination. A few samples were also chosen with high ratios of K/Ti (e.g. SL-42), in order to investigate any possible petrographic, geochemical, and isotopic differences these samples might show compare to the uncontaminated samples. Figure 3.2 shows that the samples obtained for this study are for the most part, relatively uncontaminated by crustal material, with the exception of a few samples (SL-42, EQ-15, and M-26).

The samples were also selected in part for their geographical location (Fig. 3.1) and rock type. Since previous isotopic studies of the MI have focused on the margins of the intrusion, one objective during sample selection was to obtain samples from across the entire length of the intrusion, wherever possible. Location selection was obviously limited by previous sampling and outcrop locations. Sample VD-850 comes from CU#21, the same unit which contains the Pt-bearing reef. Another objective was to obtain a relatively small but diverse sample set, with a focus towards samples that might contain the most primitive isotopic signature. Therefore emphasis was given in the selection of the more mafic rock-types. The sample distribution within the intrusion in this study differs from that of Stewart and DePaolo (1992), in that many samples were selected from lower units, which based on the geochemistry study of Francis (1994) are geochemically less contaminated.

In the following presentation of results, the data is grouped by both rock type and location, in order to illustrate particular relationships.

3.2 Petrology

This section is a general summary of the petrography of these samples. Detailed petrographic analyses are presented in Appendix A. The reader is referred to Francis (1994) for a more comprehensive description of the petrography of the entire intrusion. The terminology for rock lithologies for these samples is according to Francis (1994).

A total of seven samples from the Keel dyke are investigated. Rock types include olivine gabbronorites, gabbronorites, and one picrite. Typical textures of the rocks are diabasic, with subophitic intergrowths of clinopyroxene and plagioclase laths common (e.g. Fig. A.2, A.7). As well, orthopyroxene grains sometimes up to 12 mm in size form poikilitic textures (e.g. Fig. A.6). The most common mineral assemblage is: clinopyroxene (5-83%), orthopyroxene (1-85%), plagioclase (3-80%), biotite (<1-11%), ilmenite (<1-10%), ± olivine (3-49%), ± chlorite (<1-5%), ± apatite (<1%), ± baddeleyite (<1%), ± zirconolite (<1%). Samples are generally unaltered to moderately altered (refer to section 3.2.1). The main oxide phases are ilmenite and magnetite, which are closely associated with biotite (Fig. A.13). The oxides may be a late or secondary phase. Sulfides in the dyke samples are sparse, the main phase being pyrite, followed by chalcopyrite.

Samples from the layered series consist of olivine, clinopyroxene, and orthopyroxene cumulates. They are generally fine to medium grained with cumulate crystals up to 3 mm in diameter. Adcumulate (Fig. A.49) to heteroadcumulate textures are most common (Fig. A.44). Pyroxene oikocrysts occurring in the samples range from 1 - 7 mm in size (Fig. A.44). Chlorite and serpentine occur as alteration products, as well as biotite and ilmenite. The intercumulus minerals are predominantly orthopyroxene, clinopyroxene, or plagioclase, ± titanite, ± rutile, ± apatite, ± zircon, ± biotite, a variety of oxide minerals including magnetite, ilmenite, chromite, and a variety of sulfide minerals largely consisting of pyrite, pyrrhotite and chalcopyrite. Alteration of olivine within the dunites is pervasive, and consists mainly of serpentine (e.g. Fig. A.45 - A.48). Ilmenite and magnetite occurring after olivine is also present (Fig. A.45). Olivine in other cumulate samples is also altered, although to a somewhat lesser degree. Ilmenite and magnetite occur infrequently as intercumulus minerals, suggesting that they have formed during primary magmatic conditions. In most samples however, ilmenite occurs as thin and irregularly shaped needles in the cracks of altered olivines, thus suggesting that this phase was either remobilized during alteration, or that its growth is entirely secondary (e.g. Fig. A.47). The four megacycles of Francis (1994) begin with a thick olivine cumulate layer that becomes interbedded with pyroxenites. The crystallization sequence consists of: olivine, clinopyroxene, plagioclase, and orthopyroxene, for the lower megacycles. After CU 17, orthopyroxene replaces plagioclase in the sequence (Fig. 3.3).

Marginal rock samples consist of olivine gabbronorites, picrites, and a granophyre. The most common mineral assemblage is olivine + orthopyroxene + clinopyroxene + plagioclase + biotite + opaques, ± apatite ± baddeleyite ± zirconolite ± zircon. The rocks have non-cumulate textures (e.g. Fig. A.19). The samples show slight to moderate degrees of alteration, again largely of olivine to serpentine. In some samples oxides appear to be secondary minerals. Some orthopyroxene crystals are quite large in size and display exsolution lamellae (Fig. A.26), or are quite broken and cracked, reflective of oscillations and deviations from the cotectic (e.g. Fig. A.19, A.28).

3.2.1 Alteration

Typically the primary igneous mineralogy and textures are preserved in the rocks of the MI (Bedard and Taner, 1992). Intense hydrothermal alteration is rare. Where it

occurs, feldspar may be partially to completely sericitized, micas replaced by chlorite, and pyroxenes show development of turbidity (Bedard and Taner, 1992). Partial replacement of plagioclase by fine grained sericite is typical in the layered series (Francis, 1994). Alteration observed in nearby granophyric dykes and quartz-calcite veins may include pyroxene replacement by chlorite and actinolite, alteration of feldspars, and local development of epidote and pumpellyite (Bedard and Taner, 1992).

Of the samples observed in this study, those from the Keel Dyke are relatively fresh, showing only minor alteration of sericite after plagioclase and serpentine after olivine. All Keel Dyke samples (MR-25, MR-14, LJ-24, LJ-6, CR-6, CR-46, and CR-31) show this alteration in thin section. Samples LJ-6, CR-6, CR-46 and CR-31 show minor amounts of chlorite in thin-section. Sample CR-6 also shows a greater amount of olivine alteration to serpentine than the other Keel Dyke samples.

Alteration of olivine in the layered series is more pronounced. Within the peridotite samples (EQ-22, ES-10, V1-01, V1-05, V1-10), olivine is almost completely replaced by serpentine. Other samples which show extensive serpentinization of olivine, but are otherwise relatively unaltered include VD-707, VD-709, VD-722, EQ-20, and V1-02. Samples which show alteration of olivine to serpentine to a lesser degree include: EQ-14, EQ-13, and VD-724. Sample SL-42 shows significant alteration of plagioclase to sericite. Samples which show only minor degrees of alteration minerals, including sericite, serpentine, and chlorite are: EQ-20, EQ-19, EQ-15, EQ-6, V3-03, VD-850, M-26.

3.3 Mineral Chemistry

Whole rock samples were sectioned and the constituent minerals analyzed using the electron microprobe (JEOL 8900) at the University of Alberta. Quantitative analyses were performed using the wavelength dispersive method, using an accelerating voltage of 20 kV and a 20 nA beam current. Signal was measured for 20 seconds at peak position and for 10 seconds at each background position. Microprobe calibration was performed using natural mineral standards (Jarosewich, 2002). Detection limits for most elements analyzed were better than 150 ppm. Data reduction was performed using the $\Phi(\rho Z)$ correction according to Armstrong (1995). Back scatter electron (BSe) images were obtained for all polished thin sections to document mineral paragenesis and zoning. Quantitative electron microprobe (EMP) chemical analyses of the major minerals were obtained for 19 samples (extremely altered samples were excluded: EQ-22, ES-10, V1-01, V1-05, V1-10, CR-6, VD-707, VD-722). The data are reported in Appendix B. Efforts were made to analyze both the cores and rims of each selected grain, even if zoning was not apparent on the BSe. Chemical analyses were completed for the following major minerals: olivine, orthopyroxene, clinopyroxene, and plagioclase, and for the following minor minerals: K-feldspar, biotite, and apatite.

Olivine compositions range from Fo_{66} – Fo_{85}, with an average of Fo_{79}. These compositions are typical for olivine crystallizing from mafic mantle melts and have been reported from other LMI's (e.g. Stewart and DePaolo, 1990b). Approximately 50 grains in total were analyzed. Generally all analyzed grains were intercumulus grains in the layered series rocks. In a few samples, olivines of varying composition were observed.

In the marginal sample EQ-19, olivines of many different compositions exist, with no obvious correlation between grain size or location within the sample (Fig. 3.4). Compositions in this single sample range from Fo_{66} – Fo_{78}. Zoning was not observed. Occasionally in marginal samples, olivine exsolves magnetite (e.g. sample EQ-19). Fenner-type diagrams for olivine analyses are shown in Figure 3.5. In three samples, EQ-19, V1-02, and SL-42, Mn systematically increases with decreasing Mg#. (Fig. 3.5a,b) The average of all olivine analyses plots nearly directly in the middle of two broad clusters, which are separated by a small gap in Mg#. Figure 3.5c shows that the Mg# of olivine is dependant upon location. Samples from MC#2 have the highest Mg#s, followed by MC#3, MC#1, and finally marginal and Keel Dyke samples. Clinopyroxene and orthopyroxene also follow this general trend, as well as the whole rock data (section 3.4.2.1).

Clinopyroxene compositions are plotted in Figure 3.6. Compositionally, clinopyroxene has the following range in endmembers: $Wo_{27-45}En_{45-54}Fs_{6-25}$. The bulk of the analyses plot in the augite field. The dominant clinopyroxene composition is $Wo_{39}En_{50}Fs_{612}$. There are noticeable groupings of clinopyroxene compositions with stratigraphic level (Fig. 3.6a). Keel Dyke clinopyroxenes have slightly greater Fe contents, while clinopyroxenes from MC#2 have the lowest Fe contents. There is no observable relationship between measured core and rim compositions for the same grains (Fig. 3.6b), suggesting that clinopyroxene is generally not zoned. Zoned crystals are occasionally observed however; these crystals have Fe-rich rims (samples EQ-19, EQ-6, MR-14, and SL-42). Thin exsolution lamellae of orthopyroxene are also a common feature of clinopyroxene in the Muskox samples (Fig. 3.7). Quite often the exsolution is more pronounced on the rims of the grains. Sample LJ-6 contains some grains with a slightly different composition than the bulk of the analyses (Average: $Wo_{39}En_{41}Fs_{22}$), with higher FeO contents. This difference in mineral chemistry corresponds to a difference in whole rock geochemistry for sample LJ-6, which is discussed below. Samples MC#3, V1-02, and V3-03 have one analysis each which is slightly anomalous, plotting close to the dominant opx composition (Fig. 3.8) and may represent analysis spots which contain exsolution lamellae of opx.

Orthopyroxene compositions are plotted in Figure 3.8. Endmembers range from $Wo_{1-6}En_{49-84}Fs_{15-48}$. Compositions are generally enstatite. There is a noticeable correlation between geographical location and composition. Changes in composition are slight, with the exception of sample LJ-6, which again is distinctly different from all other analyzed opx grains. Sample LJ-6 opx grains show higher CaO and FeO, and lower SiO_2 and MgO. This also corresponds to a difference in whole rock geochemistry (section 3.4.2.1). Compositional zoning in orthopyroxene is sometimes observed in the Keel Dyke and marginal samples. Rims of the grains are higher in Fe content than the cores (e.g. CR-31, LJ-24, and MR-25). Exsolution is observed, but to a lesser extent than in clinopyroxene. Orthopyroxene and clinopyroxene are often closely associated or intergrown, especially in the layered series rocks.

Plagioclase composition is largely Bytownitic and Labradoritic, and clusters in the range of An_{60}-An_{80} (Fig. 3.9). Zoning is sometimes observed, the cores have higher An contents than the rims (e.g. EQ-6, MR-25, and VD-850). Relationships between location and composition are also noticeable in Figure 3.9. *K-feldspar* is present in several samples. It usually exhibits fine exsolution lamellae (presumably of plagioclase).

Figure 3.10 shows the average mineral analyses plotted together with the whole rock data, for select oxides. Generally, the mineral analyses outline fields in which the bulk of the whole rock analyses lie. This is consistent with the petrographic relationships, i.e. that the great majority of the rocks are made up of these few minerals.

3.4 Geochemistry

3.4.1 Analytical Methods

As mentioned above, the 27 samples selected for this study are from the collection of Don Francis and were previously analyzed for major, minor and some trace elements (Francis, 1994). A W-Carbide mill was used to process the samples into a powder. Data reported by Francis (1994) were analyzed at McGill University using a Phillips P1400 XRF on fused glass disks for major elements (precision varies between 0.001 to 0.058 wt.%), and Ba, Cr, Ni, and V (precision estimated to be ±5%). The trace elements Rb, Sr, Y, Nb, Pb, Cu, and Zn were analyzed by XRF on pressed pellets (precision estimated to be ±5%). However, none of these samples were analyzed previously for the complete suite of trace elements. For this study, the selected samples were analyzed for the full range of elements; the major, minor and some trace elements to directly compare with the results of Francis (1994) (Appendix C). The full range of trace elements analyzed in this study include the rare earth and high field strength elements, which are relatively immobile during alteration and are particularly useful for petrogenetic studies.

Samples were wrapped in multiple layers of plastic and underlain by cardboard and crushed using a sledge hammer. The gravel-sized fragments were subsequently ground to a powder using a motorized agate mill. Samples were analyzed at *Actlabs*, Ontario, using lithium metaborate/tetraborate fusion ICP for all major and several trace elements (Ba, Sr, Y, Sc, Zr, Be, and V). Trace elements were determined using ICP-MS (V, Cr, Co, Ni, Cu, Zn, Ga, Ge, As, Rb, Sr, Y, Zr, Nb, Mo, Ag, In, Sn, Sb, Cs, Ba, La, Ce, Pr, Nd, Sm, Eu, Gd, Tb, Dy, Ho, Er, Tm, Yb, Lu, Hf, Ta, W, Tl, Pb, Bi, Th, and U). Detection limits of the technique are listed in Table 3.1. The program *IGPET* (Carr, 1995) was used to plot the data.

3.4.2 Results

The geochemical data obtained in this study are reported in Table 3.1. Results obtained for this study are in good agreement with the data reported by Francis (1994). Reproducibility of results is excellent for all elements with the exception of Cr, V, Cu, Zn, and Nb (Fig. 3.11). For some elements, this may be due in part to the different powdering apparatuses used (W-Carbide vs. Agate mill), however most of the discrepancies may be due to the different analytical techniques employed (ICP versus XRF). Only the geochemical data obtained in this study are plotted on the following diagrams.

3.4.2.1 Major Elements

The samples are primarily mafic to ultramafic with SiO_2 contents that vary between 33.0 and 53.6 wt.% (Table 3.1) On an AFM diagram, nearly all samples plot towards the MgO-FeO side of the triangle, resembling a typical Fe-enrichment tholeiitic trend, just above the calc-alkaline field, with the exception of a few of the more felsic samples, the granophyre (M-26) and the migmatite (EQ-15) (Fig. 3.12). The more ultramafic samples cluster towards the high MgO apex, as would be expected. The gabbronorite sample LJ-6, has very low MgO and plots much further along the trend than the bulk of the samples. Note that the estimated liquid compositions of Francis (1994) plot in between this sample (LJ-6) and the rest of the samples.

Sample LJ-6 is from the Keel Dyke, and does not show appreciable alteration. The olivine gabbronorite sample SL-42 plots below the trend. This sample is significantly altered, and was specifically chosen as a geochemically disturbed sample from the collection of Francis (1994) in order to investigate the effect of contamination on the geochemistry of MI mafic samples (Fig. A.36). There is compositional overlap between the different rock types, which might be expected with cumulate rocks, as the proportion of intercumulus minerals can differ. Also, it appears that samples from the same mega-cycle cluster together on the diagram, apart from the few exceptions mentioned above. This observation of geochemical similarity within an individual mega-cycle is consistent with the views of Francis (1994).

Fenner variation diagrams for major elements are shown in Figure 3.13. The variation diagrams show changes in major element oxides plotted against MgO. The analyses conform broadly to evolutionary trends of increasing SiO_2, TiO_2, K_2O, Al_2O_3, and Na_2O. These trends confirm that the samples from this study are genetically related and compatible with fractional crystallization of olivine and pyroxene, but not plagioclase. Influxes of new magmas may obscure the effect of fractional crystallization of some minerals. As the MgO content decreases (due to crystallization of olivine), CaO, Al_2O_3 and Na_2O contents systematically increase (although the trend for CaO is weak), which is presumably due largely to the overlapping crystallization of pyroxene and plagioclase. As well, TiO_2 increases with decreasing MgO, consistent with the late crystallization of ilmenite. Mg # increases to a maximum of 0.88 at the beginning of MC#2, and then decreases steadily until MC #4 (Fig. 3.14).

Although the variation diagrams do show broad overall trends, the amount of scatter within some of the plots is significant. This may be attributed to the fact that many of the rock samples were formed by the accumulation of phenocrysts, and it is extremely unlikely that they represent true liquid compositions of the magma. As well, the samples were collected from different parts of the intrusion, and based on previous studies (e.g. Irvine and Smith, 1967; Francis 1994) each of the 25 cyclic units is interpreted to represent a separate pulse of magma into the intrusion. The more felsic samples, M-26 and EQ-15 have distinctly different geochemical signatures from the rest of the samples (Fig. 3.13), which is expected as they are distinctly different rock types (Appendix A).

The extent of sample alteration is detailed in Appendix A, and summarized in section 3.2.1. Comparison of the whole rock geochemistry with the petrographic observations in Appendix A reveals the following observations: (1) Samples showing

significant alteration (peridotites: EQ-22, ES-10, V1-01, V1-05, V1-10; other: CR-6, EQ-20, VD-709, VD-707, VD-722, V1-02), still conform to the tholeiitic trend and do not appear to have distinctly altered whole rock geochemical signatures, (2) Sample SL-42 is an exception to this observation and displays unusual geochemistry (low MgO content, plots off the tholeiitic trend, and consistently plots apart from the bulk of the data in Figure 3.13), presumably due to alteration and/or crustal contamination, (3) Samples EQ-14 and EQ-13 show some geochemical differences from other MC#1 samples (P_2O_5, K_2O, and TiO_2), and display only moderate signs of alteration.

3.4.2.2 Trace Elements

The abundances of compatible trace elements such as Ni, Cr, and Co, decline exponentially with the decrease of MgO, as would be expected if Ni and Cr are incorporated into cumulate olivine formed during fractional crystallizaion (Fig. 3.15). The behavior of incompatible elements is more complex. V behaves more as an incompatible element in the MI as its concentrations increase with decreasing MgO (Fig. 3.16). This feature, combined with the incompatible behavior of Ti (discussed above, Fig. 3.13) is consistent with the late crystallization of ilmenite and titanomagnetite, which sometimes occur as intercumulus phases (e.g. Fig. A.19, A.51). The concentration of high field strength elements (HFSE) and large ion lithophile elements (LILE) increases, sometimes rapidly, with decreasing Mg content (Fig. 3.16).

Rare earth element (REE) profiles for all the samples analyzed in this study are displayed in Figure 3.17a together with common mantle reservoirs, N-MORB, E-MORB, and OIB for comparison. The majority of MI samples analysed in this study show very slight to moderately enriched REE profiles (La/Yb_N = 0.5 to 5.4, excluding the felsic samples EQ-15 and M-26). REE profiles for the Keel Dyke samples are plotted separately in Fig. 3.17b and show LREE enrichment (between 5 to 40 times primitive mantle) regardless of rock type. They are mildly fractionated, and show a nearly flat HREE pattern [Average values: $(La/Yb)_N$ = 3.9, $(La/Sm)_N$ = 1.9]. This flat HREE pattern indicates that garnet was not in equilibrium with the melt at the time of segregation since garnet is known to preferentially concentrate the HREE during mantle melting if it is a residual phase. One would expect the REE pattern to be negatively sloped at the heavy end if garnet was in equilibrium with the melt at the time of segregation. There is a slight positive Eu* anomaly in two of the samples (MR-25, LJ-24) and slight negative Eu* anomaly in one sample (MR-14). Overall, the REE profiles indicate that plagioclase crystallization or accumulation was not an important process in the evolution of the Keel Dyke. REE profiles for marginal rocks are quite similar to those of the Keel Dyke (Fig. 3.17a).

Figure 3.17c shows REE profiles of the Keel Dyke samples in comparison with the estimated liquid compositions of the chilled margin of the Keel Dyke, and of the parental magma to MC#1 and MC#2 from Francis (1994). As is shown in the diagram, samples LJ-6 and CR-46 are most similar to the estimated primary liquid compositions of Francis (1994). REE profiles for the layered series (Fig. 3.17d, Fig. 3.18) are more complex. The more complex patterns may be in part due to fact that these samples are largely cumulates. Three main patterns that can be identified within the layered series are:

(1) Relatively flat to slightly LREE enriched patterns (Fig. 3.18a). These are clinopyroxenite and websterite samples. Both rock types contain moderate to large amounts of cumulus clinopyroxene (54 – 83%). The REE patterns are generally consistent with this observation. The REE pattern for sample VD-850 (Fig. 3.18b) is slightly fractionated towards the LREE end, and also shows a small positive Eu anomaly. Sample VD-850 is an orthopyroxenite, containing more than 80% cumulative orthopyroxene (Appendix A). The REE pattern itself would be more consistent with the accumulation of plagioclase rather than orthopyroxene, however this does not agree with the petrographic data. The Eu anomaly must reflect the small amount of plagioclase that is present in the rock.

(2) LREE-depleted patterns shown in Figure 3.18c (samples: EQ-22, SL-42, VD-709, VD-707, EQ-20, and V3-03). These samples all have large amounts (65 - 70%) of cumulus clinopyroxene (Appendix A). The REE pattern is also consistent with the accumulation of clinopyroxene. Sample SL-42 (Fig. 3.18c) shows a significant positive Eu anomaly ($Eu/Eu^* = 1.5$) which indicates the accumulation of plagioclase. This is in agreement with the petrographic data for this sample which shows approximately 30% plagioclase in the sample altered to sericite (Fig. A.36).

(3) Relatively LREE-enriched, flat HREE, and overall low total REE (samples: V1-10, V1-05, V1-01). Figure 3.18d shows the REE profile for the altered peridotite samples. The patterns show slight enrichment in the LREE, and likely reflect the accumulation of olivine crystals. Sample ES-10 contains much less altered olivine, and more clinopyroxene, than the other three samples (Appendix A). This difference is also reflected in the REE profile. The profile for sample ES-10 shows less fractionation between the LREE and the HREE (flatter pattern), and has overall higher abundances of these elements. Overall it bears more resemblance to the patterns of the clinopyroxenites seen in Figure 3.18a.

Mantle-normalized multi-element plots are shown in Figure 3.19. Generally the MI samples show enrichment in the incompatible elements relative to the more compatible elements. A noticeable feature in these plots is the ubiquitous presence of a negative Nb anomaly. Figure 3.19b shows the primitive mantle normalized element plots for the samples from the Keel Dyke. Noticeable features of this diagram are the positive Cs and K anomalies, and the negative Nb anomalies. As well, several samples have positive Ba and Sr anomalies. The Sr anomalies can be explained by the plagioclase accumulation in these samples (Appendix A). The negative P anomalies are consistent throughout the Keel Dyke samples. This may indicate the removal of P by a mineral phase, such as apatite, before crystallization of the magma. Cs, K, and Ba are all mobile elements which will be easily affected by contamination from crust, or later alteration. Figure 3.19c shows element plots for the altered peridotites. Relatively large negative anomalies for Ba, Nb, and Sr, and small positive Ti anomalies are the most noticeable features of this diagram. The Sr and Ba anomalies could reflect the fact that very little plagioclase or K-feldspar are seen in these cumulates, and these elements were

incorporated into these fractionating phases before the olivine accumulated. Figure 3.19d shows element plots for the clinopyroxenites. These samples show large variations in the mobile elements (Cs, Rb, and Ba), generally negative Sr anomalies, and again, negative Nb anomalies. These anomalies may indicate crustal contamination, or possibly melting of a mantle region which had already acquired the negative Nb signature. The slight positive Sr anomaly in two of the samples might reflect the clinopyroxene accumulation, as Sr is incorporated into the mineral structure to some degree. Figure 3.19e shows element plots for just two of the samples, SL-42 and VD-850. Both show large positive Sr and K anomalies, possibly reflecting plagioclase accumulation and alteration.

CHAPTER 4: Geochronology & Isotopic Analyses

4.1 Introduction

The recent development of multi-collector inductively coupled plasma source mass spectrometers has simplified the acquisition of precise hafnium isotope ratios, so the ^{176}Lu-^{176}Hf system has become a more widely applied isotopic tracer technique. As described in section 2.2.1, a combined Hf-Nd isotope study might provide additional insight into the nature of the MI mantle source, as the Lu/Hf ratio of a mantle-derived magma could be strongly influenced by the possible presence of garnet in the source. As mentioned previously, a small amount of radiogenic isotopic data has been previously reported for the Muskox intrusion but these studies have focused on the margins of the intrusion in order to evaluate the extent of crustal contamination (Stewart and DePaolo 1992; 1995; Mackie et al., 2005; 2006). The Pb isotope systematics of the MI have not been previous explored, despite the fact that Pb is a very sensitive indicator of crustal contamination. Therefore, a combined Hf-Nd-Sr-Pb isotope study of the Muskox Intrusion was conducted in order to most effectively evaluate the origins and isotopic evolution of the intrusion.

4.2 Whole Rock Isotopic Study

Eight samples representing a transect through the Muskox Intrusion and the Keel Dyke were chosen for a whole rock isotopic study. The locations of these samples within the intrusion are shown in Figure 4.1. An attempt was made to analyze samples that were generally unaltered (from a petrographic perspective), and undisturbed (from a geochemical perspective). For example, samples EQ-15, M-26, SL-42 and LJ-6 were specifically excluded because they are altered, more felsic or have an unusual geochemistry (Fig. 3.12). Although the whole rock geochemistry may be modified by magma processes, such as fractional crystallization, incompatible element ratios and radiogenic isotope ratios will not be modified by such processes. Despite the fact that many of the Muskox samples are cumulate samples and do not represent primary magma compositions, much information can still be gained from the analysis of their isotopic signatures. Thus, samples were selected based primarily on low K/Ti ratio, high Mg#, geographic location, rock type, and minimal alteration. The Hf concentrations in some samples were extremely low (< 0.2 ppm), and these samples were not chosen because it would be difficult to obtain precise isotopic analyses with the current protocol.

Samples were wrapped in multiple layers of plastic and underlain by cardboard during the coarse crushing procedure using a sledge hammer. This protocol minimized contact with metal surfaces and thus reduced the risk of possible contamination with tungsten, which could affect the Hf isotope measurements. The gravel-sized fragments were subsequently ground to a powder using a motorized agate mill.

All isotopic analyses were conducted at the Radiogenic Isotope Facility (University of Alberta) using the Nu Plasma Multi-Collector-Inductively Coupled Plasma Mass Spectrometer (MC-ICP-MS), with the exception of Rb-Sr measurements. The latter

were obtained using the Sector 54 thermal ionization mass spectrometer. An age of 1270 Ma was used in the calculation of Hf, Nd, and Sr initial ratios in order to facilitate comparisons between the results obtained in this study and previously published data (e.g. Griselin et al. 1997).

4.2.1 Analytical Methods

^{147}Sm-^{143}Nd

Sm-Nd isotopic analyses were conducted using isotope dilution thermal ionization mass spectrometry, according to the method of Creaser et al. (1997), with the exception that all isotopic measurements were conducted on a Nu Plasma MC-ICP-MS. Data was monitored by use of a Nu Alfa Nd isotopic standard for each analytical session. Measured values for the Nu Alfa standard during the time of analyses is presented in Appendix D. Total procedural blanks were <400 picograms for Nd and Sm. Isotope dilution was achieved using an in house tracer, Spike #3. Isotopic analysis of Nd was corrected for mass-fractionation using the exponential law and the accepted value of $^{146}Nd/^{144}Nd=0.7219$.

^{87}Rb-^{87}Sr

Isotope analyses were conducted using isotope dilution mass spectrometry, according to the method of Creaser et al. (2004) and references therein. Isotope dilution was achieved using in house tracer solutions, Spike #6 and Spike #4. Isotope ratio measurements were carried out on a Sector 54 multi-collector mass spectrometer. Sr aliquots were loaded using a TaF gel solution on a single Re filament. Accuracy of the Sr isotopic composition was monitored using the NIST SRM987 Sr isotopic standard. All isotopic analyses are normalized relative to a value of 0.710245 for the NIST SRM987 standard, and are corrected for mass fractionation using the exponential law by monitoring $^{86}Sr/^{88}Sr$ relative to the accepted value of 0.1194. Long-term measured values of the NIST SRM987 standard are summarized in Creaser et al. (2004), and a table of values is presented in Appendix D. Total procedural blanks were <150 pg for Sr and <200 pg for Rb.

$^{176}Lu - ^{176}Hf$

The flux fusion digestion procedure for whole rock samples and chemical procedure employed for the purification of Hf and Lu are described in Bizzarro et al. (2003). The protocol for solution mode Lu and Hf isotopic analysis on the MC-ICP-MS instrument is outlined in Schmidberger et al. (2005). For Lu/Hf isotope analysis, the samples were spiked with separate ^{180}Hf (98.3% enriched) and ^{176}Lu (70.9% enriched) tracers solutions. The procedural blanks for Hf and Lu are 80 pg and 20 pg, respectively. During this study, repeated measurements (n=18) of a 50 ppb JMC 475 Hf isotopic standard solution yielded the following average values (and 2σ standard deviation):

$^{176}Hf/^{177}Hf = 0.282157\pm14$, $^{178}Hf/^{177}Hf = 1.46728\pm7$, $^{180}Hf/^{177}Hf = 1.88678 \pm25$ (standard results are compiled in Appendix D). The Lu and Hf isotope ratios were monitored for Yb and W isobaric interferences, however, for the majority of samples investigated this correction was negligible. The measured Hf isotopic ratios were normalized to $^{179}Hf/^{177}Hf = 0.7325$ and corrected for mass bias using the exponential law (Russell et al., 1978).

4.2.2 Results

Measured Nd-, Sr-, and Hf-isotope ratios and Sm, Nd, Rb, Sr, Lu, and Hf concentrations are presented in Tables 4.1 to 4.3. Measured $^{143}Nd/^{144}Nd$ ratios for the samples range from 0.512124 ± 9 to 0.512707 ± 10, $^{87}Sr/^{86}Sr$ ratios from 0.707852 ± 13 to 0.714204 ± 11, and $^{176}Hf/^{177}Hf$ from 0.282291 ± 10 to 0.282858 ± 50.

The $^{147}Sm/^{144}Nd$ and $^{143}Nd/^{144}Nd$ ratios show a positive correlation and define an errorchron age of 1364 ± 170 Ma (MSWD=12; Fig. 4.2). The least radiogenic sample (i.e. most contaminated sample), MR-14, from the furthest extent of the Keel Dyke was omitted in the regression. This age agrees within analytical uncertainty the 1269 Ma accepted age of the intrusion based on U-Pb baddeleyite geochronology (LeCheminant and Heaman, 1989; French et al., 2002). The Rb-Sr data also show a broadly positive correlation between $^{87}Rb/^{86}Sr$ and $^{87}Sr/^{86}Sr$, but they do not appear to retain any geochronologically significant information. The Lu-Hf data however, give a very accurate and fairly precise age, defining an isochron of 1257 ± 58 Ma with a low MSWD of 1.11 (Fig. 4.3). The initial $^{176}Hf/^{177}Hf$ ratio given by this isochron corresponds to a ε_{Hf} value of +1.4. The accuracy of the Lu-Hf isochron provides some support that the initial Hf isotope ratios reported in Table 4.3 are also relatively accurate.

The Nd and Sr data reported in this study agree well with the whole rock Nd and Sr data of Stewart and DePaolo (1995) for samples from the same stratigraphic levels (Mega-cycles #3 and #4, Fig. 4.4). The Nd data for samples from MC#3 and #4 are in better agreement with the data of Stewart and DePaolo (1995) than the Sr data. This is not surprising considering that the Rb-Sr system can be more susceptible to disturbance from alteration or metamorphism. The new Nd isotopic data obtained by this study are more precise and are less variable over the length of the intrusion than the data of Stewart and DePaolo (1995), especially when viewed in direct comparison to rocks of similar stratigraphic height (MC#3 and #4). Figure 4.4 also shows that this study has effectively extended the isotopic transect across the MI to also include more samples from MC#1 and the Keel Dyke. A slight trend towards more negative ε_{Nd} values occurs with decreasing stratigraphic height. Sample MR-14 shows the lowest initial ε_{Nd} value of -3.2, the highest initial $^{87}Sr/^{86}Sr$ value (0.70747) and also one of the lowest initial ε_{Hf} values of 0.4. This is also consistent with the Sr isotope data in plagioclase (which is presented in section 4.3.2).

The Sr isotope data show fairly good correlation with the Nd isotope data over the length of the intrusion (Fig. 4.4), this is especially apparent in the Keel Dyke samples. Figure 4.5 shows that the broad correlation between initial Sr and Nd isotope ratios for the samples is typical of mantle-derived materials that show contamination from material which has a time-integrated LREE enrichment, such as the crust. Two samples that

deviate from this trend are VD-724 (clinopyroxenite) and VD-850 (orthopyroxenite), and were collected within 2 km from the north shore of Speers Lake (Francis 1994). Both of these samples originate from upper mega-cycles in the layered series (MC#3 and #4). Figure 4.6 shows their geochemical profiles. Sample VD-724 shows an anomalously low $^{87}Sr/^{86}Sr$ value, and is less radiogenic than any other analysis by Stewart and DePaolo (1995). Sample VD-850 on the other hand also has a higher initial ε_{Nd} value (-0.2) compared to most samples investigated in this study, but has one of the higher initial Sr isotope compositions of 0.706998. Sample VD-850 comes from an orthopyroxenite layer which contains the Pt-bearing reef.

Figure 4.7 shows the Hf isotope data compared to the Nd and Sr isotope data. The most notable feature is the remarkably consistent Hf isotope composition across the entire intrusion and feeder dyke. A small range of ε_{Hf} (1270 Ma) values between +1.3 and +1.5 is defined by 5 of the 8 samples. All samples plot in this range within analytical error, with the exception of samples VD-850 and MR-14. The majority of the Hf isotopic data obtained here lie within the large range of ε_{Hf} values (ε_{Hf} = -15 to +2.0) reported for the marginal rocks of the MI by Mackie et al. (2005). Sample VD-850, which comes from the upper Megacycle of the intrusion (CU#21), has an ε_{Hf} value of +3.2±0.4 just exceeding the range of the bulk of the samples. As mentioned previously, this particular sample contains an unusually high radiogenic $^{87}Sr/^{86}Sr$ composition (Fig. 4.7a), and the most primitive ε_{Nd} value. Sample MR-14 from the Keel Dyke has an ε_{Hf} value of +0.4 ±0.4, which is slightly lower than the values for the main intrusion.

The similarity of the Lu-Hf and Sm-Nd isotope systems in most mantle differentiation processes causes the initial ε_{Hf} and ε_{Nd} values to be positively correlated, in a relationship where $2\varepsilon_{Hf} = 1\ \varepsilon_{Nd}$ (Salters and White, 1998, and references therein). Figure 4.7b shows that the correlation between Hf and Nd isotopes in the Muskox samples is very slightly displaced off the terrestrial evolution trend. Figure 4.8 shows that ε_{Nd} decreases with increased evolution of the magma (decreasing Mg#), while ε_{Hf} is relatively independent of Mg#. This is further evidence that the Hf data are more robust than the Nd data.

4.3 *In Situ* Sr and Pb Isotopic Study in Plagioclase

4.3.1 Analytical Methods

The locations of samples selected for the in situ isotope study are shown in Figure 4.1. *In situ* Sr and Pb isotopic measurements were determined on single plagioclase grains (300 – 700 microns in their smallest dimension). These grains were separated by hand from sieved fractions of crushed whole rocks, mounted in 2.5 cm epoxy disks, and polished using a 0.3 micron aluminum oxide grit. Plagioclase grains were selected using a binocular microscope to be generally free of inclusions and fractures, and exhibited a low degree of alteration. The in-situ Sr and Pb isotope analyses were determined using a Nu Plasma MC-ICP-MS instrument coupled to a 213 nm Nd: YAG laser system (New Wave Research). The analytical protocol adopted in this study is similar to that described in Schmidberger et al. (2003). Plagioclase grains were ablated using a spot size of 160 μm, 20 Hz repetition rate, and laser output at approximately 3 mJ. Due to the small size

of the plagioclase grains, generally only one analysis was permissible per grain. The ablated particles were flushed out of the ablation cell with He gas (flow rate of 1.0 mL/minute). Ar gas was mixed with the ablated particles and He carrier gas via a 'y-connection' to the 'sample-out' line from a desolvating nebulizing system (DSN-100 from Nu Instruments Inc.). Sr isotope data were obtained in static, multi-collection mode using six Faraday collectors. For each analysis, data acquisition consisted of a 30 second measurement of the gas blank prior to the start of ablation, which is critical for the correction of the ^{86}Kr and ^{84}Kr isobaric interferences. For correcting the ^{87}Sr isobaric interference from ^{87}Rb, the ^{85}Rb ion signal was also monitored and used to make the correction. The duration of the laser ablation runs were variable (between 20 to 80 seconds), and depended mainly on the time taken to ablate through the grain being analyzed. Accuracy and reproducibility of the Sr isotope values were verified using an internal standard consisting of a modern-day coral yielding an average value of 0.70920 ± 0.00008 (2σ; n>50). The coral originates from the Ribbon-Reef deposit surrounding Mayotte Island in the Indian Ocean (Lat 12°50'S, Long 45°20'E). A compilation of *in situ* analyses of the standard are presented in Appendix D.

In situ Pb isotope analyses were made possible due to a modified collector block consisting of 12 Faraday buckets and three ion-counting channels dispersed on the low mass side of the collector array. The collector configuration allows for the simultaneous acquisition of ion signals ranging in mass from ^{238}U to ^{203}Tl, an important factor in obtaining highly precise and accurate isotope ratio determinations. ^{207}Pb, ^{206}Pb, and ^{204}Pb ($+^{204}Hg$) signals are measured on the ion counting channels, whereas ^{205}Tl and ^{203}Tl are measured on Faraday collectors (Simonetti et al. 2005). The Faraday-ion counter bias was determined at the start of each analytical session using a mixed 0.4 ppb standard solution of Pb (NIST SRM 981) and Tl (NIST SRM 997). This approach is similar to that adopted in previous isotopic studies involving MC-ICP-MS instruments equipped with multiple ion-counting devices (e.g. Taylor et al. 2003). Prior to the start of an ablation run, a 30 second blank measurement was conducted, which included correction for the ^{204}Hg ion signal (typically between 700 to 1000 cps). Possible isobaric interference from ^{204}Hg was evaluated with an additional peak-jump acquisition step that measured the intensity of ^{202}Hg. There was no detectable amount of excess ^{202}Hg present during the laser ablation analyses, i.e. amounts were essentially identical to those measured in the gas (+acid) blank prior to the laser ablation of the grains. For lead isotope ratio measurements, plagioclase grains were ablated using a 160 μm spot size, 20 Hz repetition rate and energy density of ~15 J/cm^2. A 140 micron spot size was used for several smaller grains. Ablation experiments were conducted in a He atmosphere (flow rate = 1.00 liter/minute), and ablated particles (+He gas) were simultaneously mixed with a 1 ppb Tl isotopic standard (NIST SRM 997); the latter was aspirated with Ar using a DSN-100 (desolvating nebulizing system) in order to monitor instrumental mass bias. The duration of the laser ablation runs ranged from 20 to 80 seconds, and depended mainly on the time taken to ablate through the analyzed grain. An image of a plagioclase grain after ablation is shown in Figure 4.9. If the grain was very thin (< 100 microns), the laser was constantly moved across the grain, rastering over the sample surface. This approach enabled a longer analysis time than would otherwise have been possible. The rastering technique increases the standard error, and was avoided wherever possible. Accuracy and reproducibility of the $^{207}Pb/^{204}Pb$, $^{206}Pb/^{204}Pb$, and $^{207}Pb/^{206}Pb$ values obtained using

the multiple ion counting system were assessed with repeated laser ablation analysis (n=10) of the NIST 612 glass wafer, and a fragment of amazonite feldspar from the Broken Hill deposit. The average values and associated standard deviations (2σ level) obtained for the NIST 612 are: $^{207}Pb/^{204}Pb$ = 15.48±0.36, $^{206}Pb/^{204}Pb$ = 17.16±0.28, and $^{207}Pb/^{206}Pb$ = 0.9034±0.0084. Average values and standard deviations (2σ level) for the Broken Hill amazonite feldspar are (n=12 analyses): $^{207}Pb/^{204}Pb$ = 15.50±0.21, $^{206}Pb/^{204}Pb$ = 16.08±0.17, and $^{207}Pb/^{206}Pb$ = 0.9638±0.0097. The average Pb isotope values for both the NIST 612 glass wafer and Broken Hill amazonite are in good agreement with their respective previously published TIMS results (e.g. NIST- Woodhead and Hergt, 2001; Broken Hill deposit- Sangster et al., 2000). $^{238}U/^{204}Pb$ (μ) values were estimated using simultaneous collection of ^{238}U in a Faraday collector. The values were generally zero or near zero, therefore the measured Pb isotope ratios are taken to represent initial ratios.

4.3.2 Results

Measured Sr- and Pb- isotope ratios for each spot analysis are presented in Tables 4.4 and 4.5. Analyses with very high standard errors are omitted (approximately 1 – 2 analyses per sample). Analyses which were only rejected for regression analyses due to high standard errors are highlighted in red in Tables 4.4 and 4.5. Analyses with clearly erroneous values are highlighted in blue. Weighted average values per sample are also presented in Tables 4.4 and 4.5 based on signal intensity obtained during analysis for the largest measured isotope (e.g. ^{88}Sr and ^{206}Pb). Each result presented in the tables represents only one spot analysis per grain. The petrographic features of each grain were recorded, including any fractures, cloudy or altered spots. Generally these features were able to be avoided, with the exception of sample SL-42. The plagioclase separated from sample SL-42 was pervasively cloudy and altered. The isotopic composition of this sample is also quite disturbed, as shown in Tables 4.4 and 4.5, and figures presented in the next section. Other than sample SL-42, there were no obvious visible distinctive petrographic features for grains which had unusual isotopic compositions or high standard errors. For example, there is no observable relationship between the measured Sr and Pb isotope values and visible alteration. As well, because only one spot analysis per grain was permissible, any possible effects of zoning on the isotopic composition of plagioclase remain undetermined.

Plagioclase In Situ Sr Isotope Compositions

Most isochron (or errorchron) ages overlap the age of the intrusion within error (e.g. Fig. 4.10). Two samples (CR-46 and LJ-24) give slightly younger ages than the actual age of the intrusion, and one sample (VD-850) gives an older age than the age of the intrusion. The associated errors for these isochrons are fairly large, thus the Sr isotopes in plagioclase do not appear to retain any geologically useful information. Figure 4.11 shows a comparison of these isochrons. Despite the range and uncertainty in

the internal Rb-Sr ages, the initial strontium ratios of most samples are similar (initial $^{87}Sr/^{86}Sr$ ranging from 0.70489 to 0.70697).

Some individual spot analyses showed a strong linear relationship between the measured values of $^{87}Rb/^{86}Sr$ and $^{87}Sr/^{86}Sr$ during a single run. Where the correlation between these measured ratios was strong (i.e. $R^2 \geq 0.9$), an internal spot isochron for the grain was calculated (Table 4.4). Generally these internal spot isochron ages are younger than the age of the intrusion. Their significance, if any, is uncertain.

The *in situ* Sr isotope plagioclase compositions are consistently lower than the measured whole rock values for the same samples (Fig. 4.12). For example, the whole rock initial $^{87}Sr/^{86}Sr$ (1270 Ma) composition for sample LJ-24 is 0.70563, whereas the average *in situ* plagioclase composition of the same sample is 0.70463. Figure 4.13 shows the initial $^{87}Sr/^{86}Sr$ values and average An contents measured on the electron microprobe for plagioclase in the same samples. Generally the data show lower initial $^{87}Sr/^{86}Sr$ values for samples with higher An content, which is consistent with increased levels of crustal contamination during an evolving magma.

Plagioclase In Situ Pb Isotope Compositions

Measured $^{206}Pb/^{204}Pb$ and $^{207}Pb/^{204}Pb$ ratios for all samples range from 11.52 to 17.98 and 11.21 to 17.02, respectively. The large variation can be accounted for by a few anomalous samples (VD-850 and SL-42). Generally the bulk of the ratios lie in the approximate ranges of: $^{206}Pb/^{204}Pb$ = 15.13 to 16.59 and $^{207}Pb/^{204}Pb$= 14.53 to 15.82. A surprising result from this study is that for some samples (e.g. sample V3-03) there is a range of Pb isotopic compositions recorded for different feldspar grains within a single sample. However a few samples have more tightly constrained compositions (e.g. sample CR-46), keeping in mind the different number of grain analyses available. The feldspar Pb isotope compositions for most samples define similar linear arrays in $^{206}Pb/^{204}Pb$ and $^{207}Pb/^{204}Pb$ space (Fig. 4.14), which overlap the single-stage model 1270 Ma isochron within error. The bulk of the data lies between primary mantle evolution curves with μ values between 7 and 9. Sample VD-850 is an exception to this trend, these analyses are more scattered with some plotting to the right of the Geochron. Figure 4.15 shows the average Pb isotope plagioclase composition from an individual sample plotted against stratigraphic height as in previous figures. The $^{207}Pb/^{206}Pb$ values don't show a great deal of variation over the length of the intrusion and feeder dyke, with the exception of sample VD-850. The plot of $^{206}Pb/^{204}Pb$ and $^{207}Pb/^{204}Pb$ ratios versus stratigraphic height shows sample SL-42 as a clear outlier. Figure 4.16 shows the $^{207}Pb/^{206}Pb$ values plotted against plagioclase composition. Again, sample VD-850 is an obvious outlier. Generally the data show decreasing $^{207}Pb/^{206}Pb$ values as An content decreases. As with the $^{87}Sr/^{86}Sr$ values (Fig. 4.13), this would suggest that the Pb isotope composition was subject to slight modification (possibly crustal contamination) as the magma progressively evolved.

Comparison

In situ Pb isotope compositions were obtained for the same plagioclase grains used in the Sr isotope study. A comparison between initial Sr and Pb compositions for each grain is shown in figure 4.17. The data shows a clear cluster of values with $^{87}Sr/^{86}Sr$ and $^{207}Pb/^{206}Pb$ values that vary between 0.70469 to 0.70581 and 0.94 to 0.97, respectively. There are two main outliers from this group of values. Sample MR-14 has consistently high initial $^{87}Sr/^{86}Sr$ ratios (~0.7070), which may be attributed to upper crustal contamination. This is in agreement with the whole rock isotope data. Sample VD-850 shows increasing Sr ratios with decreasing $^{207}Pb/^{206}Pb$ ratios. The Pb data from figure 4.14 shows that the $^{207}Pb/^{206}Pb$ values of this sample may be altered, possibly by later infiltrating fluids. The *in situ* isotope data for this sample show that some grains may be affected by both alteration and crustal contamination.

CHAPTER 5: Discussion

5.1 The Muskox Intrusion

5.1.1 Assimilation

Geochemical constraints

The mantle-normalized multi-element plots of the MI and Keel Dyke (Fig. 3.19) show enrichment in the incompatible elements and negative Nb anomalies. A negative Nb anomaly can be attributed to the presence of residual Nb (Ta)-bearing mineral (such as rutile, ilmenite, or titanite) in the source region, because Nb tends to be concentrated in Ti-bearing minerals (Elliott et al. 1997). In intraplate settings, far from subduction zones, this type of anomaly is commonly attributed to contamination of the primitive mantle-derived magmas by the upper continental crust or is a feature of the subcontinental lithospheric mantle that acquired a previous subduction geochemical imprint (McDonough, 1990). Often it is difficult to distinguish between subduction related imprints and those of crustal contamination (Davidson, 1996). For the Muskox magmas, other evidence for crustal contamination is seen in small spikes of Cs, Rb, and K. A lack of a negative Ti anomaly is also further evidence for crustal contamination rather than subduction overprint. Other features include Ba, Sr and Zr anomalies in some samples.

Other geochemical evidence for crustal contamination in the MI includes the presence of granophyric textures (Fig. A.53), elevated ratios of LIL/HFS elements, and enhanced orthopyroxene crystallization along the margins (Francis, 1994). The arguments of Francis (1994) are summarized in section 2.1.2.3.

Isotopic constraints

In addition to the study of Francis (1994), crustal contamination in the MI has been explored by Stewart and DePaolo (1992, 1995), as reviewed in Chapter 2. Stewart and DePaolo (1995) note large differences between the Sr (and Nd) isotope composition of the mafic cumulates and those of the granitic wall rock, therefore making the Sr and Nd isotopic compositions a sensitive indicator of contamination. In light of their results, it is therefore reasonable to view higher Sr isotope ratios and lower Nd isotope ratios in the Muskox and Keel Dyke samples as generally more contaminated. However, the isotopic uniformity of the Muskox samples (excluding the uppermost layer) revealed in this study cannot easily be reconciled with extensive crustal assimilation by the parental magma. Contamination with differing amounts of older crust would result in mixing arrays between end members, such as the upper crust (UCC) and depleted mantle (DM), for example. As evidenced from figures 4.4, 4.5, and 4.7, this is not the case. In this respect, the results of this study are in agreement with the findings of Stewart and DePaolo (1992), that suggest contamination of the MI was minimal until CU#25. Also, Mackie et al. (2006) suggest isotopic contamination of the marginal zone of the MI is restricted to an extremely thin zone directly adjacent to the margin of the intrusion. The

magmas which produced the layered series would have to be extremely well mixed prior to crystallization to produce such a remarkably consistent signature. It is unlikely that this level of homogeneous mixing could be achieved at near surface levels. Contamination of the original parental magma could have occurred at deeper levels in the lithosphere, and be extremely well mixed, prior to entry to the Muskox chamber (discussed below). There is virtually no isotopic proof of extensive crustal assimilation in the MI, except at the very margins of the intrusion.

The extensive geochemical contamination of the layered series documented by Francis (1994) is not reflected in the existing isotopic data for the MI. Francis (1994) suggested that the reason for this discrepancy exists because of the relatively low sampling density of Stewart and DePaolo (1995). The addition of isotopic data from a more complete transect through the intrusion in this study suggests that this may not be the case. Efforts were made to select the geochemically least contaminated samples from the collection of Francis (1994) for the purposes of this study, while the samples chosen by Stewart and DePaolo (1995) come from near the top of each cyclic unit, which in theory would be the most contaminated. Despite this difference, there is little variation between the isotopic values recorded by each study. This reinforces the case against extensive isotopic contamination in the MI. Stewart and DePaolo (1995) suggest that the trace element patterns observed by Francis (1994) reflect some other process such as mixing of chamber magmas with intercumulus liquids. In theory, it is also possible that the contamination reflected in the trace element composition of the intrusion came preferentially from wall rock with similar isotopic signatures to the intruding magma (Stewart and DePaolo, 1995). This explanation seems unlikely given the large geochemical contrast between the MI and country rocks. Also, Stewart and DePaolo (1995) report initial $^{87}Sr/^{86}Sr$ (1270 Ma) values for granitic wall rocks of 0.73842 and 0.78881, and ε_{Nd} values of -22 and -20. However, the geochemical contamination documented by Francis (1994) is selective and increases in the order: high field strength elements, HREE, LREE, LILE and chalcophile elements, which might explain the variation of disturbance in the isotopic systems. Isotopic variability between the different systems analyzed in this study similarly increases in the order: Lu-Hf, Sm-Nd, and Rb-Sr. Although there may be other factors influencing this observation, such as the increased likelihood of remobilization of LIL elements after crystallization, the possibility of selective contamination affecting certain isotopic systems to differing degrees is an interesting one. In any case, it appears as if selective diffusion rather than bulk assimilation was the dominant process at work in the main part of the MI.

Significant crustal contamination appears to be restricted to a thin boundary zone on the margins of the intrusion (Mackie et al., 2005; 2006) and to the uppermost part of the intrusion (Stewart and DePaolo, 1992). Cyclic unit 25 appears to have crystallized to completion from a single pulse of magma. Stewart and DePaolo (1992) show that assimilation during crystallization of this layer was minimal for the first 50 – 80% of crystallization, as the ε_{Nd} values remain unchanged until the last few meters of the unit. Differences in buoyancy and viscosity between the inflowing mafic magma and the silicic magma (melted wall rock) appear to have largely kept the two from mixing. Infrequent, episodic mixing is not precluded from the isotopic evidence provided by this study, and serves to explain many of the petrographic and geochemical variations observed by Irvine and Smith (1967), Francis (1994), and references therein.

Evidence for crustal contamination in the Keel Dyke is apparent from the Nd and Hf isotope composition of sample MR-14 (Fig. 5.1), compared to the relatively consistent isotopic compositions preserved throughout the intrusion. It appears as though this sample has assimilated a larger amount of crustal material than any other sample, enough to modify the composition of all three isotopic systems, which would be consistent with greater assimilation of local country rock. Stewart and DePaolo (1995) also document isotopic contamination in the Keel dyke, however, the sample showing the highest $^{87}Sr/^{86}Sr(T)$ (0.75259) and lowest $\varepsilon_{Nd}(T)$ (-10.4) is relatively silicic and thought to represent remobilized wall rock, interfingering with the chill margin of the dyke. The samples used in this study were deliberately chosen because they did not display obvious signs of interaction with wall rocks. The movement towards more negative ε_{Nd} and higher $^{87}Sr/^{86}Sr$ values southward in the Keel Dyke indicates a trend towards more contaminated values. This is consistent with the view that the older, more differentiated liquids in the MI were vented southward, through the Keel Dyke (Irvine and Smith, 1967; Stewart and DePaolo, 1995).

Details on the extent of crustal assimilation during evolution of the Muskox magmas remain uncertain. Whatever the contamination of the bulk of the MI is, it does not appear to be significant enough to have affected the Hf or for the most part, Nd isotopes. There is no isotopic evidence of large scale contamination in the main body of the intrusion. Therefore, contamination must have either been selective, and/or insignificant, probably on the order of less than 5%, as estimated in Stewart and DePaolo (1995) and confirmed by this study.

5.1.2 Isotopic Constraints for Parental Magma Source

A summary diagram for the Sr, Nd, Hf, and Pb isotope composition of the MI, along with all previous and related data is shown in Figure 5.1. This figure will be referred to throughout this chapter. The following discussion will be ordered by isotopic systems.

Hf and Nd

The accuracy and precision of the Lu-Hf isochron obtained from samples across the entire intrusion, and the extremely constant initial $^{176}Hf/^{177}Hf$ composition both indicate that the Lu-Hf data are more robust than any of the other isotope systems used in this study. The Hf isotope data do not reflect significant amounts of crustal contamination or disturbance from later metamorphic events, and therefore likely represent primary magma values. Very little published Hf isotope data exists for layered mafic intrusions. A recent study by Andersen and Griffin (2004), documented Hf and U-Pb isotope compositions of zircons from the Storgangen intrusion in Norway. The whole-rock Hf isotope data obtained in this study is the first data set of its kind ever obtained for a layered mafic intrusion. The Hf isochron age (1257±58 Ma) obtained by this study proves that in the absence of any baddeleyite, zircon, or other separable mineral, the Lu-Hf whole rock system can provide a feasible way to determine the age of

a layered mafic intrusion. In this study, the Lu-Hf isochron is significantly more accurate and precise than the Sm-Nd isochron.

The Hf and Nd whole rock isotope data are relatively homogeneous and indicate a near-chondritic source for the MI (Fig. 5.1). This is consistent with the suggestion that the Muskox magmas originated from a mantle plume of upwelling asthenosphere (LeCheminant and Heaman, 1989). The consistency of the initial ratios between different layers of the intrusion supports the concept of enrichment in incompatible elements being an inherent characteristic of the mantle source region (Francis, 1994 and references therein). The uniformity of the isotope data throughout the intrusion, in particular the Hf data, indicates that the Hf isotopic composition of the different batches of magma that entered the Muskox magma chamber were not affected by local crustal contamination and supports the conclusion that the isotopic composition of the rocks has been largely acquired from their mantle source, and that a single essentially homogeneous mantle source was responsible for the bulk of the Muskox magmatism. The incompatible element enriched magmas which fed the MI, could have originated from the subcontinental lithospheric mantle, or from plume-derived mantle. Primitive magmas from other sources such as oceanic basalts are relatively depleted in incompatible elements and are sourced in the depleted mantle. This vast reservoir of mantle material does not appear to be directly involved in the petrogenesis of the MI. Both the SCLM and a mantle plume could in theory be able to produce geochemically enriched and isotopically homogeneous magmas (Francis, 1994). The isotopic homogeneity and volume of the MI alone, without association with MIE, would support derivation from melting in the mantle in the vicinity of a rising mantle plume. Crustal contamination is isotopically only recorded at the uppermost layer of the intrusion, an extremely thin zone directly adjacent to the margin, and in the southern regions of the Keel Dyke, and appears to be relatively minor (section 5.1.1).

As mentioned in Chapter 4, one sample (VD-850) from the uppermost part of the intrusion shows a slightly more depleted Hf isotope composition with an ε_{Hf} of +3.2. If this sample has undergone any amount of crustal assimilation, it has clearly been selective, affecting only the Sr isotopes and not the Nd or Hf isotope systems. The fact that this sample VD-850 shows the most depleted ε_{Hf} signature and comes from near the top of the intrusion could indicate that the primary signature of the magma had evolved slightly from $\varepsilon_{Hf} \sim +1.4$ to +3.2. It may hint at the possibility of magma from a depleted mantle reservoir interacting with the chondritic Muskox magma towards the end of crystallization of the MI. However, since the composition of the DM at 1270 Ma is approximately $\varepsilon_{Hf} = +11$, any possible interaction with a depleted mantle reservoir would appear to have been minor. As previously indicated, this sample comes from an orthopyroxenite unit which contains the Pt-bearing reef. Irvine (1977) concluded that this layer formed when an influx of chemically primitive magma mixed with the more evolved magmas in the intrusion. The Hf isotopic data appear to support this conclusion.

Sample MR-14 from the Keel Dyke has a ε_{Hf} value of $+0.4 \pm 0.4$, which is slightly lower than the values for the main intrusion. It appears as though this sample has assimilated a significant amount of crustal material than any other sample, enough to modify the whole rock composition of all three isotopic systems (Sr, Nd, and Hf) (Fig. 5.1).

The Nd data also show a slight trend towards more negative ε_{Nd} values with decreasing stratigraphic height. If this trend represents a contamination trend, then this is contrary to previous reports within the literature (i.e. Francis, 1994; Stewart and DePaolo, 1995). These previous studies of the MI have shown that assimilation of wall rock material increases upwards in the intrusion. Francis (1994) suggest that the degree of contamination of the MI changes up section across margins of the layered series and that the Muskox magma was eroding its country rock in the upper two megacycles of the intrusion. Francis (1994) also suggests that episodic mixing between contaminated and pristine magma occurred in megacycles #3 and #4. It is therefore likely that the Nd isotope values are largely independent of local contamination and reflect the values of the magma source or small amounts of contamination at deeper crustal levels.

Sr and Pb

The Sr and Pb compositions of the MI are also relatively consistent over length of the intrusion and range from broadly chondritic to more evolved compositions (Fig. 5.1). However, there is evidence of contamination in the upper most layers and the Keel Dyke (discussed below).

As mentioned in section 4.3.2, the initial Sr isotopic compositions of plagioclase are consistently lower than the matching whole rock compositions. This could be explained by early crystallization of plagioclase, prior to significant crustal contamination; however plagioclase in these samples does not appear to be a cumulate phase. Petrographically, plagioclase does not appear to have crystallized early (Appendix A). Also, with the exception of samples SL-42 and LJ-24, the samples generally do not show positive Eu anomalies (Fig. 3.18, 4.6), which would also suggest that plagioclase was not an early crystallizing phase. It is more likely that there was an incomplete disturbance of the Rb-Sr isotopic system, causing some parts of the whole rock (perhaps along grain boundaries) to have altered Sr isotope compositions, which have pushed the whole rock compositions to higher values. The results from the *in situ* Sr isotope study are therefore interpreted to be a more accurate estimate for the undisturbed sample and have the potential to record primary magma compositions.

Figure 5.1 shows the Sr compositions of the plagioclase and whole rock data from this study, compared to that of Stewart and DePaolo (1995). Unlike the data from this study, the plagioclase fractions from Stewart and DePaolo (1995) are less primitive than the matching whole rock compositions. This contrast may be explained by different analytical techniques. It is possible that the unleached plagioclase fractions analyzed by Stewart and DePaolo have sampled extraneous Sr located on grain margins and along fractures, which were able to be avoided for the most part by the laser ablation technique used in this study. Alternatively, the plagioclase fractions selected by Stewart and DePaolo may have contained a higher proportion of grains which crystallized later in the magma evolution from a more contaminated magma.

Also shown in Chapter 4, the Rb-Sr systematics of the whole rock and of the plagioclase grains analyzed do not appear to retain any geologically useful information. The Rb-Sr isotopes of the grains analyzed may have been affected by either hydrothermal fluids or perhaps a metamorphic event. The Rb-Sr data of Stewart and DePaolo (1995)

are also suggestive of a low-grade metamorphic event, occurring around 1000 Ma, which disturbed the Rb-Sr isotope system on a millimeter to centimeter scale. Rocks of the MI however, do not show any significant evidence for metamorphism, as the samples are generally pristine. The greater mobility of Rb in hydrothermal fluids compared to Sm-Nd and Lu-Hf, and greater diffusivities of alkali elements relative to those of rare earth and high field strength elements, makes the Rb-Sr isotope system more susceptible to these types of disturbances (Stewart and DePaolo, 1995; Hofmann, 1997). Despite the more primitive Sr isotopic compositions obtained from plagioclase in this study, the values may still have been affected by later events and may not completely be representative of the source magma, as the dominant composition of the plagioclase is approximately $^{87}Sr/^{86}Sr$ of 0.705. In theory, lower primary magma values (initial $^{87}Sr/^{86}Sr_{1270\ Ma}$ for chondrite = 0.7030) for Sr would be consistent with the more chondritic values obtained for both Nd and Hf. The only sample which displays such a value is VD-724, which has a near-chondritic whole rock initial $^{87}Sr/^{86}Sr$ composition of 0.7027. It is possible that this may be the only sample analyzed from the intrusion (including those of Stewart and DePaolo, 1995) which gives an accurate primitive $^{87}Sr/^{86}Sr$ isotope composition. However, this may be unlikely given the large amount of Sr isotope data which centers between 0.7050 and 0.7065 for initial $^{87}Sr/^{86}Sr$ (1270 Ma) (Fig. 5.1). The fact that the ε_{Nd} composition of this sample is not the most primitive value, coupled with a significant negative Sr anomaly (Fig. 4.6), indicates that the Sr isotope data may be disturbed. If sample VD-724 was affected by later circulating fluids, then the initial $^{87}Sr/^{86}Sr$ composition of 0.7027 may be erroneous. It is difficult to determine exactly what the primary Sr isotopic composition of the MI is, as all Sr compositions may have been disturbed by later events (likely localized fluids). However, the evidence of this study combined with that of Stewart and DePaolo (1995) suggests that the best estimate for the primary $^{87}Sr/^{86}Sr$ isotopic composition is in the range of 0.7046 to 0.7050.

Despite the well-known sensitivity of Pb isotopes to detect crustal contamination (e.g. Taylor et al. 1980), especially of magma that has interacted with the lower crust, the Pb isotope composition of the MI has never previously been investigated. As presented in section 4.3.2, the Pb isotope data obtained for feldspar grains in this study indicate the involvement of both intermediate and high μ reservoirs in the evolution of the Muskox magma(s). Material derived from the lower crust generally shows unradiogenic values of $^{206}Pb/^{204}Pb$ and $^{207}Pb/^{204}Pb$ because lower crust typically has low values of μ (<4.5) (e.g. Doe and Zartman, 1979; Galer and Goldstein, 1995, Holm, 2002). The data obtained from this study does not show any evidence for contamination from such a reservoir. The source of enrichment seen in the incompatible element profiles (Ch. 3) is therefore likely not due to lower crustal contamination, but is a feature of the subcontinental mantle source region. Although the plagioclase samples from this study were not leached to remove foreign lead from grain boundaries and/or fractures, the in situ laser ablation MC-ICPMS technique employed here enabled these visible alteration areas of the grains to be avoided. Therefore the data should be largely free from this type of extraneous Pb contamination, and the initial ratios most likely describe the mantle source, which appears to be from an area of undepleted, fertile mantle.

As shown in Figure 4.14, the Pb data for sample VD-850 are anomalous compared to the other analyzed samples. The scatter observed in this figure, may reflect the effects of later alteration or disturbance of Pb isotope ratios by circulating fluids.

This is also supported by the Sr isotope data. This sample has one of the higher initial Sr isotope compositions, with a $^{87}Sr/^{86}Sr$ value of 0.706998 for the whole rock, but also has a relatively high initial ε_{Nd} value (-0.2) and ε_{Hf} value (+3.2). Although petrographically VD-850 does not appear unusually altered, its trace element profile (Fig. 3.19e) revealed significant Sr and K anomalies which may be suggestive of a later disturbance. The presence of a significant positive Sr anomaly (Fig. 4.6) supports this observation.

Comparison of the in situ data from this study to that of Mathez and Waight (2003) reveals a much lower analytical error with the technique applied in this study. Part of the reason for this is that the ^{204}Pb signals in the Mathez and Waight (2003) study were too low to obtain precise measurements using Faraday collectors. Interestingly, the Pb isotope results for the Bushveld and Muskox intrusions show quite different histories. The results of Mathez and Waight (2003) indicate heterogeneity between layers of the Bushveld intrusion, and require multiple sources of Pb during crystallization, while the data from this study show homogeneity between layers of the intrusion, and largely indicate a single, undepleted mantle source for the MI.

5.2 *In Situ* Techniques

The results from this study have shown that LA-MC-ICPMS is a rapid, accurate and precise method for *in situ* determination of Sr and Pb isotope ratios in plagioclase. The combination of both isotopic systems in a single plagioclase grain has been virtually unexplored, and this study helps to demonstrate its potential research power. The *in situ* Sr values obtained by MC-ICPMS in this study are interpreted to represent a more accurate estimate of the original magma composition than was obtained by the whole rock method. The advantage of the *in situ* method is that it is possible to avoid cracks and irregularities in the mineral and also the grain boundaries, which are more likely to have disturbed or extraneous isotopic compositions.

Comparison of the *in situ* isotopic data for plagioclase with microprobe data for the same mineral revealed a broad relationship between the isotopic composition and the An content of the plagioclase compositions. The comparison also easily enabled the 'isotopic outliers' to be identified, as they were easily revealed in the plots of various isotope ratios, such as $^{207}Pb/^{206}Pb$ versus $^{87}Sr/^{86}Sr$. The potential to both chemically and isotopically analyze the same mineral grains from a single grain mount is a significant advantage compared to conventional techniques.

5.3 Implications for the Mackenzie Igneous System

5.3.1 Geochemical Constraints

There are many similarities between the MI, CRB, and MD (Ch. 2). Geochemically, the rare-earth element and extended trace element diagrams share common characteristics, such as being light-rare-earth enriched and having negative Nb-Ta anomalies (Francis, 1994). However, the Muskox magmas can be distinguished from the CRB and MD geochemically. A summary discrimination diagram of Th/Ta vs.

La/Yb is shown in Figure 5.2. These element ratios are capable of providing important constraints on magma sources and magma evolution in mafic rocks (Condie, 1997). The Th/Ta ratio gives a measure of the Nb-Ta anomaly, while the La/Yb ratio gives a measure of the slope of the primitive mantle (PM) normalized incompatible element distributions. A consideration with this type of diagram however, is that both the Th/Ta and La/Yb ratios can be raised by assimilation and by the degree of mantle melting, for example the La/Yb ratio of a basaltic magma is elevated if garnet is left in the melting residue (Condie, 1997 and references therein).

The data show two possible trends for the Muskox rocks, both originating at values near primitive mantle, which is consistent with a chondritic source. The first trend is towards values of the granophyric and migmatitic samples, M-26 and EQ-15, respectively. Both are samples which are highly contaminated by the surrounding country rock. It is likely that the values for the crust in this region may vary from the general values given in Condie (1997). The majority of the samples from Megacycle #1, have Th/Ta and La/Yb values of approximately 4.9 and 6.5, respectively. These values would suggest that a homogeneous mixing with crustal values, possibly the middle crust (between values of UCC and LC on figure 5.2), took place before the crystallization of the MI. However, it also appears that some of the Muskox values show little change in La/Yb, but show increasing Th/Ta values. If this 'contamination trend' is real, the contaminant may be sourced in the subcontinental lithosphere, and be significantly depleted in Ta. As discussed above however, there is little isotopic evidence for any significant contamination, unless the contaminants had similar isotopic compositions to the Muskox magmas.

Interestingly, the Keel Dyke samples show values ranging between the two dominant Muskox trends. This is, however, not surprising considering the fact that the Muskox magmas are thought to have flowed to the south from a larger feeder system (Irvine and Smith, 1967; Stewart and DePaolo, 1995).

The most significant aspect of Figure 5.2 is the comparison between the different elements of the Mackenzie Igneous System. The data for the MD and the CRB are strikingly different from the majority of the Muskox data. The Mackenzie dyke and Coppermine River flood basalts lie along a mixing trend between depleted mantle and the upper crust. The MD values show less scatter, when compared with the CRB values. From these data, the preferred interpretation is that the MI magmas may have been derived from a chondritic-like primitive mantle, while the source for the CRB and the MD may have been derived from a depleted mantle reservoir.

The REE and extended element profiles for the Keel Dyke and MI were shown in comparison to common mantle reservoirs, N-MORB, E-MORB, and OIB in Figures 3.17 and 3.19. Inspection of these diagrams reveals that no samples analyzed from the study match the patterns of these reservoirs, although some similarities are seen. Samples of the Keel dyke have a similar LREE pattern to E-MORB, but are more depleted in the HREE. The extended element profiles (Fig. 3.19) of the Muskox samples are significantly different than the profiles of the reference mantle reservoirs. Noticeable differences include negative Nb anomalies and greater depletion in the HREE. This comparison is also consistent with the preferred interpretation that the source for the MI was not similar to the depleted mantle, and more chondritic-like in nature.

5.3.2 Isotopic Constraints

Isotopically, the various manifestations of MIE are easily distinguishable. Although much of the isotopic data for MIE has been reported previously, the summary diagrams presented here are unique and provide many new insights into the understanding of this major igneous event.

Comparison with the CRB

The CRB have been analyzed previously for Nd, Sr, and Pb isotopes (Dupuy et al. 1992; Stewart and DePaolo, 1995; Griselin et al. 1997). The data are summarized in Figures 5.1, 5.3 and 5.4. There are obvious differences between the isotopic signatures of the CRB and the MI. Uncontaminated ε_{Nd} values for the MI are generally chondritic and range between -1.7 and +0.7, while uncontaminated ε_{Nd} values from the Coppermine River Basalts range between +3.0 and +4.5, and lie close to depleted mantle values (approximately ε_{Nd} = +5.5 at 1270 Ma). Figure 5.3 shows that many CRB samples are easily distinguished from MI samples in terms of Sr and Nd isotopes. CRB samples have compositions approaching DM values, with contaminated Sr isotope values, and compositions which approach the signatures of the local wall rocks. The latter group presumably represents lavas which have undergone significant amounts of contamination, enough to alter both the Sr and Nd compositions. The former group may have experienced contamination as well, but these effects appear to be minimal in comparison to other samples. In addition, initial $^{207}Pb/^{206}Pb$ ratios of plagioclase obtained in this study (0.907902 - 0.968898) are in stark contrast with previously reported whole rock values from the Coppermine River basalts (0.812633 – 0.849748) (Dupuy et al. 1992).

Figure 5.4 illustrates how the Pb isotope data for the CRB (Dupuy et al. 1992) are not consistent with the Pb isotope data for the MI. The Pb data for the CRB plot on the right side of the Geochron, near the Atlantic and Pacific MORB field, while the data for the MI plot on the left, near the 1.27 Ga isochron. The Pb isotope values for the CRB suggest a depleted mantle component (Dupuy et al., 1992); while the Pb isotopes for the MI suggest a chondritic source. Also, Dupuy et al. (1992) have argued that contamination of the CRB occurred at least in part from the lower crust. The Pb isotope data from this study do not show any evidence of lower crustal contamination, and are more consistent with contamination from the SCLM, as argued by Francis (1994). Thus the Pb isotopes alone point to very different sources and contamination styles for the CRB and MI.

Comparison to the Mackenzie and Bear River Dykes

The limited isotopic data available for the MD, makes a detailed comparison with the MI difficult. However, some generalizations can be made. One dyke analyzed by Dupuy et al. (1992) has ε_{Nd} (1270 Ma) = +3.2. Dudas and Peterson (1992) state that Nd isotopic compositions for the MD range from ε_{Nd} (1266 Ma) = +4.9 near the inferred hotspot source, to -2.8 at the outer limits, with most samples between 0 and +2. They

also suggest the presence of multiple crustal components to explain a lack of correlation between Nd concentration and Nd isotope compositions. The ε_{Nd} value of +4.9 near the focus of the swarm is essentially identical to the values of the upper CRB lavas, and to the value of the depleted mantle at that time. From the limited details, it is difficult to say whether the MD share more in common with the MI or the CRB. However, it seems clear that a depleted mantle reservoir was involved at some point in the formation of the swarm to explain the high positive epsilon Nd values. It is also clear from geochemistry (Gibson et al. 1987) and isotopes (Dudas and Peterson, 1992) that crustal contamination of the dykes took place, although the degree to which this occurred is uncertain. The magnitude of the swarm and data available suggest that multiple crustal components did indeed influence the composition of the dykes. Also, Baragar et al. (1996) geochemically distinguish a separate subswarm within the MD. This Keewatin subswarm is compositionally distinct and may reflect a deeper source than that of the main dyke swarm.

It has been proposed that the Bear River dykes located in the Yukon are a westward extension of the Mackenzie Dyke swarm (Schwab et al. 2004). The existing Nd isotope data for these dykes is shown in comparison to the MI in Figure 5.1. The data set consists of four samples, all showing considerable variation, with ε_{Nd} (1270 Ma) values ranging from -7.2 to +1.4 (Schwab et al. 2004). The small sample set combined with the large variation of the results makes it difficult to determine the dominant source signature or the extent of contamination of the dykes. However, the fact that $\varepsilon_{Nd(T)}$ values are inversely correlated with Mg-number, Cr, and Ni, and positively correlated with incompatible elements, indicates that crustal contamination cannot solely account for the isotopic variation observed (Schwab et al. 2004). The Bear River dykes must have evolved from multiple magma sources, such as the depleted mantle ($+\varepsilon_{Nd}$) and a chondritic mantle source (Schwab et al. 2004).

Source characteristics

As shown in Ch. 4, there is no geochemical or isotopic evidence for melting in the garnet stability field (~80 km depth). In the shallow mantle, melting in the presence of garnet results in a larger Lu/Hf fractionation (compared to Sm/Nd), and results in a decoupling of the two systems. Deeper in the mantle, fractionation or melting in the presence of perovskite can also fractionate Lu/Hf differently than Sm/Nd (e.g. Patchett et al. 1984; Salters and Hart, 1991; Vervoort and Patchett, 1996). The results from this study demonstrate that significant melting in the presence of either of these minerals has not occurred, as the Lu/Hf and Sm/Nd systems are not significantly decoupled, nor do the Muskox samples show any significant depletion in the HREE. The geochemical and isotopic evidence from this study suggest that melting occurred in a region of the shallow mantle which was dominated by spinel peridotite. This would be consistent with the notion of a plume source (LeCheminant and Heaman, 1989). The plume rose to the base of the lithosphere before melting occurred at the top of the plume.

In contrast to the data from this study, Griselin et al. (1997) have shown that the lower CRB lavas were produced by melting in the garnet stability field. Although this fact does not preclude a relationship between the CRB and mantle plume source, it does

not suggest one. This points to yet another difference in the sources of the CRB and the MI.

The current isotopic and geochemical evidence for the MI generally point to a chondritic source. If, however, we assume a depleted mantle source, as may be the case for the CRB and possibly the MD, the Muskox magmas would have had to mix with the crust to obtain their chondritic-like signature. Figure 5.5 shows that the mixture would have to be about 90% depleted mantle, with about 10% crust. All attempts made during this study to model this contamination geochemically however, were generally unsuccessful. This may be due to improper estimates for the contaminant, coupled with the complexities formed by the geochemistry of cumulate rocks, or, more likely, that the source was not depleted mantle. Any such mixing of the depleted mantle and older crustal material would require thorough mixing in a remarkably consistent and reproducible manner to produce such a large amount of homogeneous magma. As shown above, the isotopic evidence would seem to suggest that this is not a likely scenario.

Summary

The new isotope data obtained in this study for the MI is consistent with a chondritic-like source and supports the mantle plume hypothesis. However, it strongly challenges previous views held that the CRB were derived from the MI, or intrusions similar to the MI (Irvine, 1970; Kerans, 1983; Dostal et al. 1983; Francis, 1994; Stewart and DePaolo, 1995; Baragar et al. 1996; Griselin et al. 1997). The data and comparisons presented by this study suggest a complex history for MIE, with multiple and very different magma reservoirs. There must be one source similar to the DM which fed the CRB and possibly the MD, and one chondritic-like source which fed the MI and possibly some of the MD. The data also suggest that there were different sources and/or styles of contamination of the various elements of the MIE. The parental magmas of the MI were enriched in incompatible elements, which must reflect enrichment from the mantle source region, rather than contamination with the lower crust.

5.3.3 Synthesis

On the basis of similar ages, spatial relations, similarities in petrological and geochemical characteristics, the CRB, MI, and MD have previously been considered as separate components of a single magma system. Compared to the data of Griselin et al. (1997), isotopic compositions for the MI are much more primitive. Therefore the isotopic composition of the mantle component suggested by Griselin et al. (1997) is inappropriate for the Mackenzie plume. It is now apparent that there was multiple magma reservoirs present during the emplacement of MIE. The data from this study indicate that the isotopic composition of the Mackenzie plume bears strong resemblance to bulk earth compositions. Isotopically different reservoirs which have interacted during the formation of MIE include the depleted mantle and the lower and upper crust. This is also supported by the Nd isotopic results presented by Schwab et al. (2004) for the Bear River dykes (discussed above).

The chondritic signature of the MI, equivalent age and relation to the Mackenzie swarm would suggest that a plume source for the MI is most reasonable. However, the relation of the CRB to the MI and the Mackenzie plume is still unclear.

The data of Griselin et al. (1997) suggests a depleted mantle source for the bulk of the CRB and evaluated separately from the MI and MD, does not require the presence of a mantle plume to explain the data. One possibility is that much of the CRB are in fact unrelated to the Mackenzie plume and are the result of decompression melting of the depleted mantle, associated with rifting. LeCheminant and Heaman (1989) proposed a rift across the proposed Mackenzie hotspot, related to the opening of the Middle Proterozoic Poseidon Ocean. Hoffman (1989) suggested the presence of a mantle 'superswell' beneath Laurentia at that time. Large convective mantle upwelling may have actually caused rifting to occur. A lack of precise U-Pb data on the CRB brings forth the possibility that the CRB, as a whole or in part, could have erupted significantly later than the MI or the MD, and thus have a different magma source, unassociated with the Mackenzie plume. Isotopically, the later flows of the CRB resemble a depleted mantle source, while earlier flows show geochemical and isotopic evidence for crustal contamination (Griselin et al. 1997). The enriched character of the basalts may not be due to derivation from the mantle plume, but sampling of the subcontinental lithosphere.

The record of uplift preceding emplacement of MIE (marked by the Dismal Lakes Group disconformity), short time span of emplacement of events (most magmas emplaced in less than 5 million years), large volume of magma, radiating nature of the dyke swarm, and changes in magma flow pattern in dykes outward from the focal region (i.e. dominantly vertical flow within 500 km of the focal region), and associated large gravity anomalies near the focus of the swarm, all point to the presence of a large mantle plume (LeCheminant and Heaman, 1989; Ernst and Baragar, 1992). Although it may not be possible to make a clear distinction between the contributions of a source in the subcontinental lithosphere and an enriched plume source for the CRB, the large volume, consistent nature, and well documented association to the Mackenzie swarm make a deep plume source very appealing. This is evident from previous isotopic studies of the CRB (Dupuy et al. 1992; Griselin et al. 1997). The possibility that the CRB are unrelated to the Mackenzie plume cannot be excluded, however, the large volume of basalts and proximity to the swarm are best explained by melting of depleted mantle in the vicinity of the Mackenzie plume. With this in mind, several scenarios which could reconcile the previously noted geochemical and isotopic discrepancies to a common plume origin can be envisaged:

(1) The composition of the Mackenzie plume may have changed over time, and evolved from a chondritic signature for the MI, to a more depleted signature for the CRB. It is possible that the plume evolved through time by mixing with material from the depleted mantle near the end of magmatism. Similar instances are found in other continental successions, such as the Midcontinent rift in the Superior Province (Nicholson et al. 1997). Nicholson and Shirey (1990) suggest that as the Midcontinent rift plume began to wane, an influx of partially melted depleted mantle may have occurred. This analogy is consistent with the assumption that the CRB are a later expression of MIE. This would then suggest that the isotopic composition for the Copper Creek lavas was similar to that of the

MI, while the Husky Creek composition evolved to a near-DM composition. Doming and rifting of the lithosphere caused by the interaction with the Mackenzie plume may have caused the thickness of the lithosphere to change significantly in a short time span (LeCheminant and Heaman, 1989; Baragar et al. 1996). This may have affected the site of melting for the various events. Griselin et al. (1997) suggest that the site of mantle melting for the upper part of the CRB became shallower due to lithosphere thinning. This is because the upper layers of the CRB show relatively less pronounced enrichment and fractionation of incompatible elements, a disappearance of negative Nb anomalies, and also a change from negative to positive ε_{Nd} values when compared to the lower basalt flows. Evidence from the MI for an evolving magma source includes a change in crystallization sequence at cyclic unit 17 (Stewart and DePaolo, 1995). A very small change in Hf isotope composition occurs above this unit as well (Fig. 5.1). These changes are not as significant as those detected for the CRB (Griselin et al. 1997); however they do show that the magma source may have changed slightly over time.

(2) Another possibility is that the mechanisms by which the magmas for the various elements of MIE traveled from their plume source may have been quite different. Based on the 1269 Ma crystallization age, the MI was an early feature of MIE (LeCheminant and Heaman, 1989, French et al., 2002). The MI may have been fed directly from the plume, and remained relatively free of contamination until emplacement in the upper crust. The area into which the MI intruded is a zone of intense structural complexity, thus providing a conduit for the magmas (Fraser et al. 1972). The magmas for the CRB, and possibly the MD, likely pooled beneath the depleted subcontinental lithosphere and mixed with this material before traveling to the surface. White and McKenzie (1989) proposed that flood basalts are due to the accumulation of plume material beneath impenetrable continental lithosphere, followed by extension, which allows large amounts of melt production to reach the surface. It is apparent that the magmas for the CRB became contaminated with the lower crust, while the Muskox magmas remained free of this type of contamination. This would agree with the conclusion made by Dupuy et al. (1992) that the CRB represent material derived from a mantle plume mixed with the base of the depleted continental lithosphere.

Preferred model

The latter scenario above is preferred for three reasons: (1) it allows for homogeneity in the MI and for heterogeneity of MIE by mixing plume magma with very different reservoirs, (2) it suitably explains the different styles of contamination between the MIE, and (3) it does not require that the CRB were derived from magmas of the MI. The model presented below draws from the isotope data presented in this study, and from the wealth of previous studies on the MI and MIE (Fig. 5.6).

The source for the Muskox magmas was a LIL element–enriched, asthenospheric plume which brought non-depleted magma from a very deep source into the shallow

subcontinental mantle. The magmas made their way to the near surface via a weakness in the crust and avoiding significant contamination. Contamination of the Muskox magmas with crustal material from its wall rocks appears to have been local and relatively minor. Formation of the MI was an early feature of MIE. The Mackenzie plume flattened and pooled beneath the lithosphere where it became mixed with the DM. The presence of the mantle plume underneath the lithosphere induced uplift and extensive fracturing. This stretching and weakness of the crust allowed magma to move from the base of the lithosphere to large crustal magma chambers. Rifting of the lithosphere allowed large amounts of upper mantle melt to form. Large sub-volcanic magma chambers for the CRB and majority of the dykes formed to the north of the MI, at the focus of the dyke swarm. Here the magmas became contaminated and differentiated. Magma then moved vertically and horizontally outwards from the plume to form the CRB and the extensive Mackenzie dyke swarm. The MI may have fed a small number of dykes, but not the basalt flows, as was previously thought. Towards the end of Mackenzie magmatism, the Husky Creek lavas became interlayered with sediments. As magmatism declined, contamination became minimal.

5.4 Comparison with other Magmatic Events in North America

The MI and the Mackenzie event is one of the world's major and best-preserved Proterozoic large igneous provinces. Its large size and extent make the MIE unique, and therefore comparison of the Muskox Intrusion and MIE with similar LMI and associated large igneous provinces is difficult. However, a brief comparison between MIE with the Voisey's Bay intrusion, and the Midcontinent Rift System will be presented, in order to evaluate other large intra-plate magmatic events occurring in the same vicinity and time as MIE. Although no ties between these magmatic events is suggested, this serves to illustrate that similar isotopic signatures and magmatic histories to MIE exist, and may serve to support the conclusions of this study.

The 1333 Ma Voisey's Bay intrusion is a troctolitic-gabbroic intrusion within the Nain Plutonic Suite in Labrador, Canada. It hosts a major Ni-Cu-Co deposit and is one of the oldest and least-contaminated intrusions in the Nain Plutonic Suite (Amelin et al., 2000). Initial isotope values reported for the Voisey's Bay intrusion are broadly similar to the Muskox intrusion: $\varepsilon_{Nd\ (1.32Ga)} = -1$ to -2, $^{87}Sr/^{86}Sr_{(1.32Ga)} = 0.7034$ to 0.7038, and are uniform throughout various phases of the intrusion (Amelin et al., 2000). Unlike MIE, Nain Plutonic Suite magmatism is not thought to have been initiated or assisted by a mantle plume (Amelin et al., 2000). According to Amelin et al. (2000), the primary magma of the intrusion may be a mantle-derived basaltic melt with initial Nd and Sr isotope values identical to assumed bulk Earth values. Enrichment observed in the lavas is attributed to derivation from an enriched continental mantle or contamination by a small amount of crustal material (Amelin et al., 2000).

Possibly the closest comparison of MIE can be made with the volcanic rocks of the Midcontinent Rift System. The Midcontinent Rift System in the Lake Superior region consists of at least 2 000 000 km^3 of dominantly tholeiitic basalts which erupted at 1.1 Ga (Nicholson et al., 1997). Like the MI, incompatible trace elements in the tholeiites are enriched compared to primitive mantle values (La/Yb = 4.3 - 5.3; Th/Ta =

2.12 - 2.16; Zr/Y = 4.3 – 4.4; for the Portage Lake Volcanics, Nicholson and Shirey, 1990). Isotope values for the Portage Lake Volcanics are $^{87}Sr/^{86}Sr_{initial}$ = 0.7038, $\varepsilon_{Nd(1095Ma)} = 0 \pm 2$, and $\mu_1 = 8.2$ (Nicholson and Shirey, 1990). Also similar to MIE, the Midcontinent rift has been attributed to the upwelling and decompression melting of a mantle plume beneath North America (Nicholson et al., 1997; and references therein). The primary magma from the plume source is believed to have an $\varepsilon_{Nd(1100Ma)}$ value of about 0, as the earliest basalts and the bulk of uncontaminated younger basalts display this signature (Nicholson et al., 1997). This dominantly chondritic source proposed for the Midcontinent rift plume, is also in agreement with the findings of this study for that of the Mackenzie plume. In addition, Nicholson et al (1997) propose that towards the end of magmatism, the magma from the chondritic plume became mixed with a depleted asthenospheric mantle source ($\varepsilon_{Nd(1100Ma)} = 0$ to +3). Conclusions drawn from this study also suggest that the DM became involved with the Mackenzie plume, after the formation of the MI.

CHAPTER 6: CONCLUSIONS

6.1 Conclusions

- The Hf isochron age (1257±58 Ma) obtained in this study proves that in the absence of any baddeleyite, zircon, or other separable mineral in a layered mafic intrusion, the Lu-Hf system can provide a viable method of dating the intrusion.

- *In situ* laser ablation MC-ICP-MS Sr and Pb isotope ratios obtained in a single feldspar grain is a virtually unexplored yet powerful new technique able to unravel the detailed isotopic evolution of layered mafic intrusions. The *in situ* Sr isotope composition of Muskox plagioclase is less radiogenic than corresponding whole rocks; possibly indicating a more primitive and accurate estimate of original magma composition.

- Nd and Hf whole rock isotope data are relatively homogeneous and indicate a chondritic source for the Muskox magmas. Crustal contamination is isotopically only recorded at the uppermost layer of the intrusion, and in the southern regions of the Keel Dyke.

- The majority of Pb isotopic compositions of feldspar are consistent with a single stage magma evolution derived from a mantle source with μ values ~ 7-9.

- Enrichment of the parent magmas did not originate from lower crustal contamination, as evidenced from the Pb isotopes from this study, but must reflect the enrichment from the subcontinental mantle source region.

- The source for the Muskox magmas was a LIL element-enriched, asthenospheric plume which brought non-depleted magma from a deep source into the shallow subcontinental mantle. The isotopic composition of the rocks has been largely acquired from the mantle source region and not as a result of lower crustal contamination, as evidenced by the Pb isotopes. Contamination of the Muskox magmas with crustal material from its wall rocks appears to have been episodic and relatively minor.

- New isotope data obtained in this study challenges a genetic relationship between the Coppermine River Basalts and the MI, and suggests a more complex history for Mackenzie Igneous Events, with multiple magma reservoirs, involvement of the depleted upper mantle, and varying styles and sources of contamination.

6.2 Recommended Future Work

A continuation of this project could involve repeat analyses of Sr and Pb isotope compositions after chemically leaching the plagioclase grains to remove excess Pb. Also,

the Hf isotope composition of zircon, baddeleyite, and/or zirconolite could be determined and compared to the whole rock compositions.

A Hf-isotope study on the CRB and the MD would serve as an invaluable comparison to the data set obtained by this study. There is very little published isotope data on the Mackenzie Dyke swarm, and to fully get an accurate picture of the Mackenzie Igneous Events, the isotopic composition of the dykes at varying distances from the focus should be analyzed. Perhaps a Hf isotopic study of the CRB and MD could provide clearer evidence of whether or not the plume source evolved, or if there were multiple mantle sources involved in the generation of the basalts or dykes. Accurate U-Pb ages of the CRB, if possible, would also be an important addition to this work.

Figure 1.1 – Location of the Muskox Intrusion and other elements of the Mackenzie igneous events. The yellow star represents the hypothetical center of the mantle plume, corresponding to the focus of the Mackenzie dyke swarm and center of gravity anomalies. Modified from LeCheminant and Heaman (1989).

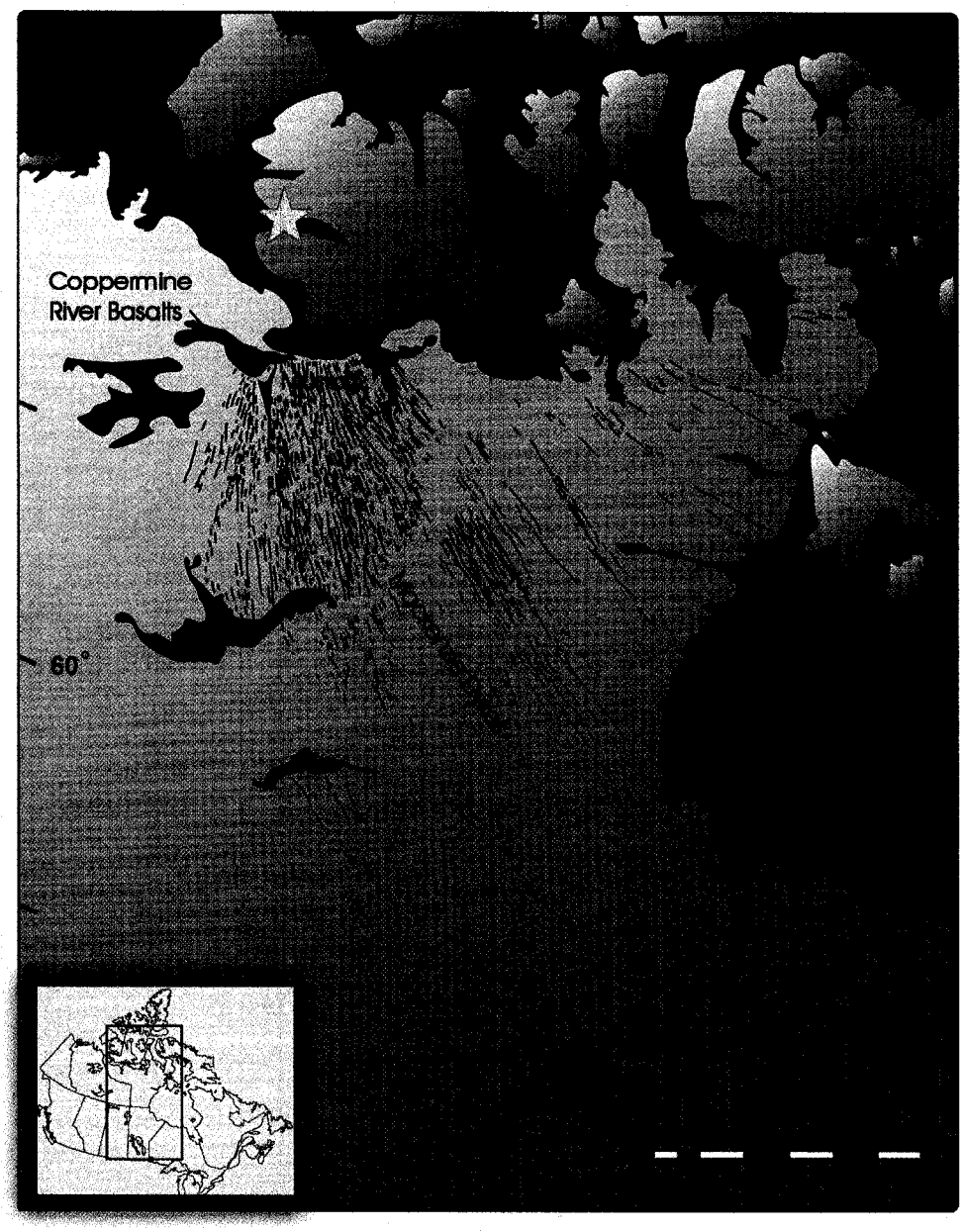

Figure 2.1 – Geological map of the Wopmay orogen. Base map obtained from Dr. Mike Thomas, NRC, personal communication (2006), adapted from Hoffman (1984).

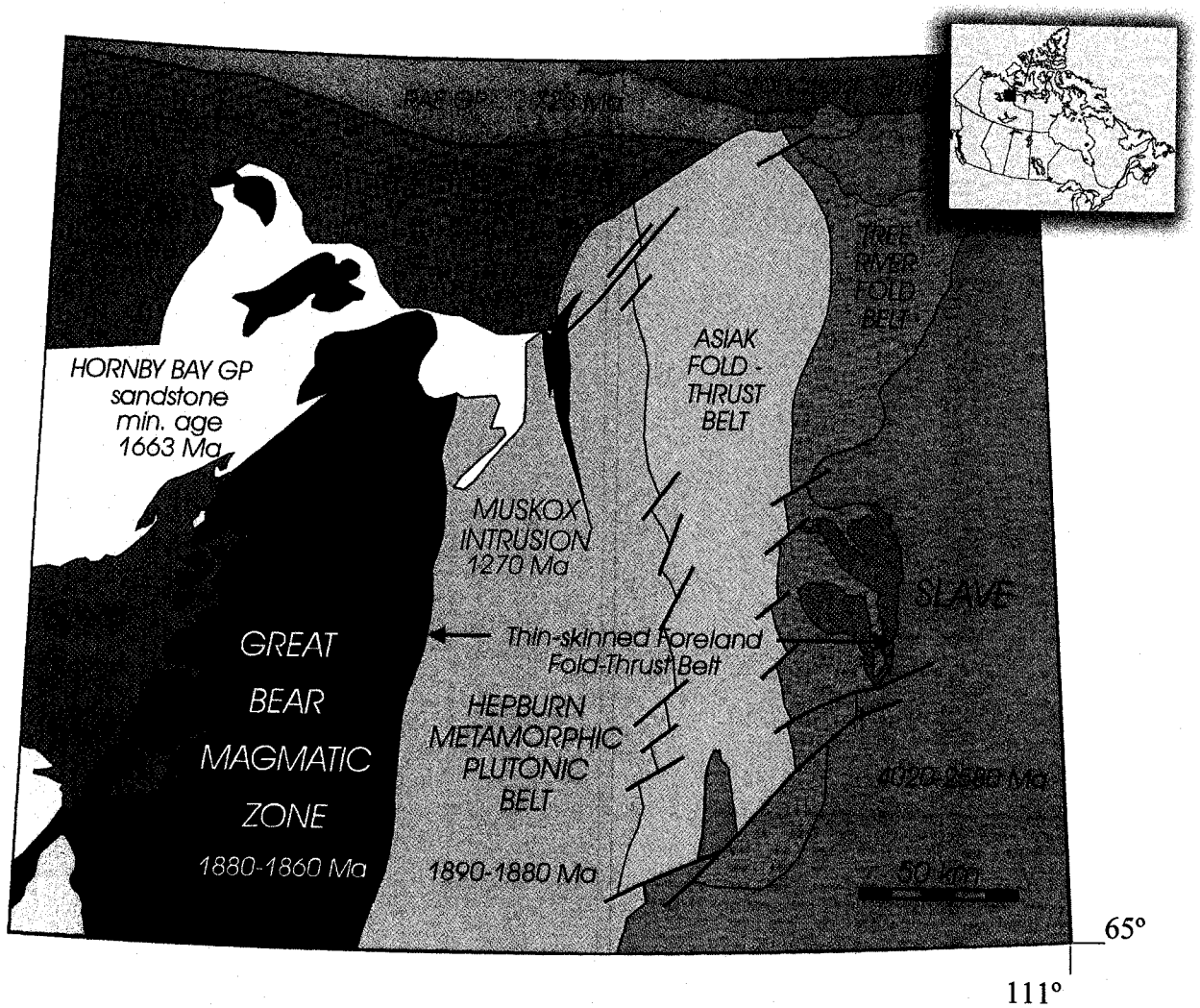

Figure 2.2 – Geological map of the Muskox Intrusion and surrounding area. Adapted from Irvine and Smith (1969).

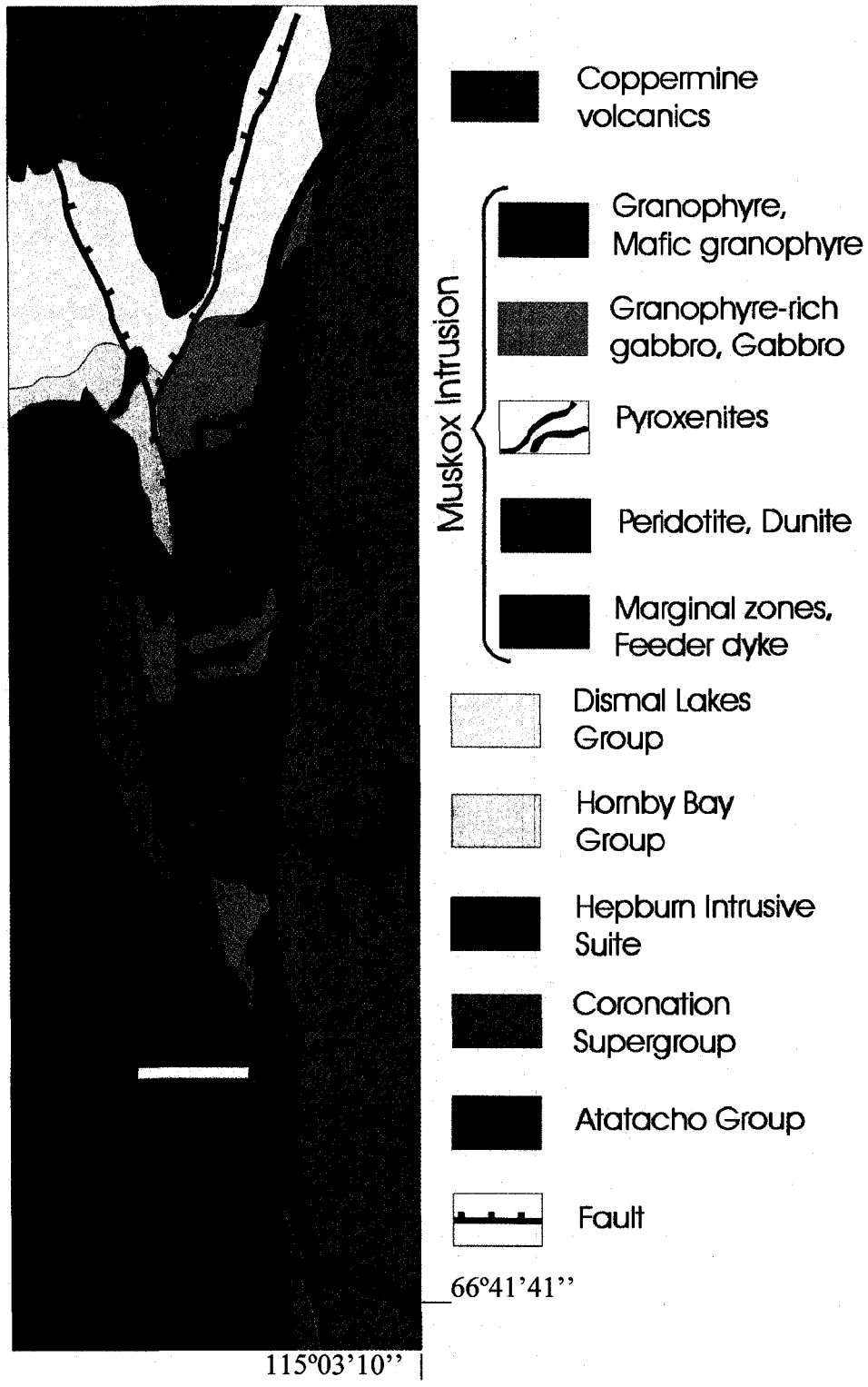

Figure 2.3 - Cross-section of the Muskox Intrusion, showing the Coppermine River Basalts closely overlying the intrusion. Names in red are transect names where the samples from this study were taken. Adapted from Francis (1994).

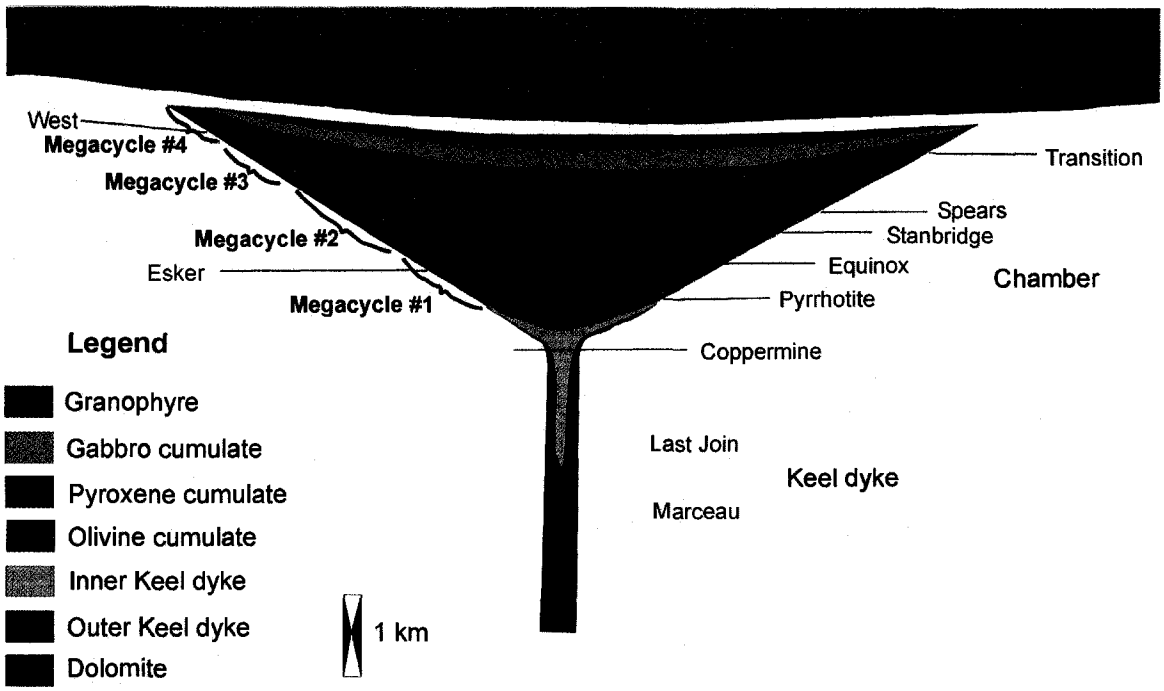

Figure 3.1 – Geological map of the Muskox Intrusion, showing sample locations. Adapted from Irvine and Smith (1969).

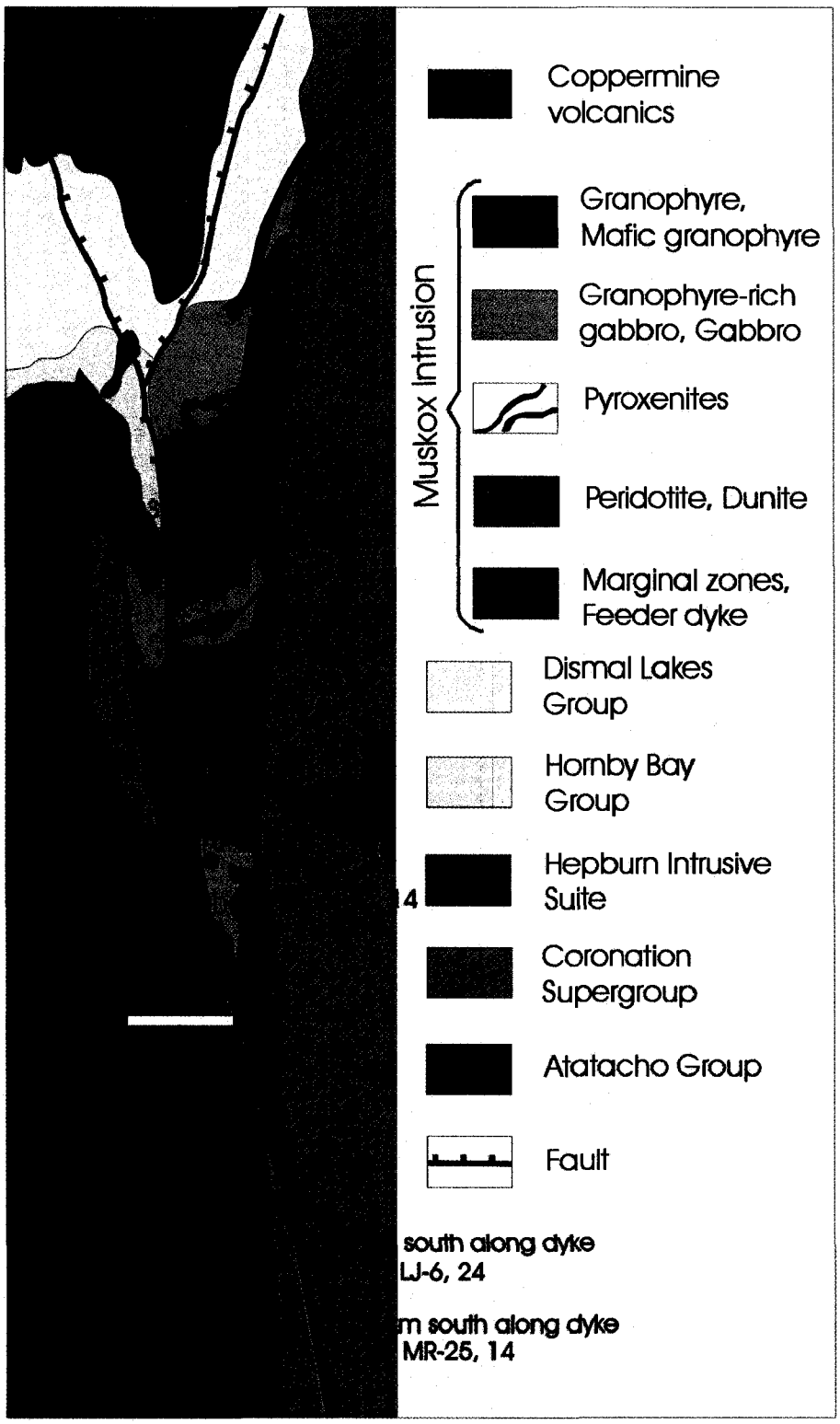

Figure 3.2 – A plot of K/Ti vs. stratigraphic position for the samples from this study. Samples indicated by a pink square are the ones chosen for isotope analysis. Stratigraphic column adapted from Francis (1994) and Irvine and Smith (1967).

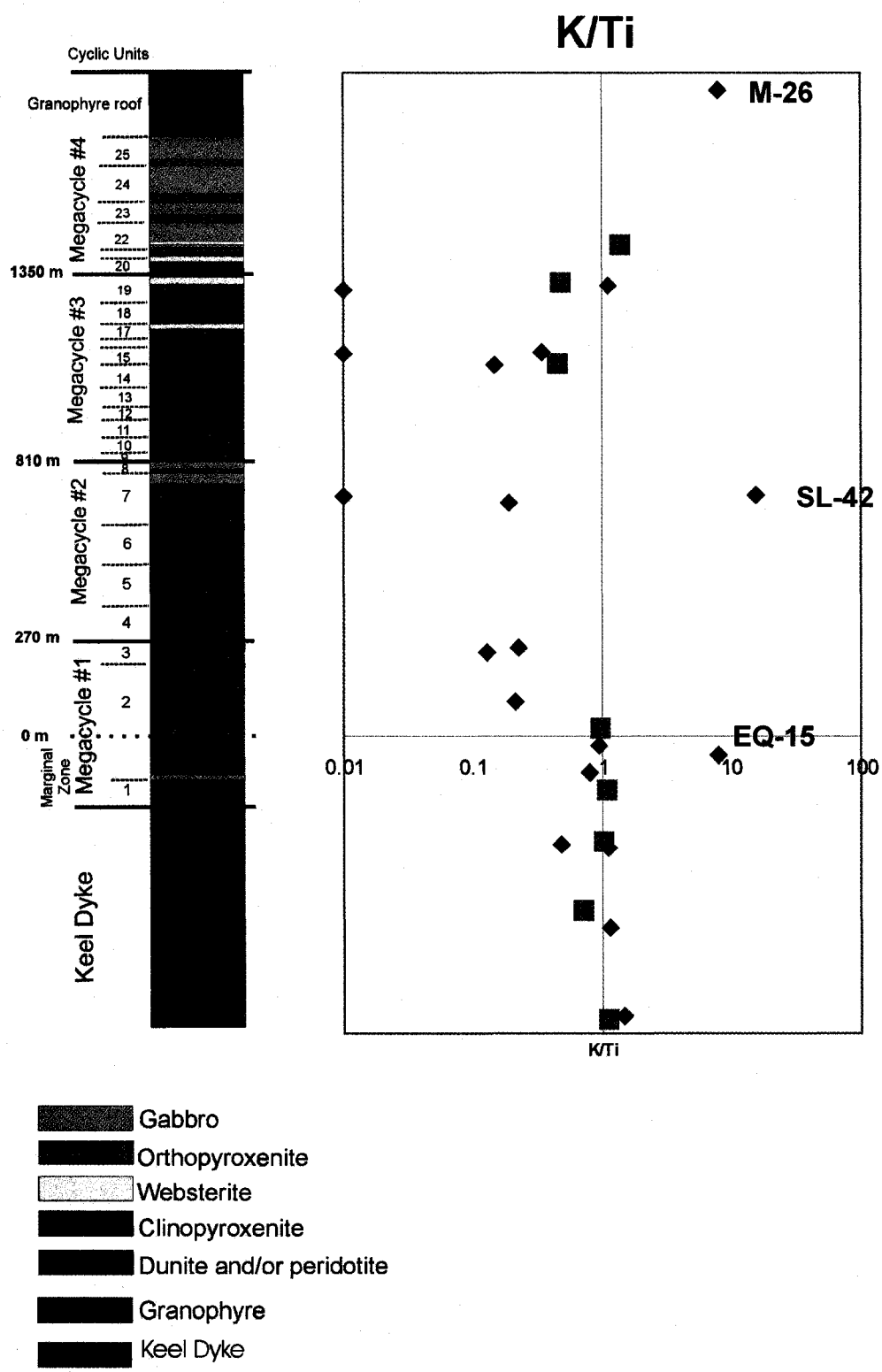

Figure 3.3 – Stratigraphic column of the Muskox intrusion showing the rock type of each cyclic unit of Irvine (1970) and the megacycles of Francis (1994). Adapted from Francis (1994).

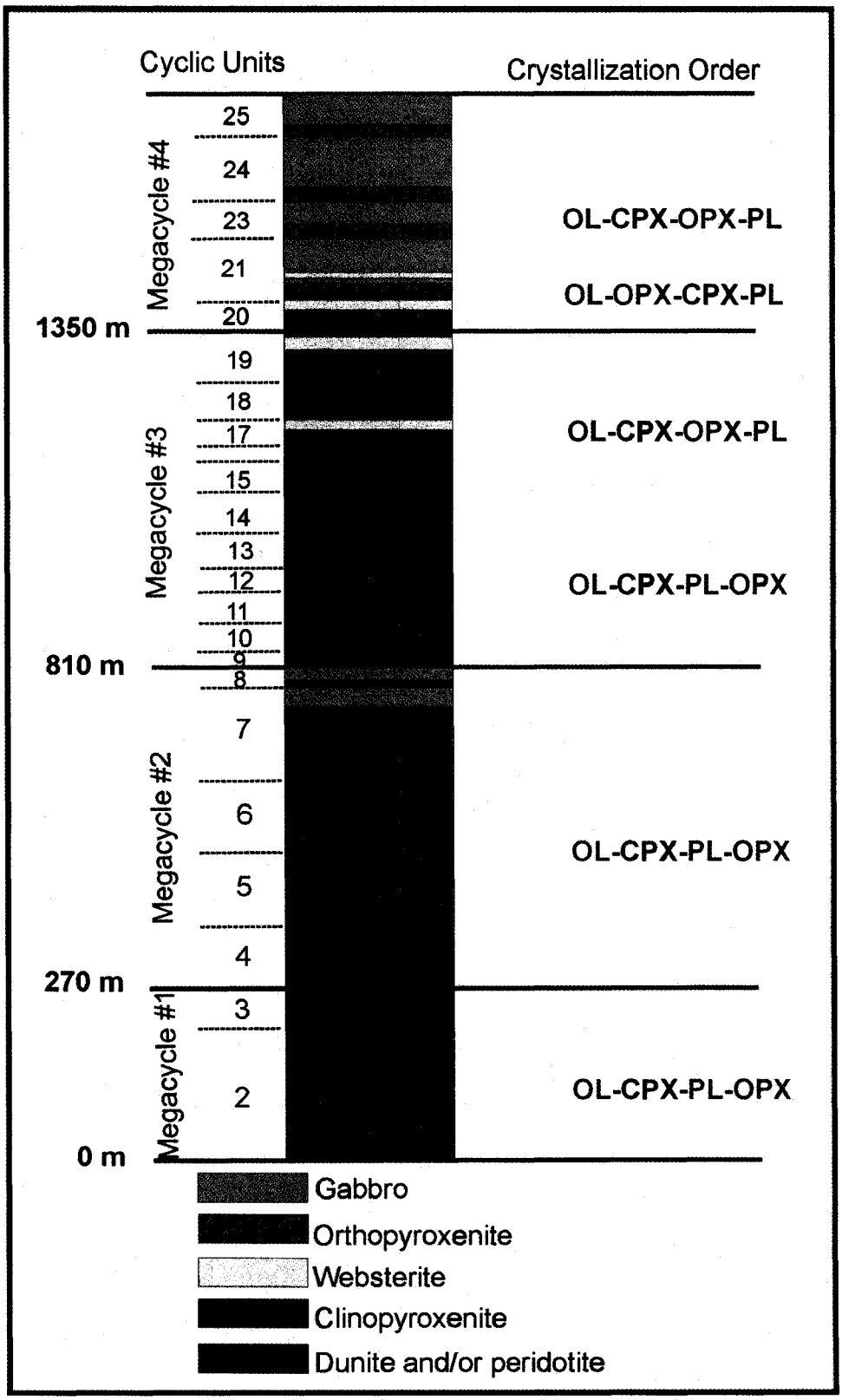

Figure 3.4 – False color BSe image of marginal sample EQ-19. Various compositions of olivine are illustrated with different colors, denoted by Ol1, Ol2, and Ol3. Neighboring crystals of clinopyroxene and orthopyroxene are also labeled.

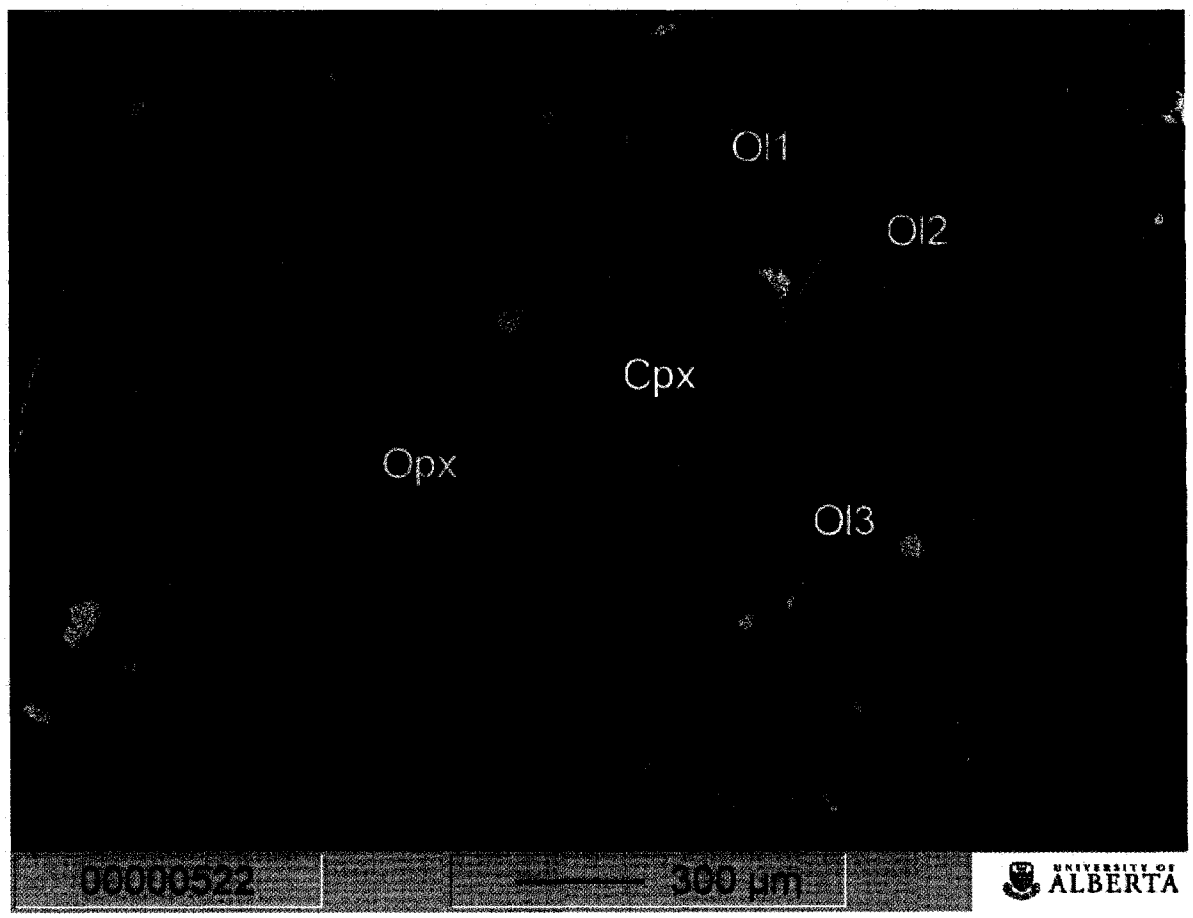

Figure 3.5 – Fenner diagrams for olivine analyses. (a) Sample EQ-19 (b) Sample V1-02 (c) all analyses, grouped according to geographical location.

(a)

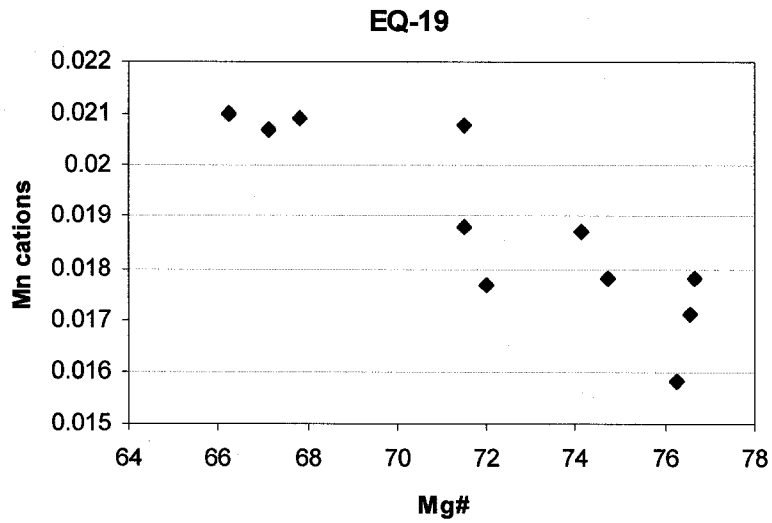

(b)

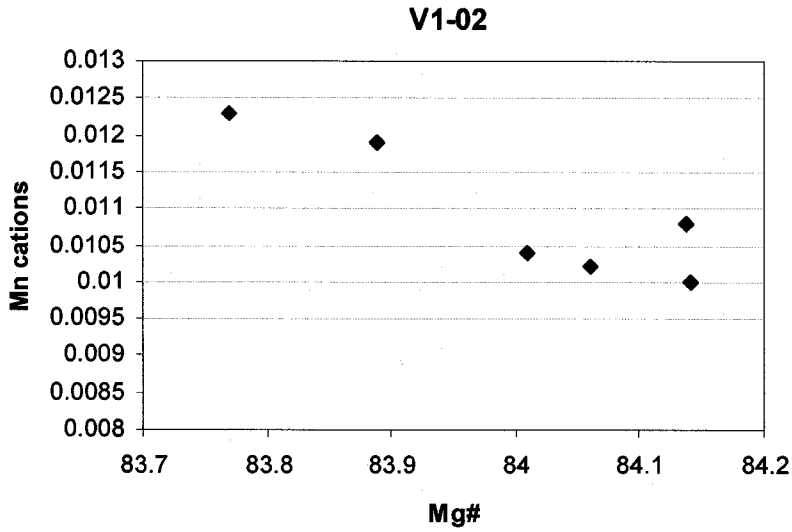

(c)

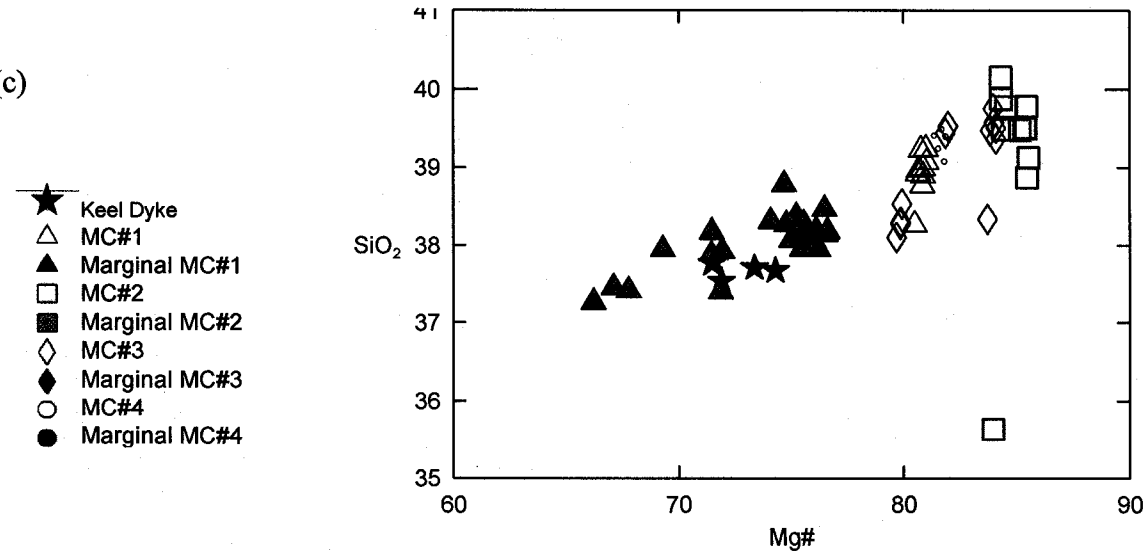

Figure 3.6 – Clinopyroxene analyses, (a) grouped according to geographical location, and (b) grouped according to location of analysis.

(a)

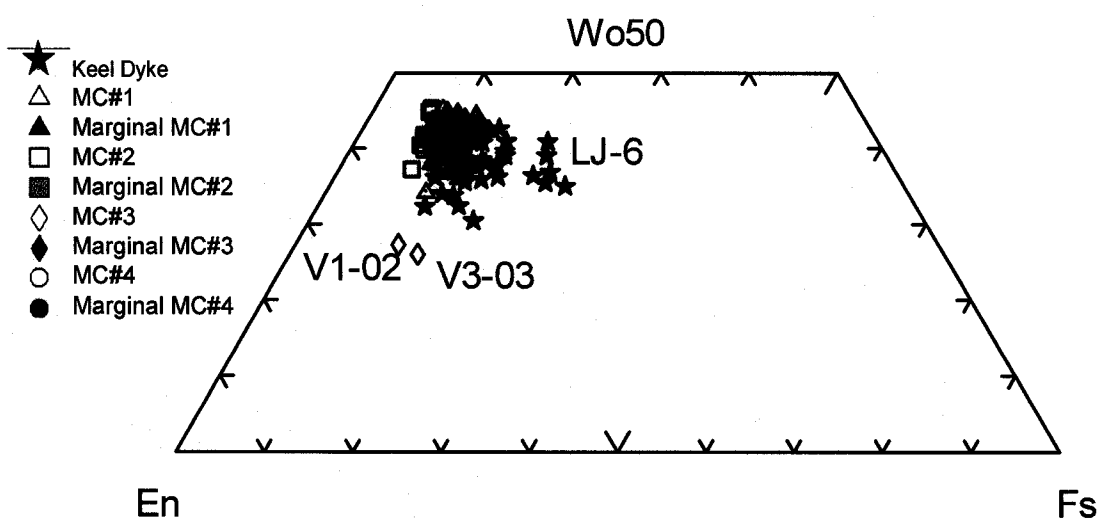

(b)

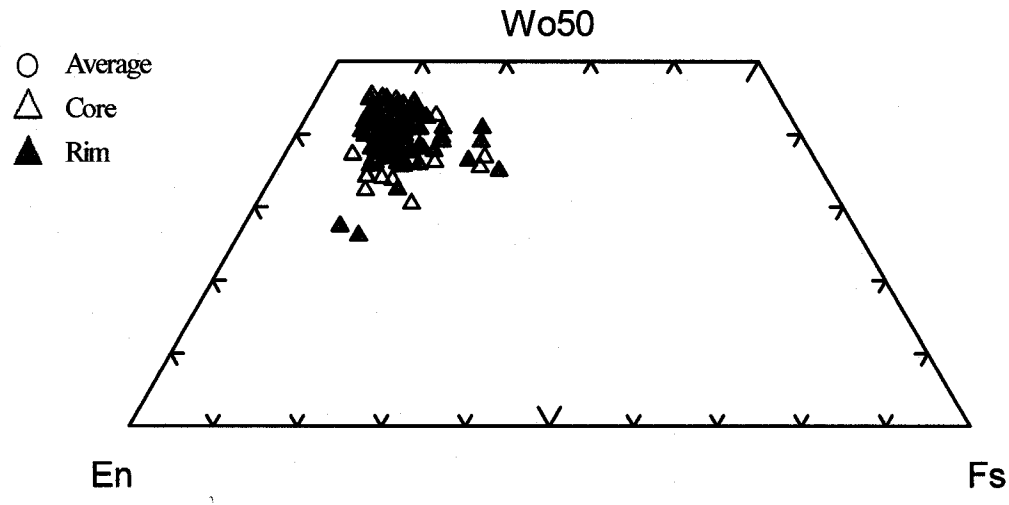

Figure 3.7 – BSe image of clinopyroxene grain showing exsolution lamellae (vertical lines) of orthopyroxene, sample VD-850 from the layered series.

Figure 3.8 – Orthopyroxene analyses. Grouped according to geographical location.

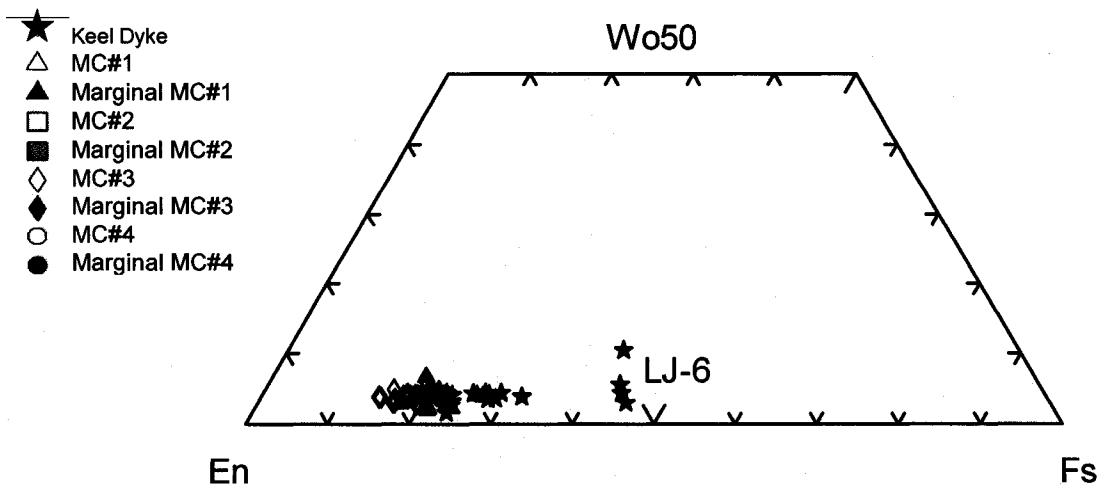

Figure 3.9 – Plagioclase analyses. Grouped according to geographical location.

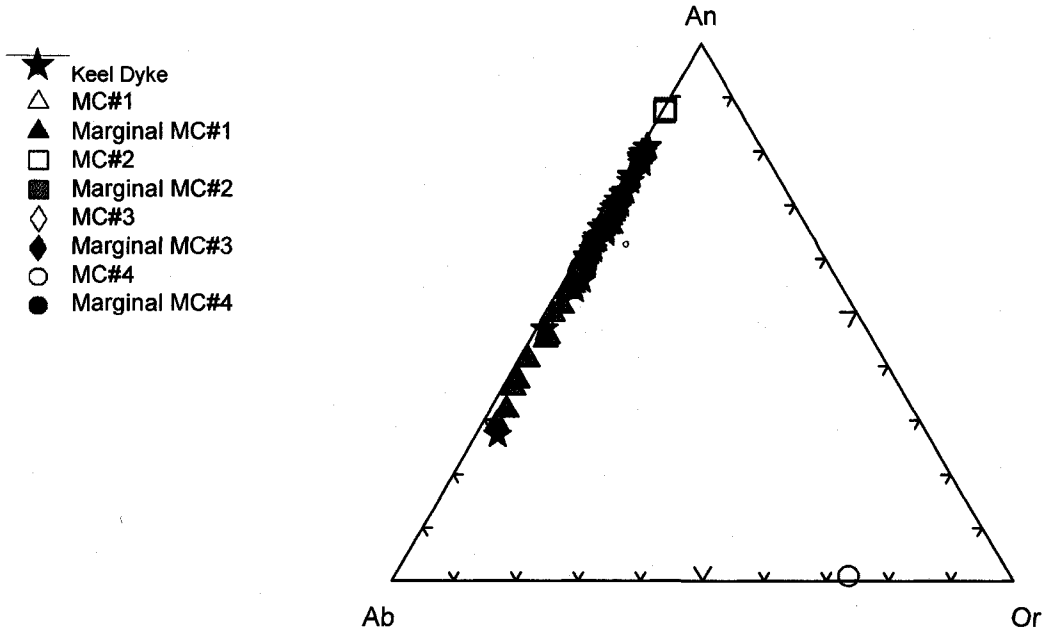

Figure 3.10– Average mineral compositions plotted with whole rock major element data, and estimated liquid compositions (from Francis, 1994). Grouped according to rock and mineral type, symbols below.

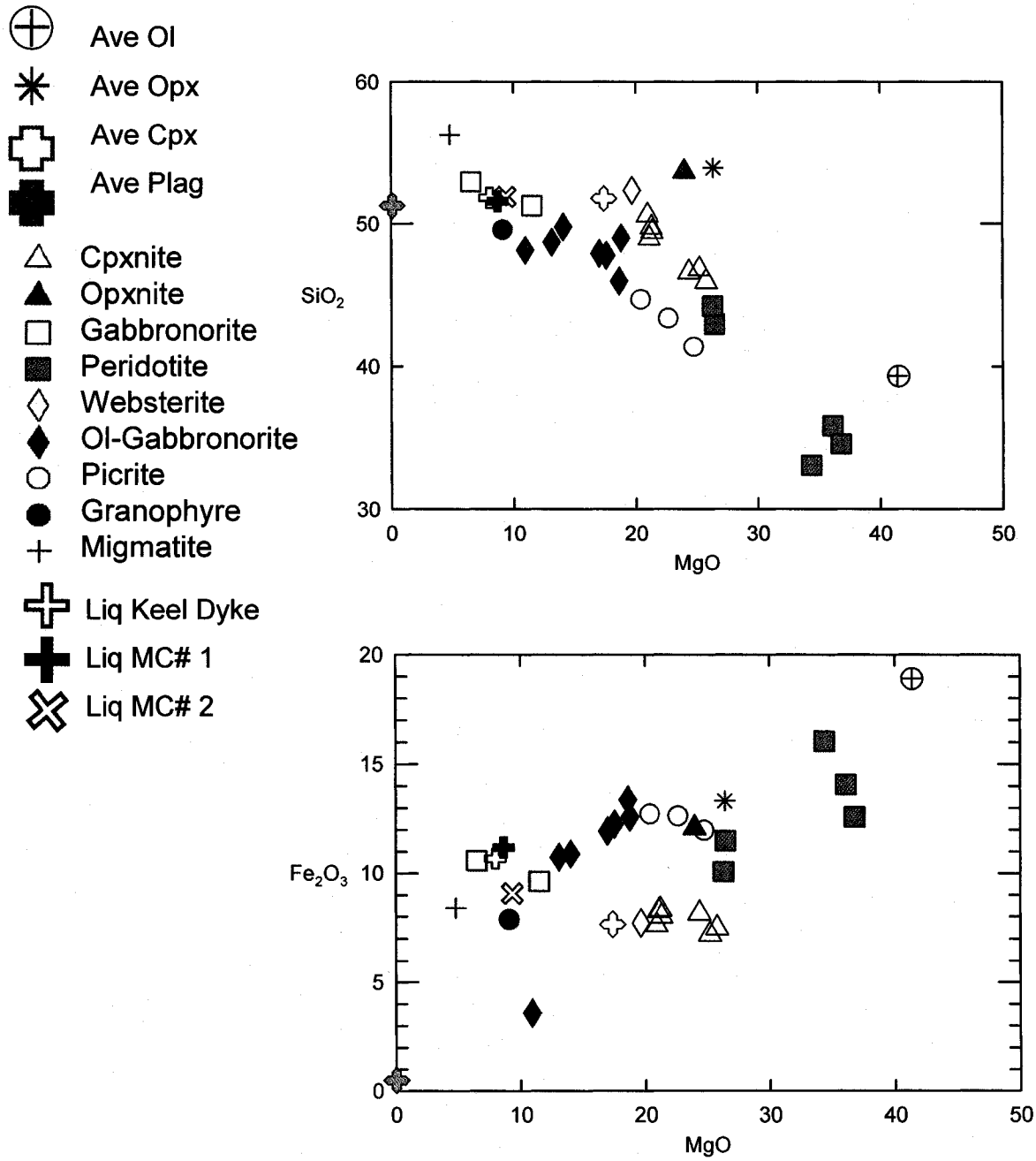

Table 3.1 – Major and trace element concentrations for whole rock powders. Measurements for major elements obtained from Actlabs, Ontario, using fusion ICP. Measurements for major elements are stated in % oxide. Detection limits for major oxides are also shown. Data for trace elements were obtained from Actlabs, Ontario, using ICP-MS. Measurements for trace elements are in ppm. Detection and upper limits are also shown. B/D indicates that the measurement was below detection. Measurements for the following elements: Rb, Sr, Hf, Lu, Nd, Sm, were determined at the University of Alberta using IDTIMS, for selected samples (VD-724, VD-850, V3-03, EQ-6, EQ-14, CR-46, LJ-24, MR-14).

Sample:	VD-724	VD-850	V3-03	EQ-6	EQ-14	CR-46	LJ-24	MR-14	MR-25
SiO2	50.57	53.62	52.33	49.05	43.69	45.97	49.77	47.91	51.25
Al2O3	2.59	4.56	3.73	14.41	5.66	9.00	11.50	10.25	12.95
Fe2O3	7.58	12.05	7.68	8.54	13.09	13.34	10.86	11.91	9.60
MnO	0.14	0.21	0.17	0.14	0.18	0.17	0.17	0.18	0.16
MgO	20.97	24.03	19.70	14.21	25.24	18.65	14.08	17.02	11.51
CaO	15.78	4.20	14.21	9.02	4.75	7.84	11.60	10.22	11.87
Na2O	0.22	0.50	0.34	1.48	0.67	1.52	1.15	1.03	1.48
K2O	0.08	0.34	0.11	0.55	0.86	0.59	0.23	0.49	0.54
TiO2	0.30	0.41	0.39	0.84	1.27	0.98	0.55	0.74	0.63
P2O5	0.10	0.02	0.03	0.07	0.12	0.12	0.05	0.08	0.05
LOI	1.29	0.12	0.34	0.41	3.50	0.59	-0.23	0.30	0.06
Total	99.62	100.06	99.02	98.72	99.02	98.78	99.72	100.13	100.09
Sc	44	27	45	20	20	25	39	32	40
V	141	130	167	162	218	212	209	200	229
Cr	5780	2790	4770	750	1870	1820	1010	1920	987
Co	57	90	68	38	69	87	66	76	54
Ni	367	519	417	280	680	702	329	503	239
Cu	43	50	64	70	110	122	112	146	90
Zn	44	99	49		70	89	60	71	60
Ga	4	7	6	13	11	13	12	12	14
Ge	3	2	2.1	0.6	0.9	1.4	1.4	1.3	1.3
Rb	1.91	4	3	13	23	13	6	11	10
Sr	17.44	117	52	281	130	153	139	111	165
Y	5	5	7	14	20	15	10	14	11
Zr	14	15	11	56	B/D	72	29	53	35
Nb	0.4	0.6	0.4	4.1	7.1	4.4	1.4	3.0	2.0
Sn	B/D	B/D	B/D	B/D	B/D	2	1	1	B/D
Sb	B/D	B/D	B/D	B/D	B/D	B/D	B/D	B/D	B/D
Cs	0.4	0.2	0.2	0.7	1.3	0.8	0.2	0.5	0.3
Ba	23	101	103	130	B/D	146	75	133	105
La	1.43	1.64	1.15	8.18	12.1	9.41	3.77	7.12	4.50
Ce	3.46	3.76	3.20	18.3	27.4	21.2	8.44	15.9	10.4
Pr	0.49	0.49	0.49	2.33	3.47	2.72	1.14	1.98	1.33
Nd	1.65	2.45	3.26	10.64	14.98	14.19	4.77	11.66	6.30
Sm	0.50	0.66	1.13	2.54	3.54	3.49	1.3	3.09	1.74
Eu	0.27	0.31	0.36	0.89	0.99	1.00	0.59	0.74	0.70
Gd	0.95	0.88	1.29	2.64	3.8	3.11	1.70	2.44	1.97
Tb	0.17	0.15	0.23	0.42	0.57	0.52	0.31	0.44	0.34
Dy	1.04	0.92	1.42	2.38	3.35	3.04	2.01	2.68	2.10
Ho	0.21	0.20	0.28	0.46	0.67	0.57	0.41	0.54	0.43
Er	0.58	0.61	0.82	1.34	1.94	1.64	1.18	1.59	1.26
Tm	0.08	0.09	0.12	0.19	0.27	0.24	0.18	0.23	0.18
Yb	0.48	0.55	0.73	1.16	1.64	1.44	1.09	1.42	1.10
Lu	0.07	0.08	0.09	0.17	0.25	0.20	0.16	0.20	0.16
Hf	0.36	0.42	0.37	1.72	3.06	2.084	0.90	1.53	1.0
Ta	0.07	0.04	B/D	0.28	0.49	0.32	0.09	0.22	0.14
W	B/D	B/D	B/D	B/D	B/D	B/D	B/D	B/D	B/D
Tl	0.06	B/D	B/D	B/D	0.08	0.09	0.06	0.12	0.07
Pb	B/D	B/D	B/D	7	B/D	B/D	B/D	B/D	B/D
Bi	B/D	B/D	B/D	B/D	B/D	B/D	B/D	0.1	B/D
Th	0.21	0.25	0.14	1.43	2.41	1.72	0.72	1.62	0.85
U	0.06	0.07	0.03	0.39	0.66	0.42	0.18	0.38	0.22

Table 3.1 continued

Sample:	V1-05	V1-10	V1-02	V1-01	SL-42	ES-10	VD-722	CR-6	VD-707
SiO2	33.01	35.79	46.56	34.52	48.14	42.99	49.72	41.42	45.92
Al2O3	1.89	0.74	2.86	1.30	16.45	2.38	2.78	6.89	1.26
Fe2O3	16.01	14.04	8.10	12.55	3.55	11.48	8.29	11.96	7.43
MnO	0.15	0.11	0.14	0.13	0.07	0.17	0.15	0.17	0.14
MgO	34.40	36.13	24.41	36.82	10.96	26.49	21.29	24.81	25.82
CaO	0.26	0.02	12.06	0.26	16.17	7.52	15.11	7.76	11.11
Na2O	B/D	B/D	0.15	B/D	0.47	0.03	0.18	0.09	B/D
K2O	B/D	0.05	0.05	B/D	1.18	0.04	0.03	0.09	0.02
TiO2	0.16	0.08	0.25	0.13	0.13	0.32	0.34	0.31	0.18
P2O5	0.02	0.02	0.02	0.02	0.02	0.03	0.03	0.04	B/D
LOI	12.69	12.26	4.53	14.18	2.34	8.03	1.81	6.27	6.98
Total	98.38	99.20	99.13	99.56	99.48	99.45	99.73	99.80	98.88
Sc	8	10	44	9	34	34	41	22	39
V	136	35	134	61	133	154	130	112	119
Cr	>10,000	6300	4430	4780	1250	3180	5270	3490	3790
Co	110	165	93	113	28	99	68	105	76
Ni	1,070	1,470	604	899	194	873	289	1,030	596
Cu	35	23	31	15	B/D	B/D	40	66	10
Zn	64	89	50	57	B/D	41	42	76	B/D
Ga	4	2	4	3	11	4	5	7	2
Ge	0.7	1.2	2.0	0.8	1.3	1.5	2.1	1.1	1.4
Rb	B/D	B/D	1		11	2	3	5	B/D
Sr	3	B/D	12	2	175	10	22	92	8
Y	1	1	5	2	2	6	6	5	4
Zr	9	5	6	7	5	17	17	22	5
Nb	0.5	0.2	0.3	0.5	B/D	0.5	0.6	1.1	B/D
Sn	B/D	B/D	B/D	B/D	1	1	1	1	B/D
Sb	B/D	B/D	B/D	B/D	B/D	B/D	B/D	B/D	B/D
Cs	B/D	B/D	0.2	B/D	0.4	0.2	0.4	0.3	B/D
Ba	6	4	5	3	78	7	42	89	8
La	0.68	0.32	0.91	0.65	0.29	1.51	1.51	2.17	0.32
Ce	1.29	0.74	2.34	1.59	0.84	3.92	3.97	5.01	1.09
Pr	0.19	0.10	0.36	0.21	0.15	0.57	0.58	0.67	0.20
Nd	0.85	0.52	2.01	1.01	0.91	3.09	2.98	3.20	1.32
Sm	0.23	0.16	0.65	0.28	0.34	0.96	0.92	0.86	0.47
Eu	0.08	0.05	0.24	0.09	0.20	0.31	0.35	0.32	0.18
Gd	0.23	0.20	0.86	0.28	0.49	1.11	1.11	0.92	0.65
Tb	0.04	0.03	0.15	0.05	0.09	0.20	0.19	0.16	0.12
Dy	0.25	0.19	0.96	0.30	0.53	1.19	1.20	0.99	0.74
Ho	0.05	0.04	0.20	0.06	0.10	0.23	0.24	0.19	0.15
Er	0.16	0.12	0.58	0.18	0.29	0.65	0.69	0.57	0.44
Tm	0.02	0.02	0.08	0.03	0.04	0.09	0.10	0.09	0.06
Yb	0.16	0.12	0.51	0.18	0.24	0.57	0.59	0.54	0.38
Lu	0.02	0.02	0.07	0.03	0.03	0.08	0.09	0.08	0.06
Hf	0.2	0.1	0.2	0.2	0.2	0.5	0.5	0.6	0.2
Ta	0.01	B/D	B/D	0.01	B/D	0.02	0.02	0.06	B/D
W	B/D	B/D	B/D	B/D	B/D	B/D	B/D	B/D	B/D
Tl	B/D	B/D	0.06	B/D	B/D	B/D	0.06	B/D	B/D
Pb	B/D	B/D	B/D	B/D	B/D	B/D	B/D	B/D	B/D
Bi	B/D	B/D	B/D	B/D	B/D	B/D	B/D	B/D	0.1
Th	0.10	0.05	0.11	0.15	B/D	0.23	0.25	0.45	B/D
U	0.04	0.06	0.04	0.04	B/D	0.06	0.05	0.10	B/D

Table 3.1 continued

Sample:	LJ-6	EQ-20	VD-709	EQ-15	EQ-19	EQ-13	M-26	EQ-22	CR-31
SiO2	52.95	48.95	46.78	56.18	49.90	46.42	64.95	44.35	47.85
Al2O3	13.67	2.24	1.30	21.58	9.64	7.55	13.14	1.45	9.13
Fe2O3	10.55	8.23	7.15	8.17	10.79	11.30	7.99	7.05	11.57
MnO	0.17	0.17	0.12	0.14	0.17	0.17	0.12	0.18	0.17
MgO	6.53	21.13	25.25	4.53	18.12	22.45	1.44	28.83	18.78
CaO	9.76	15.06	12.87	0.63	7.84	5.84	1.99	8.36	7.44
Na2O	2.25	0.18	0.13	0.99	1.21	0.93	1.37	0.11	1.18
K2O	1.14	0.05	B/D	3.26	0.24	0.56	5.57	B/D	0.74
TiO2	1.70	0.38	0.20	0.71	0.67	1.05	1.42	0.25	0.97
P2O5	0.16	0.02	B/D	0.06	0.05	0.08	0.25	B/D	0.09
LOI	B/D	2.52	5.64	2.89	0.79	2.66	1.73	8.65	1.42
Total	98.75	98.93	99.43	99.13	99.42	99.01	99.96	99.22	99.34
Sc	31	56	43	11	27	22	18	44	29
V	301	245	135	128	178	198	101	189	222
Cr	198	4830	4010	130	1240	1540	B/D	3020	1040
Co	36	65	71	18	43	51	9	39	53
Ni	155	546	545	50	380	470	B/D	360	480
Cu	127	12	11	20	40	70	20	B/D	60
Zn	69	34	B/D	120	60	60	240	B/D	50
Ga	18	4	3	29	10	11	20	2	12
Ge	0.8	1.8	1.9	2.2	0.6	0.6	1.6	0.7	1.2
Rb	30	1	B/D	135	7	17	165	2	15
Sr	270	15	9	132	155	132	179	9	135
Y	25	8	4	18	11	16	41	6	17
Zr	133	12	5	160	36	81	254	5	69
Nb	8.3	0.8	0.2	11.5	2.4	5.3	18.3	0.2	4.5
Sn	1	B/D	B/D	2	B/D	B/D	4	B/D	B/D
Sb	B/D	B/D	B/D	B/D	0.3	B/D	0.9	B/D	B/D
Cs	0.7	0.2	B/D	9.8	0.4	1	6.3	0.2	0.7
Ba	272	5	2	469	85	143	1176	5	127
La	17.5	0.90	0.30	32.4	5.23	9.26	42.6	0.63	8.36
Ce	38.5	2.84	1.07	64.9	11.6	20.8	85.6	1.64	18.9
Pr	4.76	0.50	0.20	7.18	1.55	2.62	10.1	0.29	2.47
Nd	21.2	2.95	1.33	26	6.76	11.4	38.8	1.93	10.7
Sm	5.46	1.06	0.49	4.84	1.82	2.81	8.65	0.69	2.79
Eu	1.73	0.38	0.17	0.74	0.65	0.89	2.24	0.24	0.91
Gd	5.27	1.33	0.63	3.75	1.92	2.92	7.99	0.88	3
Tb	0.87	0.25	0.13	0.57	0.32	0.5	1.26	0.15	0.5
Dy	4.96	1.48	0.83	2.81	1.83	2.93	7.27	0.94	2.98
Ho	0.94	0.28	0.16	0.56	0.37	0.57	1.37	0.19	0.58
Er	2.71	0.80	0.49	1.69	1.08	1.58	4.07	0.57	1.67
Tm	0.38	0.12	0.07	0.24	0.16	0.22	0.58	0.08	0.24
Yb	2.31	0.72	0.42	1.5	0.97	1.39	3.59	0.45	1.49
Lu	0.34	0.10	0.06	0.22	0.13	0.20	0.49	0.07	0.21
Hf	3.8	0.6	0.2	4.5	1.1	2.3	6.9	0.3	2
Ta	0.64	B/D	B/D	1.02	0.17	0.37	1.44	0.02	0.3
W	B/D	B/D	B/D	0.8	B/D	B/D	1.5	5.3	B/D
Tl	0.18	B/D	B/D	0.57	B/D	0.06	1.34	B/D	0.06
Pb	B/D	B/D	B/D	27	B/D	B/D	64	B/D	B/D
Bi	B/D	B/D	B/D	0.2	B/D	B/D	1	B/D	B/D
Th	3.71	0.11	B/D	12.6	0.81	1.79	11.2	B/D	1.68
U	0.93	0.02	B/D	2.61	0.22	0.49	3.2	B/D	0.44

Table 3.1 continued

Oxide	Detection Limit (%)
SiO_2	0.01
Al_2O_3	0.01
Fe_2O_3	0.01
MgO	0.01
MnO	0.001
CaO	0.01
TiO_2	0.001
Na_2O	0.01
K_2O	0.01
P_2O_5	0.01
Loss on Ignition	0.01

Element	Detection Limit	Upper Limit
Ag	0.5	100
As	5	2,000
Ba	3	
Be	1	
Bi	0.1	2,000
Co	1	1,000
Cr	20	10,000
Cs	0.1	1,000
Cu	10	10,000
Ga	1	500
Ge	0.5	500
Hf	0.1	1,000
In	0.1	200
Mo	2	100
Nb	0.2	1,000
Ni	20	10,000
Pb	5	10,000
Rb	1	1,000
Sb	0.2	200
Sc	1	
Sn	1	1,000
Sr	2	10,000
Ta	0.01	500
Tl	0.05	1,000
V	5	10,000
W	0.5	5,000
Y	0.5	1,000
Zn	30	10,000
Zr	4	10,000
La	0.05	2,000
Ce	0.05	3,000
Pr	0.01	1,000
Nd	0.05	2,000
Sm	0.01	1,000
Eu	0.005	1,000
Gd	0.01	1,000
Tb	0.01	1,000
Dy	0.01	1,000
Ho	0.01	1,000
Er	0.01	1,000
Tm	0.005	1,000
Yb	0.01	1,000
Lu	0.002	1,000
U	0.01	1,000
Th	0.05	2,000

Figure 3.11– Comparison of whole rock data from that of D. Francis, and results from this study. (a) Major element data show excellent correlation, with R^2 values between 0.999 and 1.0 (regressions not shown). (b) Select trace element data, one showing good correlation (Rb) and one showing poor correlation (Cu).

(a)

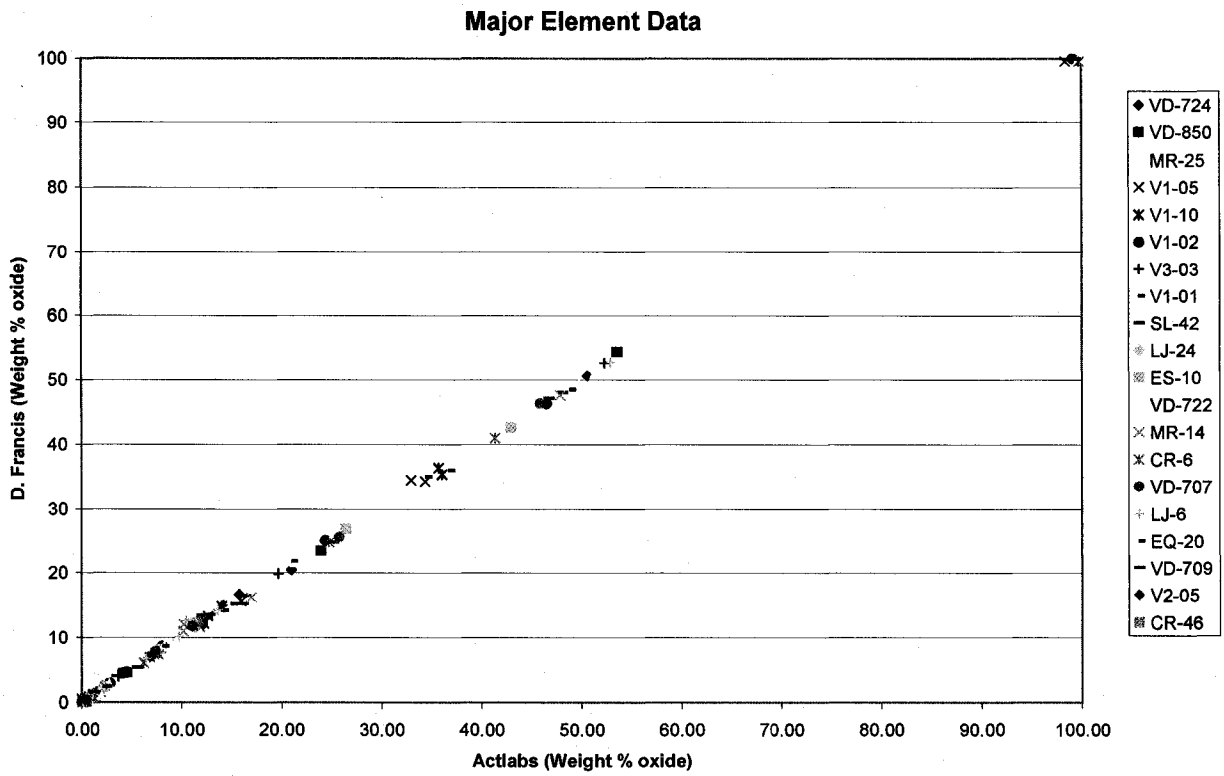

* All R^2 values are between 0.999 and 1.

(b)

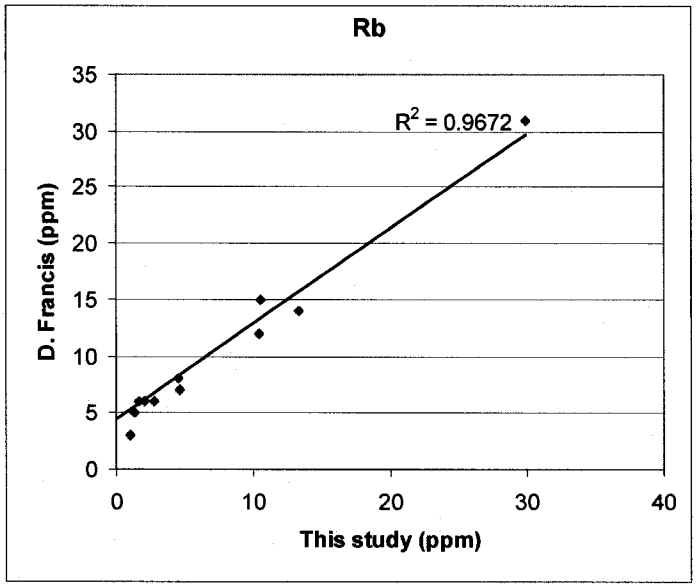

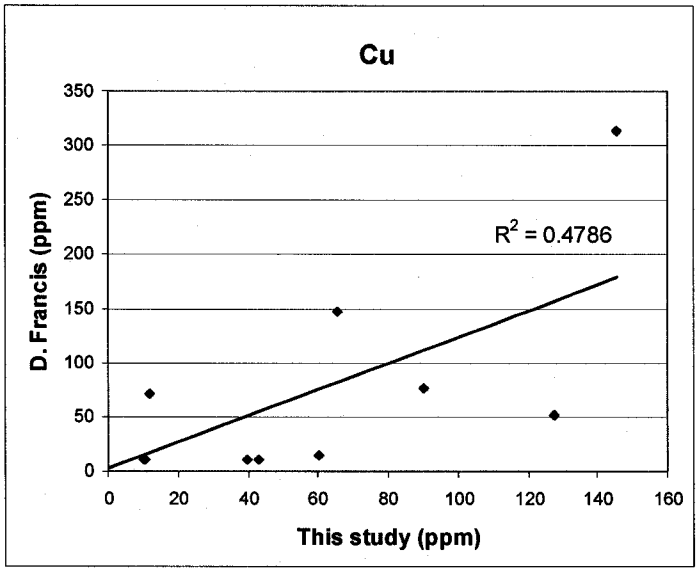

Figure 3.12 – AFM diagram for all samples, and liquid compositions estimated by Francis (1994). Liquid compositions for MC#1 and #2 were obtained by mathematically removing cumulate olivine from marginal samples. The liquid composition of the Keel Dyke came from a chilled margin GBN. Samples are grouped by rock type (top) and location (bottom).

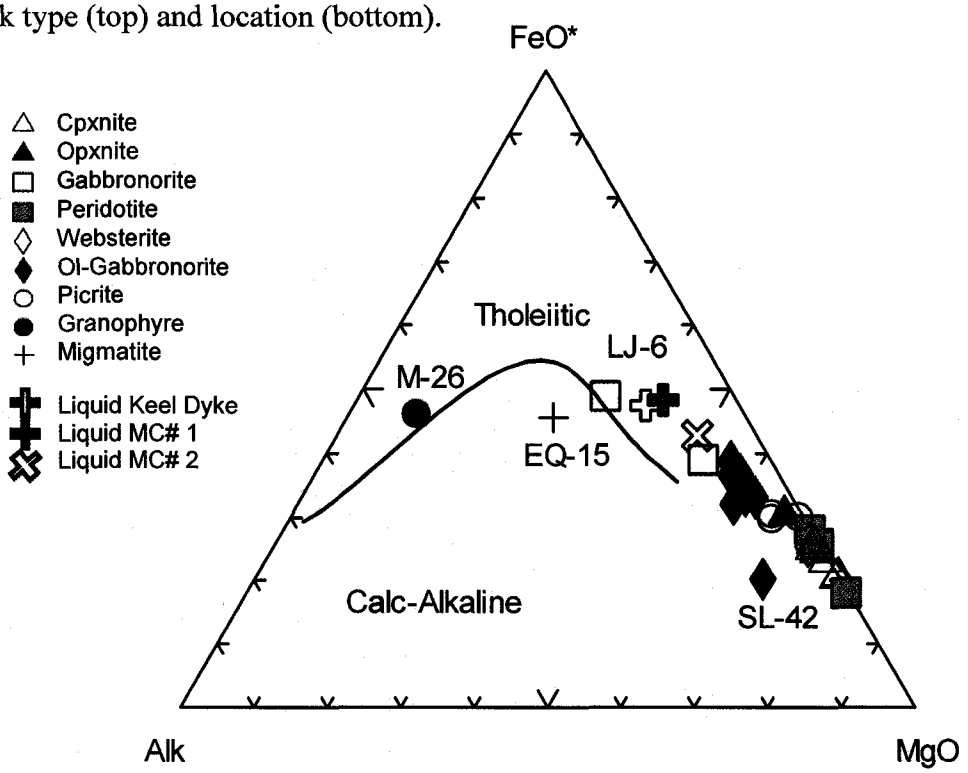

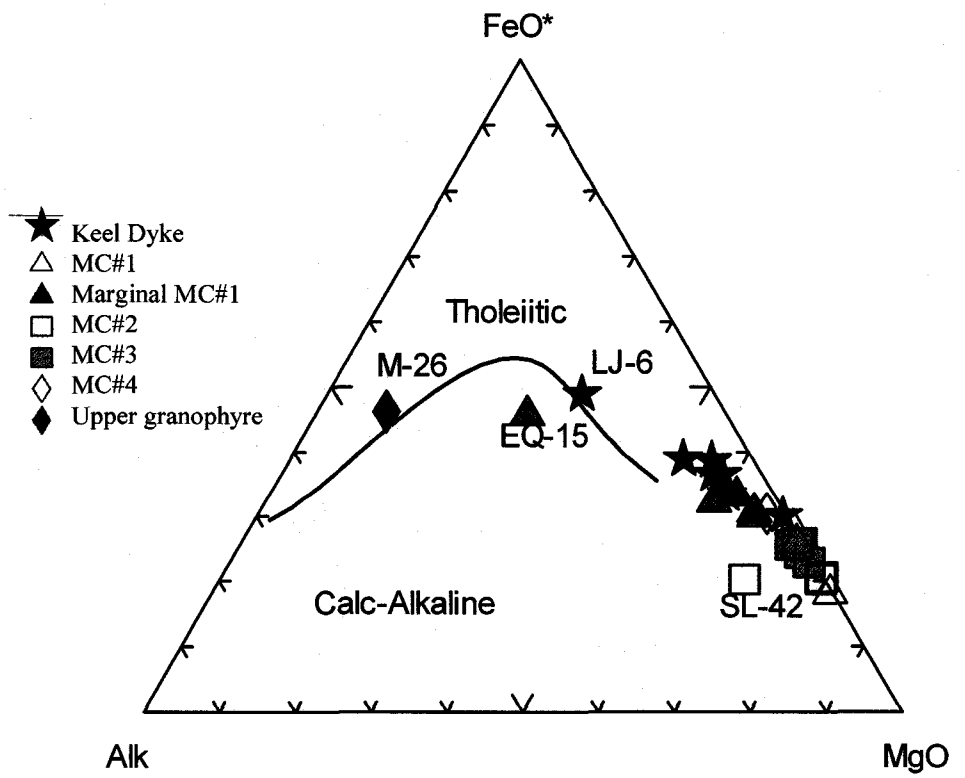

Figure 3.13 – Fenner variation diagrams. Samples are grouped according to location. Average mineral compositions are plotted for reference. Red arrow shows direction of evolution. Small arrows show mineral crystallization.

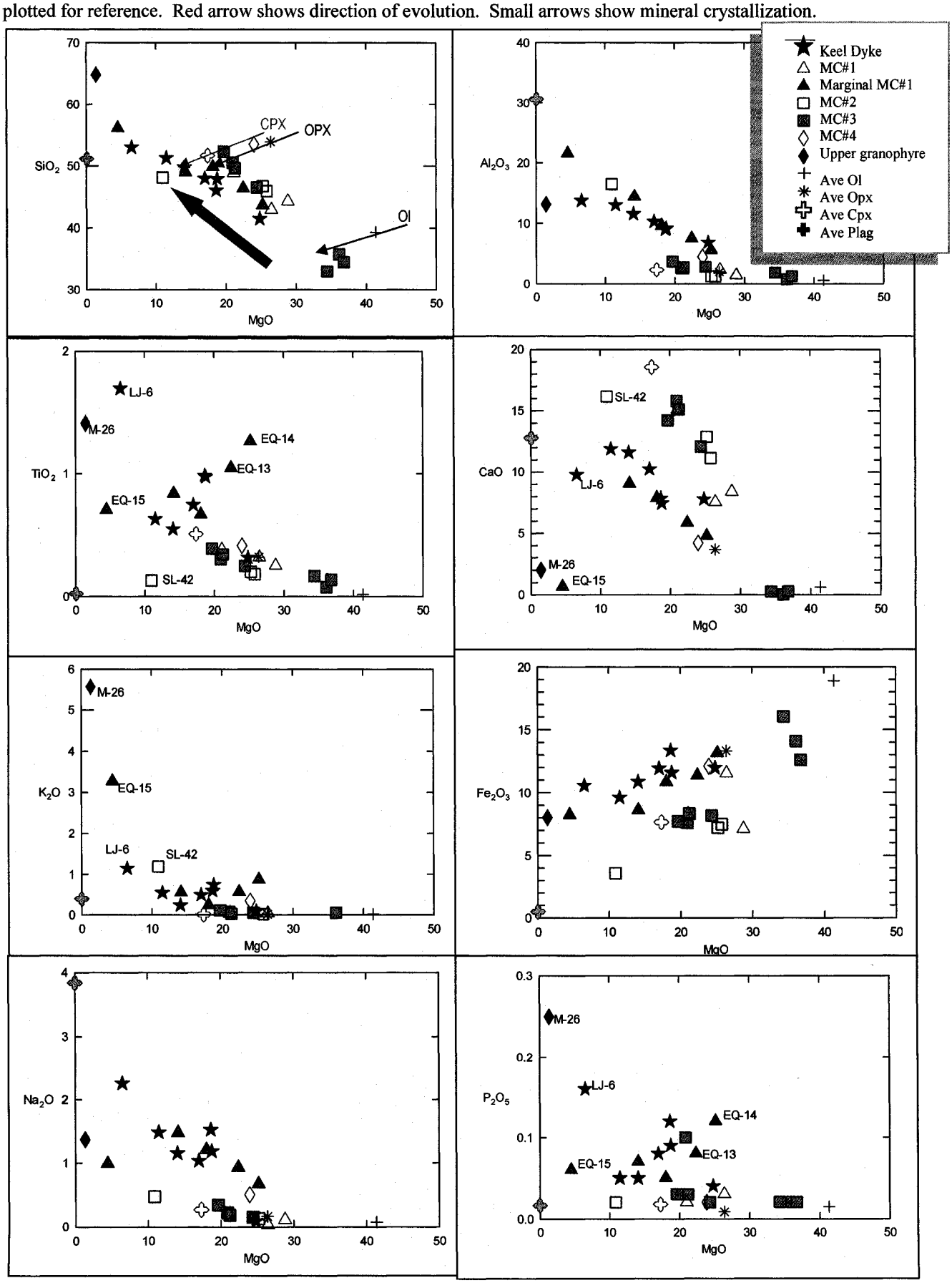

Figure 3.14- A plot of Mg # vs. stratigraphic height for the samples from this study. Samples indicated by a pink square are the ones chosen for isotope analysis. The numbers for chosen samples are shown to the left of the data. Stratigraphic column adapted from Francis (1994) and Irvine and Smith (1967). Stratigraphic column legend as in Figure 3.3.

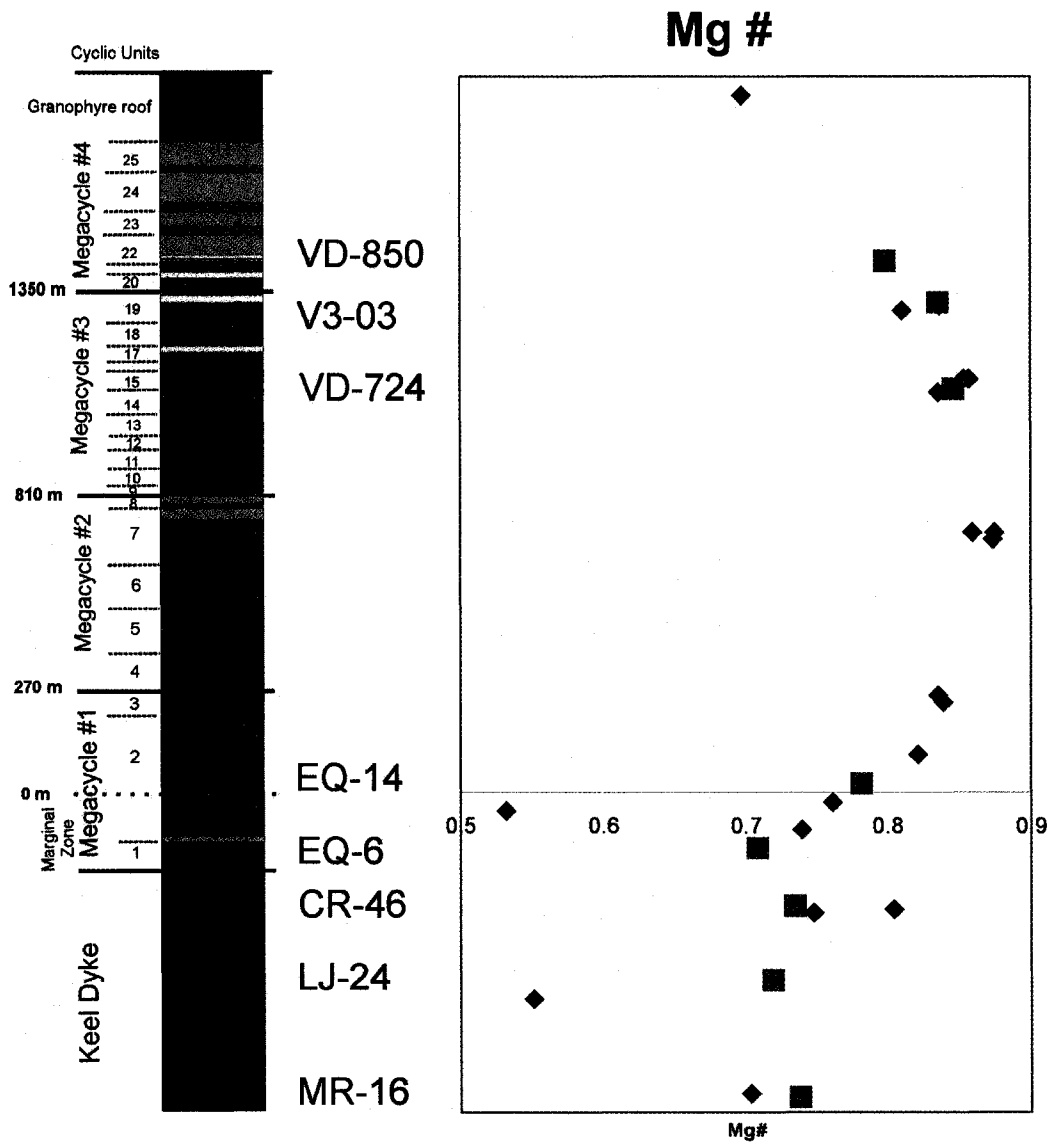

Figure 3.15 – Compatible trace elements Ni & Cr (ppm) vs. MgO (wt %). Red arrow shows direction of evolution. Grouped according to rock type.

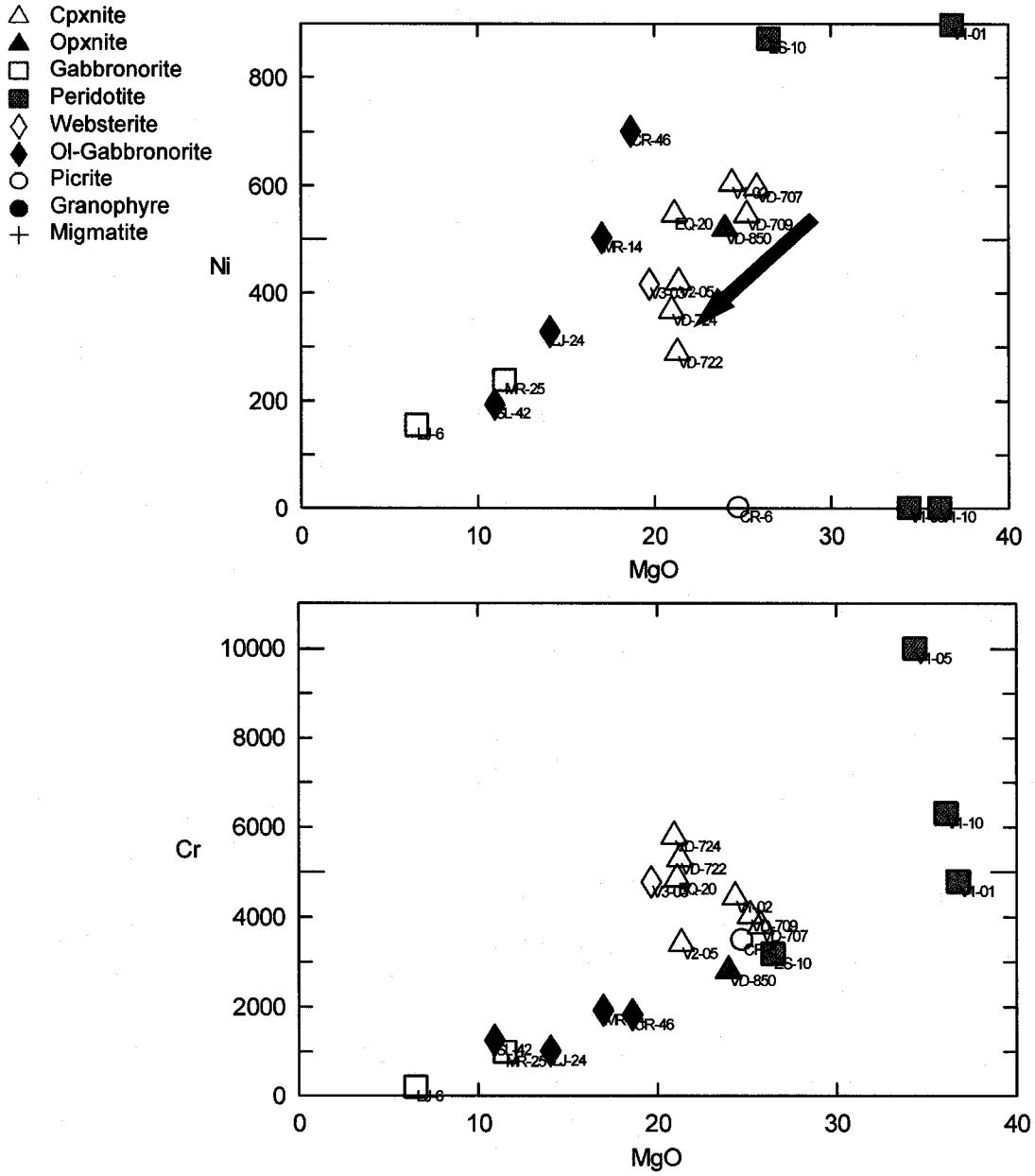

Figure 3.16 – Incompatible trace elements V, Zr, and Rb (ppm) vs. MgO (wt.%). Red arrow shows direction of evolution. Grouped according to rock type.

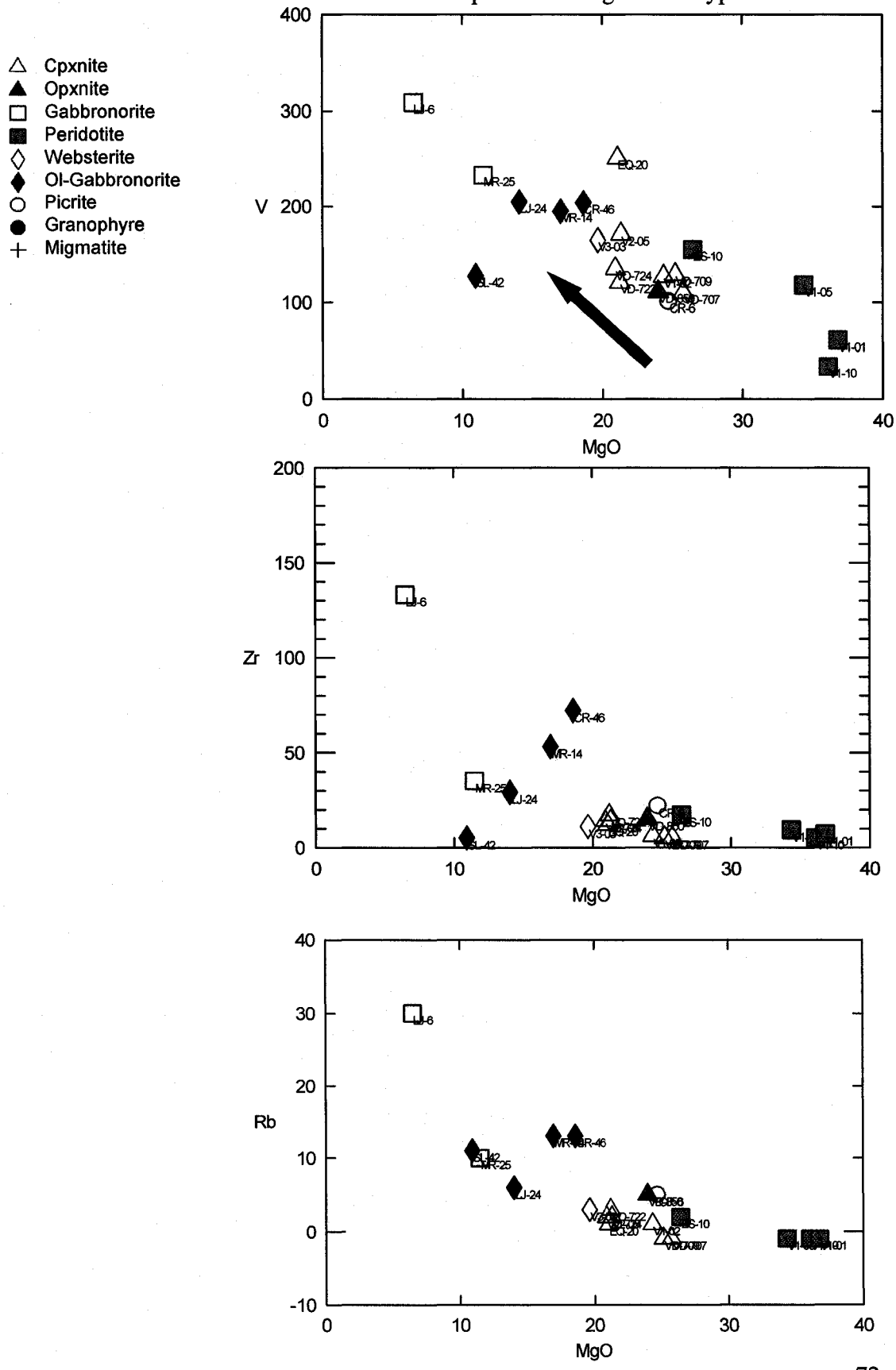

Figure 3.17 – (a) REE profile of samples analyzed in this study. (b) REE profile of samples from the Keel Dyke. (c) REE profile of estimated liquid compositions of the Keel Dyke and Layered Series, and of the Keel Dyke samples analyzed in this study. Liquid composition data from Francis (1994). (d) REE profile of samples from the layered series. Symbol color is indicative of location, symbol shape is indicative of rock type. See legend below. Data are normalized to the primitive mantle values of Sun and McDonough (1989). Mantle reservoirs N-MORB, E-MORB, and OIB are plotted for comparison, data from Sun and McDonough (1989).

× - granophyre
△ - orthopyroxenite
▲ - picrite
○ - websterite
● - peridotite
◇ - clinopyroxenite
□ - olivine gabbronorite
■ - gabbronorite
✳ - migmatite

red - keel dyke
light blue - MC1
orange - marginal MC1
green - MC2
blue - MC3
pink - MC4
black – mantle reservoirs

(a)

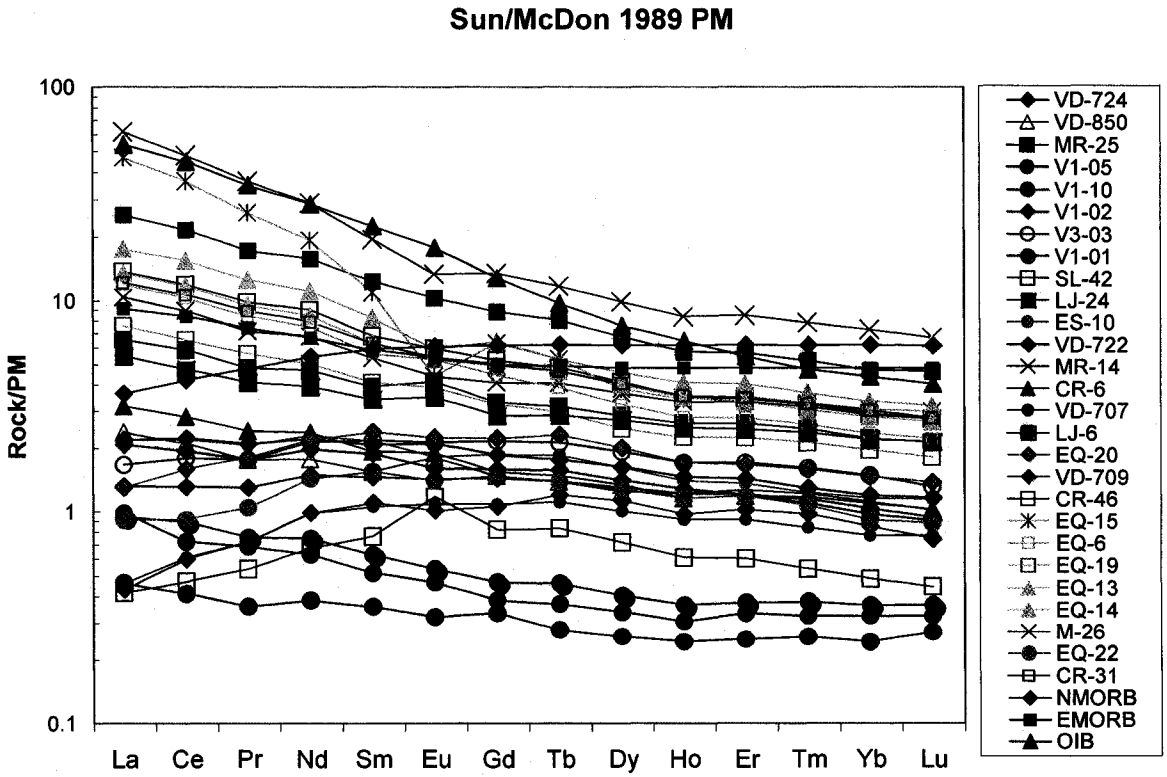

(b)

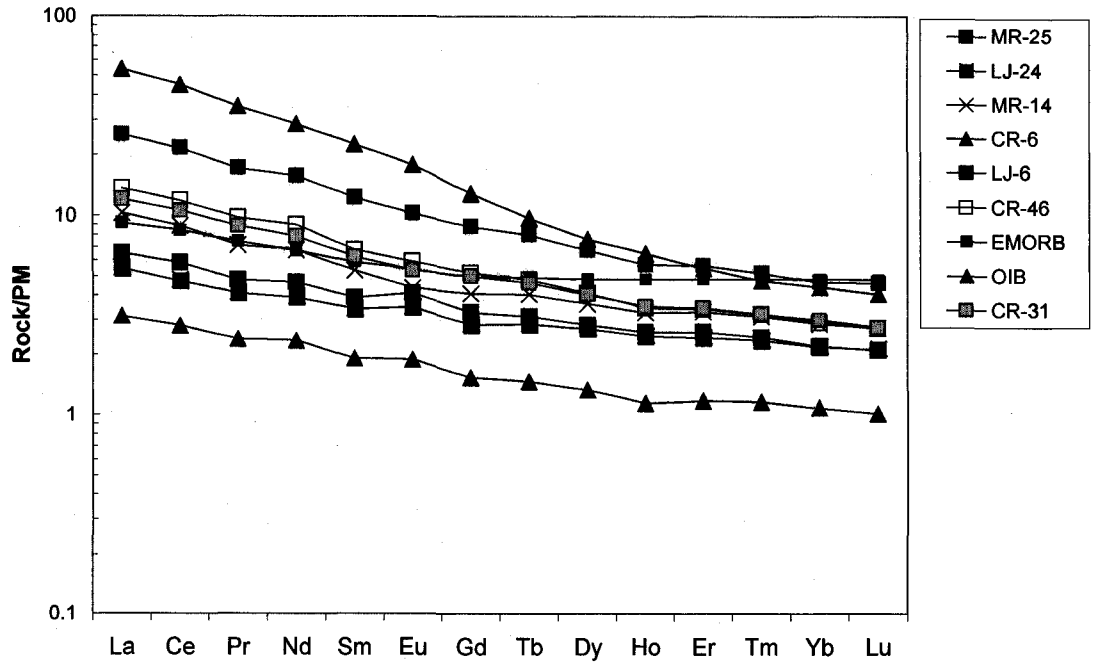

(c)

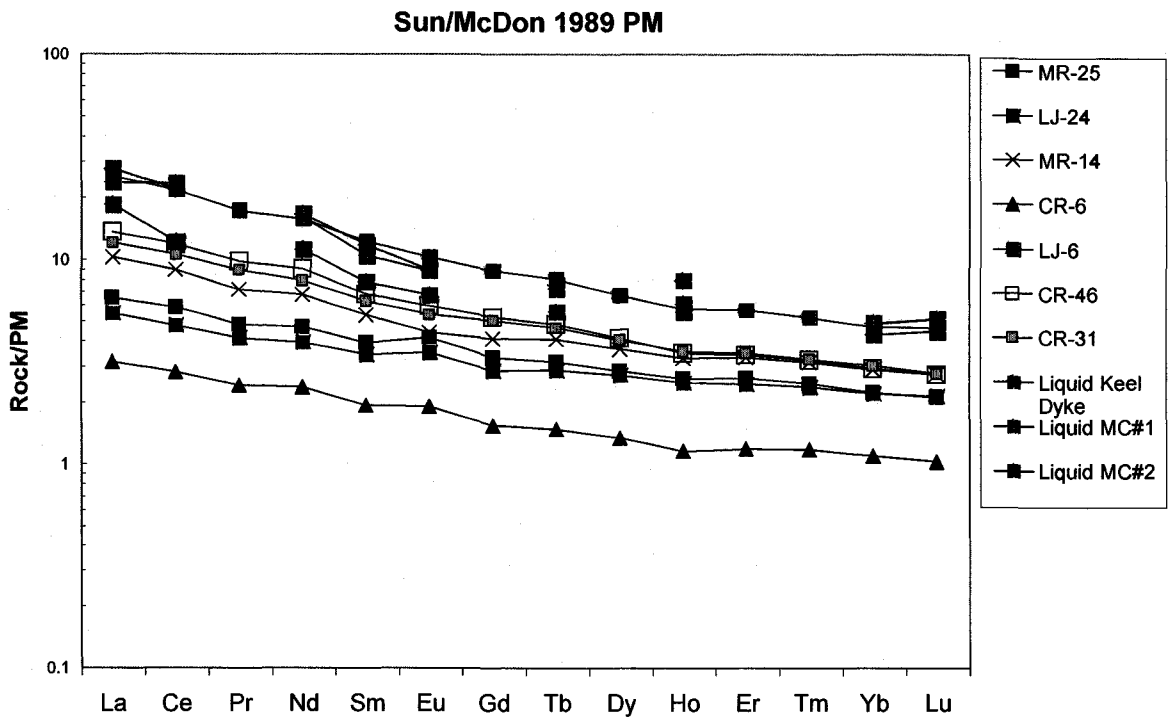

(d)

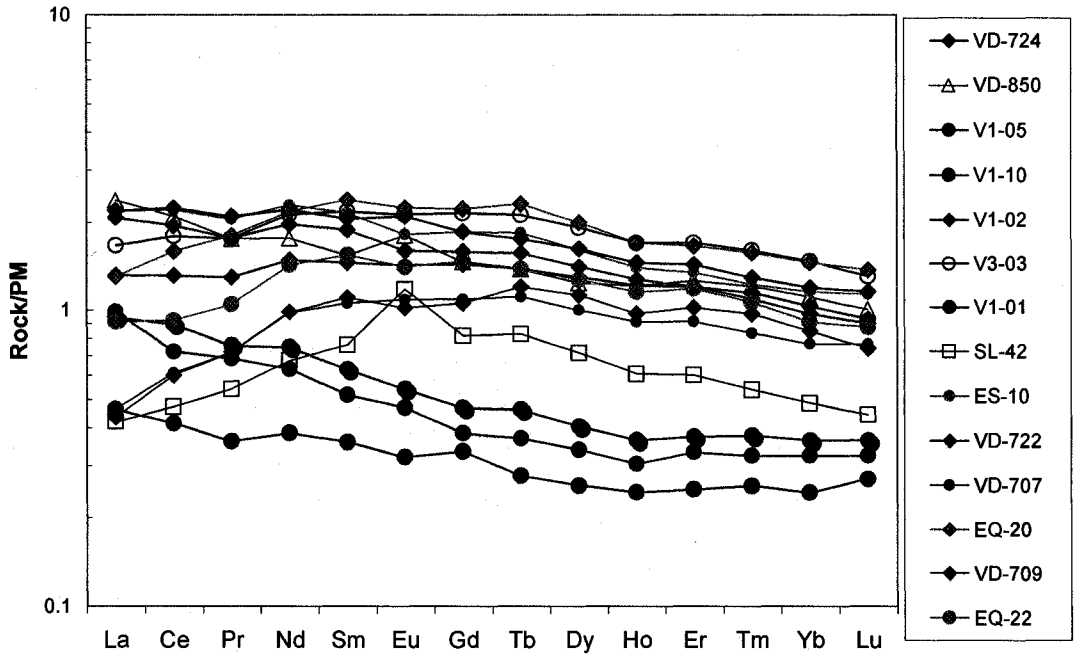

Figure 3.18 – (a) to (d) REE profiles of select samples from the layered series. See text for discussion. Legend as in Figure 3.17. Data are normalized to the primitive mantle values of Sun and McDonough (1989).

(a)

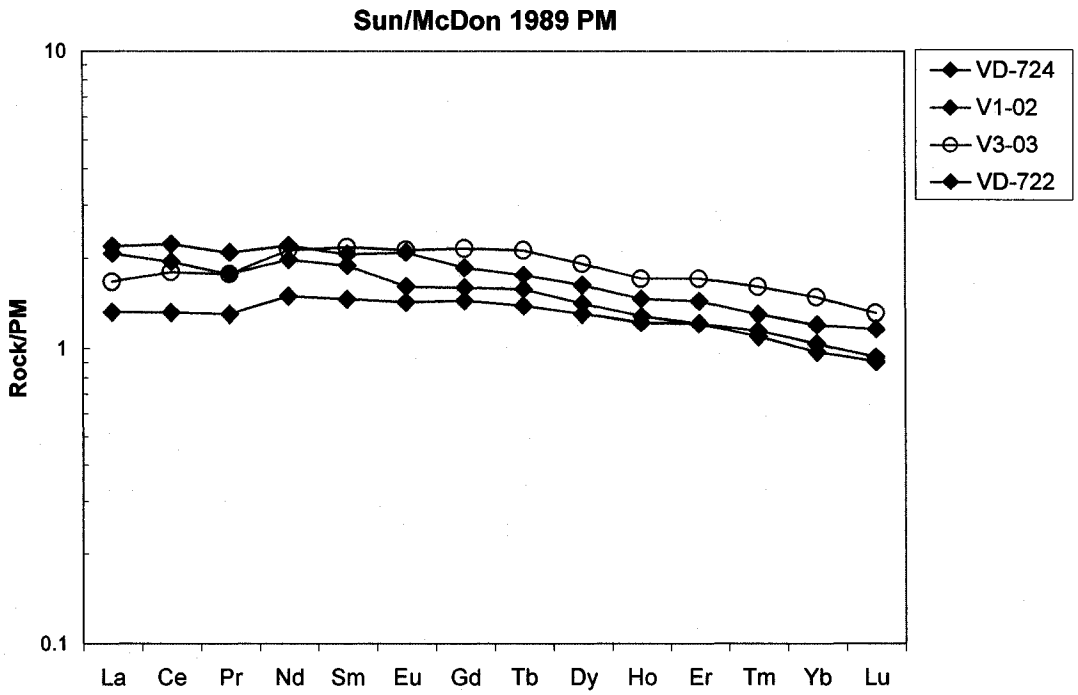

(b)

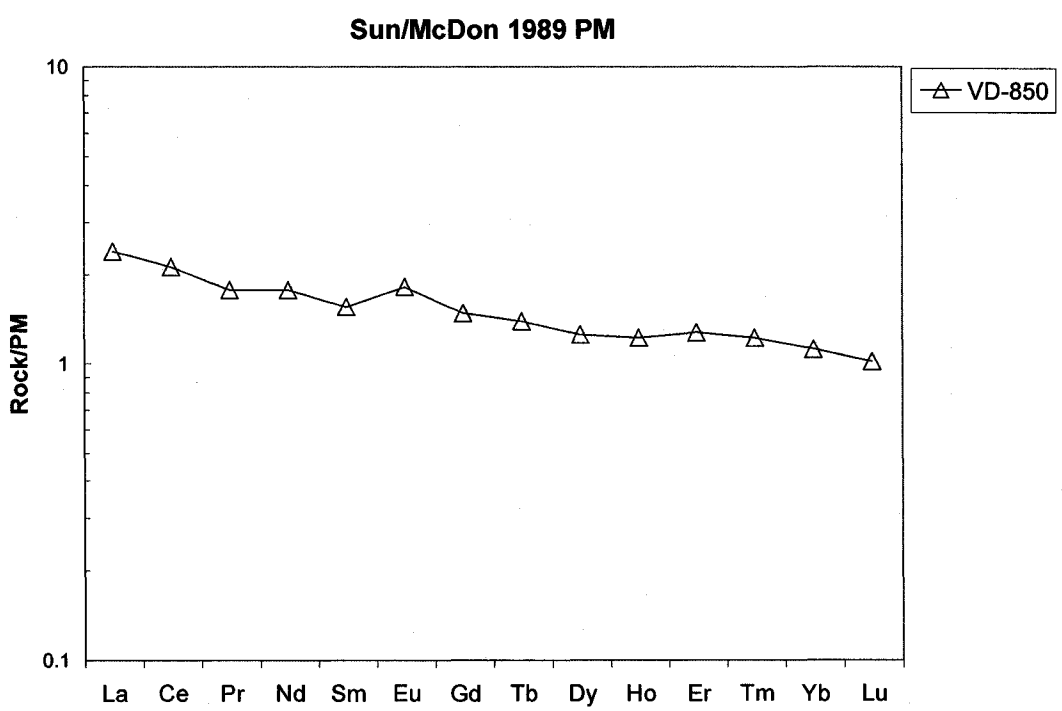

(c)

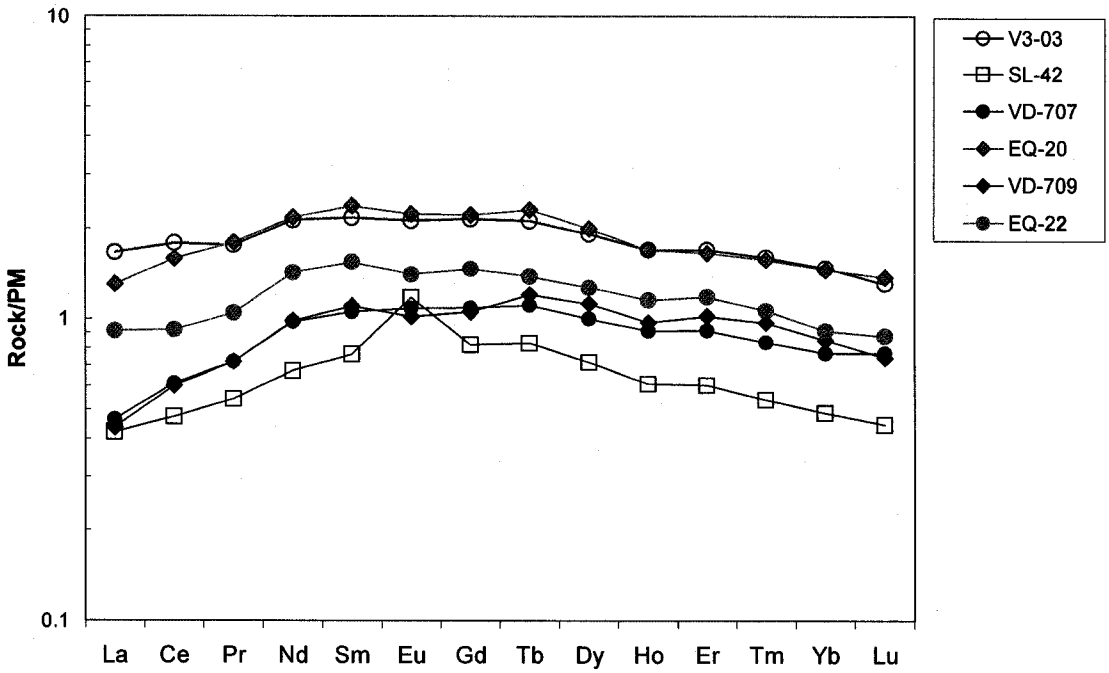

(d)

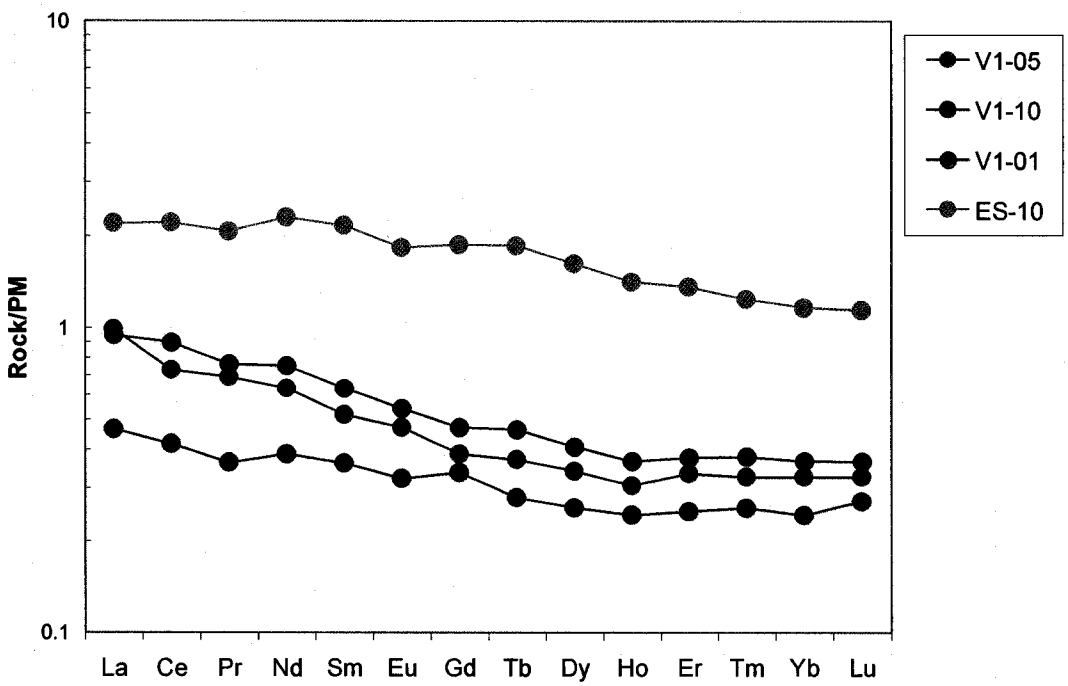

Figure 3.19 – Multi element spider-diagrams (a) of all samples analyzed for this study, (b) of the Keel Dyke samples, (c) of the altered peridotite samples, (d) of the clinopyroxenites and websterites, and (e) of samples SL-42 and VD-850. Symbol color is indicative of location, symbol shape is indicative of rock type. See legend in (a)

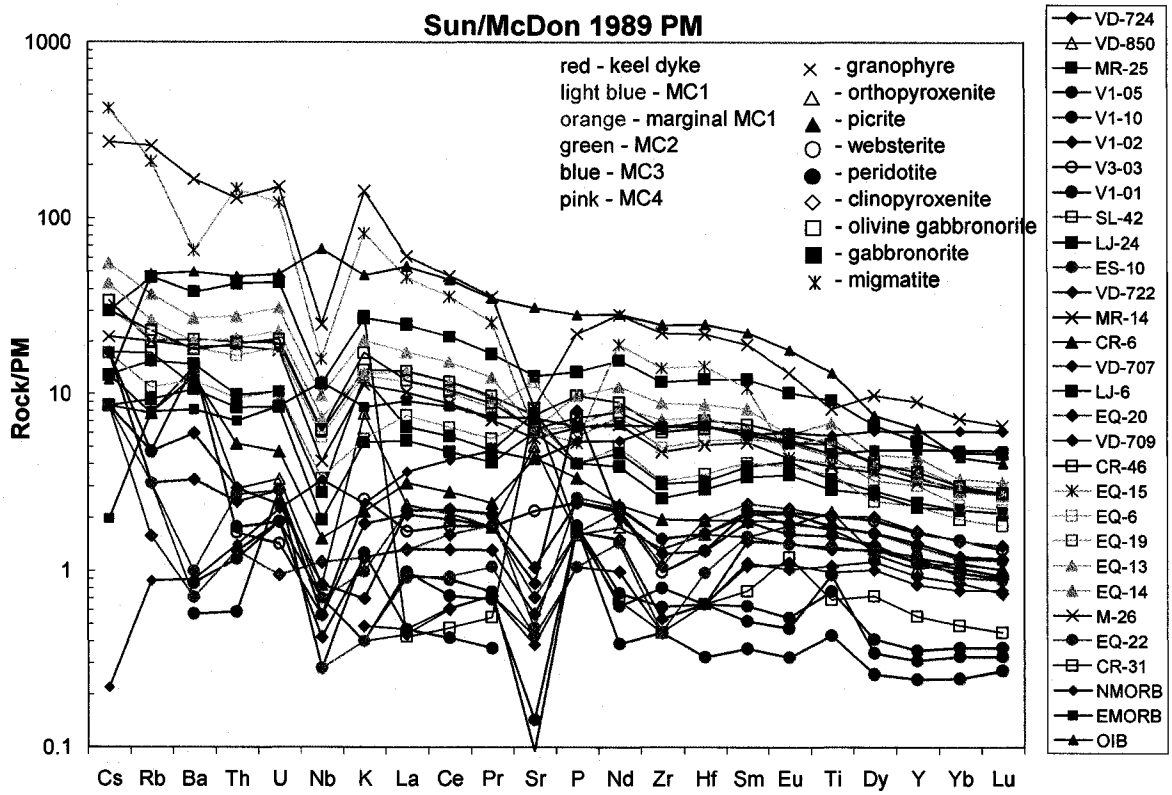

(b)

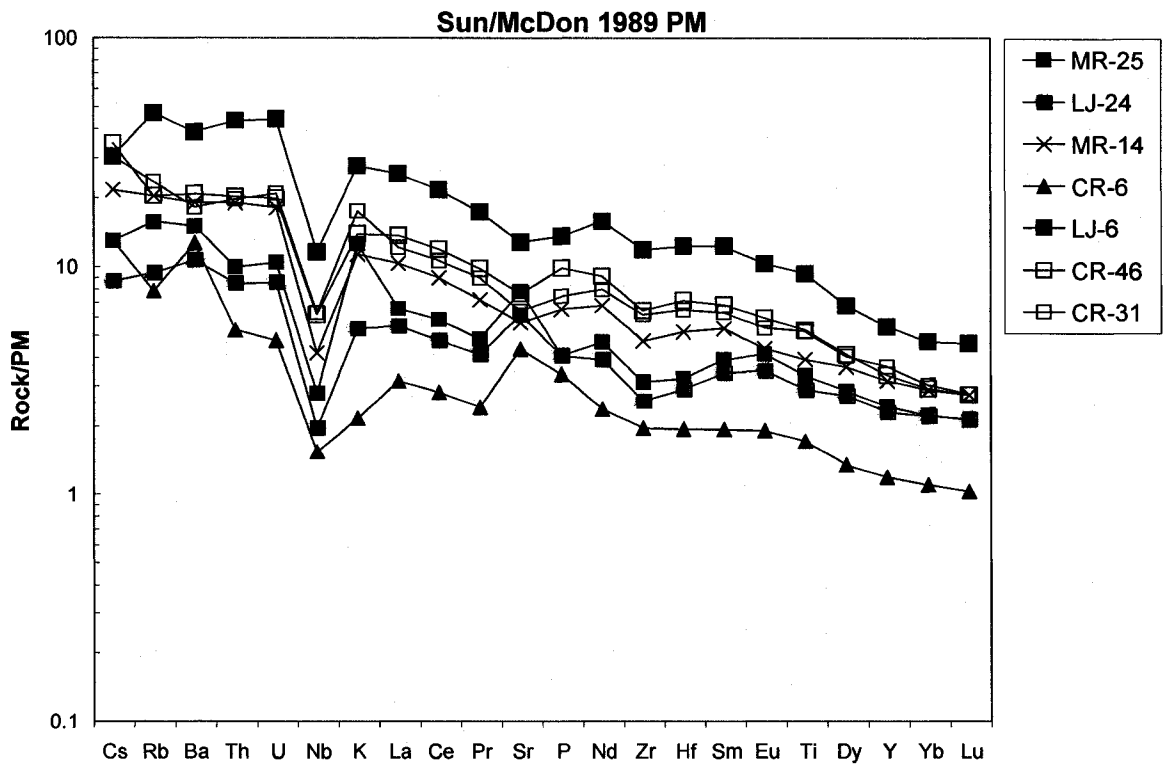

(c)

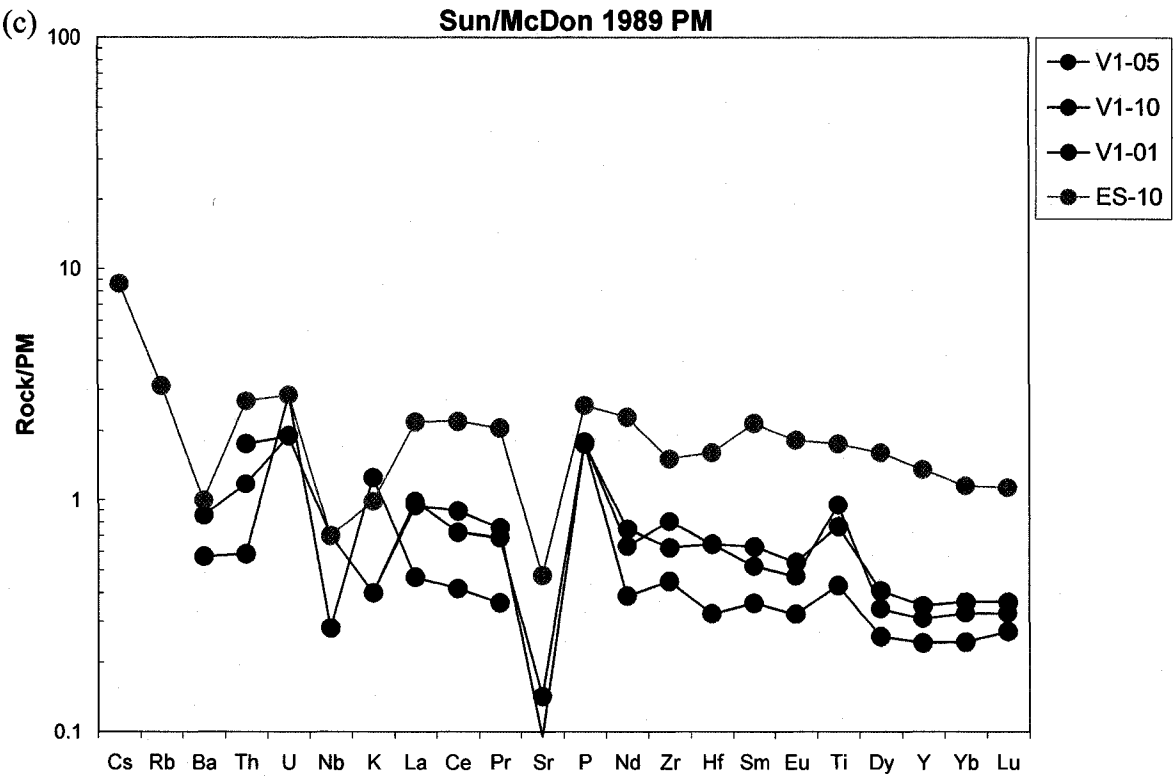

(d)

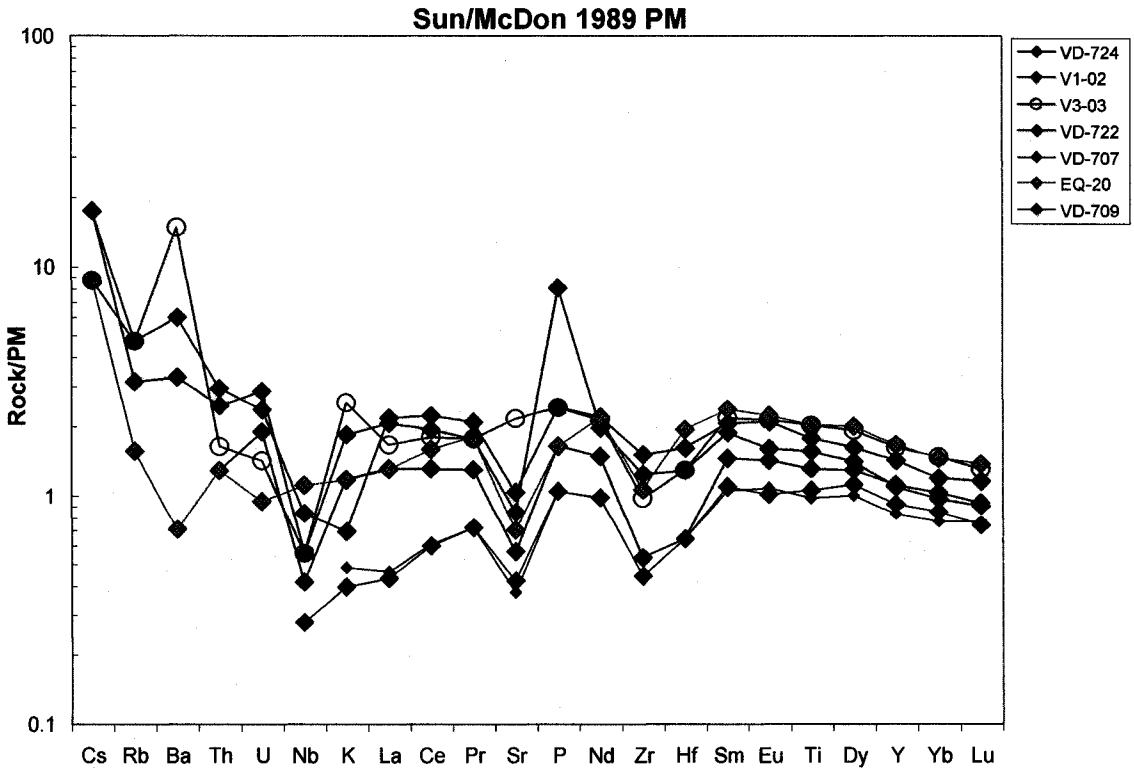

(e)

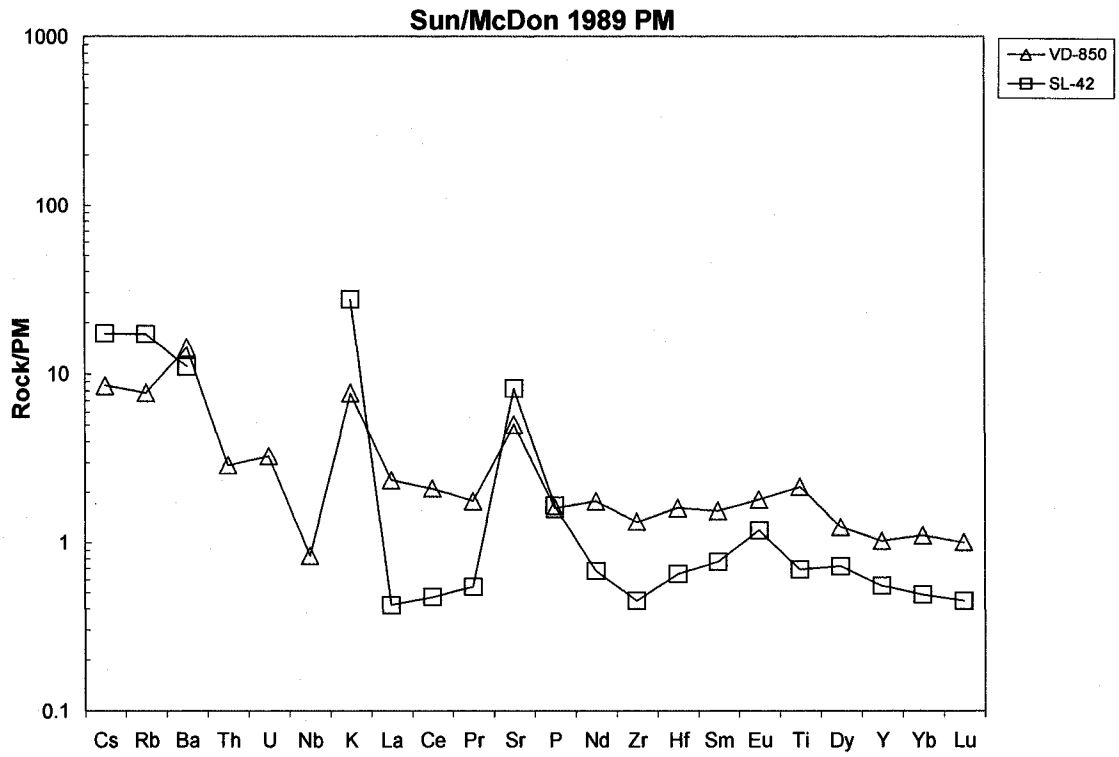

Figure 4.1 – Geological map of the Muskox Intrusion, showing sample locations, and the locations of samples chosen for the whole rock isotope study (yellow stars), as well as the samples from the *in situ* isotope study (white stars). Adapted from Irvine and Smith (1969).

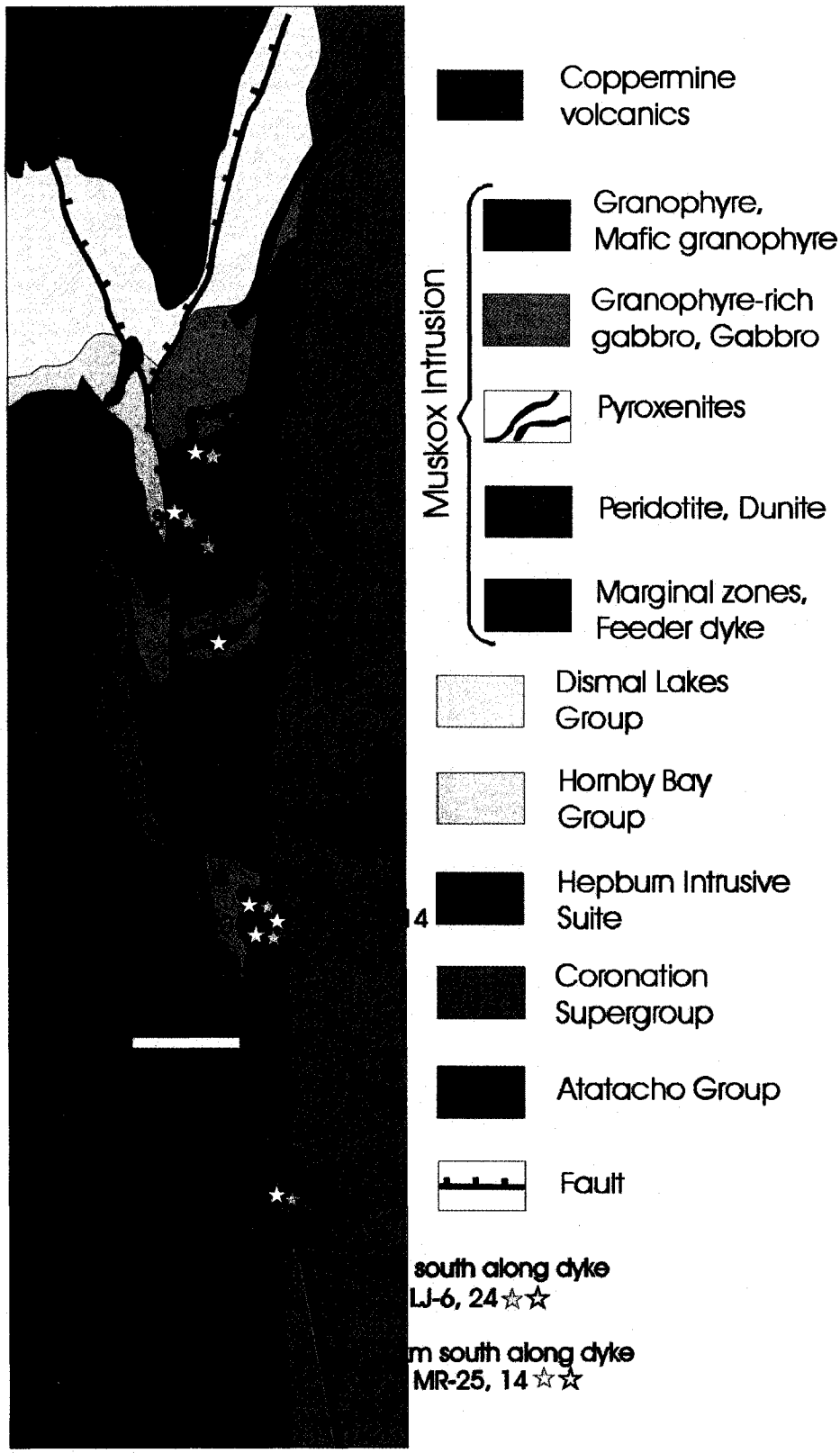

Table 4.1 – Sm and Nd concentrations and isotopic data.

Sample	Nd ppm	Sm ppm	$^{147}Sm/^{144}Nd$	$^{143}Nd/^{144}Nd$	± 2 SE	ε_{Nd}	ε_{Nd} 1.27Ga*	T_{CHUR} Ga**
VD-724	1.65	0.50	0.18258	0.512497	0.000018	-2.7	-0.4	1.51
VD-850	2.45	0.66	0.16399	0.512353	0.000019	-5.6	-0.2	1.33
V3-03	3.26	1.13	0.20894	0.512707	0.000011	1.3	-0.6	0.86
EQ-6	10.64	2.54	0.14464	0.512124	0.000009	-10.0	-1.6	1.50
EQ-14	14.98	3.54	0.14305	0.512137	0.000010	-9.8	-1.0	1.42
CR-46	14.19	3.49	0.14889	0.512175	0.000018	-9.0	-1.3	1.47
LJ-24	4.77	1.30	0.16465	0.512287	0.000008	-6.8	-1.6	1.67
MR-14	11.66	3.09	0.16017	0.512168	0.000014	-9.2	-3.2	1.96

* Where $\varepsilon_{Nd} = [((^{143}Nd/^{144}Nd)_{sample(T)}/(^{143}Nd/^{144}Nd)_{CHUR(T)})-1]\times10^4$ (DePaolo and Wasserburg, 1976a) and present day $^{143}Nd/^{144}Nd_{CHUR}=0.512638$, and $^{147}Sm/^{144}Nd_{CHUR}=0.1967$.
** T_{CHUR} based on the model of (DePaolo and Wasserburg, 1976b)
Measured ratios were normalized to $^{143}Nd/^{144}Nd = 0.7219$
The decay constant used for ^{147}Sm is $6.54*10^{-12}$ a^{-1}
Uncertainties are given as +/- 2 Standard Errors on $^{143}Nd/^{144}Nd$, which is equivalent to +/- 2 standard deviations of the mean
Error for $^{147}Sm/^{144}Nd$ =0.5%, based on replication of the standard rock powder BCR-1.

Table 4.2 – Rb and Sr concentrations and isotopic data.

Sample	Rb ppm	Sr ppm	$^{87}Rb/^{86}Sr$	$^{87}Sr/^{86}Sr$	± 2 SE	T Ma	Initial $^{87}Sr/^{86}Sr$
VD-724	1.91	17.44	0.3171	0.708518	0.000012	1270	0.702747
VD-850	4.21	116.76	0.1044	0.708899	0.000013	1270	0.706998
V3-03	2.52	52.44	0.1392	0.707852	0.000013	1270	0.705320
EQ-6	13.25	280.95	0.1365	0.708586	0.000014	1270	0.706102
EQ-14	22.61	129.76	0.5045	0.714204	0.000011	1270	0.705023
CR-46	12.53	153.03	0.2371	0.709365	0.000010	1270	0.705051
LJ-24	6.32	138.99	0.1317	0.708032	0.000022	1270	0.705636
MR-14	11.29	110.90	0.2947	0.712829	0.000012	1270	0.707466

Uncertainty is 2 standard errors on Uncertainties are given as +/- 2 Standard Errors on $^{87}Sr/^{86}Sr$, which is equivalent to +/- 2 standard deviations of the mean
Error assigned to $^{87}Rb/^{86}Sr$ =± 1%, based on known uncertainties in spike calibration and replication of Rb analyses
The decay constant used for ^{87}Rb is = $1.42*10^{-11}$ a^{-1} (Steiger and Jager, 1977)

Table 4.3 – Lu and Hf concentrations and isotopic data.

Sample	Lu ppm	Hf ppm	$^{176}Lu/^{177}Hf$	$^{176}Hf/^{177}Hf$	± 2 SE	$^{176}Hf/^{177}Hf$ 1.27Ga	ε_{Hf}	ε_{Hf} 1.27Ga*	T_{CHUR} Ga
VD-724	0.068	0.358	0.0272	0.282621	0.000050	0.281968	-5.3	-0.3	1.3
VD-850	0.082	0.416	0.0280	0.282737	0.000030	0.282065	-1.2	3.2	0.4
V3-03	0.092	0.373	0.0350	0.282858	0.000050	0.282017	3.0	1.5	2.4
EQ-6	0.173	1.721	0.0143	0.282352	0.000020	0.282008	-14.8	1.2	1.2
EQ-14	0.245	3.060	0.0114	0.282291	0.000010	0.282018	-17.0	1.5	1.2
CR-46	0.203	2.084	0.0139	0.282349	0.000010	0.282015	-15.0	1.4	1.2
LJ-24	0.158	0.903	0.0250	0.282617	0.000010	0.282019	-5.5	1.5	1.0
MR-14	0.202	1.533	0.0188	0.282437	0.000010	0.281986	-11.9	0.4	1.2

* Where $\varepsilon_{Hf} = [((^{176}Hf/^{177}Hf)_{sample(T)}/(^{176}Hf/^{177}Hf)_{CHUR(T)})-1]\times10^4$ (DePaolo and Wasserburg, 1976a) and present day $^{176}Hf/^{177}Hf_{CHUR}$ = 0.282772 and $^{176}Lu/^{177}Hf_{CHUR}$=0.033200 (Blichert-Toft et al. 2002).
* $\lambda_{Lu} = 1.876\times10^{-11}$ a^{-1} (Söderlund et al., 2004)
** T_{CHUR} based on the model of (DePaolo and Wasserburg, 1976b)
Uncertainty is 2 standard errors on $^{176}Hf/^{177}Hf$, which is equivalent to +/- 2 standard deviations of the mean
Error assigned to $^{176}Lu/^{177}Hf$ =± 1% based on repeated digestions and measurements (n=5) using the BE-N (basalt) whole rock standard (obtained from CRPG, Nancy France). Measurements conducted by S. Schmidberger. .

Table 4.4 – *In situ* Sr-isotope data for analyzed plagioclase grains. Red values are those with high errors.

Sample	Grain	$^{84}Sr/^{86}Sr$	error 2s	$^{84}Sr/^{88}Sr$	error 2s	$^{87}Rb/^{86}Sr$	error 2s	$^{87}Sr/^{86}Sr$ measured	Rb & mass bias corrected $^{87}Sr/^{86}Sr$	error 2s	Rb & mass bias corrected $^{87}Sr/^{86}Sr$ 1270 Ma	error 2s	Internal spot isochron age (Ma)	Ave ^{88}Sr signal voltage
VD-850	1	0.05630	0.00006	0.00672	0.00001	0.20298	0.03479	0.92860	0.71094	0.00041	0.70724	0.00026	798	6.03154
	2	0.05631	0.00005	0.00672	0.00001	0.14795	0.01504	0.87292	0.71014	0.00018	0.70745	0.00014	770	5.77371
	3	0.05575	0.00021	0.00666	0.00002	0.06018	0.00913	0.78199	0.70663	0.00013	0.70553	0.00015		2.32542
	4	0.05595	0.00012	0.00668	0.00001	0.08270	0.01365	0.80421	0.70659	0.00024	0.70509	0.00011	1125	1.98139
	5	0.05553	0.00046	0.00663	0.00006	0.09808	0.02322	0.82271	0.70928	0.00058	0.70750	0.00027	1560	3.06191
	6	0.05509	0.00038	0.00658	0.00005	0.04212	0.00328	0.76373	0.70622	0.00018	0.70545	0.00015		1.75637
	7	0.05596	0.00019	0.00668	0.00002	0.01157	0.00126	0.73187	0.70536	0.00011	0.70515	0.00011		1.82928
	8	0.05564	0.00025	0.00664	0.00003	0.02256	0.00522	0.74395	0.70612	0.00026	0.70571	0.00020		1.92772
	9	0.05569	0.00021	0.00665	0.00003	0.01600	0.00411	0.73652	0.70542	0.00012	0.70513	0.00013		1.87072
	10	0.05581	0.00018	0.00666	0.00002	0.01242	0.00213	0.73294	0.70542	0.00013	0.70520	0.00011		1.79222
	11	0.05600	0.00016	0.00669	0.00002	0.12739	0.02298	0.85209	0.70955	0.00035	0.70724	0.00016	979	4.12823
weighted average:		**0.05595**	**0.00018**	**0.00668**	**0.00002**	**0.10467**	**0.01664**		**0.70841**	**0.00028**	**0.70651**	**0.00017**		
LJ-24	1	0.05534	0.00038	0.00661	0.00005	0.08658	0.02669	0.80756	0.70690	0.00038	0.70533	0.00035		0.98744
	2	0.05476	0.00093	0.00654	0.00011	0.45303	0.11404	1.17900	0.71184	0.00133	0.70359	0.00095	770	0.84858
	3	0.05517	0.00059	0.00659	0.00007	0.38986	0.05465	1.11583	0.71190	0.00082	0.70481	0.00055	875	1.43270
	4	0.05552	0.00034	0.00663	0.00004	0.04956	0.01037	0.77067	0.70694	0.00021	0.70604	0.00022		0.99634
	5	0.05301	0.00202	0.00633	0.00024	0.02048	0.00764	0.74102	0.70600	0.00056	0.70563	0.00053		0.69200
	6	0.05361	0.00093	0.00640	0.00011	0.43436	0.08086	1.16083	0.71136	0.00107	0.70345	0.00063	854	1.05931
	7	0.05428	0.00094	0.00648	0.00011	0.37002	0.04842	1.09694	0.71174	0.00045	0.70501	0.00063		0.92740
	8	0.05516	0.00034	0.00659	0.00004	0.45743	0.08260	1.18340	0.71084	0.00092	0.70251	0.00068	750	1.37753
	9	0.05518	0.00042	0.00659	0.00005	0.12562	0.01781	0.84879	0.70809	0.00028	0.70581	0.00021		1.09480
	10	0.05435	0.00056	0.00649	0.00007	0.26710	0.03790	0.99182	0.70932	0.00039	0.70446	0.00036	673	1.14752
	11	0.05385	0.00091	0.00643	0.00011	0.16841	0.05288	0.89125	0.70754	0.00068	0.70448	0.00057	736	0.79271
	12	0.05525	0.00026	0.00660	0.00003	0.21927	0.03802	0.94287	0.70853	0.00048	0.70454	0.00031	812	0.96719
	13	0.05492	0.00044	0.00656	0.00005	0.03593	0.00949	0.75727	0.70614	0.00019	0.70549	0.00018		0.89113
weighted average:		**0.05472**	**0.00065**	**0.00653**	**0.00008**	**0.25328**	**0.04627**		**0.70924**	**0.00061**	**0.70463**	**0.00047**		

Sample	Grain	$^{84}Sr/^{86}Sr$	error 2s	$^{84}Sr/^{88}Sr$	error 2s	$^{87}Rb/^{86}Sr$	error 2s	$^{87}Sr/^{86}Sr$ measured	Rb & mass bias corrected $^{87}Sr/^{86}Sr$	error 2s	Rb & mass bias corrected $^{87}Sr/^{86}Sr$ 1270 Ma	error 2s	Internal spot isochron age (Ma)	Ave ^{88}Sr signal voltage
CR-46	1	0.05535	0.00026	0.00661	0.00003	0.04941	0.01158	0.76986	0.70574	0.00016	0.70484	0.00019		1.66539
	2	0.05484	0.00111	0.00655	0.00013	0.04136	0.00853	0.76171	0.70547	0.00024	0.70471	0.00025		1.08618
	3													
	4													
	5	0.05533	0.00057	0.00661	0.00007	0.05644	0.00428	0.77699	0.70572	0.00018	0.70469	0.00016		1.37003
	6	0.05380	0.00096	0.00642	0.00011	0.01766	0.00340	0.73848	0.70561	0.00023	0.70528	0.00023		1.28979
weighted average:		**0.05487**	**0.00068**	**0.00655**	**0.00008**	**0.04201**	**0.00717**		**0.70565**	**0.00020**	**0.70488**	**0.00020**		
EQ-13	1	0.05589	0.00021	0.00667	0.00002	0.01582	0.00070	0.73526	0.70583	0.00015	0.70554	0.00015		0.76094
	2	0.05611	0.00016	0.00670	0.00002	0.05902	0.00638	0.77896	0.70634	0.00017	0.70526	0.00017		0.77784
	3													
	4	0.05601	0.00017	0.00669	0.00002	0.03724	0.00170	0.75704	0.70593	0.00017	0.70525	0.00017		1.61738
	5	0.05565	0.00025	0.00664	0.00003	0.08252	0.02241	0.80289	0.70633	0.00026	0.70483	0.00024	673	1.72373
	7	0.05531	0.00023	0.00660	0.00003	0.04576	0.00529	0.76654	0.70600	0.00013	0.70516	0.00012		0.11459
	8	0.05517	0.00034	0.00659	0.00004	0.02256	0.00208	0.74305	0.70575	0.00020	0.70534	0.00019		1.41428
	9	0.05440	0.00081	0.00649	0.00010	0.02163	0.00214	0.74210	0.70574	0.00030	0.70535	0.00030		1.01557
weighted average:		**0.05553**	**0.00031**	**0.00663**	**0.00004**	**0.04304**	**0.00709**		**0.70599**	**0.00021**	**0.70521**	**0.00020**		
SL-42	1	0.05619	0.00012	0.00671	0.00001	0.10119	0.01543	0.82194	0.70698	0.00025	0.70514	0.00019	847	0.76207
	2	0.05526	0.00041	0.00660	0.00005	0.14763	0.02227	0.86946	0.70759	0.00031	0.70490	0.00032		0.94233
	3	0.05622	0.00016	0.00671	0.00002	0.22292	0.01788	0.94560	0.70861	0.00019	0.70455	0.00024		0.96523
	4	0.05564	0.00020	0.00664	0.00002	0.12719	0.01247	0.84875	0.70725	0.00015	0.70493	0.00020		1.14376
	5	0.05487	0.00066	0.00655	0.00008	0.11495	0.01172	0.83743	0.70780	0.00039	0.70571	0.00034		0.77518
	6	0.05052	0.00277	0.00603	0.00033	0.24653	0.04461	0.97027	0.70840	0.00060	0.70391	0.00054	701	0.59092
	7	0.05632	0.00014	0.00672	0.00002	0.79078	0.05067	1.51625	0.71113	0.00043	0.69674	0.00061	498	0.92097
weighted average:		**0.05525**	**0.00051**	**0.00660**	**0.00006**	**0.25243**	**0.02399**		**0.70825**	**0.00031**	**0.70366**	**0.00034**		

Sample	Grain	$^{84}Sr/^{86}Sr$	error 2s	$^{84}Sr/^{88}Sr$	error 2s	$^{87}Rb/^{86}Sr$	error 2s	$^{87}Sr/^{86}Sr$ measured	Rb & mass bias corrected $^{87}Sr/^{86}Sr$	error 2s	Rb & mass bias corrected $^{87}Sr/^{86}Sr$ 1270 Ma	error 2s	Internal spot isochron age (Ma)	Ave ^{88}Sr signal voltage
V3-03	1	0.05499	0.00078	0.00657	0.00009	0.00816	0.00046	0.72951	0.70610	0.00065	0.70595	0.00064		1.35560
	2	0.05606	0.00031	0.00669	0.00004	0.04249	0.00305	0.76291	0.70559	0.00014	0.70481	0.00017		1.36773
	3	0.05583	0.00023	0.00667	0.00003	0.01042	0.00073	0.73061	0.70522	0.00011	0.70503	0.00011		1.72383
	4	0.05609	0.00012	0.00670	0.00001	0.03739	0.00384	0.75782	0.70551	0.00015	0.70483	0.00012		1.30929
	5	0.05577	0.00021	0.00666	0.00003	0.01565	0.00157	0.73615	0.70536	0.00013	0.70508	0.00013		1.57424
	6	0.05589	0.00016	0.00667	0.00002	0.04661	0.00407	0.76746	0.70585	0.00017	0.70501	0.00012	2334	1.77591
	7	0.05603	0.00021	0.00669	0.00002	0.02859	0.00234	0.74931	0.70590	0.00022	0.70537	0.00023		1.66387
	8	0.05568	0.00036	0.00665	0.00004	0.01170	0.00135	0.73190	0.70524	0.00027	0.70502	0.00025		1.28052
	9	0.05586	0.00029	0.00667	0.00003	0.01225	0.00123	0.73234	0.70510	0.00018	0.70488	0.00016	5008	1.49317
	10	0.05605	0.00012	0.00669	0.00001	0.02385	0.00324	0.74459	0.70570	0.00016	0.70526	0.00014		1.99323
	11	0.05628	0.00007	0.00672	0.00001	0.01213	0.00120	0.73191	0.70495	0.00016	0.70473	0.00015		1.45535
weighted average:		**0.05595**	**0.00020**	**0.00668**	**0.00002**	**0.02420**	**0.00229**		**0.70546**	**0.00017**	**0.70502**	**0.00016**		
EQ-19	1	0.05572	0.00016	0.00665	0.00002	0.02462	0.00420	0.74564	0.70572	0.00014	0.70527	0.00013		1.61199
	2	0.05563	0.00024	0.00664	0.00003	0.01845	0.00299	0.73935	0.70571	0.00011	0.70537	0.00010		1.74497
	3	0.05591	0.00015	0.00668	0.00002	0.01969	0.00172	0.74048	0.70578	0.00014	0.70542	0.00013		1.52085
	4	0.05566	0.00023	0.00665	0.00003	0.01445	0.00136	0.73551	0.70576	0.00012	0.70550	0.00011		1.85164
	5	0.05597	0.00015	0.00668	0.00002	0.01630	0.00234	0.73720	0.70574	0.00017	0.70544	0.00015		1.84730
	6	0.05582	0.00023	0.00667	0.00003	0.01588	0.00176	0.73674	0.70568	0.00016	0.70539	0.00017		1.48657
weighted average:		**0.05578**	**0.00019**	**0.00666**	**0.00002**	**0.01811**	**0.00239**		**0.70573**	**0.00014**	**0.70540**	**0.00013**		
EQ-6	1	0.05621	0.00011	0.00671	0.00001	0.02091	0.00115	0.74171	0.70576	0.00013	0.70538	0.00012		1.72728
	2	0.05561	0.00029	0.00664	0.00003	0.04545	0.00722	0.76764	0.70658	0.00026	0.70575	0.00018	910	1.48772
	3	0.05581	0.00023	0.00666	0.00003	0.03253	0.00371	0.75499	0.707065	0.00010	0.70647	0.00011		1.62729
	4	0.05519	0.00074	0.00659	0.00009	0.01997	0.00278	0.74118	0.70582	0.00020	0.70546	0.00021		1.08336
	5	0.05586	0.00018	0.00667	0.00002	0.06766	0.01216	0.78988	0.70702	0.00027	0.70579	0.00018	1159	1.31652
weighted average:		**0.05578**	**0.00028**	**0.00666**	**0.00003**	**0.03692**	**0.00522**		**0.70646**	**0.00018**	**0.70579**	**0.00015**		

Sample	Grain	$^{84}Sr/^{86}Sr$	error 2s	$^{84}Sr/^{88}Sr$	error 2s	$^{87}Rb/^{86}Sr$	error 2s	$^{87}Sr/^{86}Sr$ measured	Rb & mass bias corrected $^{87}Sr/^{86}Sr$	error 2s	Rb & mass bias corrected $^{87}Sr/^{86}Sr$ 1270 Ma	error 2s	Internal spot isochron age (Ma)	Ave ^{88}Sr signal voltage
MR-14-a	1	0.05564	0.00027	0.00664	0.00003	0.01594	0.00382	0.73828	0.70715	0.00030	0.70686	0.00029		1.21207
	2	0.05566	0.00035	0.00665	0.00004	0.03247	0.00685	0.75536	0.70760	0.00023	0.70701	0.00022		1.07635
	3	0.05583	0.00032	0.00667	0.00004	0.05050	0.01465	0.77351	0.70761	0.00020	0.70669	0.00024		1.28686
	4	0.05598	0.00034	0.00668	0.00004	0.02271	0.00342	0.74555	0.70757	0.00017	0.70716	0.00019		0.97599
MR-14b	2	0.05535	0.00028	0.00661	0.00003	0.22803	0.05165	0.95412	0.71120	0.00064	0.70705	0.00041	812	0.68090
	3													
	5	0.05662	0.00066	0.00676	0.00008	0.02933	0.00578	0.75031	0.70735	0.00034	0.70681	0.00032		0.42250
	6	0.05491	0.00038	0.00656	0.00004	0.08460	0.00429	0.80702	0.70847	0.00029	0.70693	0.00028		0.44468
weighted average:		**0.05572**	**0.00034**	**0.00665**	**0.00004**	**0.05684**	**0.01209**		**0.70796**	**0.00028**	**0.70692**	**0.00026**		

Table 4.5 – *In situ* Pb-isotope data for analyzed plagioclase grains. Red values are those with high errors.

Sample	Grain	$^{238}U/^{204}Pb$	$^{207}Pb/^{206}Pb$ meas.	error 2s	$^{206}Pb/^{204}Pb$ meas.	error 2s	$^{207}Pb/^{204}Pb$ meas.	error 2s	$^{206}Pb/^{204}Pb$ initial	error 2s	Average ^{206}Pb signal voltage
VD-850	1	0.1248	0.862	0.014	16.670	0.241	14.356	0.151	16.643	0.241	1.33E-03
	2	0.0000	0.843	0.007	16.620	0.161	14.006	0.151	16.620	0.161	1.14E-03
	3	0.0000	0.929	0.010	15.970	0.177	14.834	0.138	15.970	0.177	1.59E-03
	4	0.0000	0.960	0.008	15.232	0.159	14.614	0.075	15.232	0.159	1.72E-03
	5a	0.1618	0.907	0.013	16.754	0.249	15.186	0.186	16.719	0.249	1.51E-03
	5b	0.0000	0.851	0.018	16.690	0.545	14.184	0.418	16.690	0.545	6.87E-04
	6	0.0695	0.925	0.002	15.693	0.140	14.507	0.118	15.677	0.140	2.26E-03
	7	0.1433	0.941	0.003	16.263	0.155	15.298	0.161	16.232	0.155	1.73E-03
	8	0.0000	0.903	0.004	16.445	0.078	14.854	0.086	16.445	0.078	1.96E-03
	9	0.0377	0.949	0.006	15.986	0.104	15.178	0.134	15.978	0.104	1.72E-03
	10	0.0000	0.836	0.015	17.414	0.159	14.541	0.230	17.414	0.159	2.01E-03
	11	0.0411	0.940	0.003	15.721	0.173	14.771	0.169	15.712	0.173	1.29E-03
weighted average:			**0.908**	**0.0078**	**16.261**	**0.173**	**14.737**	**0.154**	**16.250**	**0.173**	
LJ-24	1	7.8658	0.946	0.008	16.591	0.297	15.687	0.189	14.878	0.297	1.38E-03
	2	0.7106	0.912	0.022	15.891	0.494	14.489	0.478	15.736	0.494	7.03E-04
	3	0.6092	0.968	0.003	15.893	0.132	15.388	0.087	15.760	0.132	3.50E-03
	5	0.7220	0.961	0.004	15.880	0.219	15.267	0.177	15.723	0.219	1.71E-03
	6	0.7087	0.969	0.003	15.704	0.145	15.215	0.108	15.550	0.145	8.94E-03
	7	0.7668	0.959	0.003	16.043	0.071	15.382	0.072	15.876	0.071	4.85E-03
	8	0.0052	0.969	0.002	15.718	0.102	15.231	0.093	15.717	0.102	4.08E-03
	9	0.4486	0.966	0.002	15.770	0.055	15.236	0.041	15.672	0.055	9.42E-03
	10	0.2487	0.973	0.002	15.681	0.080	15.260	0.052	15.626	0.080	7.70E-03
	11	1.6846	0.926	0.019	14.773	0.444	13.672	0.402	14.407	0.444	5.07E-04
	12	0.3648	0.968	0.002	15.634	0.052	15.135	0.041	15.554	0.052	1.10E-02
	13	0.4477	0.975	0.003	15.181	0.104	14.805	0.068	15.083	0.104	4.02E-03
weighted average:			**0.967**	**0.00295**	**15.723**	**0.10381**	**15.197**	**0.07972**	**15.58156**	**0.10381**	

Sample	Grain	$^{238}U/^{204}Pb$	$^{207}Pb/^{206}Pb$ meas.	error 2s	$^{206}Pb/^{204}Pb$ meas.	error 2s	$^{207}Pb/^{204}Pb$ meas.	error 2s	$^{206}Pb/^{204}Pb$ initial	error 2s	Average ^{206}Pb signal voltage
CR-46	1	0.1715	0.969	0.002	15.786	0.059	15.298	0.043	15.749	0.059	1.04E-02
	2	0.0316	0.967	0.002	15.914	0.057	15.391	0.065	15.907	0.057	5.36E-03
	3	1.7767	0.893	0.011	17.758	0.207	15.851	0.174	17.371	0.207	3.08E-03
	4	0.1276	0.969	0.001	15.813	0.065	15.320	0.056	15.785	0.065	7.25E-03
	5	0.0871	0.970	0.001	15.756	0.053	15.282	0.041	15.737	0.053	9.67E-03
	6	0.0631	0.969	0.001	15.979	0.060	15.477	0.048	15.965	0.060	9.87E-03
weighted average:			**0.964**	**0.002**	**15.973**	**0.069**	**15.385**	**0.057**	**15.822**	**0.059**	
EQ-13	1	0.0000	0.968	0.003	15.717	0.261	15.216	0.231	15.717	0.261	1.19E-03
	2	0.0000	0.958	0.002	15.688	0.136	15.036	0.126	15.688	0.136	2.02E-03
	3	0.1045	0.934	0.006	16.228	0.308	15.161	0.252	16.205	0.308	2.98E-03
	4	1.3129	0.947	0.006	15.699	0.188	14.858	0.106	15.413	0.188	2.47E-03
	5	0.3932	0.962	0.002	15.748	0.147	15.146	0.125	15.662	0.147	3.15E-03
	7	0.0587	0.944	0.002	15.529	0.093	14.653	0.075	15.516	0.093	1.81E-03
	8	0.4241	0.940	0.003	16.002	0.245	15.041	0.239	15.909	0.245	7.38E-04
	9	0.3751	0.943	0.004	16.364	0.388	15.441	0.401	16.282	0.388	7.38E-04
weighted average:			**0.950**	**0.004**	**15.840**	**0.203**	**15.043**	**0.168**	**15.829**	**0.206**	
SL-42	1	1.5450	0.960	0.006	12.121	0.288	11.630	0.250	11.784	0.288	4.98E-04
	2	0.2898	0.975	0.005	12.401	0.792	12.073	0.737	12.338	0.792	3.57E-04
	3	0.6160	0.979	0.004	11.456	0.272	11.209	0.258	11.322	0.272	3.59E-04
	4	0.1534	0.980	0.004	11.516	0.165	11.287	0.152	11.482	0.165	4.07E-04
	5	0.4065	0.961	0.006	12.564	0.400	12.067	0.329	12.475	0.400	4.75E-04
	6	1.2057	0.947	0.006	13.876	0.714	13.144	0.721	13.614	0.714	3.59E-04
weighted average:			**0.967**	**0.005**	**12.306**	**0.423**	**11.882**	**0.390**	**12.148**	**0.423**	

Sample	Grain	$^{238}U/^{204}Pb$	$^{207}Pb/^{206}Pb$ meas.	error 2s	$^{206}Pb/^{204}Pb$ meas.	error 2s	$^{207}Pb/^{204}Pb$ meas.	error 2s	$^{206}Pb/^{204}Pb$ initial	error 2s	Average ^{206}Pb signal voltage
V3-03	1	0.0000	0.948	0.004	17.977	0.606	17.025	0.548	17.977	0.606	3.42E-04
	2	0.4538	0.959	0.002	15.779	0.150	15.133	0.148	15.680	0.150	4.11E-04
	3	0.0161	0.958	0.002	15.978	0.186	15.300	0.174	15.975	0.186	4.28E-04
	4	0.0172	0.955	0.003	16.904	0.207	16.138	0.196	16.901	0.207	3.05E-04
	5	0.0523	0.964	0.002	15.196	0.117	14.655	0.114	15.184	0.117	6.47E-04
	6	0.0253	0.958	0.003	16.232	0.188	15.556	0.184	16.226	0.188	4.50E-04
	7	0.2255	0.958	0.002	16.292	0.116	15.600	0.113	16.243	0.116	8.77E-04
	8	0.0000	0.959	0.002	15.972	0.156	15.308	0.141	15.972	0.156	6.11E-04
	9	0.4263	0.951	0.002	16.878	0.244	16.039	0.223	16.785	0.244	5.44E-04
	10	0.2751	0.961	0.002	16.113	0.149	15.475	0.131	16.053	0.149	6.48E-04
	11	0.0642	0.959	0.002	15.544	0.156	14.907	0.149	15.530	0.156	6.87E-04
weighted average:			**0.958**	**0.002**	**16.042**	**0.160**	**15.371**	**0.151**	**16.023**	**0.160**	
EQ-19	1	0.5050	0.959	0.002	16.019	0.170	15.357	0.156	15.909	0.170	4.90E-04
	2	0.0000	0.959	0.003	16.443	0.138	15.762	0.137	16.443	0.138	8.33E-04
	3	0.1540	0.949	0.003	16.023	0.180	15.208	0.166	15.989	0.180	4.73E-04
	4	0.0420	0.955	0.003	16.542	0.139	15.791	0.127	16.533	0.139	6.83E-04
	5	0.1080	0.957	0.002	16.501	0.078	15.793	0.074	16.477	0.078	1.40E-03
	6	0.0000	0.962	0.003	16.006	0.145	15.395	0.141	16.006	0.145	5.41E-04
weighted average:			**0.957**	**0.002**	**16.331**	**0.128**	**15.627**	**0.121**	**16.306**	**0.128**	
EQ-6	1	0.1320	0.941	0.005	16.589	0.123	15.610	0.075	16.560	0.123	1.66E-03
	2	0.3160	0.942	0.003	16.468	0.117	15.510	0.108	16.400	0.117	1.24E-03
	3	0.2060	0.942	0.002	15.914	0.168	14.986	0.157	15.869	0.168	3.79E-04
	4	0.0000	0.953	0.002	16.301	0.138	15.541	0.129	16.301	0.138	7.15E-04
	5	0.0000	0.940	0.004	16.111	0.209	15.140	0.188	16.111	0.209	3.57E-04
weighted average:			**0.943**	**0.003**	**16.409**	**0.135**	**15.477**	**0.110**	**16.375**	**0.135**	

Sample	Grain	$^{238}U/^{204}Pb$	$^{207}Pb/^{206}Pb$ meas.	error 2s	$^{206}Pb/^{204}Pb$ meas.	error 2s	$^{207}Pb/^{204}Pb$ meas.	error 2s	$^{206}Pb/^{204}Pb$ initial	error 2s	Average ^{206}Pb signal voltage
MR-14-*a*	1	0.0730	0.964	0.002	16.223	0.104	15.640	0.095	16.207	0.104	1.66E-03
	2	0.1650	0.958	0.004	16.313	0.122	15.634	0.091	16.277	0.122	2.03E-03
	3	0.2680	0.962	0.002	16.048	0.159	15.438	0.153	15.990	0.159	7.18E-04
	4	0.1720	0.955	0.003	16.567	0.092	15.815	0.058	16.530	0.092	3.55E-03
MR-14b	2	0.0595	0.972	0.002	15.527	0.068	15.096	0.065	15.515	0.068	4.45E-03
	3	0.3990	0.960	0.004	15.132	0.143	14.531	0.131	15.045	0.143	2.70E-03
	5a	2.3466	0.963	0.002	15.618	0.081	15.044	0.076	15.107	0.081	4.37E-03
	6	0.2925	0.976	0.002	15.446	0.083	15.080	0.061	15.382	0.083	4.96E-03
weighted average:			**0.966**	**0.003**	**15.762**	**0.095**	**15.217**	**0.079**	**15.750**	**0.098**	

Figure 4.2 – Sm-Nd isochron obtained by this study. Data were plotted using IsoPlot (Ludwig, 2003). The least radiogenic sample (i.e. most contaminated sample), MR-14, from the furthest extent of the Keel Dyke was omitted in the regression. Data-point error crosses are at the 2σ level.

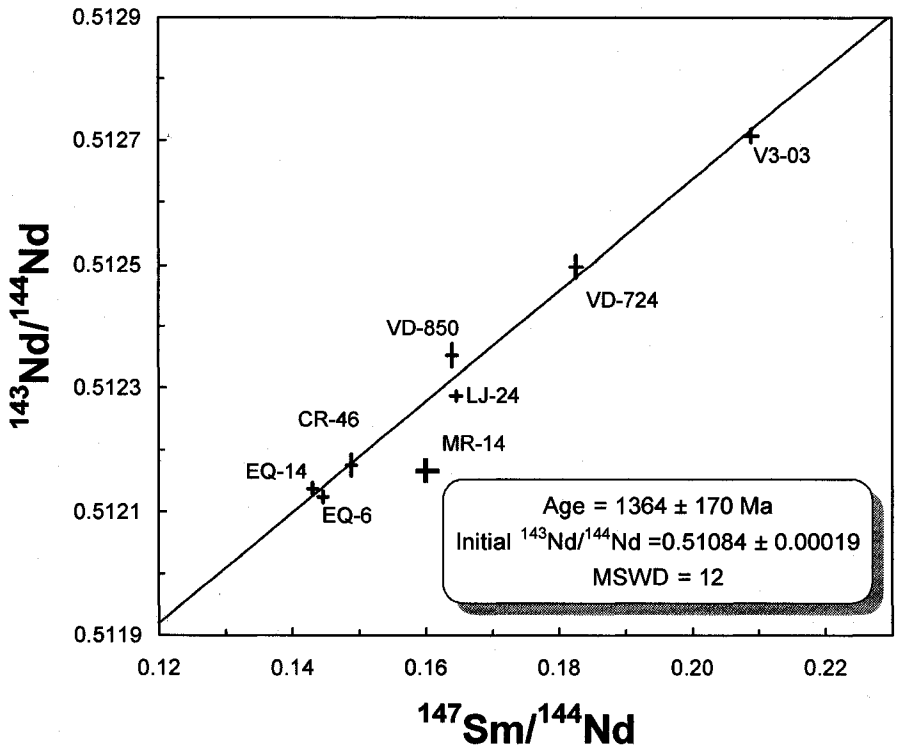

Figure 4.3 – Lu-Hf isochron obtained by this study. Data were plotted using IsoPlot (Ludwig, 2003), and using the Lu decay constant of 1.876E-11 (Söderlund et al., 2004). Samples MR-14 and VD-850 (green symbols) were omitted in the regression to increase the precision of the age. Data-point error crosses are at the 2σ level.

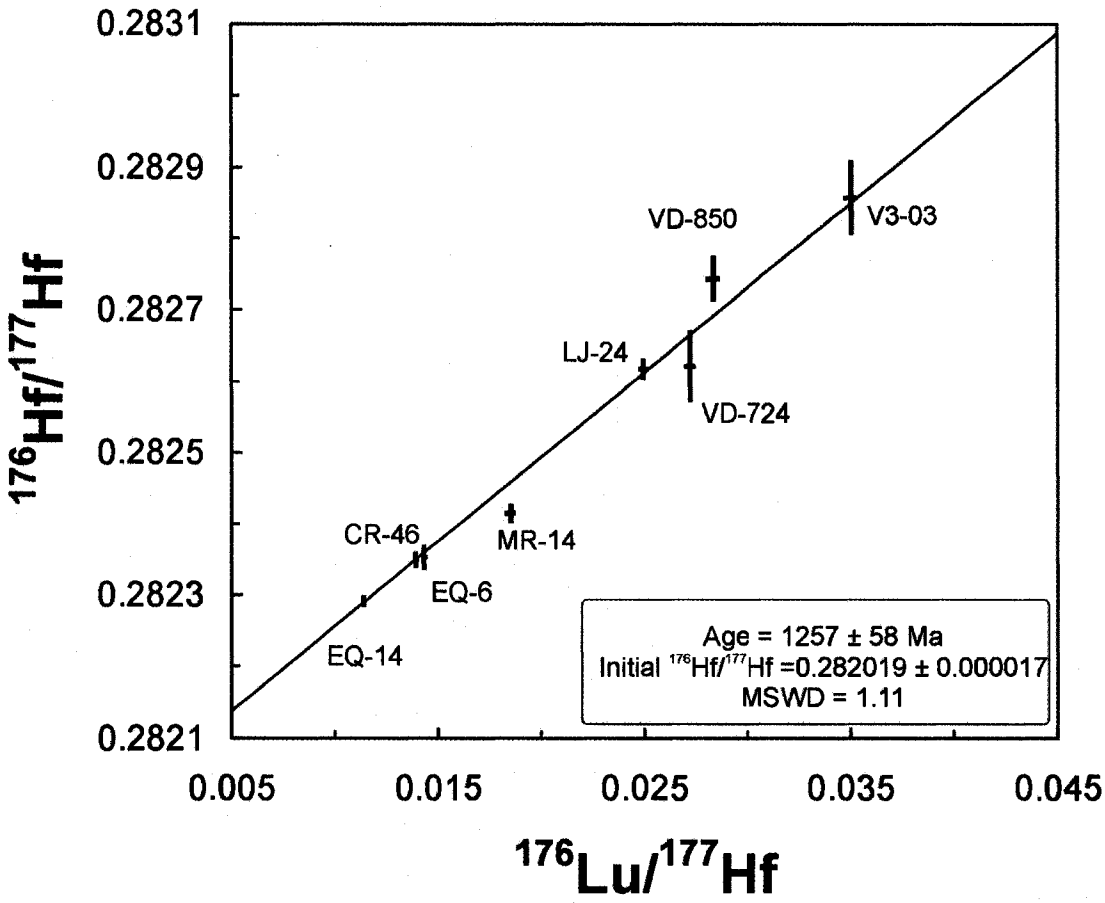

Figure 4.4 – New Nd, Sr, and Hf isotope data from this study (pink squares) plotted with the data of Stewart and DePaolo (1995) (blue diamonds), and plotted against stratigraphic height. Associated errors for initial $^{87}Sr/^{86}Sr$ values are less than the symbol size. Position of the Keel Dyke samples are relative. Note the $^{87}Sr/^{86}Sr$ axis is plotted in reverse for ease of comparison. Stratigraphic column adapted from Francis (1994) and Irvine and Smith (1967). Stratigraphic column legend as in Figure 3.3.

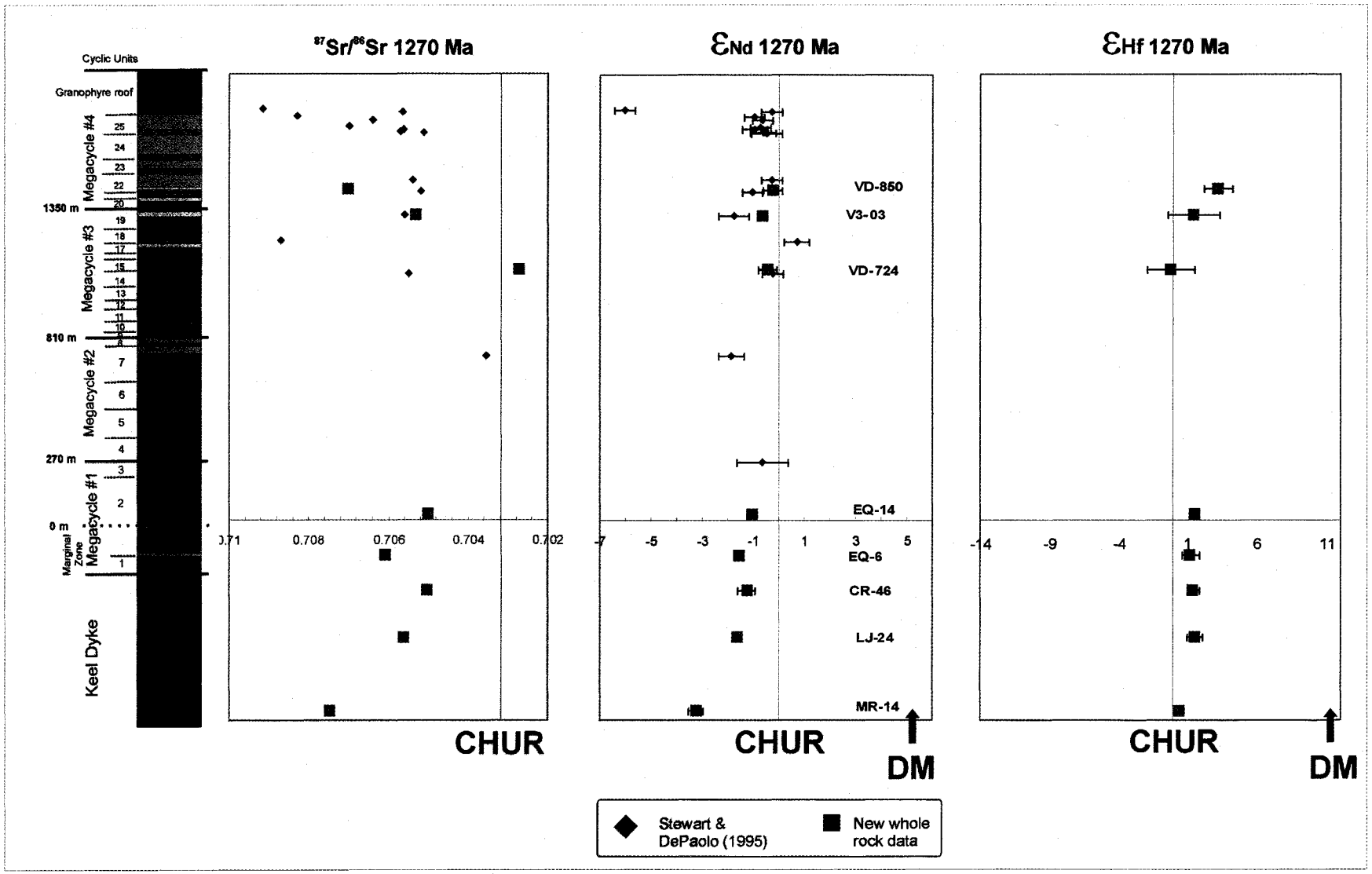

Figure 4.5 – Variations in $^{87}Sr/^{86}Sr$ and ε_{Nd} for whole rock samples analyzed in this study, corrected for decay to an age of 1270 Ma. The intersection of axis indicates the values of the bulk earth at the time. The arrow indicates a plausible contamination trend towards crustal values, which is typical for mantle-derived material.

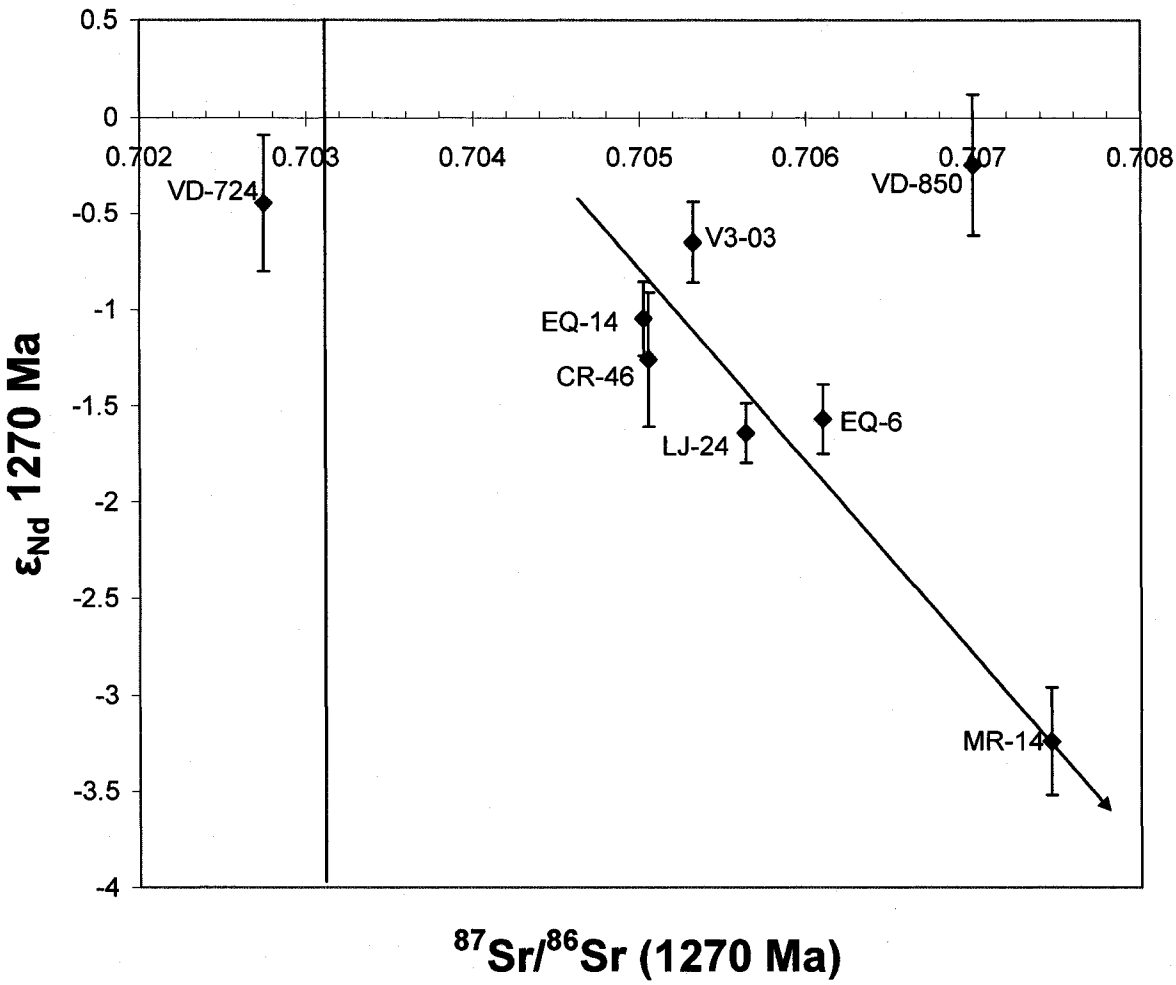

Figure 4.6 – Rare earth element plot and multi-element plot of samples used in the whole-rock isotopic study. Normalization values according to Sun and McDonough (1989).

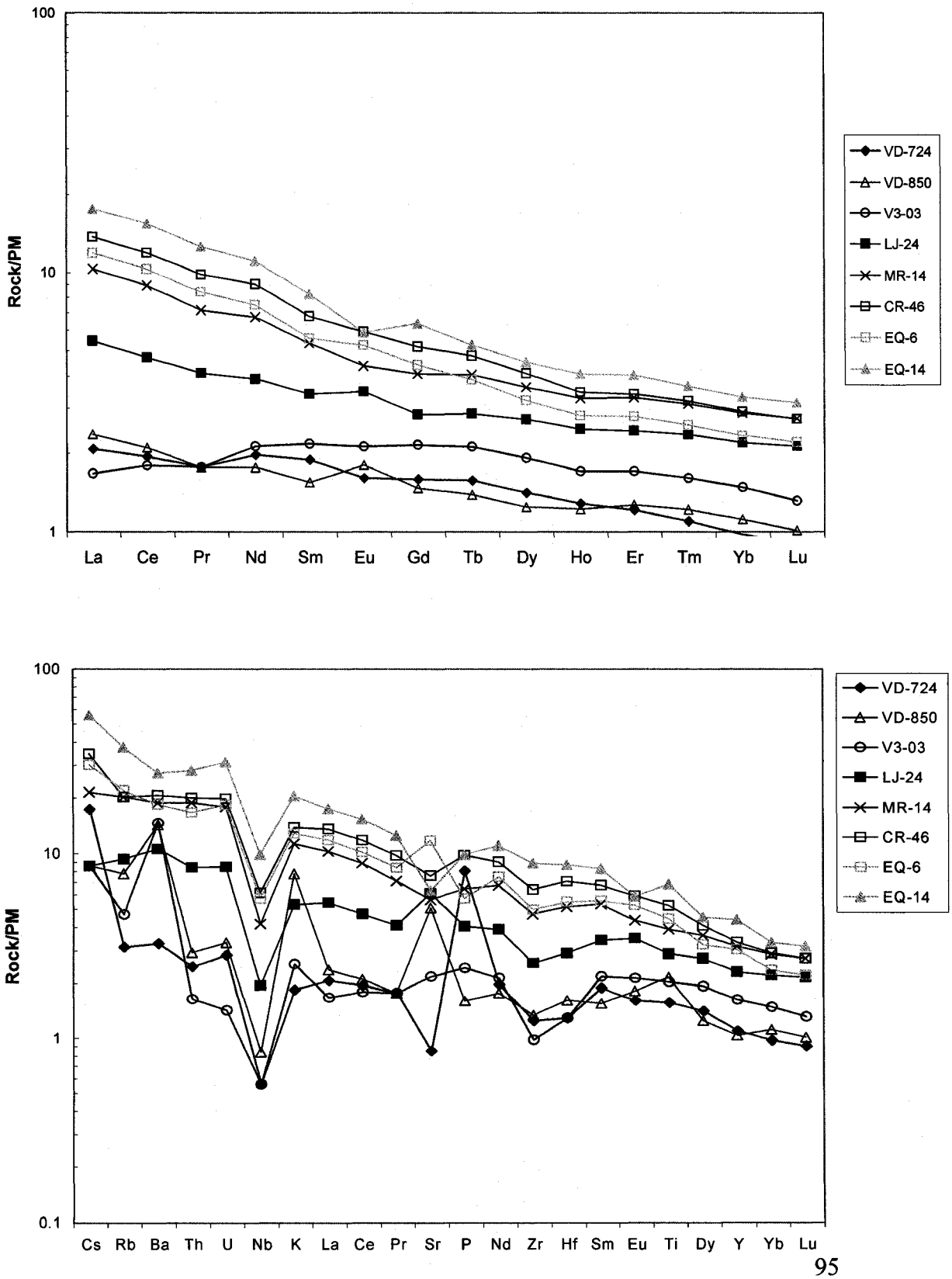

Figure 4.7 – (a) Variations in ε_{Hf} and $^{87}Sr/^{86}Sr$ for whole rock samples analyzed in this study, corrected for decay to an age of 1270 Ma. **(b)** Variations in ε_{Hf} and ε_{Nd} for whole rock samples analyzed in this study, corrected for decay to an age of 1270 Ma. The intersection of axis indicates the values of the bulk earth at the time. Blue line indicates terrestrial evolution trend.

(a)

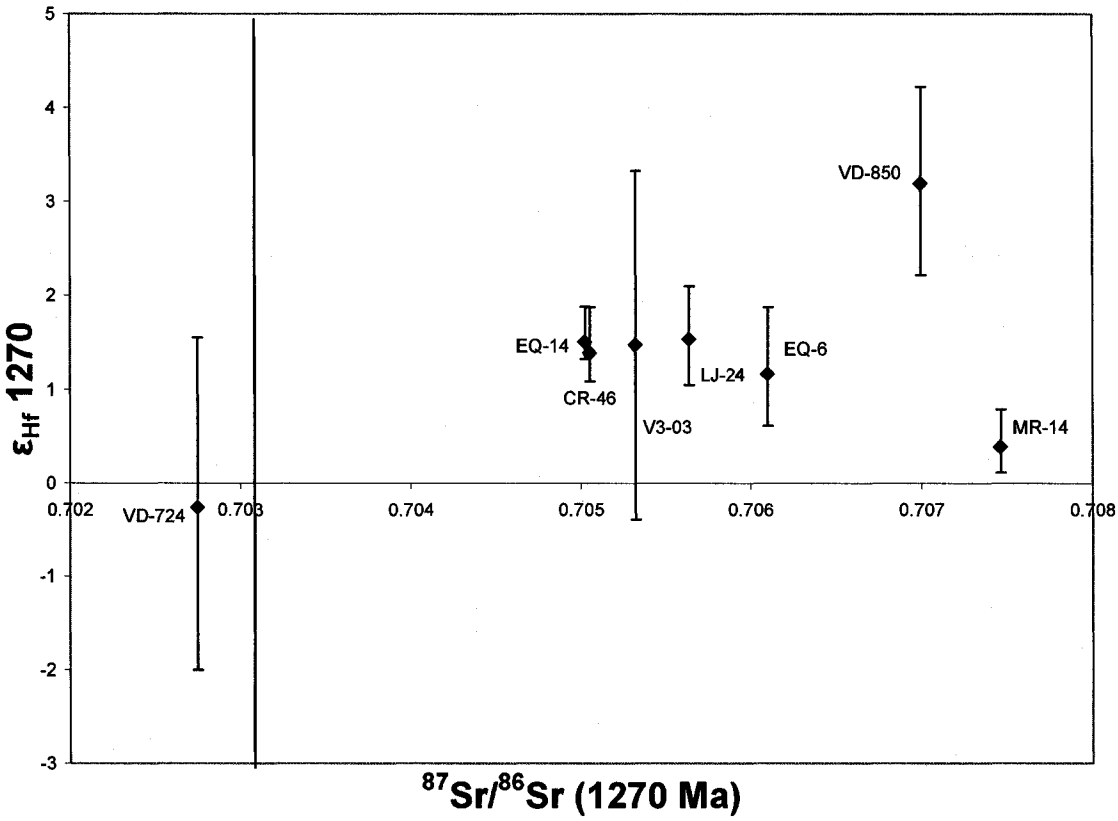

(b)

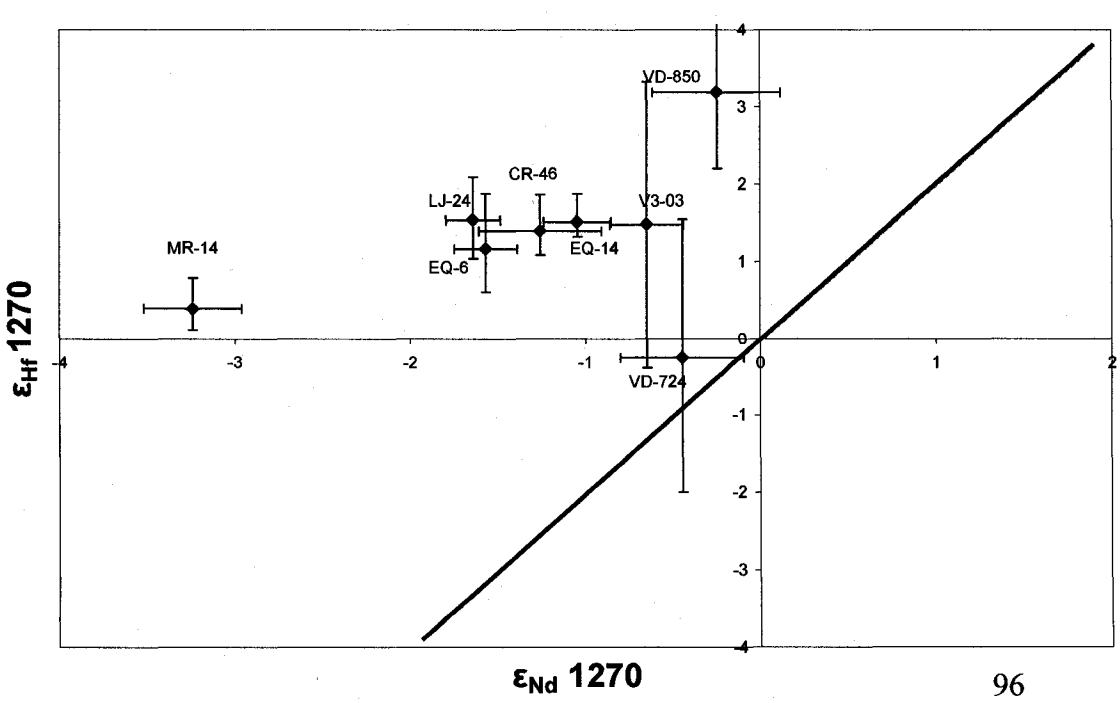

Figure 4.8 – Nd and Hf isotope compositions compared to Mg# for the Muskox and Keel Dyke samples. The red arrow indicates the direction of evolution. Samples are grouped according to location.

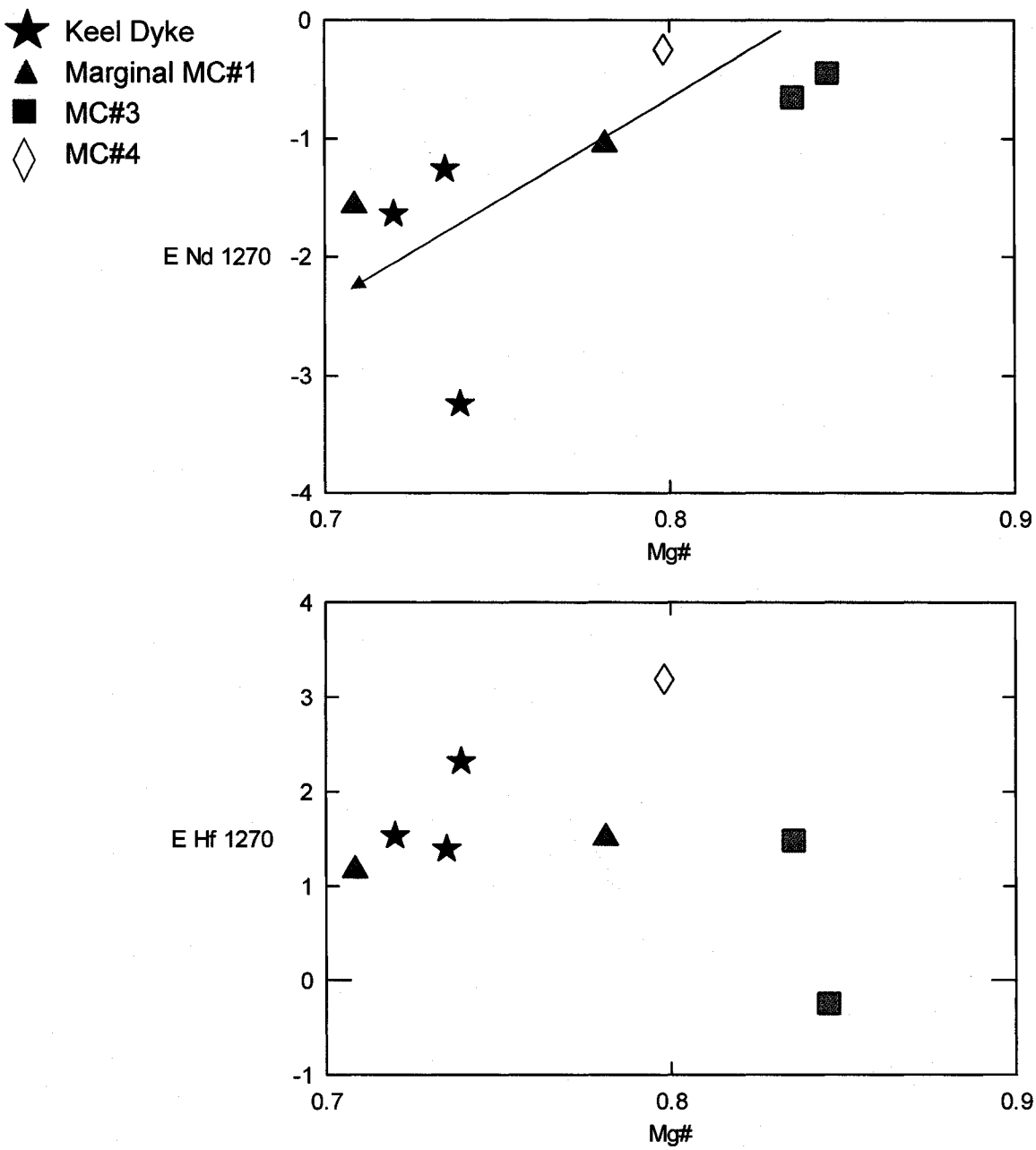

Figure 4.9 – Plagioclase grain (sample VD-850) after laser ablation.

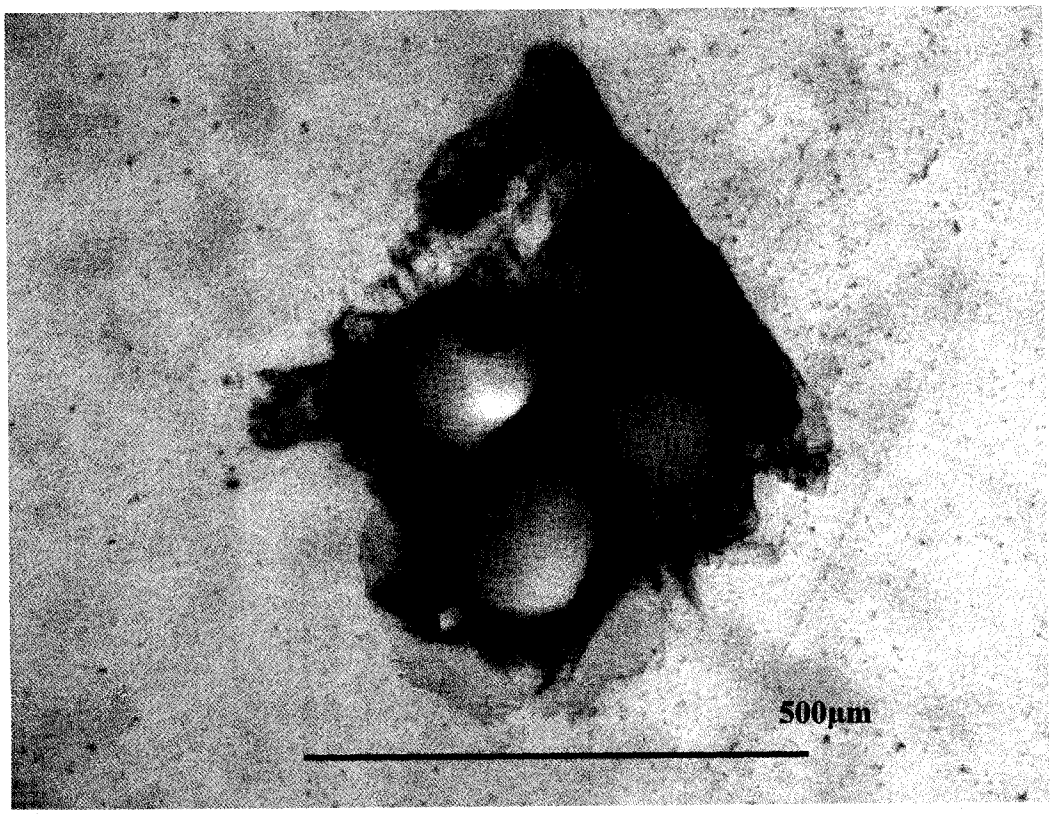

Figure 4.10 – Rb-Sr errorchron obtained from plagioclase analyses for sample V3-03. Grain #1 had the highest error and was omitted from the graph. Grains #7, and 10 (red color) were omitted from the regression to increase precision of the age. Data plotted using *Isoplot.*

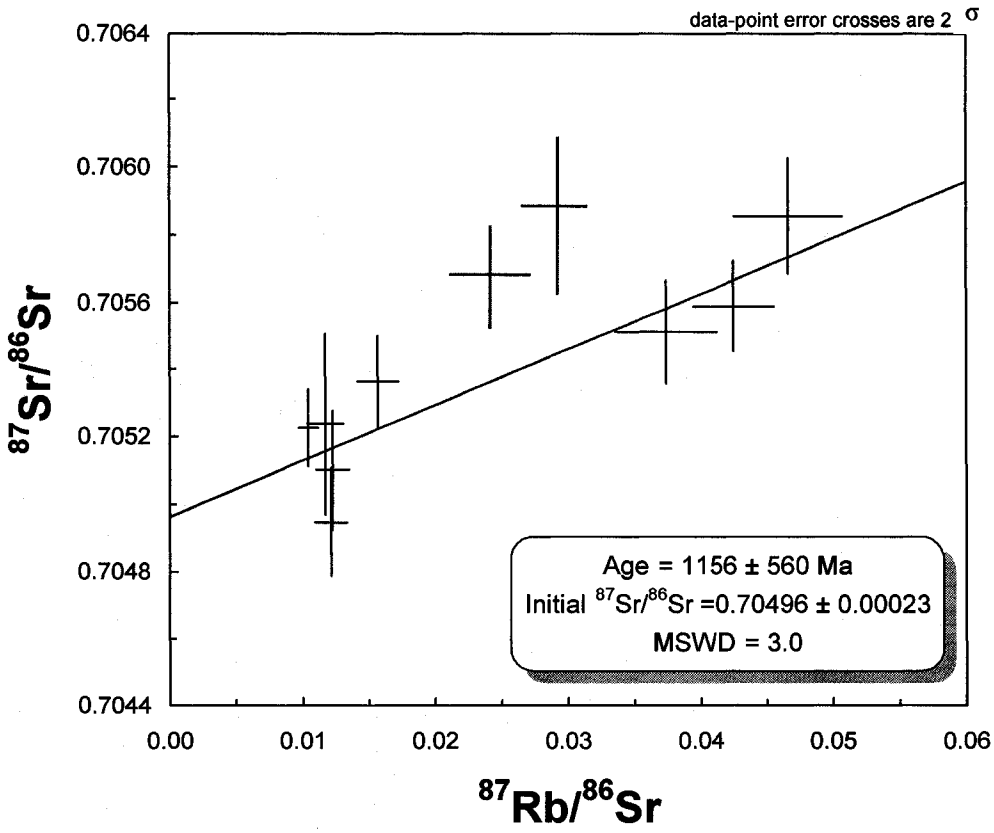

Figure 4.11 – Rb-Sr isochrons obtained from plagioclase analyses for all samples. All grain spots included in regressions, with the exception of spots with large associated errors (these spots are all high-lighted in red in Table 4.4). Summary information for each regression is included to the right of the diagram; data obtained using *Isoplot*, assuming $\lambda^{87}Rb = 1.42*10^{-11}$ a^{-1}. The same chart is shown at two different scales.

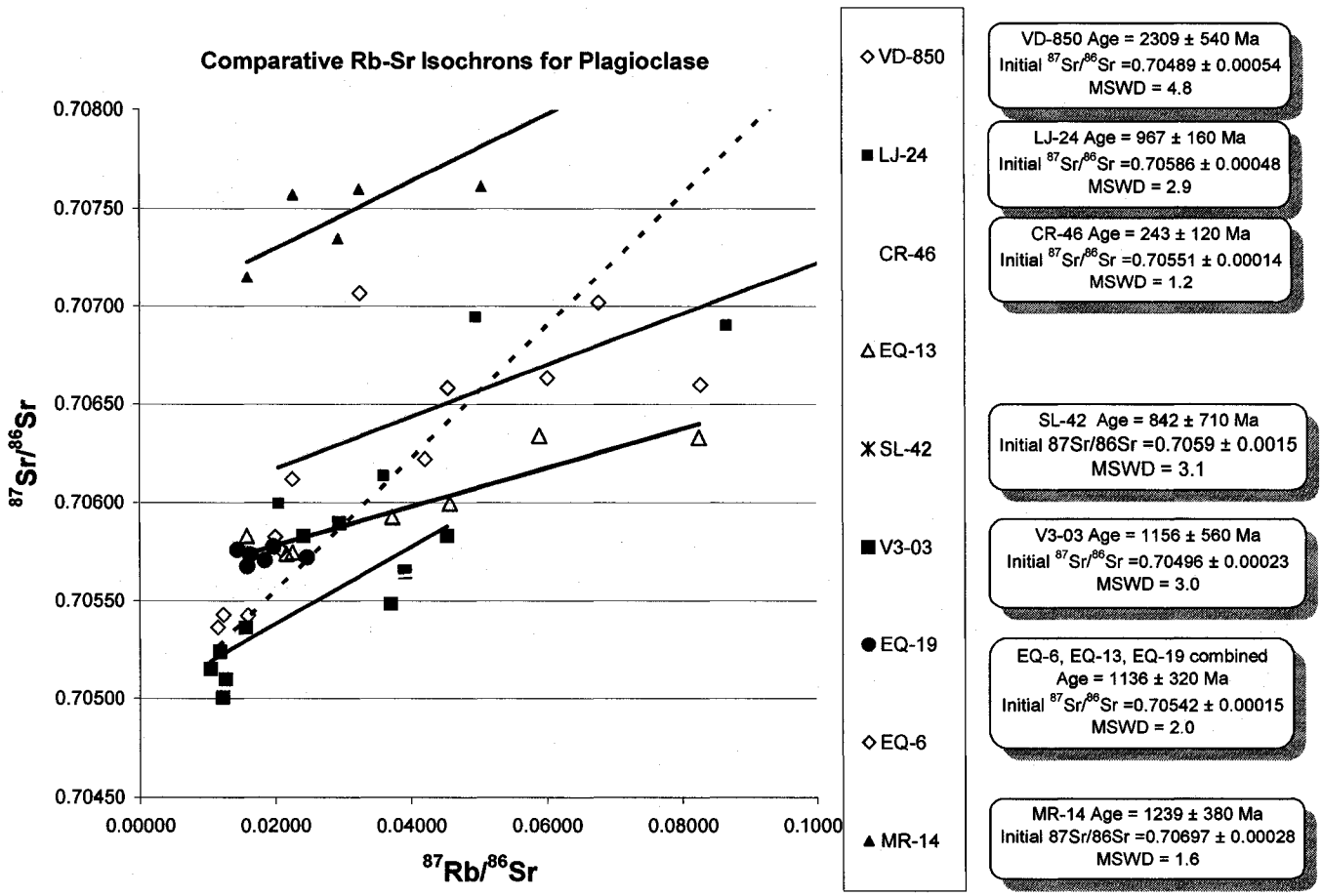

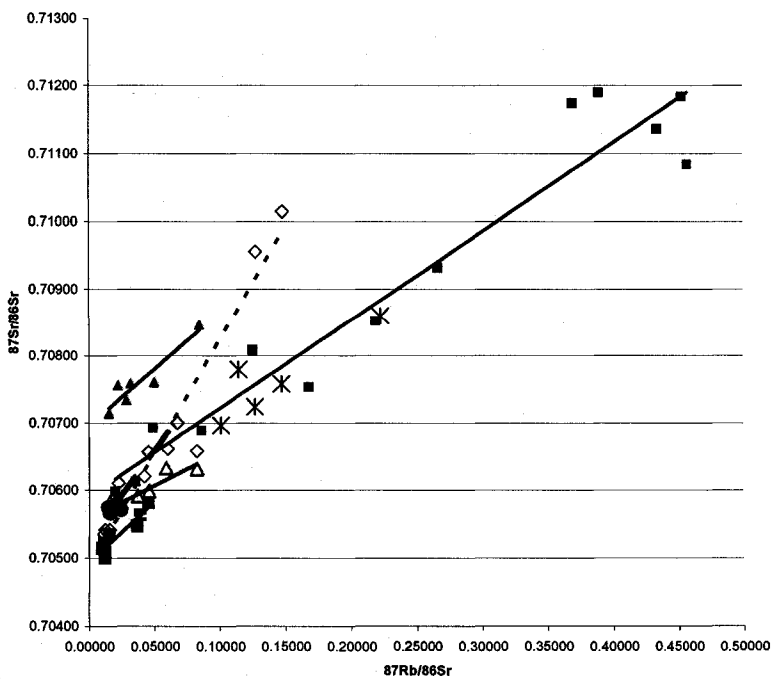

Figure 4.12 – In situ Sr isotope data from plagioclase (orange squares) plotted with whole rock Sr isotope data from this study (pink squares) and the data of Stewart and DePaolo (1995) (diamonds), plotted against stratigraphic height. The data of Stewart and DePaolo (1995) are presented relative to a value of 0.710245 for NBS987, to enable a direct comparison of the data with that obtained in this study. Initial ratio data for Sr and Nd were also corrected to a crystallization age of 1270 Ma. Associated errors for initial $^{87}Sr/^{86}Sr$ values are less than the symbol size. Position of the Keel Dyke samples are relative. Stratigraphic column adapted from Francis (1994) and Irvine and Smith (1967). Note the reversal of x-axis values. Stratigraphic column legend as in Figure 3.3.

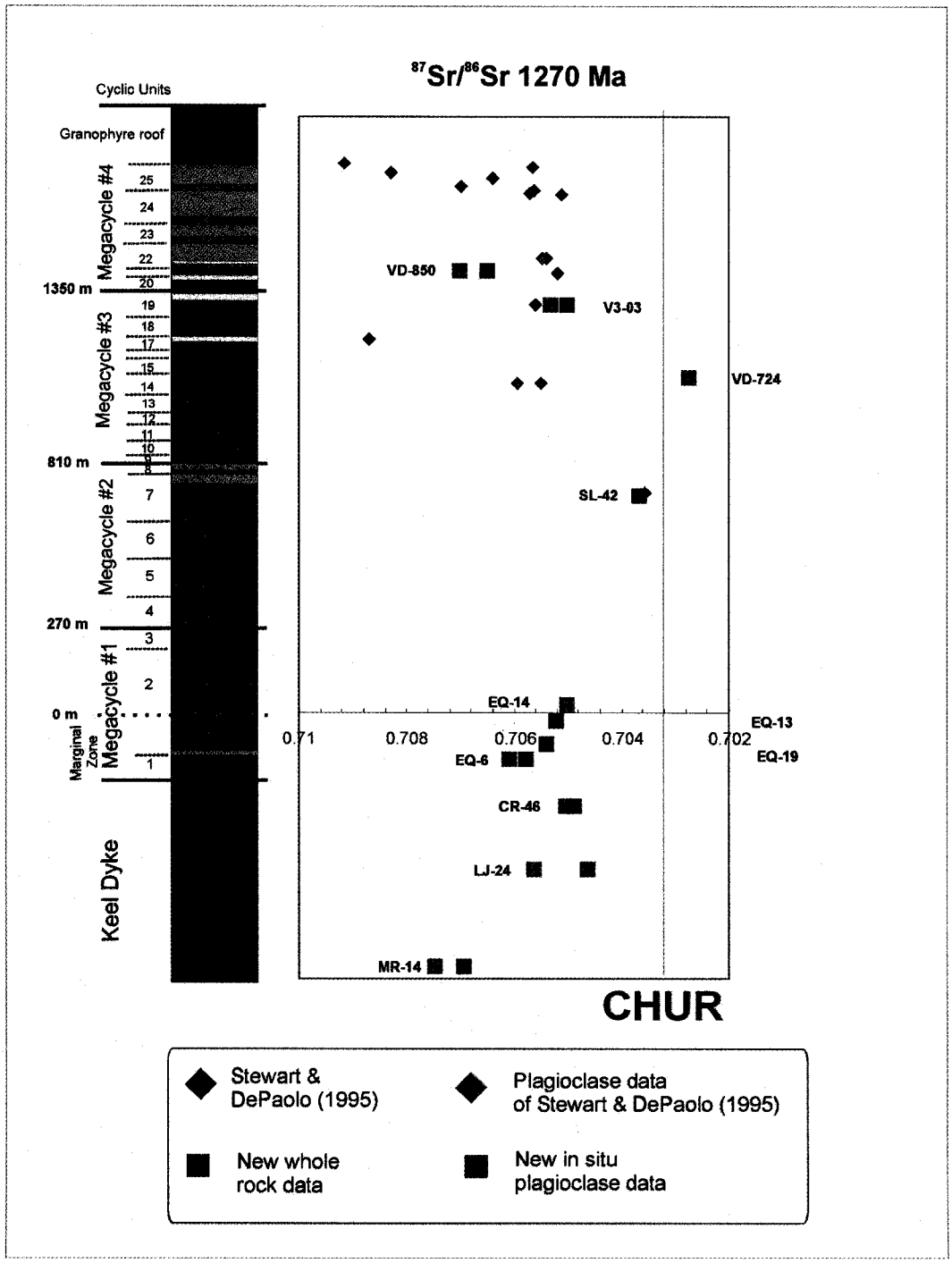

Figure 4.13 – Average initial $^{87}Sr/^{86}Sr$ and plagioclase compositions. An content of plagioclase is calculated from electron microprobe data. The arrow shows direction of evolution of the magma. Sample MR-14, from the Keel Dyke is an obvious outlier.

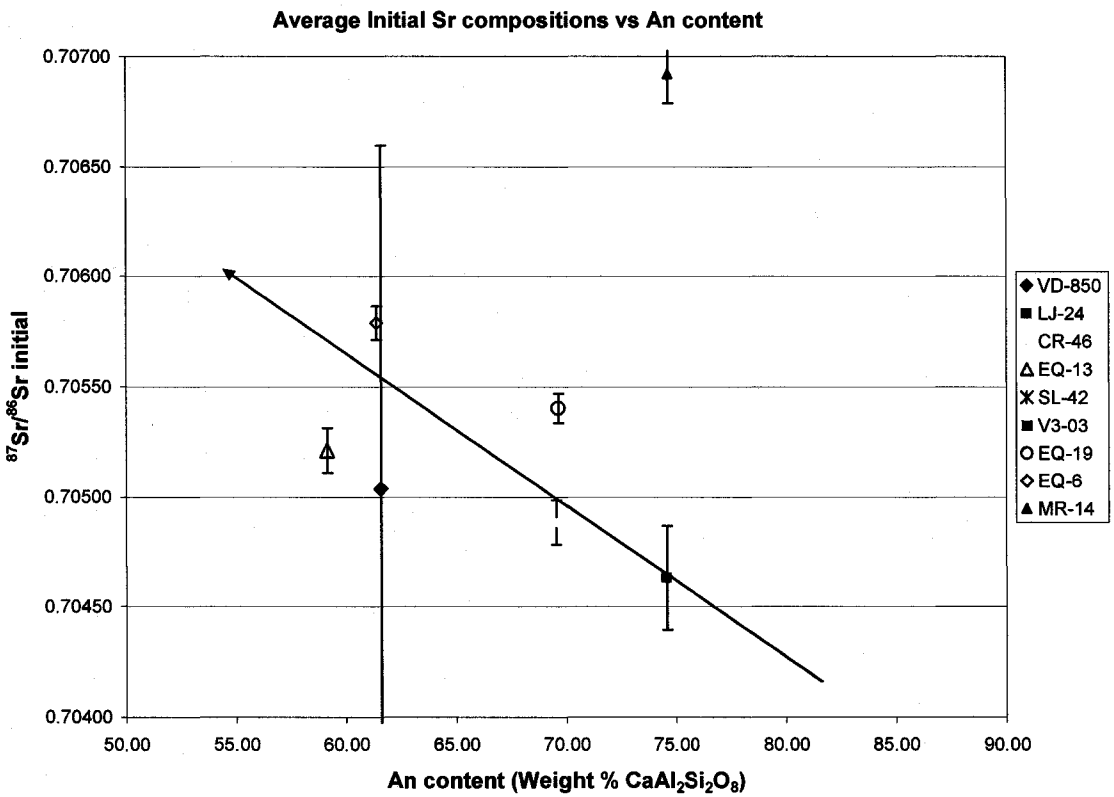

Figure 4.14 - $^{206}Pb/^{204}Pb$ and $^{207}Pb/^{204}Pb$ ratios of individual plagioclase grains. Average error bar is shown for scale. The mantle evolution curves were drawn assuming a single-stage model, with μ values of 7, 8, and 9, 4.55 Ga as the age of the Earth, and Canyon Diablo values (Tatsumoto et al. 1973) for the starting composition.

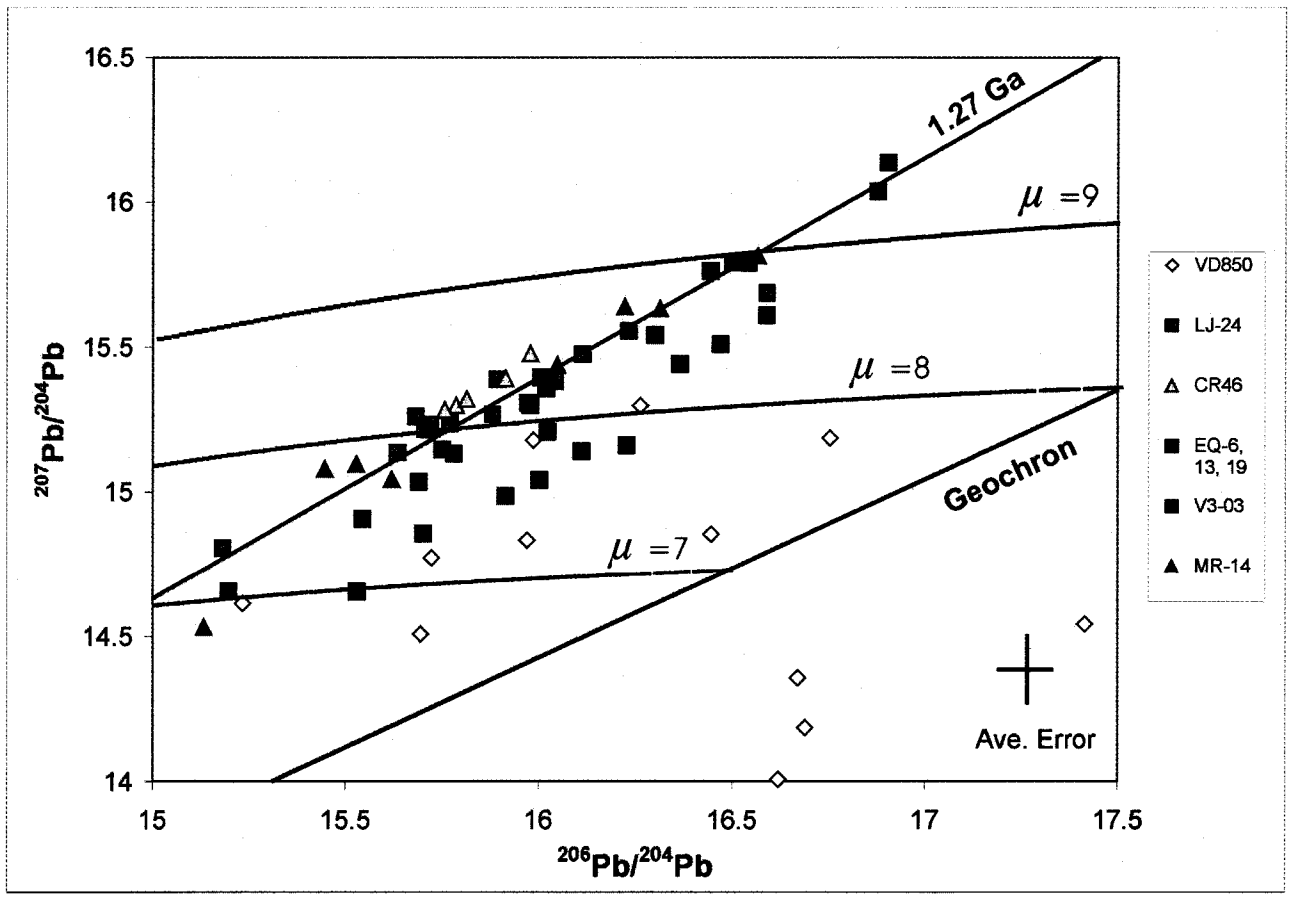

Figure 4.15 - Variations in initial Sr and Pb isotope compositions with stratigraphic height. Stratigraphic column adapted from Francis (1994) and Irvine and Smith (1967). Stratigraphic column legend as in Figure 3.3.

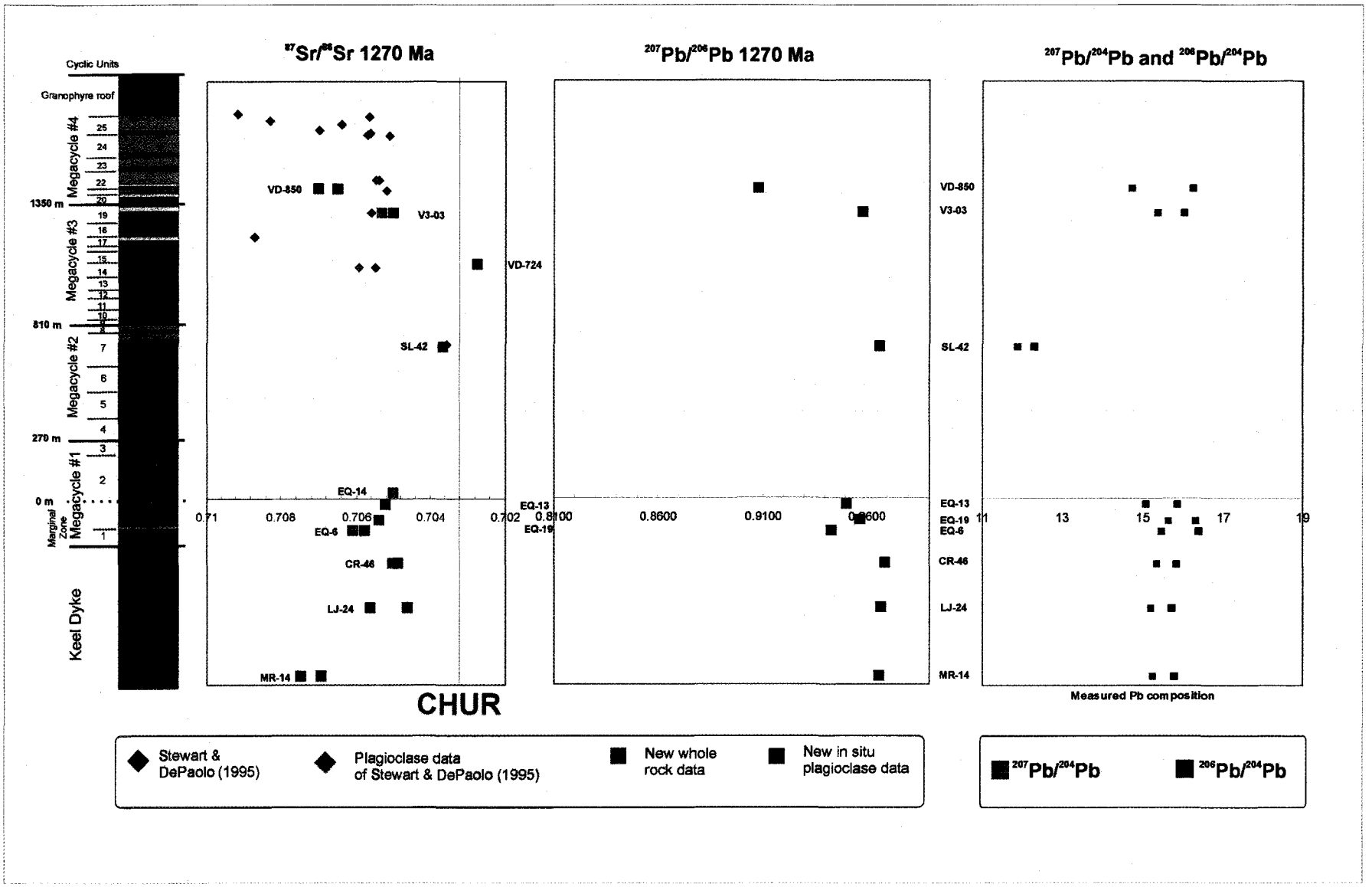

Figure 4.16 - Average initial $^{207}Pb/^{206}Pb$ and plagioclase compositions. An content of plagioclase is calculated from electron microprobe data. The arrow shows direction of evolution of the magma. As seen in the previous figure, sample VD-850, from the top of the intrusion has Pb ratios that are disturbed.

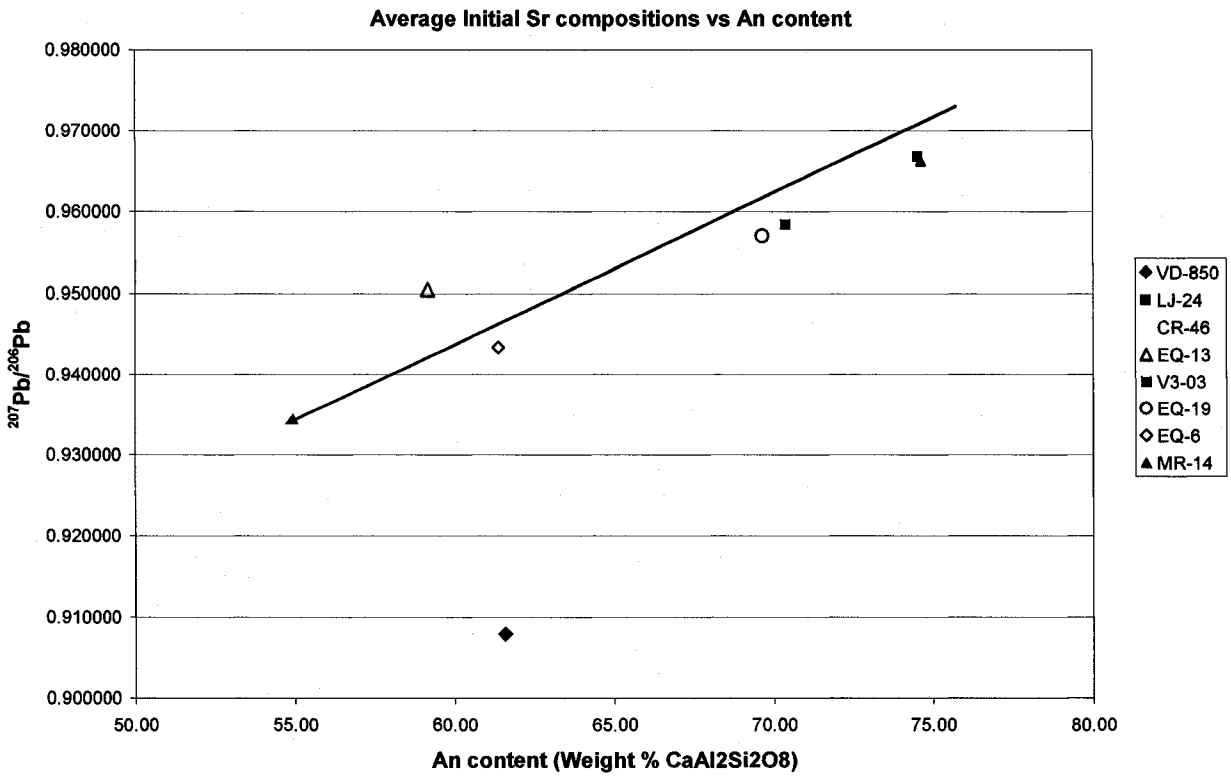

Figure 4.17 – $^{207}Pb/^{206}Pb$ versus $^{87}Sr/^{86}Sr$ ratios for plagioclase. Each point on the graph represents a different grain of plagioclase. The green arrow shows a plausible directional alteration trend. The red arrow points to values affected by crustal contamination. Stewart and DePaolo (1995) report initial $^{87}Sr/^{86}Sr$ (1270 Ma) values for granitic wall rocks of 0.73842 and 0.78881, which is a plausible contaminant.

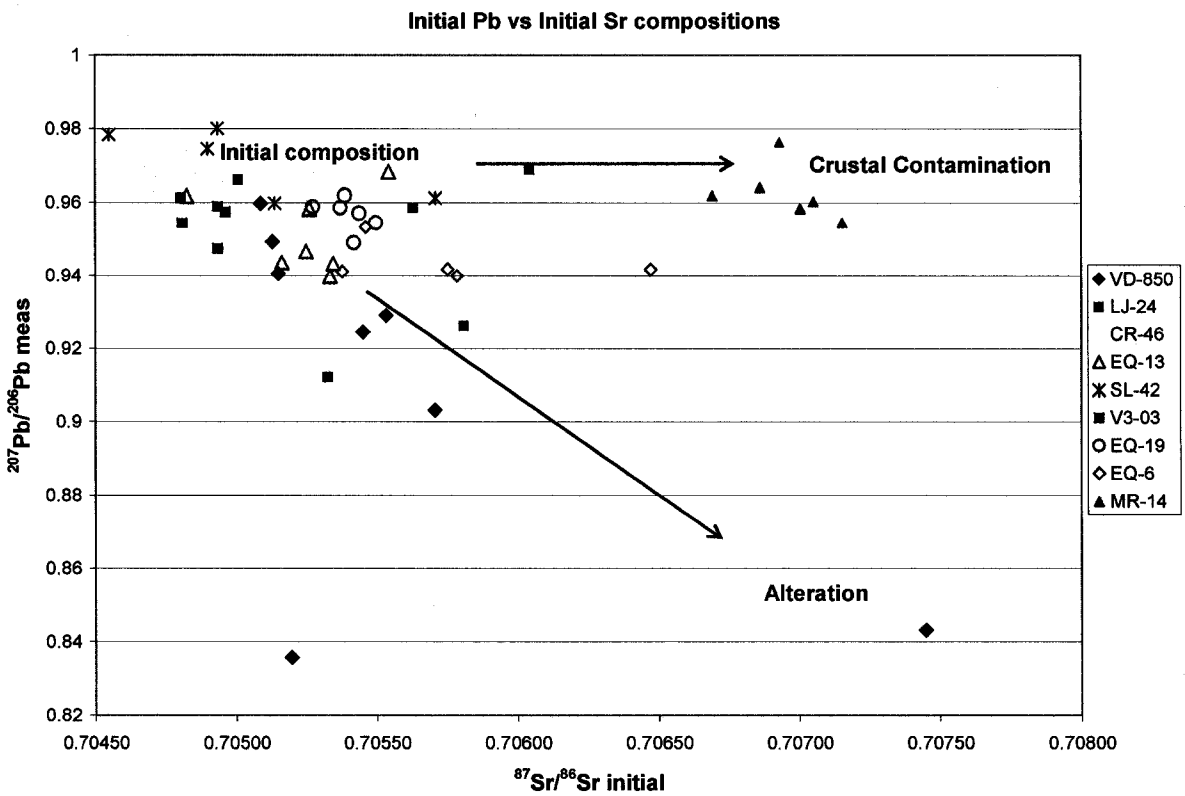

Figure 5.1 - Variations in initial Nd, Sr, Hf and Pb isotope compositions with stratigraphic height. Previous data for the Muskox Intrusion (Stewart and DePaolo, 1995), initial isotopic ratios reported for the Coppermine River Basalts (blue shaded field – Griselin et al. 1997; Dupuy et al. 1992), and the Bear River Dykes (yellow shaded field - Schwab et al. 2004) are shown for comparison. Values for CHUR and the depleted mantle at 1270 Ma are indicated. Stratigraphic column adapted from Francis (1994) and Irvine and Smith (1967). Stratigraphic column legend as in Figure 3.3.

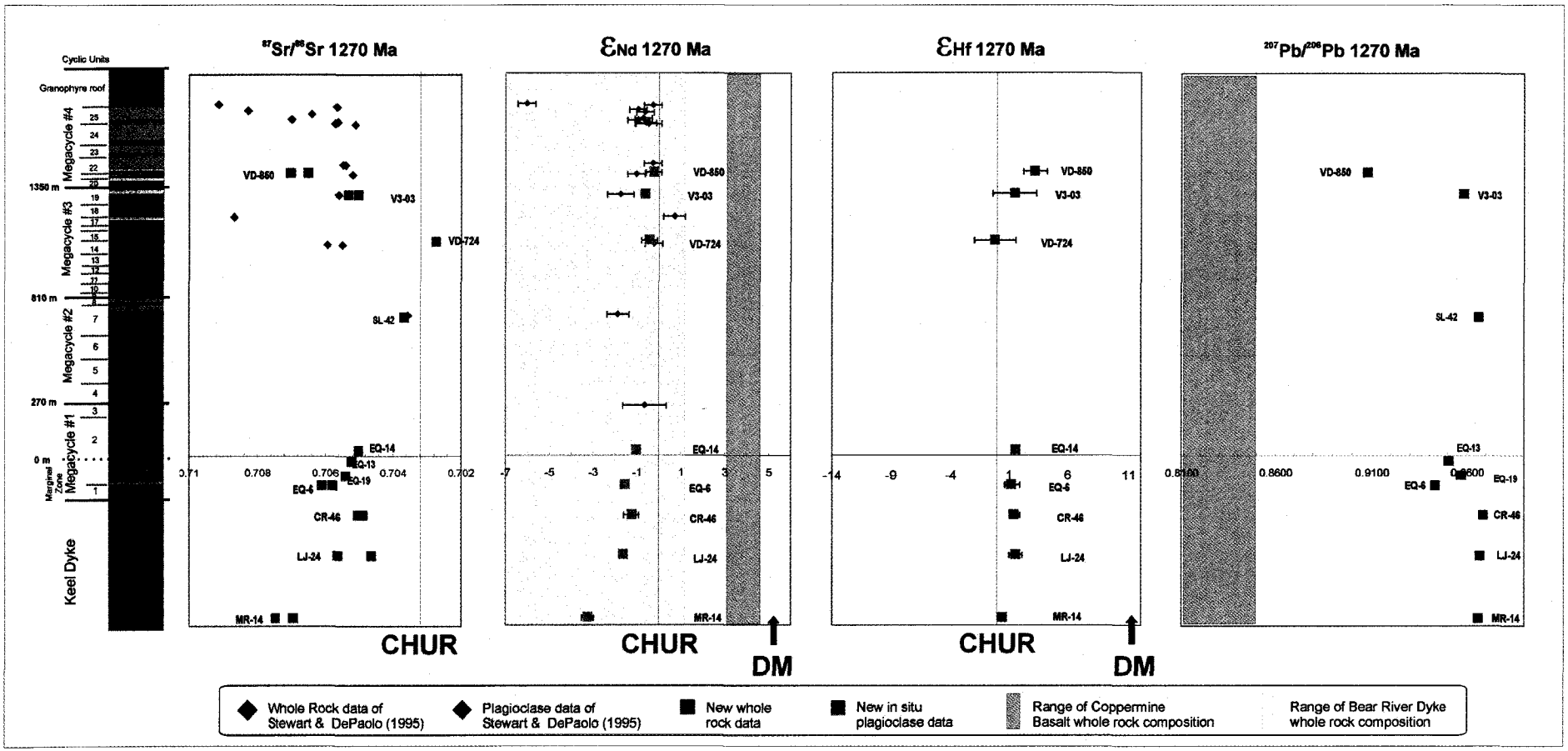

Figure 5.2 – Th/Ta versus La/Yb plot for Mackenzie Igneous Events. Data for the Muskox Intrusion (grouped by megacycle) and the Keel Dyke are from this study. Data for the Coppermine River Basalts are grouped by formation (HC = Husky Creek, CC = Copper Creek) and member (LM = lower member, MM = middle member, UM = upper member) from Griselin et al. (1997), for the Mackenzie Dykes from Baragar et al. (1996). Values of the lower crust (LC), upper continental crust (UCC), depleted mantle (DM), and primitive mantle (PM) are from Condie (1997) and references therein. Black arrows indicate possible contamination trends of the Muskox data, one towards crustal values, and one towards and unknown component, possibly the SCLM. The green arrow shows the trend of the Keel Dyke data, the red arrow shows the contamination trend of the CRB and MD data.

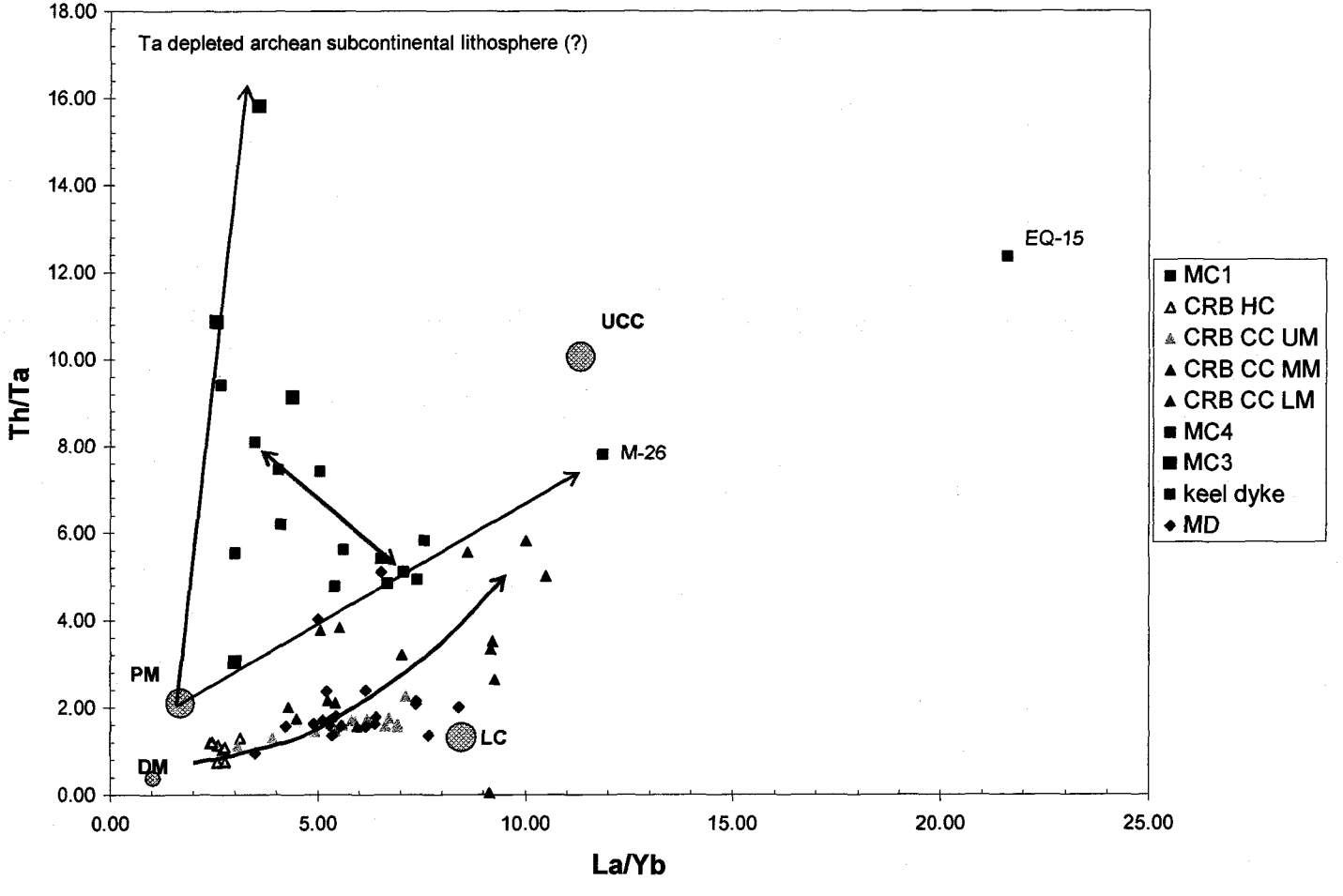

Figure 5.3 – Summary diagram for ε_{Nd} and initial $^{87}Sr/^{86}Sr$ compositions at 1270 Ma for Mackenzie Igneous Events, shown at two different scales.

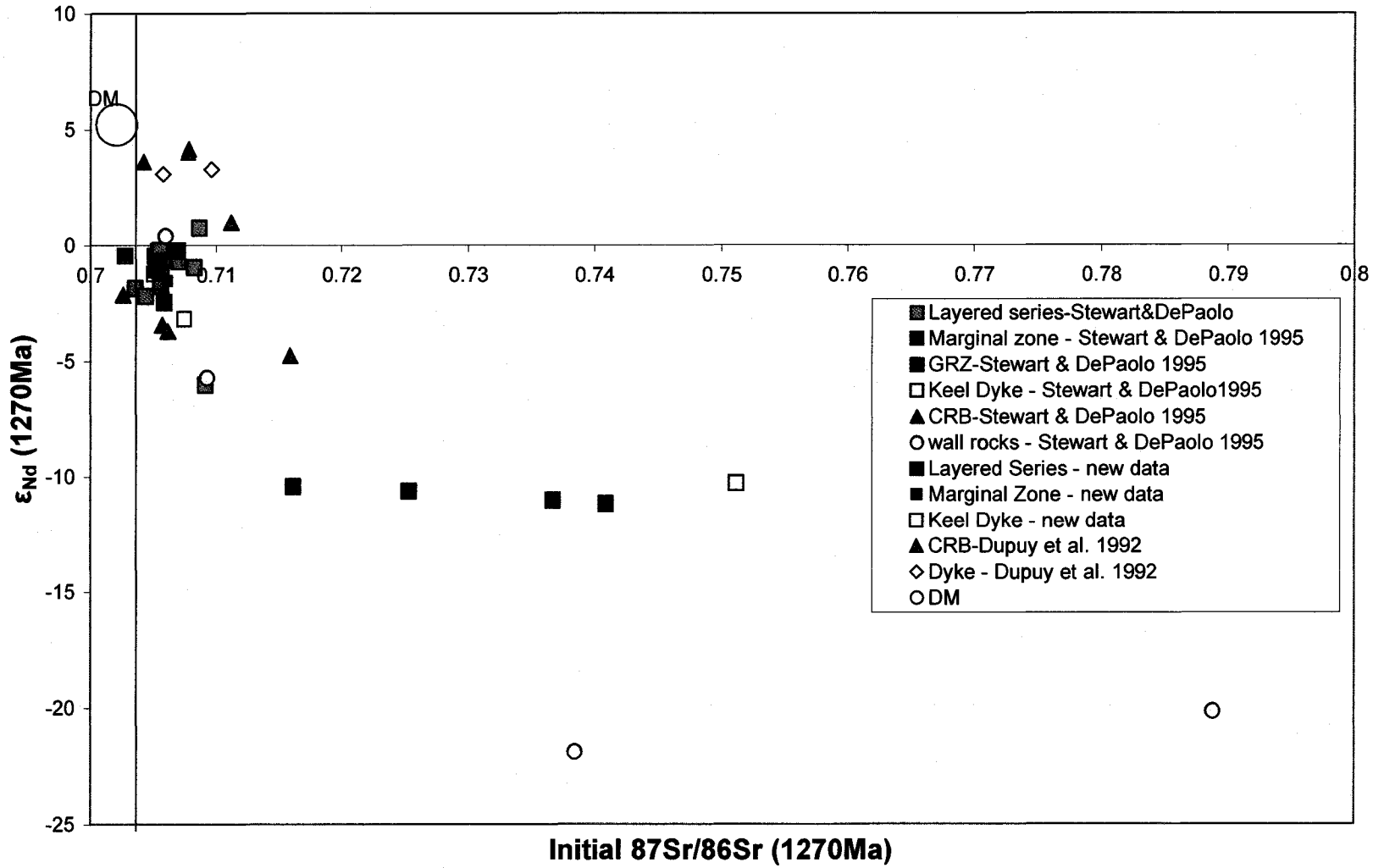

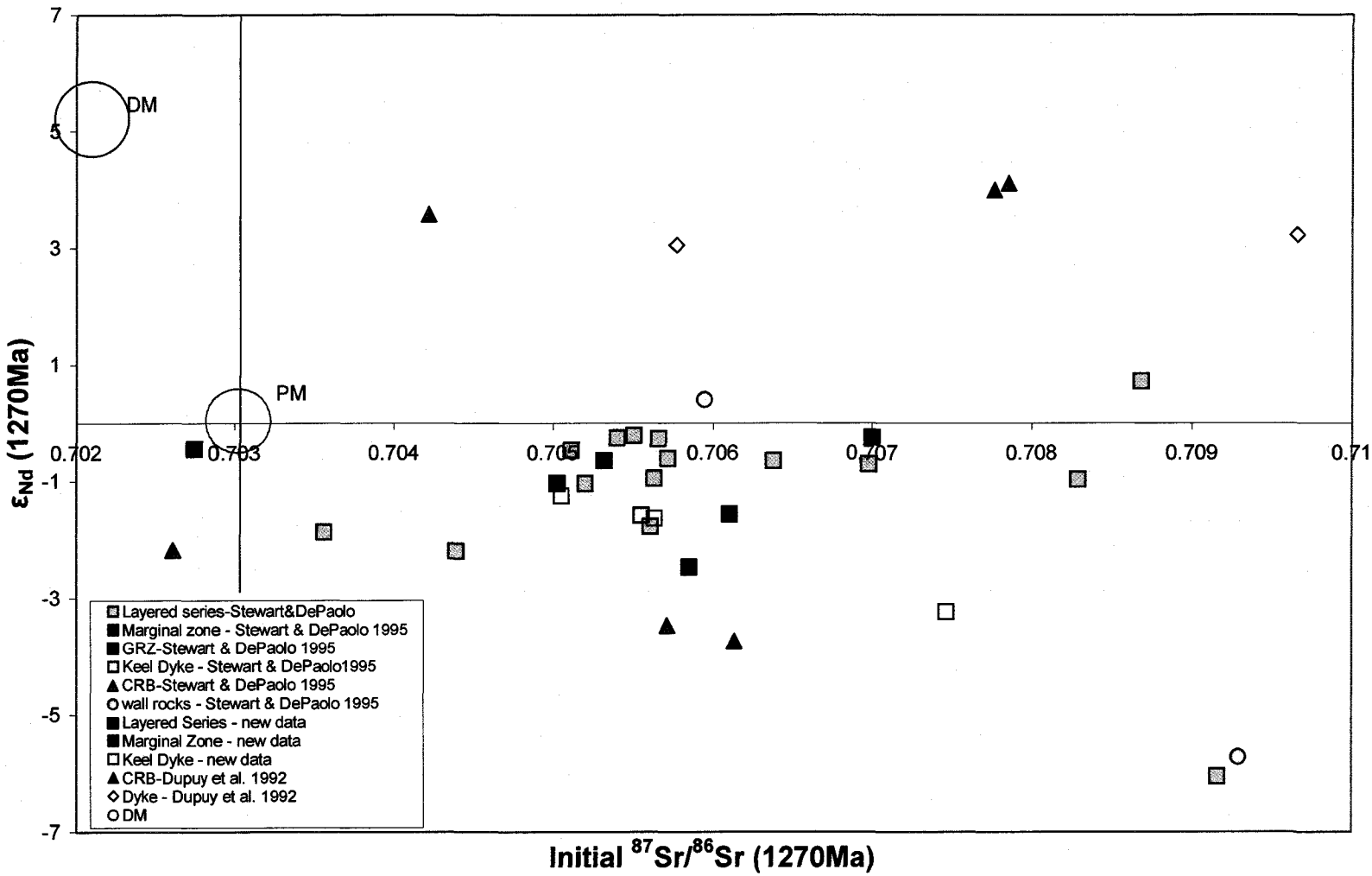

Figure 5.4 – Comparison of Pb isotopes for the Coppermine River Basalts and Muskox Intrusion. $^{206}Pb/^{204}Pb$ and $^{207}Pb/^{204}Pb$ ratios of MI samples are shown with squares, while the CRB are shown with triangles. The mantle evolution curves were drawn assuming a single-stage model, with μ values of 7, 8, and 9, 4.55 Ga as the age of the Earth, and Canyon Diablo values (Tatsumoto et al. 1973) for the starting composition. Pb data for the CRB is from Dupuy et al. (1992). The grey shaded area shows the field for Atlantic and Pacific MORB from White et al. (1987) and Ito et al. (1987).

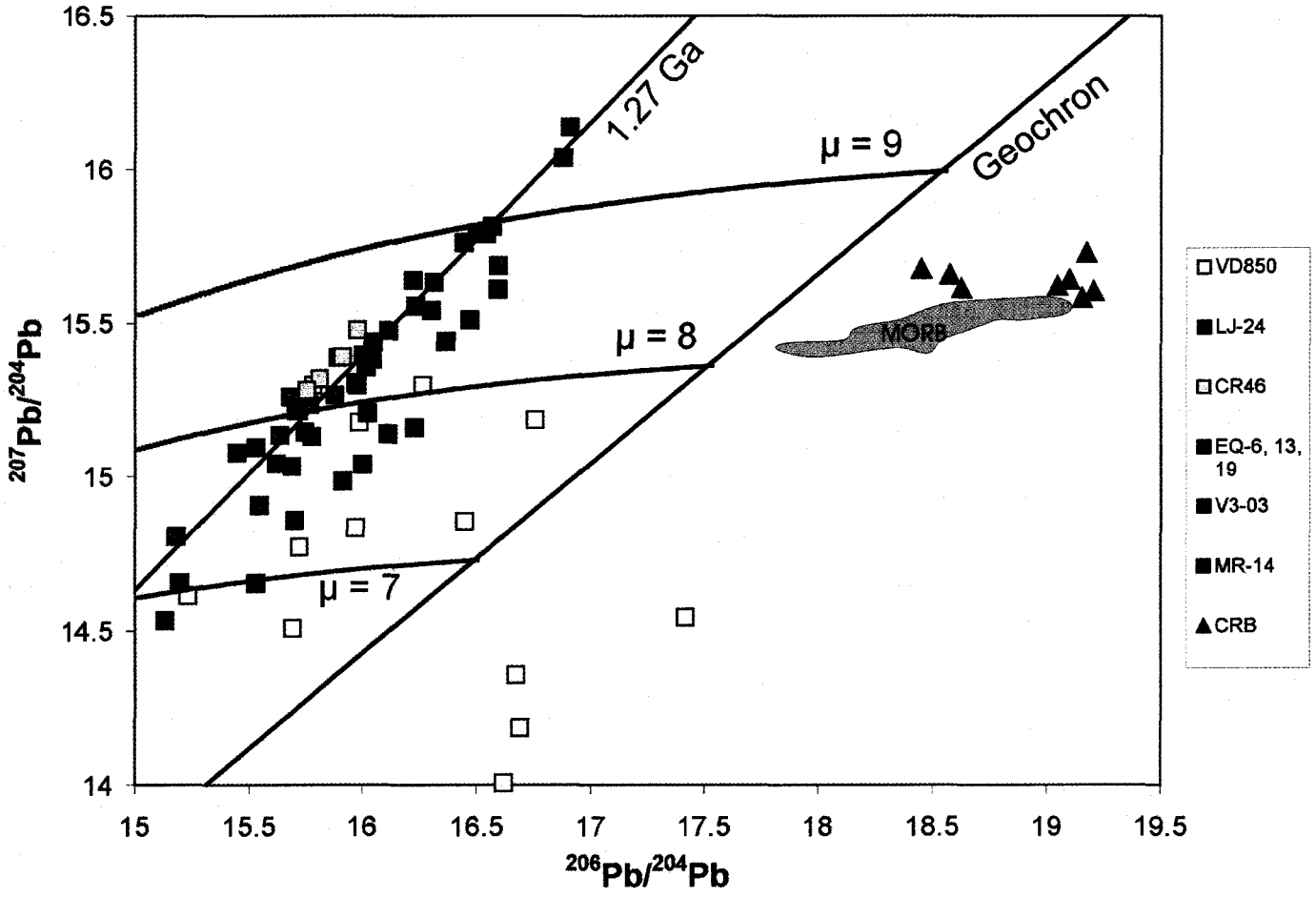

Figure 5.5 - Graph showing ε_{Nd} (1270 Ma) values versus Nd. Measured values for the Muskox samples from this study are shown with squares. Diamonds show values obtained by mixing depleted mantle with the Muskox country rock in increments of 5% (values from Stewart and DePaolo, 1995). DM = Depleted mantle, CC = Continental Crust. Parameters of the model are: Nd in DM = 10ppm, Nd in crust = 40ppm, ε_{Nd} (1270 Ma) of DM = +5.5, ε_{Nd} (1270 Ma) of crust = -20. Arrow shows the direction that the values for the Muskox samples are altered because of their cumulate nature.

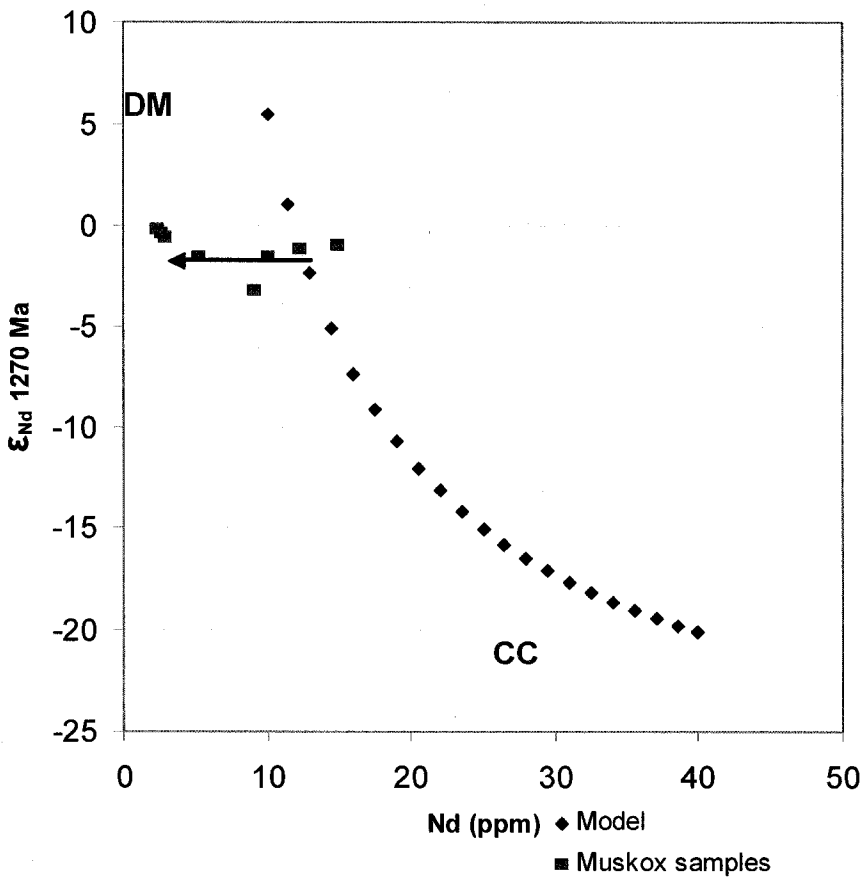

Figure 5.6 – Schematic diagram depicting the emplacement of Mackenzie Igneous Events. See text for further discussion.

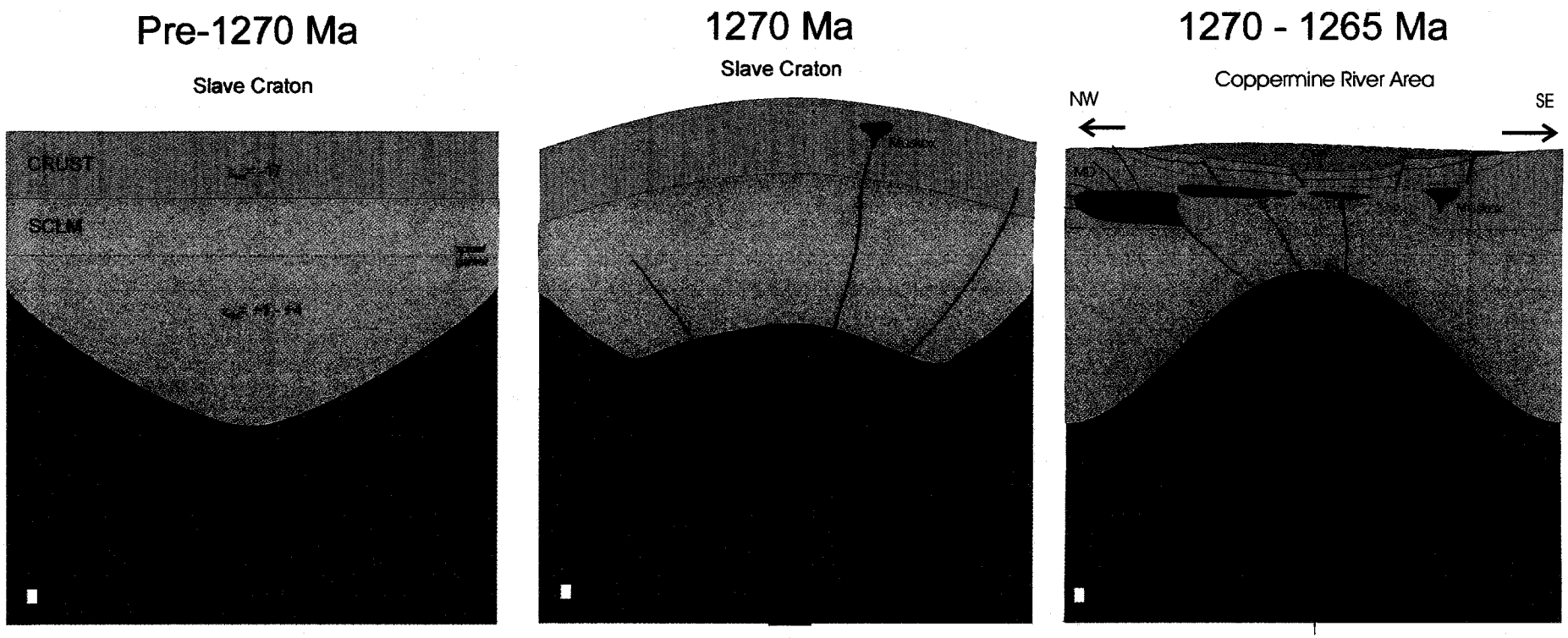

Pre-1270 Ma
Diagram shows the structure of the Slave craton, prior to the appearance of the Mackenzie plume. Approximate vertical scale and estimated Nd compositions of the various reservoirs are shown.

1270 Ma
Diagram shows the upwelling of the Mackenzie plume from the deep mantle. The lithosphere domes as a result of this large thermal anomaly. The lithospheric mantle root begins to erode. The Muskox intrusion and some Mackenzie dykes are shown feeding directly from the plume.

1270 - 1265 Ma
Diagram shows the Mackenzie plume pooling beneath the lithosphere, where it becomes extensively mixed with depleted mantle material. Rifting occurs, allowing the magma to move up into large crustal magma chambers (generally to the north of the MI). There the magma differentiates and becomes contaminated, before moving vertically to form the Coppermine River flood basalts, and horizontally to form more Mackenzie Dykes.

References

Amelin, Y., Chusi, L., Valeyev, Ol, and Naldrett, A.J. 2000. Nd-Pb-Sr Isotope Systematics of Crustal Assimilation in the Voisey's Bay and Mushuau Intrusions, Labrador, Canada. Economic Geology, **95**: 815-830.

Amelin, Y., Lee, D.C., Halliday, A.N., and Pidgeon, R.T. 1999. Nature of the Earth's earliest crust from hafnium isotopes in single detrital zircons. Nature, **399**: 252-255.

Andersen, T., and Griffin, W. L. 2004. Lu-Hf and U-Pb isotope systematics of zircons from the Storgangen intrusion, Rogaland Intrusive Complex, SW Norway: Implications for the composition and evolution of Precambrian lower crust in the Baltic Shield. Lithos, **73**: 271-288.

Armstrong, J.T. 1995. A Package of Correction Programs for the Quantitative Electron Microbeam X-ray Analysis of Thick Polished Materials, Thin Films, and Particles. Microbeam Analysis, **4**: 177-200

Baragar, W.R.A. 1969. The Geochemistry of Coppermine River basalts. Geological Survey of Canada, Paper, 69-44.

Baragar, W.R.A. 1972. Coppermine River basalts: geological setting and interpretation. *In* Rubidium-strontium isochron age studies: Report 1. *Edited by* R. K. Wanless, and W.D. Love. Geological Survey of Canada Paper, Canada: pp.21-24.

Baragar, W.R.A., Ernst, R.E., Hulbert, L., and Peterson, T. 1996. Longitudinal petrochemical variation in the Mackenzie dyke swarm, northwestern Canadian Shield. Journal of Petrology, **37**: 317-359.

Barnes, S.J., and Francis, D. 1995. The Distribution of Platinum-Group Elements, Nickel, Copper, and Gold in the Muskox Layered Intrusion, Northwest-Territories, Canada. Economic Geology and the Bulletin of the Society of Economic Geologists, **90**: 135-154.

Bedard, J.H., and Taner, M.F. 1992. The upper part of the Muskox Intrusion, Northwest Territories. Geological Survey of Canada, Paper, 92-01C: 91-101.

Bizzarro, M., Baker, J.A., and Ulfbeck, D. 2003. A new digestion and chemical separation technique for rapid and highly reproducible determination of Lu/Hf and Hf isotope ratios in geological materials by MC-ICP-MS. Geostandards Newsletter, **27**: 133-145.

Blichert-Toft, J., Boyet, M., and Albarede, F. 2002. (super 176) Lu- (super 176) Hf, (super 147) Sm- (super 143) Nd, and (super 92) Zr isotope systematics in eucrites. Geochimica et Cosmochimica Acta, **66**: 82.

Bowring, S.A., and Podosek, F.A. 1989. Nd isotopic evidence from Wopmay Orogen for 2.0 - 2.4 Ga crust in western North America. Earth and Planetary Science Letters, **94**: 217-230.

Bowring, S.A., and Ross, G.M. 1985. Geochronology of the Narakay Volcanic Complex: implications for the age of the Coppermine Homocline and Mackenzie igneous events. Canadian Journal of Earth Sciences, **22**: 774-781.

Camp, V.E. 1995. Mid-Miocene propagation of the Yellowstone mantle plume head beneath the Columbia River Basalt source region. Geology, **23**: 435-438.

Campbell, I.H., and Griffiths, R.W. 1990. Implications of mantle plume structure for the evolution of flood basalts. Earth and Planetary Science Letters, **99**: 79-93.

Carr, M. 1995. Program IGPET, Terra Softa Inc. Somerset, New Jersey, U.S.A.
Condie KC 1997. Sources of Proterozoic mafic dyke swarms: Constraints from Th/Ta and La/Yb ratios. Precambrian Research, **81**: 3-14.
Cook, F.A. 1988. Middle Proterozoic compressional orogen in northwestern Canada. Journal of Geophysical Research, **93**: 8985-9005.
Cook, F.A., van der Velden, A.J., and Hall, K.W. 1999. Frozen subduction in Canada's Northwest Territories: Lithoprobe deep lithospheric reflection profiling of the western Canadian Shield. Tectonics, **18**: 1-24.
Creaser, R.A., Erdmer, P., Stevens, R.A., and Grant, S.L. 1997. Tectonic affinity of Nisutlin and Anvil assemblage strata from the Teslin tectonic zone, northern Canadian Cordillera: Constraints from neodymium isotope and geochemical evidence. Tectonics, **16**: 107-121.
Creaser, R.A., Gruetter, H.S., Carlson, J.A., and Crawford, B.B. 2004. Macrocrystal phlogopite Rb/Sr dates for the Ekati property kimberlites, Slave Province, Canada; evidence for multiple intrusive episodes in the Paleocene and Eocene. Lithos, **76**: 339-414.
Davidson, J., Tepley III, F.J., Palacz, Z., and Meffan-Main, S. 2001. Magma recharge, contamination and residence times revealed by in situ laser ablation isotopic analysis of feldspar in volcanic rocks. Earth and Planetary Science Letters, **184**: 427-442.
DePaolo, D.J., and Wasserburg, G.J. 1976a. Nd isotopic variations and petrogenetic models. Geophysical Research Letters, **3**: 249-252.
DePaolo, D.J., and Wasserburg, G.J. 1976b. Inferences about magma sources and mantle structure from variations of Nd-143/ Nd-144. Geophysical Research Letters, 3: 743-746.
DePaolo, D.J., and Wasserburg, G.J. 1979. Sm-Nd age of the Stillwater Complex and the mantle evolution curve for neodymium. Geochimica et Cosmochimica Acta, 43: 999-1008.
Doe, B.R., and Zartman, R.E. 1979. Plumbotectonics. *In* Geochemistry of Hydrothermal Ore Deposits *Edited by* Barnes, H.L.. Wiley: pp.22-70.
Dostal, J., Baragar, W.R.A., and Dupuy, C. 1983. Geochemistry and petrogenesis of basaltic rocks from Coppermine River area, Northwest Territories. Canadian Journal of Earth Sciences, **20**: 684-698.
Dudas, F.O., and Peterson, T.D. 1992. Nd isotopic composition of Mackenzie dikes, Northwest Territories, Canada. Eos, Transaction, American Geophysical Union, **73**: 339.
Dupuy, C., Michard, A., Dostal, J., Dautel, D., and Baragar, W.R.A. 1992. Proterozoic flood basalts from the Coppermine River area, Northwest Territories; isotope and trace element geochemistry. Canadian Journal of Earth Sciences, **29**: 1937-1943.
Elliott, T., Plank, T., Zindler, A., White, W., and Bourdon, B. 1997. Element transport from slab to volcanic front at the Mariana Arc. Journal of Geophysical Research, **102**: 14991-15019.
Ernst, R.E., and Baragar, W.R.A. 1992. Evidence from magnetic fabric for the flow pattern of magma in the Mackenzie giant radiating dyke swarm. Nature, **356**: 511-513.

Ernst, R.E., and Buchan, K.L. 1997. Layered mafic intrusions; a model for their feeder systems and relationship with giant dyke swarms and mantle plume centres. South African Journal of Geology, **100**: 319-334.

Fahrig, W.F. 1987. The tectonic settings of continental mafic dyke swarms: failed arm and early passive margin. *In* Mafic Dyke Swarms. *Edited by* H.C. Halls and W.F. Fahrig.. GSC Special Paper 34, Geological Association of Canada: pp.331-348.

Fahrig, W.F., and Jones, D.L. 1969. Paleomagnetic evidence for the extent of Mackenzie igneous events. Canadian Journal of Earth Sciences, **6**: 679-688.

Francis, D. 1994. Chemical interaction between picritic magmas and upper crust along the margins of the Muskox intrusion, Northwest Territories. Geological Survey of Canada, Paper, 92-12: 1-94.

Fraser, J.A., Hoffman, P.F., Irvine, T.N., and Mursky, G. 1972. The Bear Province. Special Paper - Geological Association of Canada, **11**: 453-503.

French, J.E., Heaman, L.M., and Chacko, T. 2002. Feasibility of chemical U-Th-total Pb baddeleyite dating by electron microprobe. Chemical Geology, **188**: 85-104.

Gagnevin, D., Daly, J.S., Waight, T.E., Morgan, D., and Poli, G. 2005. Pb isotopic zoning of K-feldspar megacrysts determined by Laser Ablation Multi-Collector ICP-MS: Insights into granite petrogenesis. Geochimica et Cosmochimica Acta, **69**: 1899-1915.

Galer, S.J.G., and Goldstein, S.L. 1995. Influence of Accretion on Lead in the Earth *In* Earth processes: Reading the isotopic code: American Geophysical Union, Geophysical Monograph, 95. *Edited by* Basu, A., and Hart, S.: pp.75-98.

Gibson, I.L., Sinha, M.N., and Fahrig, W.F. 1987. The geochemistry of the Mackenzie dyke swarm, Canada. *In* Mafic dyke swarms; a collection of papers based on the proceedings of an international conference. *Edited by* H.C. Halls and W.F. Fahrig. Geological Association of Canada, Toronto, ON, Canada. pp.109-121.

Gibson, S.A., Thompson, R.N., Dickin, A.P., Leonardos, O.H. 1996. Erratum To: Title: High-Ti and low-Ti mafic potassic magmas: Key to plume-lithosphere interactions and continental flood-basalt genesis (vol 136, pg 149, 1995). Earth and Planetary Science Letters, **141**: 325-341.

Goodacre, A. K., Grieve, R.A.F., and Halpenny, J.F. 1987. Bouguer gravity anomaly map of Canada. Geological Survey of Canada, Canadian Geophysical Atlas, 3.

Griselin, M., Arndt, N.T., and Baragar, W.R.A. 1997. Plume-lithosphere interaction and crustal contamination during formation of Coppermine River basalts, Northwest Territories, Canada. Canadian Journal of Earth Sciences, **34**: 958-975.

Heaman, L.M., and LeCheminant, A.N. 1993. Paragenesis and U-Pb systematics of baddeleyite (ZrO_2). Chemical Geology, **110**: 95-126.

Hildebrand, R. S. 1981. Early Proterozoic Labine Group of Wopmay Orogen; remnant of a continental volcanic arc developed during oblique convergence. *In* Geological Survey of Canada Paper 81-10. *Edited by* F.H.A. Campbell. Publisher: Geological Survey of Canada, Ottawa, ON, Canada. pp.133-156.

Hildebrand, R.S., Bowring, S.A., Steer, M.E., and Van Schmus, W.R. 1983. Geology and U-Pb geochronology of parts of the Leith Peninsula and Riviere Granin map areas, District of Mackenzie. Geological Survey of Canada Paper, 83-1A: 329-342.

Hildebrand, R.S., Hoffman, P.F., and Bowring, S.A. 1987. Tectono-magmatic evolution of the 1.9-Ga great bear magmatic zone, Wopmay orogen, northwestern Canada. Journal of Volcanology and Geothermal Research, **32**: 99-118.

Hoffman, P. 1984. Geology, Northern Internides of Wopmay Orogen, District of Mackenzie, Northwest Territories. Geological Survey of Canada, Map 1567A: Scale 1:250 000.

Hoffman, P.F. 1989. Speculations on Laurentia's first gigayear (2.0 to 1.0 Ga). Geology, **17**: 135-138.

Hoffman, P.F., and Bowring, S.A. 1984. Short-lived 1.9 Ga continental margin and its destruction, Wopmay orogen, northwest Canada. Geology, 12: 68-72.

Hofmann, A.W. 1997. Mantle geochemistry: the message from oceanic volcanism. Nature, **385**: 219-229.

Holm, P.M. 2002. Sr, Nd and Pb isotopic composition of in situ lower crust at the Southwest Indian Ridge; results from ODP Leg 176. Chemical Geology, **184**: 195-216.

Holmden, C., Creaser, R. A., Muehlenbachs, K., Bergstrom, S. M., and Leslie, S. A. 1996. Isotopic and elemental systematics of Sr and Nd in 454 Ma biogenic apatites; implications for paleoseawater studies. Earth and Planetary Science Letters, **142**: 425-437.

Irvine, T.N. 1977. Origin of Chromitite Layers in Muskox Intrusion and other Stratiform Intrusions - New Interpretation. Geology, **5**: 273-277.

Irvine, T.N., and Smith, C.H. 1967. The ultramafic rocks of the Muskox intrusion, Northwest Territories, Canada. *In* Ultramafic and related rocks. *Edited by* P.J. Wyllie. John Wiley & Sons, Inc., N.Y.. pp.38-49.

Irvine, T.N., and Smith, C.H. 1969. Primary oxide minerals in the layered series of the Muskox intrusion. *In* Magmatic ore deposits; a symposium. *Edited by* H.D.B. Wilson. Economic Geology Publishing Co., Lancaster, PA, United States. pp.76-94.

Irvine, T.N., and Smith, C.H. 1979. The ultramafic rocks of the Muskox Intrusion, Northwest Territories, Canada.; 2. *In* Ultramafic and related rocks. *Edited by* P.J. Wyllie. Robert E. Krieger Publ. Co.. , Huntington, NY, United States. pp.38-49.

Irvine, T. N. 1970. Crystallization sequences in the Muskox intrusion and other layered intrusions; 1, Olivine-pyroxene-plagioclase relations. Special Publication - Geological Society of South Africa, **1**: 441-476.

Ito, E., White, W.M., and Gopel, C. 1987. The O, Sr, Nd, and Pb isotope geochemistry of MORB. Chemical Geology, **62**: 167-176.

Jarosewich, E. 2002. Smithsonian Microbeam Standards. Journal of Research of the National Institute of Standards and Technology, **107**: 681-685.

Kerans, C. 1983. Timing of Emplacement of the Muskox Intrusion - Constraints from Coppermine Homocline Cover Strata. Canadian Journal of Earth Sciences, **20**: 673-683.

Kretz, R. 1983. Symbols for rock-forming minerals. American Mineralogist, **68**: 277-279 .

LeCheminant, A.N., and Heaman, L.M. 1989. Mackenzie igneous events, Canada; middle Proterozoic hotspot magmatism associated with ocean opening. Earth and Planetary Science Letters, **96**: 38-48.

Ludwig, K.R. 2003. ISOPLOT 3.0 a geochronological toolkit for Microsoft Excel. Berkeley Geochronology Center Special Publication No. 4.

Mackie, R.A., Scoates, J.S., Weis, D., and Peck, D. 2006. Formation of the marginal zone in the 1.27 Ga Muskox layered mafic-ultramafic Intrusion, Nunavut. Geological Association of Canada Conference abstracts, 2006: 93.

Mackie, R.A., Scoates, J.S., Weis, D., Maerschalk, C., and Peck, D. 2005. Trace element and Hf-Nd isotopic profiling of crustal contamination across the marginal zone of the Muskox intrusion, Nunavut. Geochimica et Cosmochimica Acta Supplement, **69**: 863.

Mathez, E.A., and Waight, T.E. 2003. Lead isotopic disequilibrium between sulfide and plagioclase in the Bushveld Complex and the chemical evolution of large layered intrusions. Geochimica et Cosmochimica Acta, **67**: 1875-1888.

McDonough, W.F. 1990. Contraints on the composition of the continental lithospheric mantle. Earth and Planetary Science Letters, **101**: 1-18.

Nicholson, S.W., and Shirey, S.B. 1990. Midcontinent rift volcanism in the Lake Superior region: Sr, Nd and Pb isotopic evidence for a mantle plume origin. Journal of Geophysical Research, **95**: 10851-10868.

Nicholson, S.W., Shirey, S.B., Schulz, K.J., and Green, J.C. 1997. Rift-wide correlation of 1.1 Ga Midcontinent Rift System basalts; implications for multiple mantle sources during rift development. Canadian Journal of Earth Sciences, **34**: 504-520.

Nir-El, Y., and Lavi, N. 1998. Measurement of half-life of 176Lu. Applied Radiation and Isotopes, **43**: 1653-1655.

Paces, J.B., and Bell, K. 1989. Non-depleted sub-continental mantle betneath the Superior province of the Canadian Shield: Nd-Sr isotopic and trace element evidence from Midcontinent rift basalts. Geochimica et Cosmochimica Acta, **53**: 2023-2035.

Patchett, P.J., and Tatsumoto, M. 1981. Lu/Hf in chondrites and definition of a chondritic hafnium growth curve. Lunar and Planetary Science, XII: 822-824.

Patchett, P.J., White, W.M., Feldmann, H., Kielinczuk, S., and Hofmann, A.W. 1984. Hafnium/rare earth element fractionation in the sedimentary system and crustal recycling into the Earth's mantle. Earth and Planetary Science Letters, **69**: 365–378.

Pearson, D.G., and Nowell, G.M. 2004. Re–Os and Lu–Hf Isotope Constraints on the Origin and Age of Pyroxenites from the Beni Bousera Peridotite Massif: Implications for Mixed Peridotite–Pyroxenite Mantle Sources. Journal of Petrology, **45**: 439-455.

Peate, D.W., Hawkesworth, C.J., Mantovani, M., and Shukowsky, W. 1990. Mantle plumes and flood-basalt stratigraphy in the Parana, South America. Geology, **18**: 1223-1226.

Salters, V.J.M., and Hart, S.R. 1991. The mantle sources of ocean ridges, islands and arcs: the Hf-isotope connection. Earth and Planetary Science Letters, **104**: 364-380.

Salters, V.J.M., and White, W.M. 1998. Hf isotope constraints on mantle evolution. Chemical Geology, **145**: 447-460.

Sangster, D.F., Outridge, P.M., and Davis, W.J. 2000. Stable lead isotope characteristics of lead ore deposits of environmental significance. Environmental Reviews, **8**: 115-147.

Scherer, E., Munker, C., and Mezger, K. 2001. Calibrating the Lu-Hf clock. Science, **293**: 683-686.

Schmidberger, S.S., Heaman, L.M., Simonetti, A., Creaser, R.A., and Cookenboo, H.O. 2005. Formation of Paleoproterozoic eclogitic mantle, Slave Province (Canada): Insights from in-situ Hf and U-Pb isotopic analyses of mantle zircons. Earth and Planetary Science Letters, **240**: 621-633.

Schmidberger, S.S., Simonetti, A., and Francis, D. 2003. Small-scale Sr isotope investigation of clinopyroxenes from peridotite xenoliths by laser ablation MC-ICP-MS - implications for mantle metasomatism. Chemical Geology, **199**: 317-329.

Schmidberger, S.S., Simonetti, A., Francis, D., and Gariepy, C. 2002. Probing Archean lithosphere using the Lu-Hf isotope systematics of peridotite xenoliths from Somerset Island kimberlites, Canada. Earth and Planetary Science Letters, **197**: 245-259.

Schwab D.L., Thorkelson D.J., Mortensen J.K., et al. 2004. The Bear River dykes (1265-1269 Ma): Westward continuation of the Mackenzie dyke swarm into Yukon, Canada. Precambrian Research, **133**: 175-186.

Simonetti, A., Heaman, L.M., Hartlaub, R.P., Creaser, R.A., MacHattie, T.G., and Böhm, C. 2005. U-Pb zircon dating by laser ablation-MC-ICP-MS using a new multiple ion counting-faraday collector array. Journal of Analytical Atomic Spectrometry, **20**: 677-686.

Söderlund, U., Patchett, P.J., Vervoort, J.J., and Isachsen, C.E. 2004. The ^{176}Lu decay constant determined by Lu-Hf and U-Pb isotope systematics of Precambrian mafic intrusions. Earth and Planetary Science Letters, **219**: 311-324.

Steiger, R.H., and Jager, E. 1977. Subcommission on Geochronology: convention on the use of decay constants in geo- and cosmochronology. Earth and Planetary Science Letters, **36**: 359-362.

Stewart, B.W., and DePaolo, D.J. 1988. Sm-Nd age and Nd and Sr isotopic variations within the Muskox Intrusion, Northwest Territories, Canada. GSA Abstracts with programs, **20**: 156.

Stewart, B.W., and DePaolo, D.J. 1989. Mixing of mafic and silicic magmas in magma chambers; Nd and Sr isotopic constraints. GSA Abstracts with programs, **21**: 263.

Stewart, B.W., and DePaolo, D.J. 1990a. Liquid evolution in a multiply-recharged magmatic system; isotopic evidence from the Muskox Intrusion, Canada. GSA Abstracts with programs, **22**: 256.

Stewart, B.W., and DePaolo, D.J. 1990b. Isotopic studies of processes in mafic magma chambers; II, The Skaergaard Intrusion, East Greenland. Contributions to Mineralogy and Petrology, **104**: 125-141.

Stewart, B.W., and DePaolo, D.J. 1992. Diffusive Isotopic Contamination of Mafic Magma by Coexisting Silicic Liquid in the Muskox Intrusion. Science, **255**: 708-711.

Stewart, B.W., and DePaolo, D.J. 1995. Isotopic studies of processes in mafic magma chambers: III, The Muskox Intrusion, Northwest Territories, Canada. *In* Earth processes: Reading the isotopic code: Geophysical Monograph, **95**. *Edited by* A. Basu and S. Hart. American Geophysical Union, Washington, DC. pp.277-292.

Sun, S., and McDonough, W.F. 1989. Chemical and isotopic systematics of oceanic basalts: implications for mantle composition and processes. *In* Magmatism in the ocean basins, Geological Society Special Publication No. 42. *Edited by* S. S. Sun and W.F. McDonough. Geological Society of London. London, United Kingdom., pp.313-345.

Tatsumoto, M., Knight, R.J., and Allegre, C.J. 1973. Time differences in the formation of meteorites as determined from the ratio of lead 207 to lead 206. Science, **180**: 1279-1283.

Taylor, P.N., Moorbath, S., Goodwin, R., and Petrykowski, A.C. 1980. Crustal contamination as an indicator of the extent of early Archaean continental crust: Pb isotopic evidence from the late Archaean gneisses of West Greenland. Geochimica et Cosmochimica Acta, **44**: 1437-1453.

Taylor, R.N., Warneke, T., Milton, J.A., Croudace, I.W., Warwick, P.E. and Nesbitt, R.W. 2003. Multiple ion counting determination of plutonium isotope ratios using multi-collector ICP-MS. Journal of Analytical Atomic Spectrometry, **18**: 480-484.

Vandamme, D., Courtillot, V. and Besse, J. 1991. Paleomagnatism and age determinations of the Deccan Traps (India): results of a Nagpur-Bombay traverse and review of earlier work. Reviews of Geophysics, **29**: 159-190.

Vervoort, J.D., and Patchett, P.J. 1996. Behavior of hafnium and neodymium isotopes in the crust: constraints from Precambrian crustally derived granites. Geochimica et Cosmochimica Acta, **60**: 3717-3733.

Vervoort, J.D., and Toft, J.B. 1999. Evolution of the depleted mantle: Hf isotope evidence from juvenile rocks through time. Geochimica et Cosmochimica Acta, **63**: 533-556.

Vervoort, J.D., Patchett, P.J., Gehrels, G.E., and Nutman, A.P. 1996. Constraints on early Earth differentiation from hafnium and neodymium isotopes. Nature, **379**: 624-627.

White, R., and McKenzie, D. 1989. Magmatism at rift zones: the generation of volcanic continental margins and flood basalts. Journal of Geophysical Research, **94**: 7685-7729.

White, W.M., Hofmann, A.W., and Puchelt, H. 1987. Isotope geochemistry of Pacific Mid-Ocean Ridge basalt. Journal of Geophysical Research, **92**: 4881-4893.

Winter, J.D. 2001. *In* An Introduction to Igneous and Metamorphic Petrology. *Edited by* Winter, J.D. Prentice Hall, New Jersey. pp.697.

Woodhead, J. D., and Hergt, J. M. 2001. Strontium, neodymium and lead isotope analyses of NIST glass certified reference materials; SRM 610, 612, 614. Geostandards Newsletter, **25**: 261-266.

APPENDIX A – Petrographic Descriptions

NOTES:

All grain sizes estimated from longest diameter of the crystal
Coarse-grained = crystal diameters >5 mm
Medium-grained = crystal diameters = 1 – 5 mm
Fine-grained = crystal diameters <1 mm

Measurements are in mm unless otherwise stated.

Features seen in all thin sections include:
- Holocrystalline textures
- Generally ultramafic to mafic mineral assemblages

See text for further discussion.

Sample: MR-25
Location: Keel Dyke
Rock Type: GBN

Figure A.1 - Ppl, Mag: 4x

Figure A.2 - Xn, Mag: 4x

Major & Minor phases:

	Approx %	Min	Max	Ave	Crystal shape	Notes
Ol	1	0.25	0.75	0.3	subhedral	
Opx	40	0.1	3	1.25	anhedral	very fractured
Cpx	21	0.2	1	0.75	anhedral	
Plag	35	0.05	1.5	0.25	anhedral	Some slightly sericitized
Bt	1	0.05	0.25	0.1	anhedral	
Opaq	2	<.05	0.3	0.05	anhedral	

Accessories: Ap

Description:

- Non-cumulate
- Generally unaltered, although some olivines are quite serpentinized
- shows extremely weak compositional layering (of pyroxenes)
- subophitic texture
- large phenocrystic phase of opx, quite fractured, thin section contains many holes inside opx
- Biotites are closely associated with opaque minerals
- Opaq: ilm, chr, mag, cp, py
- Ol → Cpx → Plag just before Opx → Bt + Opaq

Sample: MR-14
Location: Keel Dyke
Rock Type: Ol-GBN

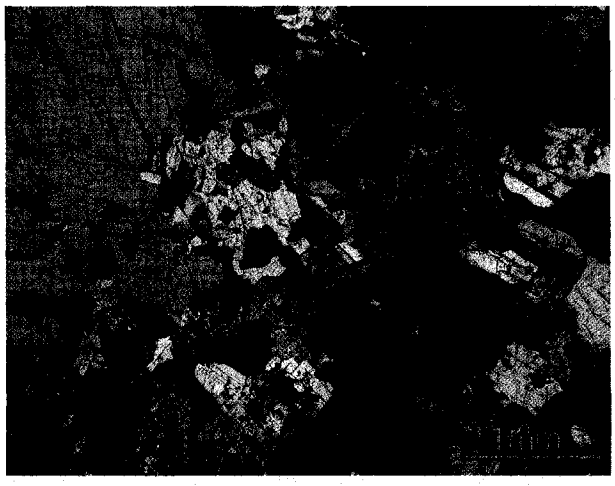

Figure A.3 - Xn, Mag: 4x

Figure A.4 - Xn, Mag: 4x

Major & Minor phases:

	Approx %	Min	Max	Ave	Crystal shape	Notes
Ol	23	0.1	1	0.3	subhedral	
Opx	13	1	6	4.6	anhedral	abundant cracks & holes
Cpx	22	0.2	2.3	0.5	anhedral	
Plag	38	0.2	1	0.5	anhedral	some centers altered to sericite
Bt	1	0.05	0.4	0.25	anhedral	
Opaq	3	<.1	0.5	0.1	anhedral	

Accessories: Bd

Description:

- Non-cumulate
- Generally unaltered, although some olivines are serpentinized, some have opaques in center
- large phenocrystic phase of opx, quite fractured, thin section contains many holes inside opx
- Biotites are closely associated with opaque minerals
- Minor spinel
- Opaq: chr, py, ilm,
- Ol → Cpx → Plag just before Opx → Bt + Opaq

Sample: LJ-24
Location: Keel Dyke
Rock Type: Ol-GBN

Figure A.5 - Xn, Mag: 10x

Figure A.6 - Xn, Mag: 4x

Major & Minor phases:

	Approx %	Min	Max	Ave	Crystal shape	Notes
Ol	25	0.1	0.7	0.3	subhedral	most look very fresh
Opx	20	5	8	6.5	anhedral	oikocryst phase
Cpx	18	0.25	0.75	0.5	anhedral	
Plag	36	0.05	1.75	0.25	anhedral	slightly sericitized
Bt	<1	0.05	0.25	0.1	anhedral	
Opaq	1	0.05	0.3	0.1	anhedral	

Accessories: Ap

Description:

- Non-cumulate, porphyritic (poikilitic) texture, ground mass is fine-grained
- Generally unaltered, although a few olivines are serpentinized, and some feldspars are sericitized
- subophitic texture
- large oikocrystic phase of opx contain inclusions of mainly plag, but also ol and cpx
- opx sometimes fractured, thin section contains some holes inside opx, some crystals show very small exsolution lamellae
- Opaq: ilm, cp, chr, py, mag
- Ol → Cpx → Plag just before Opx → Bt + Opaq

Sample: LJ-6
Location: Keel Dyke
Rock Type: GBN

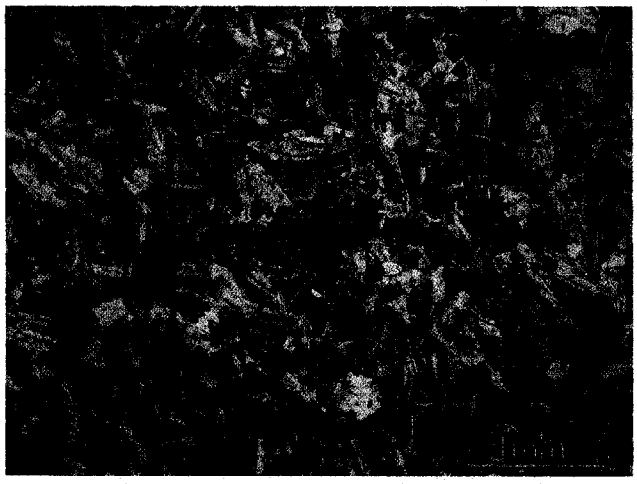

Figure A.7 - Xn, Mag: 4x

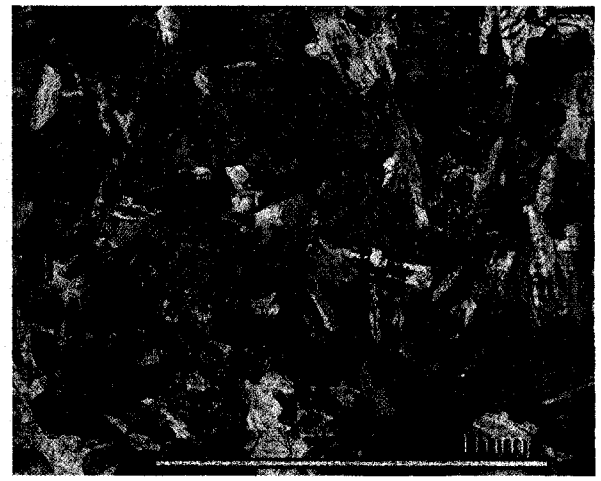

Figure A.8 - Xn, Mag: 10x

Major & Minor phases:

	Approx %	Min	Max	Ave	Crystal shape	Notes
Opx	10	0.1	1.25	1	anhedral	slightly larger in size
Cpx	40	0.1	0.8	0.3	anhedral	
Plag	46	0.1	0.75	0.25	anhedral	few are zoned
Bt	1	0.1	0.3	0.15	anhedral	
Opaq	3	0.1	1	0.25	anhedral	

Accessories: Bd, ~15 μm

Description:

- Non-cumulate
- subophitic texture
- some opx crystals show very small exsolution lamellae
- one grain of opx has corroded rims
- some minor alteration of plag to sericite
- Biotites are closely associated with opaque minerals
- Very minor chlorite seen throughout section
- Opaq: ilm, mag, py, sph
- plag → Cpx + Opx → - Opx(?) → Bt + Opaq

Sample: CR-6
Location: Keel Dyke
Rock Type: PIC

Figure A.9 - Xn, Mag: 4x

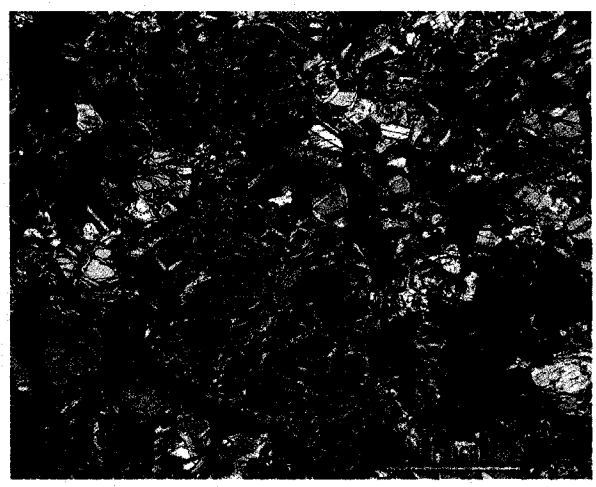

Figure A.10 - Xn, Mag: 4x

Major & Minor phases:

	Approx %	Min	Max	Ave	Crystal shape	Notes
Ol	35	0.25	1.25	0.5	subhedral	approx 50% altered to serp
Opx	19	1	12	5	anhedral	large oikocrysts
Cpx	38	0.1	0.6	0.5	anhedral	
Plag	5	0.1	0.4	0.2	subhedral	
Bt	1	0.2	0.4	0.25	anhedral	
Opaq	2	<.05	0.2	0.1	subhedral	

Accessories:

Description:

- Non-cumulate
- some minor alteration of plag to sericite
- Biotites are closely associated with opaque minerals
- minor chlorite seen throughout section along with serpentine, secondary alteration
- Ol → Cpx + Plag → Opx → Bt + Opaq

Sample: CR-46
Location: Keel Dyke
Rock Type: Ol-GBN

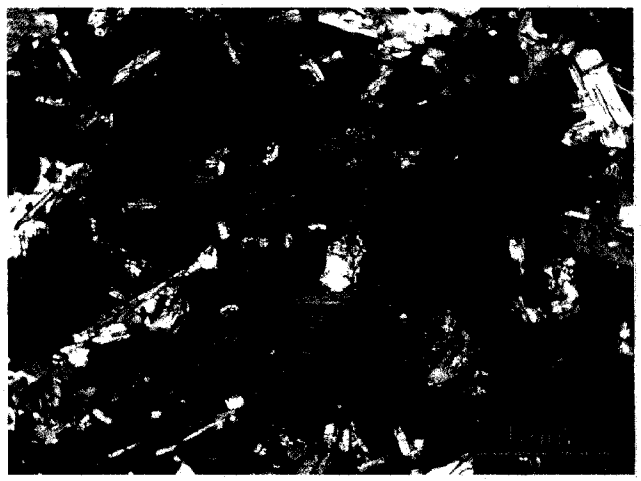

Figure A.11 - Xn, Mag: 4x

Figure A.12 - Xn, Mag: 4x

Major & Minor phases:

	Approx %	Min	Max	Ave	Crystal shape	Notes
Ol	20	0.2	1.25	0.5	subhedral	
Opx	25	4	8	6.5	anhedral	Large oikocrysts
Cpx	15	0.25	0.5	0.4	anhedral	
Plag	25	0.1	0.5	0.2	subhedral	
Bt	6	0.2	1.25	0.5	anhedral	
Opaq	4	<.1	0.75	0.1	anhedral	

Accessories: Ap, Znlt ~20 μm, Bd >50 μm

Description:

- Non-cumulate
- Large oikocrystic phase of Opx contains inclusions of all main phases
- some opx crystals show very small exsolution lamellae
- some minor alteration of plag to sericite
- Biotites are closely associated with opaque minerals
- Minor alteration of olivine to serpentine
- Minor chlorite throughout, associated with serpentine
- Opaq: ilm, py, chr, mag, pn,
- Ol → Cpx + plag → Bt → Opaq → Opx

Sample: CR-31
Location: Keel Dyke
Rock Type: Ol-GBN

Figure A.13 - Xn, Mag: 4x

Figure A.14 - Xn, Mag: 4x

Major & Minor phases:

	Approx %	Min	Max	Ave	Crystal shape	Notes
Ol	20	0.2	1	0.5	subhedral	
Opx	25	1	4	2	anhedral	some slightly zoned
Cpx	18	0.5	1.5	0.75	anhedral	
Plag	25	0.75	2	1	subhedral	
Bt	7	0.2	1.75	0.5	anhedral	
Opaq	3	0.1	1	0.4	anhedral	some blocky, some along fractures in bt

Accessories: Bd ~20 μm

Description:

- Non-cumulate
- Coarser-grained compared to other dyke samples
- some alteration of plag to sericite and of olivine to serpentine
- Some opaque minerals grow along fractures of bt, secondary mineral
- minor chlorite seen throughout section, some small veins
- Opaq: ilm, mag, py, pn
- Ol → Cpx + Opx+ Plag → Bt → Opaq → chl & serp alteration

Sample: EQ-22
Location: MC#1
Rock Type: Perid

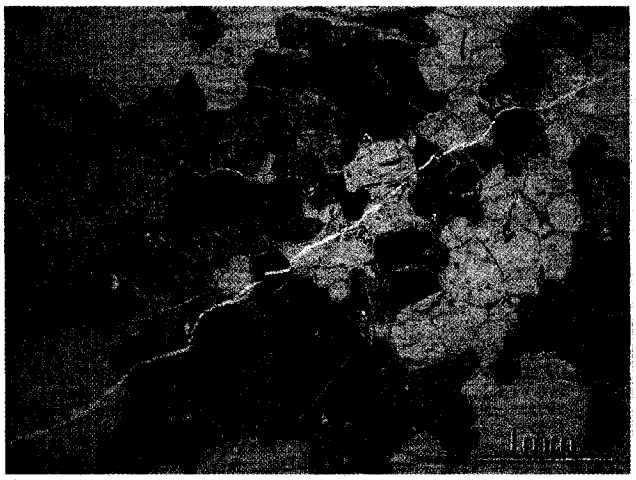

Figure A.15 - Ppl, Mag: 4x

Figure A.16 - Xn, Mag: 4x

Major & Minor phases:

	Approx %	Min	Max	Ave	Crystal shape	Notes
Ol	50	0.25	1	0.5	subhedral	completely replaced by serpentine
Opx	30	0.25	1	0.5	subhedral	altered
Cpx	19	0.25	1	0.5	subhedral	altered, twinning
Opaq	1			0.1	anhedral	most occur along cracks in ol, secondary growth

Accessories:

Description:

- Cumulate
- Sample is fairly altered
- Equigranular
- Ol → Cpx + Opx → Opaq

Sample: EQ-20
Location: MC#1
Rock Type: Cpxnite

Figure A.17 - Ppl, Mag: 4x

Figure A.18 - Xn, Mag: 4x

Major & Minor phases:

	Approx %	Min	Max	Ave	Crystal shape	Notes
Ol	27	0.25	3	1	subhedral	approx 90% are altered to serpentine
Cpx	70	0.25	1.5	0.75	subhedral	altered, twinning
Opaq	<1			<.05	subhedral	
Chl	3				anhedral	some veining
Opx	<1				subhedral	

Accessories:

Description:

- Cumulate
- Sample is fairly altered
- Equigranular
- Opaq: py, chr, ttn, pn
- Ol + Cpx → Opaq → Chl alteration

Sample: EQ-19
Location: Marginal MC#1
Rock Type: Ol-GBN

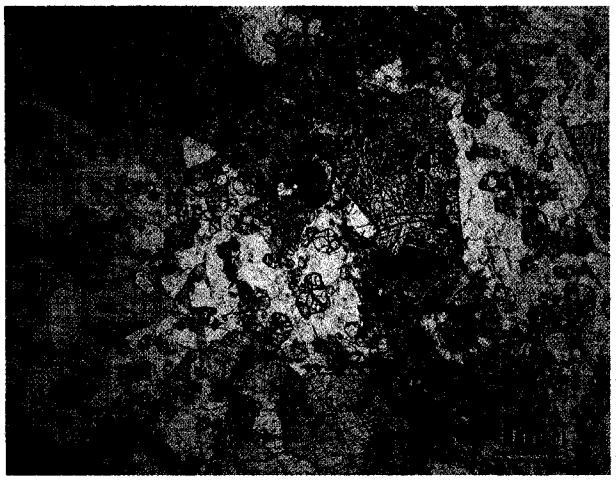

Figure A.19 - Ppl, Mag: 2x

Figure A.20 - Xn, Mag: 2x

Major & Minor phases:

	Approx %	Min	Max	Ave	Crystal shape	Notes
Ol	23	0.1	2	0.3	subhedral	
Opx	15	0.5	4	1	anhedral	some quite fractured with holes
Cpx	23	0.2	3	2	anhedral	many small inclusion of bt & opaq
Plag	35	0.25	6	2	anhedral	
Bt	2	0.1	1	0.25	anhedral	
Opaq	2	<.1	0.5	0.2	subhedral	
Chl	<1				anhedral	

Accessories: Znlt ~20 μm, Bd ~ 15 μm, Zr ~ 80 μm, Mon, Ap

Description:

- Non-cumulate
- some slight alteration of plag to sericite and of olivine to serpentine
- minor chlorite seen throughout section, minor veins of chlorite
- Oqaq: ilm, mag, py,
- Ol → Cpx + Opx→ Plag → Bt + Opaq → chl & serp alteration

Sample: EQ-15
Location: Marginal MC#1
Rock Type: MIGMA

Figure A.21 - Ppl, Mag: 4x

Figure A.22 - Xn, Mag: 4x

Major & Minor phases:

	Approx %	Min	Max	Ave	Crystal shape	Notes
Plag	5	<.1	0.4	0.25	anhedral	An & Ab
Bt	11	0.1	1	0.25	anhedral	
Opaq	1	<.1	0.6	0.25	subhedral to euhedral	
Spinel	3			<.1	subhedral to euhedral	hercynite
Qtz	5	0.1	1	0.3	anhedral	
Kspar	75	<.1	1.75	0.3	anhedral	

Accessories: Mon ~ >100 μm, Zr ~ <10 μm

Description:

- Non-cumulate, quite different from other samples
- Section shows curvy flow-like band of spinel
- some slight alteration of feldspars to sericite
- some minor muscovite also seen in section
- Opaq: ilm

Sample: EQ-14
Location: Marginal MC#1
Rock Type: PIC

Figure A.23 - Xn, Mag: 4x

Figure A.24 - Xn, Mag: 4x

Major & Minor phases:

	Approx %	Min	Max	Ave	Crystal shape	Notes
Ol	23	0.1	1.25	0.25	subhedral	approx 50% altered to serpentine
Opx	30	1.5	12	5.5	anhedral	some are cracked, while others are not, some show exsolution with cpx
Cpx	10	1.5	3	2.3	anhedral	some show exsolution with opx
Plag	25	0.3	6	2	anhedral	inclusions of all other minerals
Bt	8	0.1	4.5	0.75	anhedral	
Opaq	4	<.05	1.5	0.2	subhedral to anhedral	some occur along cracks in cleavage planes in bt, some are cube shaped
Chl	<1					

Accessories: Ap, Bd ~ 70 μm, Znlt ~70 μm

Description:

- Non-cumulate
- Minor chlorite veining
- Opaq: chr, ilm, pn
- Ol → Cpx + Opx→ Bt + Opaq → Plag → chl & serp alteration & Opaq growth along cracks

Sample: EQ-13
Location: Marginal MC#1
Rock Type: PIC

Figure A.25 - Xn, Mag: 4x

Figure A.26 - Xn, Mag: 4x

Major & Minor phases:

	Approx %	Min	Max	Ave	Crystal shape	Notes
Ol	25	0.1	1	0.25	subhedral	varying Fe contents, approx 50% altered to serp
Opx	35	0.75	6	2	subhedral to anhedral	some cracked, some not
Cpx	17	0.75	2.3	1	subhedral to anhedral	some zoned
Plag	17	0.75	5	3.5	subhedral to anhedral	
Bt	1	0.1	1.5	0.75	subhedral to anhedral	
Opaq	5	<.1	1	0.2	subhedral to anhedral	some replace olivines, some assoc with bt, some cubes

Accessories: Bd ~ 15 μm

Description:

- Non-cumulate
- Oqaq: chr, ilm, mag
- Ol → Cpx + Opx→ Bt + Opaq → Plag → chl & serp alteration & Opaq replacement of olivine

Sample: EQ-6
Location: Marginal MC#1
Rock Type: Ol-GBN

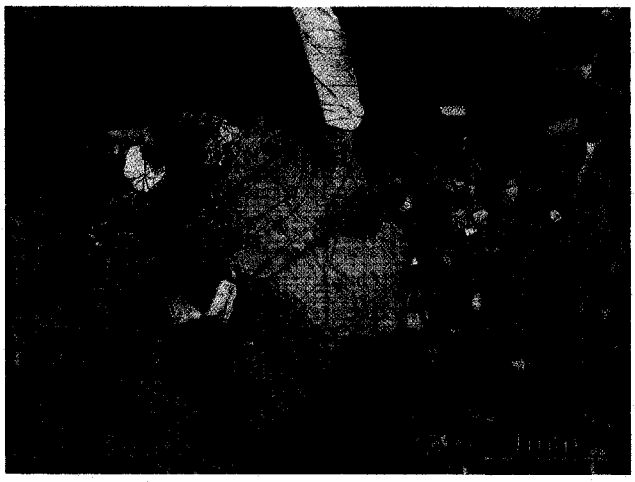

Figure A.27 - Xn, Mag: 4x

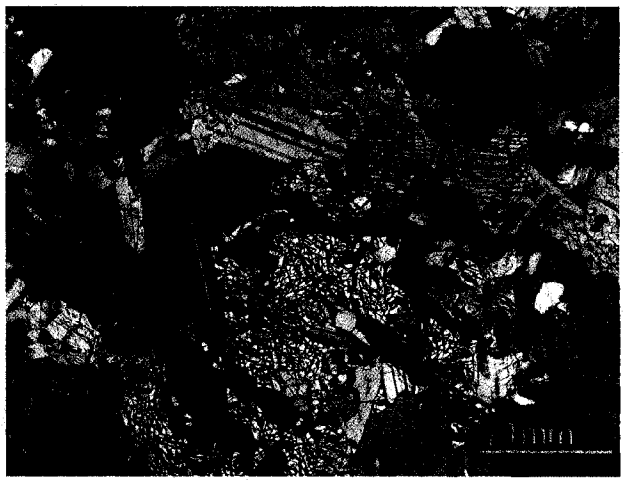

Figure A.28 - Xn, Mag: 4x

Major & Minor phases:

	Approx %	Min	Max	Ave	Crystal shape	Notes
Ol	15	0.2	1.25	0.5	subhedral	very few are altered, varying compositions
Opx	15	1	4	2.5	anhedral	some cracked with holes, some look very fresh, some are zoned
Cpx	12	0.25	2	1	anhedral	
Plag	50	0.25	2.3	0.4	subhedral	zoned, some sericitization
Bt	4	0.1	1	0.25	anhedral	
Opaq	4	<.1	1.25	0.25	anhedral to euhedral	some assoc with bt, some cubes, some

Accessories: Bd ~ 50 μm, Znlt ~20 μm

Description:

- Cumulate
- Opaq: ilm, py, chr
- Ol → Plag + Cpx + Opx → Bt → Opaq

Sample: ES-10
Location: MC#1
Rock Type: Perid

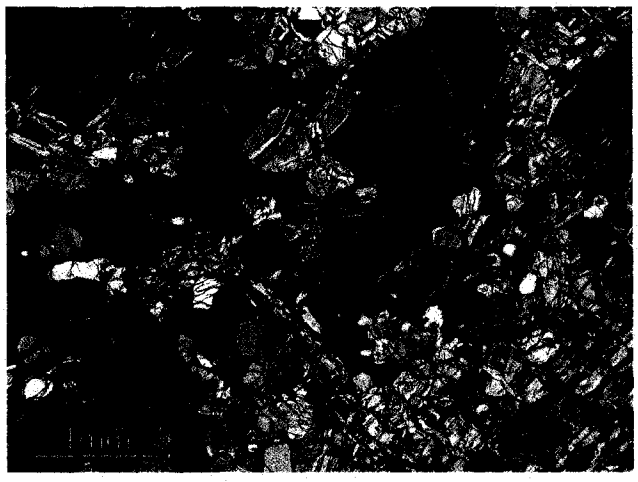

Figure A.29 - Xn, Mag: 4x

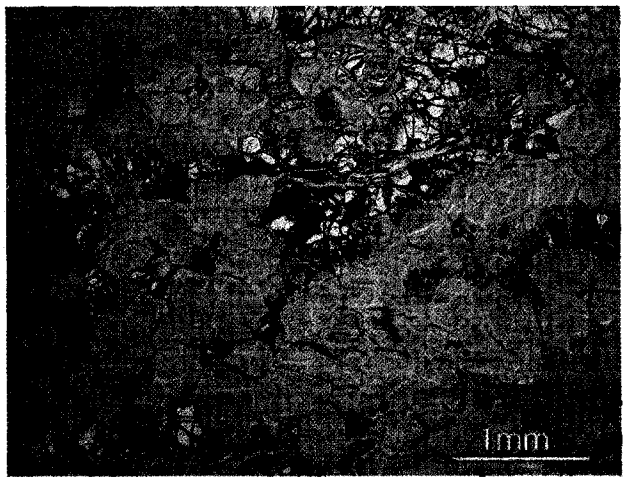

Figure A.30 - Ppl, Mag: 4x

Major & Minor phases:

	Approx %	Min	Max	Ave	Crystal shape	Notes
Ol	50	0.25	1.5	0.75	subhedral	approx. 70% altered to serpentine
Opx	8	4	7	5	anhedral	Oikocryst, with exsolution lamellae
Cpx	40	0.1	1	0.5	subhedral	
Bt	<1			<.1	anhedral	
Opaq	2			<.1	anhedral	some elongate & fill in cracks (secondary), few cube-shaped
Chl	<1			<.1	anhedral	

Accessories:

Description:

- Cumulate
- Shows weak foliation, compositional layering present – alternating olivine (serpentine) rich and pyroxene rich layers
- Ol → Cpx → Opx→ Bt + Opaq → chl & serp alteration & Opaq growth along cracks

Sample: VD-709
Location: MC#2
Rock Type: Cpxnite

Figure A.31 - Ppl, Mag: 4x

Figure A.32 - Xn, Mag: 4x

Major & Minor phases:

	Approx %	Min	Max	Ave	Crystal shape	Notes
Ol	25	0.25	1.25	0.75	subhedral	approx 85% altered to serpentine
Opx	<1				subhedral	
Cpx	70	0.2	1.25	0.75	subhedral	simple twinning, minor exsolution
Opaq	5	<.05	0.75	0.1	subhedral	

Accessories:

Description:

- Cumulate
- Equigranular
- Minor vermicular texture seen on rims of cpx
- Opaq: mag
- Ol → Cpx → Opaq & serp alteration

Sample: VD-707
Location: MC#2
Rock Type: Cpxnite

Figure A.33 - Ppl, Mag: 4x

Figure A.34 - Xn, Mag: 4x

Major & Minor phases:

	Approx %	Min	Max	Ave	Crystal shape	Notes
Ol	34	0.25	0.75	0.5	subhedral	completely serpentinized
Cpx	65	0.25	0.75	0.5	subhedral	
Opaq	1				anhedral	elongate & irregular, form in cracks, secondary

Accessories:

Description:

- Cumulate
- Equigranular
- Few minor chlorite veins
- Ol → Cpx → Opaq growth & serp alteration

Sample: SL-42
Location: MC#2
Rock Type: Ol-GBN

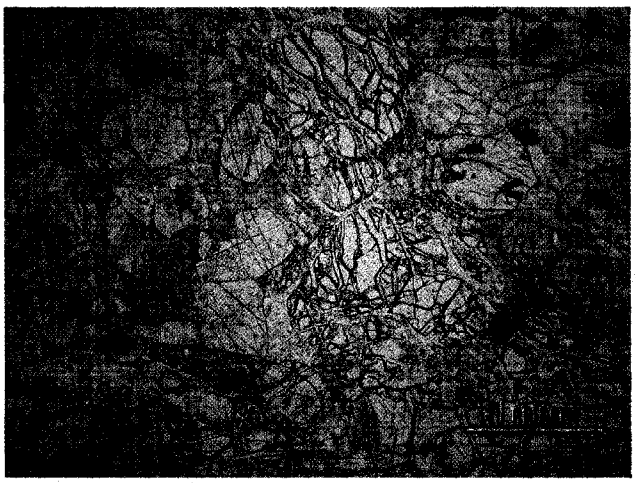

Figure A.35 - Ppl, Mag: 4x

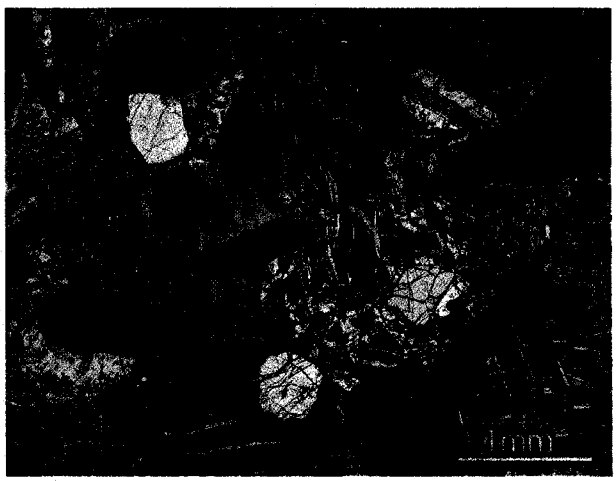

Figure A.36 - Xn, Mag: 4x

Major & Minor phases:

	Approx %	Min	Max	Ave	Crystal shape	Notes
Ol	10	0.25	2	0.75	subhedral	approx 25% altered to serpentine
Cpx	60	0.25	2	0.75	subhedral	
Plag	30	0.2	1	0.5	subhedral	fairly altered to sericite
Opaq	<<1					growth in cracks

Accessories:

Description:

- Cumulate
- Equigranular
- Opaq: py,
- Ol → Cpx → Plag → Opaq + serp alteration

Sample: VD-722
Location: MC#3
Rock Type: Cpxnite

Figure A.37 - Ppl, Mag: 4x

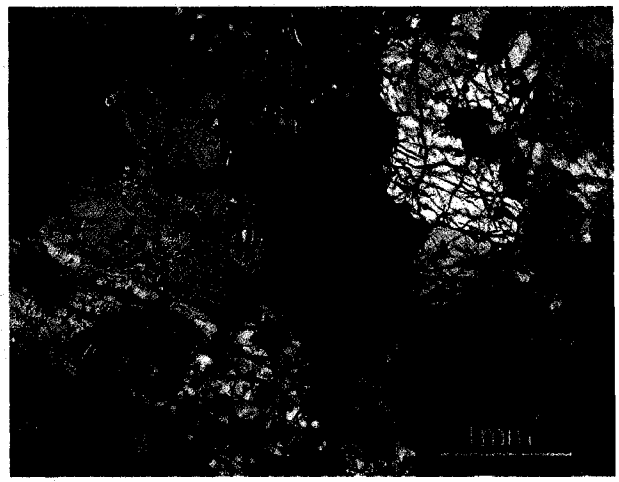

Figure A.38 - Xn, Mag: 4x

Major & Minor phases:

	Approx %	Min	Max	Ave	Crystal shape	Notes
Ol	35	0.5	2	1	subhedral	almost completely altered to serp
Opx	3	0.75	2.75	1	subhedral	cracked
Cpx	54	2	4	2.75	anhedral	some quite altered, simple twinning
Bt	<1			0.2	anhedral	
Ttn	8			0.5	euhedral to anhedral	some cubes, some filling in cracks

Accessories:

Description:

- Cumulate
- Equigranular
- Some cores of cpx's are quite altered, while rims are more fresh
- Grain boundaries of cpx's are rather sutured
- Some small veins of chlorite and other dark minerals present
- Ol → Cpx + Opx→ ttn → Bt + Opaq + serp alteration

Sample: VD-724
Location: MC#3
Rock Type: Cpxnite

Figure A.39 - Xn, Mag: 4x

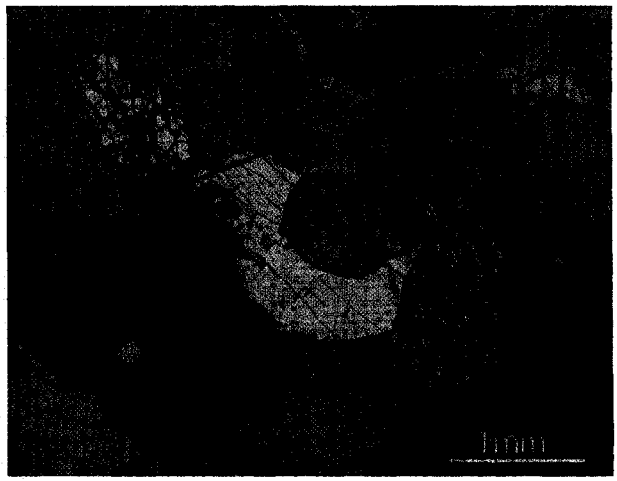

Figure A.40 - Xn, Mag: 4x

Major & Minor phases:

	Approx %	Min	Max	Ave	Crystal shape	Notes
Ol	10	0.3	3	0.5	euhedral	approx 25% altered to serp
Opx	5	0.75	3	1	subhedral	have inclusions of ol & cpx
Cpx	83	0.2	4	0.7	anhedral	some fractures, simple twinning, exsolution
Bt	<1			<.05	anhedral	
Opaq	1			<.1	euhedral & anhedral	some cubes, some filling in cracks
Chl	<<1			<.05	anhedral	
Ttn	1				anhedral	

Accessories:

Description:

- Cumulate
- Equigranular
- Bears resemblance to VD-722, although not as altered
- Grain boundaries of cpx's are rather sutured
- Opaq: chr, py, pn
- Ol → Cpx → Opx→ ttn → Bt + Opaq + serp alteration

Sample: V1-01
Location: MC#3
Rock Type: Perid

Figure A.41 - Ppl, Mag: 10x

Figure A.42 - Xn, Mag: 10x

Major & Minor phases:

	Approx %	Min	Max	Ave	Crystal shape	Notes
Ol	96	0.2	1.25	0.75	euhedral to subhedral	completely serpentinized
Bt	<1			0.2	anhedral	could all be secondary
Opaq	4	0.05	0.75	0.2	anhedral	secondary growth
Chl	<1				anhedral	

Accessories:

Description:

- Cumulate
- Sample is quite altered
- Opaq: mag, chr
- Ol → Bt + Opaq + serp alteration

Sample: V1-02
Location: MC#3
Rock Type: Cpxnite

Figure A.43 - Ppl, Mag: 4x

Figure A.44 - Xn, Mag: 4x

Major & Minor phases:

	Approx %	Min	Max	Ave	Crystal shape	Notes
Ol	25	0.25	5	0.6	euhedral	approx 75% altered to serp
Opx	2			7	anhedral	exsolution, oikocryst with inclusions of ol, cpx
Cpx	71	0.25	3	0.75	subhedral	exsolution
Bt	<1	0.05	2	0.25		secondary?
Opaq	2	<.05	0.25	0.1		secondary, forming along cracks
Chl	<1					minor, assoc with bt & opaq & serp

Accessories: Ap (chlorapatite)

Description:

- Hetero-cumulate texture
- Large oikocrystic phase of opx contains inclusions of all main phases
- some opx crystals show very small exsolution lamellae
- some edges of cpx grains are very sutured
- Opaq: chr, mag, pn
- Ol → Cpx → Opx → Bt + Opaq

Sample: V1-05
Location: MC#3
Rock Type: Dunite

Figure A.45 - Ppl, Mag: 4x

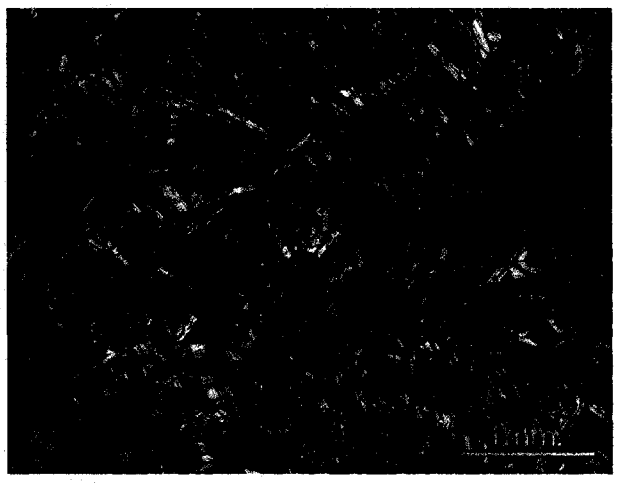

Figure A.46 - Xn, Mag: 4x

Major & Minor phases:

	Approx %	Min	Max	Ave	Crystal shape	Notes
Ol	96	0.5	1	0.75	euhedral	completely serpentinized
Bt	<1					
Opaq	4	<.1	0.5	0.3	anhedral	most in cracks, some round
Chl	<1					
Mus	<1					

Accessories:

Description:

- Cumulate
- Sample is quite altered
- Ol + Opaq → Bt + Opaq + serp alteration

Sample: V1-10
Location: MC#3
Rock Type: Perid

Figure A.47 - Ppl, Mag: 4x

Figure A.48 - Xn, Mag: 4x

Major & Minor phases:

	Approx %	Min	Max	Ave	Crystal shape	Notes
Ol	90	0.25	1	0.5	subhedral	completely serpentinized
Bt	1	0.1	1	0.3	anhedral	
Opaq	9				anhedral	occurs in cracks, along grain boundaries
Chl	<1					

Accessories:

Description:

- Cumulate
- Sample is quite altered
- Ol → Bt + Opaq + serp alteration

Sample: V3-03
Location: MC#3
Rock Type: Webst

Figure A.49- Xn, Mag: 4x, FOV= 5.5mm

Figure A.50 - Xn, Mag: 4x, FOV= 5.5mm

Major & Minor phases:

	Approx %	Min	Max	Ave	Crystal shape	Notes
Ol	3	1	4	2	subhedral	5% altered to serpentine
Opx	7	1	4.5	2	anhedral	grains have cracks and holes, exsolution texture
Cpx	83	0.5	3	0.8	anhedral	exsolution lamellae seen in cores
Plag	7	0.2	2	0.75	anhedral	zoning?

Accessories: Ap

Description:

- Adcumulate texture
- Cores of cpx crystals show very small exsolution lamellae
- some edges of cpx grains are very sutured
- some alkali feldspar present
- Opaq: py, ilm, chr,
- Ol → Cpx + Opx → Plag

Sample: VD-850
Location: MC#4
Rock Type: Opxnite

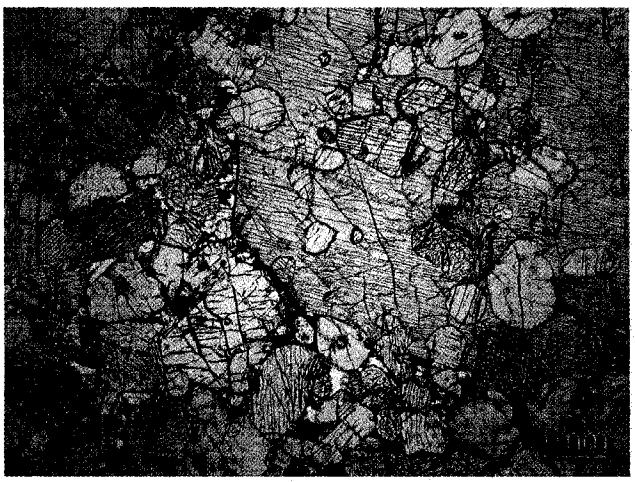

Figure A.51 - Ppl, Mag: 2x

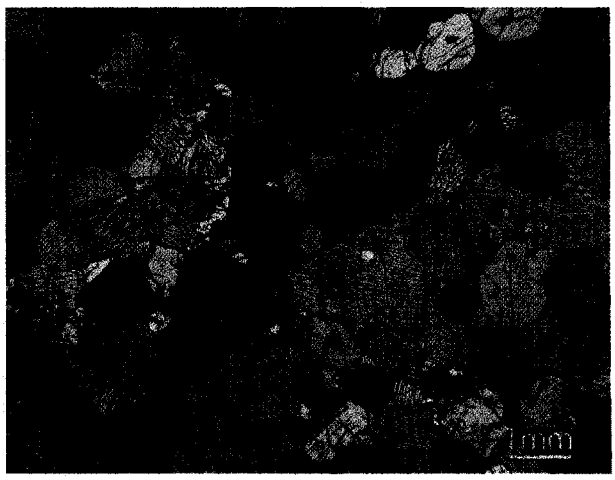

Figure A.52 - Xn, Mag: 2x

Major & Minor phases:

	Approx %	Min	Max	Ave	Crystal shape	Notes
Opx	85	0.3	3	6	euhedral to subhedral	some are altered to talc?
Cpx	10	5	7	6	subhedral	oikocryst phase with inclusions of opx, simple twinning
Plag	5	0.2	1.25	0.5	anhedral	some altered to sericite
Bt	<1			<.1	anhedral	seems to fill intersitial places
Opaq	<1	<.1	1	0.2	anhedral	seems to fill intersitial places

Accessories: Rt, Ap, Zr ~30 μm

Description:

- Heteroadcumulate texture
- Opaq: ilm, py, chr, sph
- Opx + Plag → Cpx + Opx → opaq + bt

Sample: M-26
Location: MC#4
Rock Type: GRPHYR

Figure A.53 - Xn, Mag: 10x

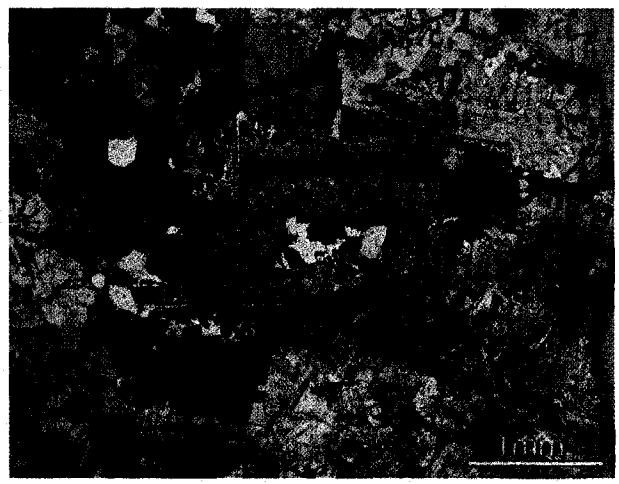

Figure A.54 - Xn, Mag: 4x

Major & Minor phases:

	Approx %	Min	Max	Ave	Crystal shape	Notes
Ksp	67	0.1	6	0.75	subhedral	rimmed with altered anorthite
Bt	10	0.1	2.5	0.5	anhedral	assoc with qtz
Opaq	4	0.1	4	0.75	subhedral	needles
Chl	3	0.1	0.5	0.25	anhedral	
Amp	8	0.5	4	0.1	anhedral	green & blue
Qtz	8	0.1	0.5	0.3	anhedral	sympletic intergrowth with ksp

Accessories: Mon >1000 μm, Bd >10 μm, Zr ~25 μm

Description:

- Non-cumulate, granophyric texture
- Sympletic intergrowth of qtz & ksp
- Opaq: ilm, sph, py,
- Ksp → -Ksp + An → -An
- → Opaq + Bt + Qtz + Amp

Appendix B – Mineral Chemistry

The following charts contain electron microprobe (EMP) chemical analyses of the major minerals for 20 samples from the Muskox Intrusion and the Keel Dyke. Whole rock samples were sectioned and the constituent minerals analyzed using the electron microprobe (JEOL 8900) at the University of Alberta. Chemical analyses are separated by mineral.

Olivine

Sample	EQ-19	EQ-19	EQ-19	EQ-19	EQ-19	EQ-19	EQ-19	EQ-19	EQ-19	EQ-19	EQ-19	EQ-20	EQ-20
Grain	1	1	2	2	2	3	3	3	4	4	4	1	1
Location	core	rim	core	core	rim	core	core	rim	core	core	rim	core	core
TiO_2	0.00	0.00	0.04	0.00	0.00	0.00	0.00	0.01	0.00	0.00	0.00	0.00	0.00
SiO_2	38.30	38.77	37.41	37.44	37.26	37.91	38.16	37.87	38.17	38.14	37.94	38.96	38.76
CaO	0.05	0.05	0.05	0.01	0.02	0.02	0.03	0.06	0.04	0.03	0.07	0.07	0.08
Na_2O	0.02	0.02	0.01	0.00	0.00	0.00	0.00	0.00	0.01	0.00	0.00	0.01	0.00
FeO	24.18	23.78	29.83	30.16	31.10	26.05	26.56	26.58	22.28	22.34	22.51	18.59	18.43
Cl	0.02	0.00	0.00	0.00	0.05	0.00	0.01	0.00	0.00	0.00	0.00	0.00	0.04
MgO	38.90	39.49	35.24	34.57	34.24	37.53	37.38	37.39	41.04	40.99	40.55	43.64	43.71
K_2O	0.00	0.02	0.01	0.03	0.01	0.00	0.01	0.01	0.01	0.00	0.02	0.00	0.00
Al_2O_3	0.00	0.03	0.01	0.09	0.00	0.03	0.03	0.03	0.01	0.02	0.03	0.05	0.04
MnO	0.29	0.28	0.31	0.31	0.31	0.27	0.32	0.29	0.27	0.26	0.24	0.20	0.21
P_2O_5	0.00	0.00	0.03	0.00	0.05	0.00	0.03	0.00	0.06	0.00	0.01	0.01	0.02
F	0.02	0.02	0.01	0.00	0.00	0.00	0.00	0.01	0.03	0.00	0.00	0.01	0.02
Cr_2O_3	0.01	0.00	0.01	0.01	0.00	0.00	0.00	0.00	0.00	0.02	0.00	0.02	0.01
Total	101.77	102.44	102.98	102.62	103.03	101.80	102.53	102.24	101.90	101.80	101.37	101.55	101.29

Sample	EQ-20	EQ-20	EQ-20	EQ-20	EQ-20	EQ-20	EQ-20	EQ-14	EQ-14	EQ-14	EQ-14	EQ-14	EQ-14
Grain	1	2	2	2	3	3	3	1	1	1	2	2	3
Location	rim	core	core	rim	core	core	rim	core	core	rim	core	rim	core
TiO_2	0.00	0.00	0.00	0.00	0.00	0.00	0.04	0.00	0.01	0.00	0.00	0.00	0.00
SiO_2	38.98	39.23	39.06	39.21	38.89	38.91	38.26	38.06	38.12	38.04	37.94	38.15	38.26
CaO	0.08	0.09	0.06	0.08	0.06	0.08	0.08	0.04	0.04	0.02	0.04	0.00	0.04
Na_2O	0.00	0.00	0.01	0.00	0.01	0.02	0.00	0.00	0.03	0.00	0.03	0.01	0.03
FeO	18.47	18.33	18.16	18.50	18.53	18.33	18.43	22.62	22.75	22.29	22.92	22.76	23.42
Cl	0.00	0.00	0.01	0.02	0.00	0.04	0.00	0.00	0.00	0.05	0.01	0.00	0.01
MgO	43.89	43.92	43.57	43.70	44.03	42.94	42.77	39.93	39.51	39.72	39.68	39.94	39.09
K_2O	0.01	0.00	0.01	0.01	0.00	0.00	0.01	0.00	0.01	0.01	0.02	0.02	0.00
Al_2O_3	0.03	0.03	0.01	0.03	0.03	0.00	0.05	0.00	0.02	0.00	0.00	0.02	0.00
MnO	0.24	0.21	0.20	0.21	0.22	0.22	0.22	0.26	0.25	0.28	0.24	0.24	0.27
P_2O_5	0.00	0.01	0.00	0.00	0.05	0.04	0.03	0.00	0.05	0.00	0.00	0.01	0.03
F	0.04	0.00	0.00	0.02	0.02	0.02	0.00	0.00	0.00	0.01	0.00	0.00	0.01
Cr_2O_3	0.01	0.01	0.04	0.01	0.02	0.01	0.02	0.00	0.00	0.01	0.00	0.00	0.00
Total	101.73	101.82	101.12	101.78	101.86	100.60	99.91	100.91	100.77	100.40	100.87	101.14	101.14

Sample	EQ-14	CR-46	CR-46	CR-46	EQ-13	EQ-13	EQ-13	EQ-13	EQ-13	EQ-6	EQ-6	EQ-6	MR-14
Grain	3	1	1	3	2	1	1	3	3	3	3	4	1
Location	rim	core	rim	core	core	core	rim	core	rim	core	rim	core	core
TiO_2	0.00	0.01	0.00	0.00	0.00	0.37	0.43	0.00	0.03	0.01	0.00	0.00	0.01
SiO_2	38.06	37.53	37.76	37.77	37.39	53.86	54.04	38.18	38.45	38.27	38.36	37.94	37.67
CaO	0.03	0.04	0.04	0.03	0.03	2.28	2.16	0.04	0.09	0.04	0.07	0.03	0.05
Na_2O	0.00	0.01	0.00	0.00	0.02	0.01	0.02	0.00	0.00	0.03	0.01	0.00	0.01
FeO	23.05	26.06	26.69	26.45	26.10	12.43	12.74	22.52	22.18	23.08	23.24	28.62	24.23
Cl	0.03	0.01	0.00	0.01	0.00	0.01	0.00	0.00	0.02	0.00	0.00	0.01	0.00
MgO	38.91	37.43	37.55	37.36	37.46	28.80	28.64	40.37	40.59	40.13	39.72	36.26	39.35
K_2O	0.02	0.01	0.02	0.00	0.01	0.01	0.00	0.01	0.01	0.01	0.00	0.00	0.02
Al_2O_3	0.00	0.03	0.01	0.00	0.00	1.93	1.76	0.03	0.02	0.02	0.00	0.01	0.03
MnO	0.28	0.32	0.30	0.31	0.27	0.20	0.23	0.27	0.27	0.26	0.27	0.32	0.29
P_2O_5	0.00	0.03	0.03	0.03	0.00	0.02	0.05	0.07	0.03	0.01	0.04	0.00	0.02
F	0.06	0.00	0.00	0.00	0.04	0.00	0.04	0.00	0.00	0.00	0.00	0.00	0.00
Cr_2O_3	0.01	0.02	0.02	0.00	0.02	0.51	0.44	0.00	0.02	0.01	0.00	0.01	0.00
Total	100.41	101.50	102.42	101.95	101.33	100.42	100.54	101.49	101.72	101.86	101.71	103.20	101.66

Sample	MR-14	V1-02	V1-02	V1-02	V1-02	V1-02	V1-02	VD-724	VD-724	SL-42	SL-42	SL-42	SL-42
Grain	2	1	1	2	2	3	3	1	1	1	1	2	2
Location	rim	core	core	core	rim	core	rim		rim	core	rim	core	rim
TiO_2	0.00	0.00	0.00	0.00	0.00	0.00	0.00	0.01	0.00	0.02	0.00	0.00	0.00
SiO_2	37.70	39.57	39.50	39.46	38.33	39.74	39.36	39.43	39.52	39.87	39.77	40.15	39.48
CaO	0.06	0.03	0.03	0.06	0.06	0.06	0.03	0.06	0.05	0.09	0.07	0.06	0.09
Na_2O	0.03	0.00	0.00	0.03	0.01	0.01	0.00	0.00	0.00	0.00	0.00	0.02	0.03
FeO	24.91	15.51	15.41	15.71	15.54	15.62	15.55	17.42	17.41	15.25	15.08	15.25	15.23
Cl	0.00	0.00	0.00	0.00	0.00	0.01	0.00	0.01	0.00	0.00	0.00	0.00	0.05
MgO	38.55	45.90	45.86	45.87	44.99	46.05	46.28	44.23	44.57	46.08	46.38	46.07	46.31
K_2O	0.02	0.01	0.00	0.01	0.01	0.01	0.02	0.01	0.00	0.00	0.02	0.01	0.01
Al_2O_3	0.02	0.00	0.03	0.01	0.01	0.00	0.04	0.02	0.03	0.00	0.00	0.00	0.00
MnO	0.28	0.16	0.17	0.19	0.19	0.17	0.16	0.19	0.19	0.20	0.18	0.21	0.20
P_2O_5	0.02	0.00	0.01	0.00	0.01	0.04	0.02	0.01	0.00	0.00	0.00	0.01	0.02
F	0.00	0.01	0.02	0.00	0.00	0.05	0.04	0.00	0.00	0.00	0.02	0.00	0.01
Cr_2O_3	0.00	0.02	0.02	0.03	0.02	0.01	0.02	0.02	0.01	0.02	0.01	0.01	0.02
Total	101.60	101.20	101.05	101.36	99.16	101.73	101.48	101.41	101.78	101.54	101.52	101.79	101.43

Sample	SL-42	VD-709	VD-709	VD-709	VD-709	VD-709	VD-709	V3-03	V3-03	V3-03	V3-03
Grain	3	1	1	2	2	3	3	1	1	2	2
Location	rim	core	rim			core	rim	core	rim	core	rim
TiO_2	0.00	0.00	0.00	0.00	0.00	0.00	0.00	0.00	0.00	0.00	0.00
SiO_2	35.63	39.78	39.49	39.50	39.47	39.12	38.86	38.09	38.26	38.29	38.52
CaO	0.06	0.03	0.03	0.06	0.03	0.06	0.02	0.08	0.05	0.09	0.07
Na_2O	0.01	0.00	0.00	0.01	0.00	0.00	0.00	0.00	0.00	0.00	0.02
FeO	15.42	14.28	14.21	14.29	14.30	14.08	14.05	19.39	19.08	19.09	19.02
Cl	0.00	0.00	0.00	0.00	0.00	0.00	0.03	0.00	0.01	0.00	0.00
MgO	46.34	47.13	46.59	47.04	46.12	46.81	46.46	42.81	42.61	42.66	42.64
K_2O	0.01	0.01	0.01	0.00	0.01	0.01	0.01	0.01	0.01	0.01	0.01
Al_2O_3	0.02	0.01	0.00	0.00	0.02	0.02	0.02	0.00	0.02	0.00	0.00
MnO	0.20	0.16	0.17	0.18	0.18	0.15	0.17	0.22	0.23	0.25	0.24
P_2O_5	0.00	0.00	0.00	0.04	0.00	0.00	0.00	0.00	0.00	0.01	0.01
F	0.00	0.01	0.00	0.00	0.02	0.00	0.00	0.01	0.00	0.00	0.01
Cr_2O_3	0.01	0.04	0.01	0.02	0.02	0.01	0.01	0.02	0.00	0.04	0.03
Total	97.71	101.43	100.50	101.12	100.18	100.26	99.63	100.62	100.27	100.44	100.57

Plagioclase

Sample	EQ-19	EQ-19	EQ-19	EQ-19	EQ-14	EQ-14	EQ-14	EQ-14	CR-31	CR-31	CR-31	CR-31	CR-46	CR-46
Grain	1	1	1	1	1	1	2	2	1	1	2	2	1	1
Location					core	rim	core	rim	core	rim	core	rim	core	rim
TiO_2	0.00	0.01	0.02	0.03	0.03	0.06	0.04	0.00	0.02	0.06	0.00	0.00	0.00	0.00
SiO_2	50.43	50.54	50.48	50.66	51.18	52.09	51.64	52.09	50.63	51.47	50.06	50.46	48.63	46.27
CaO	14.36	14.14	14.13	14.09	12.57	12.41	12.60	12.60	13.30	12.83	14.01	14.14	15.01	12.52
Na_2O	3.29	3.49	3.46	3.41	4.26	4.37	4.25	4.36	3.57	3.88	3.44	3.31	2.61	2.34
FeO	0.66	0.69	0.56	0.68	0.26	0.41	0.29	0.45	0.49	0.52	0.36	0.43	0.35	2.75
Cl	0.00	0.02	0.08	0.00	0.01	0.00	0.01	0.00	0.02	0.01	0.00	0.05	0.02	0.01
MgO	0.11	0.11	0.06	0.15	0.03	0.02	0.01	0.02	0.01	0.02	0.04	0.00	0.07	2.33
K_2O	0.20	0.23	0.26	0.22	0.24	0.22	0.23	0.19	0.23	0.26	0.20	0.19	0.15	0.25
Al_2O_3	31.95	31.82	32.17	31.50	30.84	30.76	31.19	31.13	31.42	31.04	32.40	32.33	32.88	31.03
MnO	0.00	0.00	0.00	0.00	0.00	0.00	0.00	0.00	0.00	0.01	0.01	0.00	0.01	0.03
P_2O_5	0.00	0.01	0.00	0.03	0.02	0.00	0.01	0.00	0.01	0.02	0.04	0.06	0.03	0.01
F	0.07	0.00	0.01	0.01	0.04	0.00	0.00	0.00	0.01	0.00	0.00	0.00	0.00	0.00
Cr_2O_3	0.00	0.00	0.00	0.00	0.00	0.00	0.00	0.01	0.00	0.00	0.00	0.00	0.00	0.04
Total	101.04	101.04	101.19	100.77	99.46	100.34	100.27	100.83	99.69	100.11	100.55	100.95	99.76	97.57

An	70.66	69.15	69.30	69.54	61.99	61.08	62.10	61.51	67.32	64.63	69.22	70.22	76.05	74.76
Ab	29.34	30.85	30.70	30.46	38.01	38.92	37.90	38.49	32.68	35.37	30.78	29.78	23.95	25.24

Sample	CR-46	CR-46	CR-46	LJ-6	LJ-6	LJ-6	LJ-6	LJ-6	EQ-15	EQ-15	EQ-15	EQ-15	EQ-13	EQ-13
Grain	2	2	3	1	2	2	3	3	1	1	2	2	1	1
Location	core		core	core	core	rim	core	rim	core	rim	core	rim	core	rim
TiO_2	0.08	0.07	0.05	0.00	0.02	0.03	0.06	0.06	0.00	0.00	0.01	0.01	0.07	0.07
SiO_2	51.14	53.65	49.11	51.24	51.20	52.05	49.53	52.36	58.17	56.92	54.83	58.00	53.33	54.51
CaO	13.32	11.18	14.44	13.28	12.92	12.34	14.30	12.17	7.51	8.52	10.21	7.76	11.25	10.42
Na_2O	3.71	4.57	2.96	3.79	3.90	4.32	3.14	4.32	7.20	6.56	5.59	7.01	4.89	5.33
FeO	0.27	0.26	0.31	0.69	0.56	0.56	0.45	0.76	0.07	0.12	0.08	0.07	0.25	0.23
Cl	0.02	0.01	0.01	0.00	0.09	0.04	0.01	0.01	0.01	0.03	0.00	0.00	0.02	0.01
MgO	0.02	0.01	0.02	0.19	0.02	0.01	0.04	0.07	0.00	0.00	0.00	0.00	0.01	0.05
K_2O	0.30	0.48	0.20	0.17	0.19	0.24	0.18	0.28	0.32	0.25	0.22	0.31	0.31	0.36
Al_2O_3	31.33	29.40	32.16	31.11	30.74	29.84	31.86	29.63	26.85	27.79	29.23	26.66	29.76	28.83
MnO	0.00	0.00	0.00	0.01	0.01	0.00	0.01	0.01	0.02	0.00	0.01	0.01	0.02	0.00
P_2O_5	0.02	0.00	0.00	0.02	0.03	0.03	0.00	0.01	0.01	0.06	0.05	0.06	0.00	0.01
F	0.00	0.04	0.00	0.01	0.06	0.00	0.00	0.00	0.00	0.02	0.00	0.00	0.00	0.00
Cr_2O_3	0.00	0.00	0.00	0.00	0.00	0.00	0.00	0.00	0.01	0.00	0.00	0.01	0.01	0.01
Total	100.20	99.66	99.27	100.49	99.68	99.45	99.58	99.66	100.16	100.24	100.22	99.90	99.90	99.82

An	66.50	57.46	72.93	65.95	64.69	61.24	71.58	60.91	36.57	41.76	50.22	37.96	55.97	51.93
Ab	33.50	42.54	27.07	34.05	35.31	38.76	28.42	39.09	63.43	58.24	49.78	62.04	44.03	48.07

Sample	EQ-13	EQ-13	EQ-13	EQ-13	EQ-13	EQ-13	EQ-6	EQ-6	EQ-6	EQ-6	EQ-6	EQ-6	LJ-24	LJ-24
Grain	1	1	2	2	3	3	1	1	2	2	3	3	1	1
Location	core	rim	core	rim	core	rim	core	rim	core	rim	core	rim	core	rim
TiO_2	0.03	0.07	0.03	0.02	0.00	0.01	0.05	0.11	0.00	0.05	0.06	0.05	0.00	0.07
SiO_2	55.90	55.65	50.44	50.16	50.62	50.67	52.30	51.90	51.88	51.08	50.45	53.53	47.54	51.62
CaO	9.17	9.34	13.63	13.43	13.69	13.61	12.24	12.24	11.64	13.41	13.79	11.21	16.02	12.84
Na_2O	5.97	5.92	3.46	3.56	3.44	3.54	4.56	4.44	4.42	3.79	3.57	5.14	2.20	3.99
FeO	0.22	0.38	0.34	0.53	0.30	0.35	0.32	0.38	0.46	0.30	0.31	0.40	0.51	0.65
Cl	0.00	0.03	0.00	0.08	0.00	0.01	0.13	0.00	0.06	0.01	0.00	0.01	0.00	0.00
MgO	0.03	0.01	0.02	0.01	0.02	0.04	0.01	0.02	0.03	0.00	0.01	0.03	0.04	0.06
K_2O	0.43	0.44	0.24	0.39	0.20	0.19	0.25	0.21	0.31	0.17	0.14	0.29	0.10	0.21
Al_2O_3	27.82	28.24	31.74	31.40	32.29	31.85	30.64	30.57	30.39	31.52	31.69	29.42	33.42	30.64
MnO	0.00	0.01	0.00	0.00	0.01	0.00	0.00	0.00	0.01	0.00	0.01	0.00	0.01	0.01
P_2O_5	0.04	0.02	0.01	0.00	0.02	0.04	0.00	0.01	0.01	0.03	0.00	0.02	0.00	0.02
F	0.00	0.04	0.01	0.00	0.00	0.05	0.06	0.00	0.00	0.00	0.00	0.00	0.02	0.06
Cr_2O_3	0.00	0.00	0.00	0.02	0.00	0.00	0.02	0.00	0.00	0.02	0.00	0.00	0.00	0.00
Total	99.61	100.12	99.92	99.58	100.59	100.33	100.53	99.90	99.19	100.38	100.03	100.11	99.85	100.13

An	45.92	46.58	68.56	67.59	68.72	68.02	59.72	60.37	59.29	66.17	68.09	54.63	80.10	64.02
Ab	54.08	53.42	31.44	32.41	31.28	31.98	40.28	39.63	40.71	33.83	31.91	45.37	19.90	35.98

Sample	LJ-24	LJ-24	LJ-24	LJ-24	MR-25	MR-25	MR-25	MR-25	VD-850	VD-850	VD-850	VD-850	VD-850	VD-850
Grain	2	2	3	3	1	1	2	2	1	1	2	2	3	3
Location	core	rim	core	rim	core	rim	core	rim	core	rim	core	rim	core	rim
TiO_2	0.05	0.02	0.05	0.00	0.00	0.00	0.02	0.00	0.05	0.11	0.02	0.09	0.05	0.00
SiO_2	50.20	48.81	49.12	47.95	50.34	49.67	48.02	52.11	52.82	52.45	50.89	52.49	52.15	51.29
CaO	14.06	15.07	15.23	16.22	14.10	14.59	16.05	12.50	11.89	11.70	13.14	12.01	12.26	12.88
Na_2O	3.22	2.62	2.64	2.20	3.14	2.92	2.28	4.13	4.54	4.61	3.69	4.35	4.20	4.08
FeO	0.57	0.57	0.52	0.65	0.54	0.55	0.45	0.63	0.58	0.53	0.53	0.60	0.49	0.57
Cl	0.04	0.00	0.01	0.00	0.01	0.00	0.06	0.07	0.00	0.03	0.00	0.00	0.02	0.01
MgO	0.05	0.02	0.07	0.02	0.05	0.07	0.03	0.04	0.04	0.04	0.07	0.04	0.03	0.03
K_2O	0.23	0.16	0.17	0.13	0.29	0.26	0.13	0.30	0.25	0.26	0.23	0.31	0.27	0.19
Al_2O_3	31.46	32.63	32.99	33.80	30.60	31.80	33.60	30.12	29.78	30.05	31.14	30.06	30.18	31.14
MnO	0.00	0.00	0.02	0.00	0.00	0.00	0.00	0.02	0.01	0.00	0.01	0.00	0.00	0.00
P_2O_5	0.01	0.01	0.05	0.01	0.02	0.00	0.03	0.02	0.01	0.01	0.00	0.06	0.01	0.02
F	0.05	0.00	0.01	0.00	0.00	0.00	0.01	0.00	0.02	0.00	0.00	0.00	0.00	0.00
Cr_2O_3	0.00	0.01	0.00	0.02	0.00	0.00	0.00	0.02	0.00	0.00	0.00	0.00	0.01	0.01
Total	99.90	99.93	100.86	100.99	99.07	99.85	100.65	99.95	99.99	99.79	99.71	100.00	99.66	100.22

An	70.73	76.07	76.15	80.29	71.30	73.43	79.54	62.58	59.13	58.35	66.32	60.43	61.76	63.59
Ab	29.27	23.93	23.85	19.71	28.70	26.57	20.46	37.42	40.87	41.65	33.68	39.57	38.24	36.41

Sample	MR-14	MR-14	MR-14	MR-14	MR-14	MR-14	MR-14	MR-14	SL-42	SL-42	SL-42
Grain	1	1	2	2	3	3	4	4	1	1	2
Location	core	rim	core	rim	core	rim	core	rim	core	rim	core
TiO_2	0.00	0.02	0.00	0.00	0.00	0.00	0.08	0.00	0.00	0.00	0.00
SiO_2	47.66	50.97	47.46	47.57	46.91	47.08	53.52	48.61	46.24	46.06	45.88
CaO	15.98	13.24	16.42	16.11	16.42	15.99	11.29	14.89	17.38	17.60	17.37
Na_2O	2.32	3.76	2.08	2.33	2.06	2.29	5.05	2.71	1.37	1.34	1.33
FeO	0.45	0.63	0.51	0.54	0.53	0.49	0.57	0.96	0.40	0.40	0.47
Cl	0.00	0.00	0.01	0.00	0.02	0.00	0.02	0.01	0.00	0.00	0.02
MgO	0.07	0.03	0.03	0.03	0.05	0.04	0.09	0.09	0.14	0.14	0.13
K_2O	0.18	0.38	0.15	0.18	0.16	0.14	0.47	0.22	0.07	0.04	0.06
Al_2O_3	33.62	31.00	34.11	33.59	33.76	33.29	29.63	32.67	34.66	34.37	34.80
MnO	0.00	0.00	0.02	0.00	0.00	0.00	0.01	0.01	0.00	0.00	0.01
P_2O_5	0.02	0.00	0.00	0.01	0.00	0.03	0.01	0.00	0.00	0.00	0.00
F	0.03	0.00	0.00	0.01	0.00	0.00	0.00	0.00	0.02	0.00	0.00
Cr_2O_3	0.00	0.00	0.02	0.00	0.00	0.00	0.00	0.00	0.00	0.01	0.00
Total	100.31	100.03	100.79	100.37	99.92	99.35	100.72	100.16	100.27	99.94	100.06

An	79.20	66.07	81.32	79.26	81.49	79.43	55.26	75.23	87.53	87.88	87.80
Ab	20.80	33.93	18.68	20.74	18.51	20.57	44.74	24.77	12.47	12.12	12.20

Sample	V3-03	V3-03	V3-03	V3-03	V3-03	V3-03	M-26	M-26	M-26
Grain	1	1	2	2	3	3	1	1	1
Location	core	rim	core	rim	core	rim	core	rim	
TiO_2	0.05	0.06	0.00	0.03	0.00	0.01	0.00	0.04	0.00
SiO_2	49.92	49.31	49.69	49.57	49.85	49.47	49.58	51.02	48.64
CaO	13.52	13.81	13.99	14.32	13.86	14.16	13.26	12.66	14.27
Na_2O	3.31	3.21	3.21	3.18	3.39	3.16	3.61	3.93	3.05
FeO	0.42	0.45	0.40	0.46	0.50	0.49	0.49	0.42	0.50
Cl	0.00	0.00	0.00	0.00	0.00	0.00	0.00	0.00	0.02
MgO	0.11	0.07	0.09	0.04	0.06	0.09	0.02	0.01	0.00
K_2O	0.33	0.29	0.28	0.28	0.28	0.24	0.22	0.16	0.25
Al_2O_3	30.56	30.57	30.82	31.39	30.51	31.63	30.29	30.26	30.58
MnO	0.01	0.00	0.03	0.00	0.00	0.01	0.02	0.02	0.01
P_2O_5	0.00	0.00	0.03	0.00	0.00	0.01	0.04	0.00	0.05
F	0.00	0.00	0.00	0.04	0.00	0.05	0.01	0.02	0.00
Cr_2O_3	0.00	0.00	0.00	0.00	0.02	0.00	0.00	0.01	0.00
Total	98.23	97.76	98.54	99.29	98.47	99.30	97.53	98.54	97.37

An	69.28	70.41	70.68	71.34	69.30	71.27	67.01	64.02	72.14
Ab	30.72	29.59	29.32	28.66	30.70	28.73	32.99	35.98	27.86

Clinopyroxene

Sample	EQ-19	EQ-19	EQ-19	EQ-19	EQ-19	EQ-19	EQ-19	EQ-19	EQ-19	EQ-19	EQ-20	EQ-20	EQ-20	EQ-20	EQ-20	EQ-20
Grain	1	1	1	1	1	1	1	2	2	2	1	1	1	2	2	2
Location	rim	rim	rim	core	core	core	core	core	core	rim	core	core	rim	core	core	rim
TiO_2	0.46	0.91	0.83	0.91	1.05	1.05	0.69	0.49	0.40	0.59	0.34	0.48	0.37	0.40	0.46	0.49
SiO_2	52.29	51.02	51.35	50.52	50.60	51.29	51.78	51.75	51.96	52.30	52.94	51.64	52.99	52.13	51.87	51.69
CaO	20.90	21.46	18.47	19.37	21.06	19.74	18.61	19.48	18.69	17.76	17.06	20.37	19.11	18.43	20.11	20.64
Na_2O	0.40	0.36	0.28	0.31	0.41	0.39	0.31	0.29	0.21	0.24	0.17	0.32	0.21	0.24	0.27	0.28
FeO	8.98	7.20	8.89	7.31	6.46	7.44	8.17	6.60	6.65	8.71	7.09	5.86	6.45	6.52	5.83	5.70
Cl	0.00	0.02	0.00	0.00	0.00	0.00	0.06	0.00	0.00	0.00	0.00	0.00	0.01	0.00	0.05	0.00
MgO	15.37	15.16	16.89	16.65	15.52	16.53	17.11	17.18	18.10	17.69	19.58	16.97	18.29	18.06	17.35	16.96
K_2O	0.02	0.01	0.01	0.01	0.02	0.02	0.00	0.01	0.01	0.01	0.00	0.02	0.00	0.01	0.00	0.02
Al_2O_3	1.26	3.15	2.76	2.54	3.32	3.06	2.55	3.57	2.90	2.25	2.23	2.54	2.26	2.81	2.48	2.52
MnO	0.17	0.16	0.19	0.16	0.15	0.16	0.15	0.11	0.12	0.18	0.15	0.13	0.13	0.12	0.11	0.13
P_2O_5	0.01	0.01	0.02	0.04	0.04	0.02	0.01	0.01	0.00	0.01	0.01	0.00	0.00	0.00	0.00	0.00
F	0.00	0.03	0.00	0.05	0.00	0.01	0.00	0.13	0.02	0.00	0.02	0.00	0.00	0.01	0.02	0.00
Cr_2O_3	0.07	0.65	0.58	0.62	0.73	0.72	0.77	1.00	0.97	0.47	0.72	0.96	0.84	0.88	0.89	0.87
Total	99.92	100.11	100.27	98.46	99.34	100.39	100.17	100.56	100.02	100.20	100.31	99.30	100.65	99.60	99.40	99.28

Sample	EQ-20	EQ-20	EQ-20	EQ-14	EQ-14	EQ-14	EQ-14	EQ-14	EQ-14	CR-31	CR-31	CR-31	CR-31	CR-31	CR-31	CR-46
Grain	3	3	3	1	1	1	2	2	2	1	1	2	2	3	3	1
Location	core	core	rim	core	core	rim	core	core	rim	core	rim	core	rim	core	rim	rim
TiO_2	0.45	0.38	0.43	0.37	0.36	0.17	0.37	0.56	0.38	0.70	0.88	0.52	0.45	0.40	0.42	0.72
SiO_2	51.58	51.75	52.00	51.33	50.92	52.80	51.44	51.52	52.37	51.65	50.94	52.56	52.08	51.86	51.83	52.04
CaO	20.58	20.09	20.16	19.92	21.53	21.53	19.99	17.80	20.86	18.17	17.99	16.77	18.60	17.51	19.99	15.82
Na_2O	0.30	0.28	0.28	0.29	0.19	0.44	0.18	0.26	0.50	0.30	0.30	0.29	0.44	0.24	0.49	0.37
FeO	5.76	5.83	5.91	5.86	5.02	6.17	5.79	7.39	6.37	7.69	9.60	8.18	7.23	6.94	6.94	9.78
Cl	0.02	0.00	0.02	0.01	0.00	0.04	0.00	0.00	0.00	0.00	0.04	0.02	0.00	0.00	0.03	0.03
MgO	16.97	17.06	17.06	16.73	16.08	15.97	17.10	17.83	16.04	17.55	17.95	18.69	17.30	18.29	16.11	18.15
K_2O	0.00	0.01	0.01	0.01	0.00	0.02	0.01	0.00	0.01	0.01	0.01	0.02	0.00	0.02	0.01	0.03
Al_2O_3	2.85	2.55	2.36	2.89	2.73	0.99	2.61	2.72	1.24	2.82	2.75	2.46	2.86	3.44	2.73	2.19
MnO	0.12	0.14	0.11	0.12	0.11	0.14	0.12	0.15	0.14	0.13	0.11	0.18	0.14	0.14	0.14	0.18
P_2O_5	0.05	0.03	0.03	0.00	0.01	0.02	0.00	0.00	0.00	0.01	0.04	0.00	0.00	0.01	0.02	0.00
F	0.05	0.01	0.00	0.00	0.02	0.00	0.00	0.02	0.03	0.01	0.00	0.00	0.00	0.04	0.07	0.03
Cr_2O_3	0.97	0.88	0.86	1.01	0.95	0.22	0.93	0.89	0.32	0.65	1.37	0.65	0.92	0.95	0.78	0.46
Total	99.68	99.00	99.23	98.53	97.91	98.50	98.54	99.14	98.24	99.70	101.98	100.32	100.01	99.82	99.51	99.79

Sample	CR-46	CR-46	CR-46	CR-46	LJ-6	LJ-6	LJ-6	LJ-6	LJ-6	LJ-6	EQ-13	EQ-13	EQ-13	EQ-13	EQ-13	EQ-6
Grain	2	2	3	3	1	1	2	2	3	3	1	2	2	3	3	1
Location	core	rim	core	rim	core	rim	core	rim	core	rim	core	core	rim	core	rim	core
TiO_2	0.94	0.76	0.53	0.70	0.78	0.66	0.61	0.68	0.63	0.55	0.61	0.43	0.72	0.29	0.62	0.44
SiO_2	50.91	49.46	51.57	51.41	50.12	50.39	50.64	50.90	50.96	50.79	51.34	51.27	51.19	52.25	51.60	52.22
CaO	19.74	17.96	18.67	20.57	16.55	16.86	17.67	18.78	17.51	17.44	21.37	18.59	18.08	18.33	18.93	18.52
Na_2O	0.40	0.37	0.41	0.42	0.32	0.25	0.25	0.24	0.21	0.27	0.26	0.22	0.24	0.29	0.28	0.22
FeO	7.79	9.55	8.06	7.68	14.27	16.23	14.53	13.71	8.78	13.50	5.75	6.43	7.51	6.04	6.75	7.15
Cl	0.01	0.00	0.05	0.00	0.03	0.01	0.01	0.05	0.00	0.00	0.00	0.00	0.00	0.00	0.00	0.03
MgO	15.99	15.58	16.87	15.37	13.54	13.31	13.48	13.34	16.92	14.23	15.70	17.88	17.30	18.02	16.90	18.21
K_2O	0.01	0.01	0.02	0.02	0.06	0.00	0.00	0.01	0.00	0.01	0.02	0.01	0.00	0.01	0.01	0.01
Al_2O_3	2.29	3.56	2.27	1.93	2.91	2.02	1.80	1.74	3.36	1.96	2.66	3.05	2.68	2.34	2.80	2.81
MnO	0.17	0.22	0.15	0.14	0.21	0.26	0.26	0.24	0.15	0.24	0.15	0.13	0.14	0.13	0.14	0.13
P_2O_5	0.04	0.05	0.01	0.03	0.00	0.06	0.00	0.01	0.01	0.02	0.02	0.07	0.06	0.00	0.00	0.00
F	0.00	0.02	0.05	0.00	0.00	0.00	0.00	0.01	0.00	0.04	0.02	0.01	0.03	0.00	0.01	0.01
Cr_2O_3	0.39	0.35	0.58	0.34	0.35	0.15	0.14	0.05	0.58	0.24	0.82	1.12	0.75	0.82	0.85	0.97
Total	98.68	97.87	99.19	98.60	99.13	100.17	99.37	99.72	99.11	99.27	98.69	99.19	98.70	98.52	98.88	100.70

Sample	EQ-6	EQ-6	EQ-6	EQ-6	EQ-6	LJ-24	LJ-24	LJ-24	LJ-24	LJ-24	LJ-24	MR-25	MR-25	MR-25	MR-25	MR-25
Grain	1	2	2	3	3	1	1	2	2	3	3	1	1	2	2	3
Location	rim	core	rim	core	rim	core	rim	core	rim	core	rim	core	rim	core	rim	core
TiO_2	0.45	0.35	0.25	0.50	0.69	0.26	0.43	0.67	0.70	0.59	0.83	0.65	0.80	0.34	0.69	0.84
SiO_2	52.31	52.36	52.57	51.90	52.04	52.42	51.97	51.85	51.91	52.28	51.30	51.27	50.32	51.80	50.93	51.14
CaO	17.99	18.21	20.87	18.42	20.90	18.46	18.64	19.88	19.84	15.12	17.53	17.50	18.21	20.74	19.80	19.27
Na_2O	0.28	0.27	0.34	0.21	0.37	0.25	0.30	0.33	0.29	0.25	0.31	0.28	0.28	0.27	0.24	0.25
FeO	8.80	7.98	8.81	7.24	8.32	8.18	9.51	8.85	8.77	11.58	10.30	11.21	10.70	9.47	10.41	10.75
Cl	0.01	0.00	0.00	0.00	0.00	0.02	0.00	0.00	0.01	0.02	0.00	0.00	0.01	0.00	0.00	0.00
MgO	17.54	17.84	15.28	17.60	15.31	17.46	16.08	15.74	15.69	18.24	16.67	15.78	15.51	14.69	14.63	15.00
K_2O	0.01	0.00	0.01	0.01	0.01	0.00	0.00	0.01	0.00	0.01	0.01	0.01	0.02	0.01	0.02	0.01
Al_2O_3	2.06	2.20	1.05	2.63	1.74	2.37	2.23	2.17	2.10	2.07	2.57	2.10	2.28	1.36	1.96	2.03
MnO	0.18	0.15	0.19	0.13	0.17	0.17	0.18	0.16	0.19	0.24	0.17	0.22	0.20	0.16	0.20	0.20
P_2O_5	0.00	0.02	0.02	0.01	0.03	0.03	0.00	0.00	0.04	0.00	0.02	0.03	0.02	0.04	0.02	0.03
F	0.01	0.00	0.00	0.00	0.00	0.04	0.01	0.00	0.01	0.00	0.01	0.05	0.00	0.05	0.00	0.00
Cr_2O_3	0.60	0.70	0.07	0.94	0.09	0.59	0.26	0.36	0.28	0.25	0.27	0.13	0.16	0.18	0.15	0.20
Total	100.22	100.07	99.46	99.57	99.66	100.23	99.60	100.02	99.82	100.66	99.99	99.20	98.49	99.09	99.06	99.73

Sample	MR-25	VD-850	VD-850	VD-850	VD-850	VD-850	VD-850	MR-14	MR-14	MR-14	MR-14	MR-14	MR-14	MR-14	V1-02	V1-02
Grain	3	1	1	2	2	3	3	1	1	2	2	2	3	3	1	1
Location	rim	core	rim	core	rim	core	rim	core	rim	core	rim	core	core	rim	core	rim
TiO_2	0.84	1.26	1.24	0.52	1.01	0.42	0.94	0.26	0.86	0.84	0.86	1.08	0.42	0.80	0.35	0.70
SiO_2	51.08	50.78	50.63	51.46	50.10	51.43	50.69	52.72	50.78	50.31	50.84	50.77	51.75	50.75	52.37	51.62
CaO	18.84	20.09	20.20	18.70	20.08	20.67	20.46	16.23	19.82	20.26	20.78	18.61	16.63	19.24	19.12	21.04
Na_2O	0.28	0.33	0.33	0.30	0.33	0.23	0.36	0.17	0.43	0.42	0.44	0.38	0.22	0.35	0.26	0.31
FeO	10.85	7.47	7.19	7.56	7.24	6.15	6.96	7.65	7.78	7.70	7.50	8.70	9.04	7.89	5.40	4.95
Cl	0.02	0.00	0.00	0.00	0.00	0.00	0.00	0.00	0.00	0.00	0.02	0.02	0.00	0.01	0.00	0.00
MgO	14.97	15.89	15.97	17.07	15.81	16.46	15.77	20.07	16.00	15.76	15.63	16.64	18.29	16.37	17.69	17.07
K_2O	0.01	0.01	0.00	0.00	0.02	0.02	0.01	0.01	0.01	0.01	0.01	0.01	0.02	0.01	0.02	0.01
Al_2O_3	2.11	2.28	2.29	2.34	2.45	2.77	2.42	2.22	2.65	2.95	2.88	3.01	2.70	2.75	2.72	2.95
MnO	0.23	0.17	0.14	0.13	0.12	0.13	0.13	0.16	0.18	0.15	0.14	0.17	0.20	0.18	0.12	0.10
P_2O_5	0.04	0.03	0.05	0.00	0.01	0.03	0.01	0.00	0.04	0.02	0.03	0.00	0.00	0.02	0.02	0.02
F	0.01	0.00	0.00	0.00	0.03	0.03	0.00	0.02	0.00	0.00	0.00	0.00	0.00	0.00	0.01	0.02
Cr_2O_3	0.18	0.56	0.57	0.67	0.66	0.88	0.65	0.80	0.65	0.76	0.59	0.52	0.62	0.48	0.89	0.90
Total	99.45	98.88	98.59	98.73	97.85	99.20	98.40	100.28	99.19	99.16	99.72	99.89	99.88	98.84	98.95	99.69

Sample	V1-02	V1-02	V1-02	V1-02	VD-724	VD-724	VD-724	VD-724	VD-724	VD-724	SL-42	SL-42	SL-42	SL-42	SL-42	VD-709
Grain	2	2	3	3	1	1	2	2	3	3	1	1	2	2	3	1
Location	core	rim	core	rim	core	rim	core	rim	core	rim	core	rim	core	rim	rim	core
TiO_2	0.48	0.22	0.21	0.21	0.30	0.27	0.31	0.31	0.18	0.43	0.28	0.11	0.18	0.23	0.21	0.19
SiO_2	52.38	52.46	52.25	52.30	52.50	52.32	52.44	52.70	52.69	52.38	52.77	52.94	52.93	52.50	46.42	53.02
CaO	20.72	21.03	20.56	13.75	20.89	21.05	20.39	21.16	21.48	21.79	21.58	20.40	20.72	20.39	19.09	20.39
Na_2O	0.29	0.20	0.22	0.17	0.32	0.33	0.31	0.32	0.21	0.37	0.17	0.13	0.16	0.11	0.11	0.21
FeO	5.02	4.69	4.69	7.34	5.19	5.14	5.55	5.22	4.49	4.74	4.64	4.92	4.77	4.91	4.98	4.57
Cl	0.00	0.00	0.00	0.01	0.00	0.00	0.00	0.00	0.00	0.04	0.00	0.00	0.01	0.02	0.00	0.00
MgO	17.59	17.45	17.56	22.08	16.96	16.61	17.40	16.71	17.32	16.38	17.29	18.09	18.06	17.99	17.88	17.91
K_2O	0.01	0.01	0.00	0.03	0.01	0.01	0.00	0.01	0.01	0.01	0.00	0.01	0.00	0.02	0.02	0.01
Al_2O_3	2.36	2.25	2.23	2.23	2.24	2.64	2.34	2.37	1.80	2.31	2.36	2.37	2.40	2.23	2.18	1.95
MnO	0.11	0.08	0.11	0.13	0.11	0.11	0.12	0.11	0.09	0.10	0.11	0.11	0.13	0.10	0.12	0.12
P_2O_5	0.04	0.01	0.03	0.01	0.03	0.00	0.01	0.00	0.01	0.01	0.02	0.00	0.00	0.03	0.00	0.06
F	0.03	0.00	0.00	0.02	0.02	0.07	0.00	0.00	0.06	0.02	0.00	0.00	0.00	0.00	0.00	0.00
Cr_2O_3	0.80	0.86	0.86	0.70	0.91	0.96	0.95	0.90	1.00	0.85	0.38	0.44	0.39	0.40	0.41	0.86
Total	99.82	99.26	98.72	98.96	99.46	99.47	99.82	99.81	99.31	99.39	99.60	99.52	99.74	98.91	91.39	99.28

Sample	VD-709	VD-709	VD-709	VD-709	VD-709	V3-03	V3-03	V3-03	V3-03	V3-03	V3-03
Grain	1	2	2	3	3	1	1	2	2	3	3
Location	rim	core	rim	core	rim	core	rim	core	rim	core	rim
TiO_2	0.19	0.21	0.19	0.27	0.24	0.23	0.36	0.31	0.49	0.27	0.37
SiO_2	52.47	52.01	50.97	50.78	51.23	51.90	52.96	50.83	51.11	51.49	50.78
CaO	19.75	18.48	21.82	21.97	20.49	19.54	13.04	20.33	20.49	20.41	20.33
Na_2O	0.18	0.16	0.21	0.21	0.16	0.28	0.18	0.26	0.29	0.25	0.28
FeO	4.66	5.10	3.88	3.86	4.46	6.09	9.09	5.46	5.53	5.45	5.74
Cl	0.00	0.00	0.00	0.00	0.01	0.02	0.01	0.00	0.00	0.00	0.00
MgO	18.26	19.51	17.04	16.79	17.94	17.71	21.41	16.82	16.88	16.95	16.50
K_2O	0.01	0.00	0.01	0.01	0.00	0.02	0.01	0.01	0.00	0.00	0.00
Al_2O_3	1.94	1.95	1.94	2.03	2.04	1.74	1.89	2.39	2.20	2.05	2.65
MnO	0.08	0.10	0.07	0.10	0.11	0.14	0.16	0.13	0.11	0.11	0.13
P_2O_5	0.01	0.03	0.04	0.00	0.00	0.01	0.01	0.04	0.00	0.02	0.04
F	0.00	0.00	0.01	0.03	0.00	0.01	0.00	0.00	0.00	0.04	0.00
Cr_2O_3	0.85	0.88	0.88	0.81	0.80	0.76	0.51	0.77	0.74	0.78	0.73
Total	98.39	98.42	97.07	96.83	97.49	98.44	99.63	97.35	97.84	97.80	97.53

Sample	EQ-19	EQ-19	CR-31	CR-31	CR-46	LJ-6	LJ-6	MR-14	MR-14
Grain	2	2	2	2	1	1	2	1	3
Location	core	core	core	rim	rim	rim	rim	core	core
TiO_2	0.96	0.92	0.40	0.61	0.75	0.06	0.30	0.86	0.36
SiO_2	51.09	51.58	51.53	51.60	51.49	52.44	51.65	51.22	51.04
CaO	18.43	18.49	19.66	17.90	20.43	12.57	19.99	19.32	19.52
Na_2O	0.34	0.32	0.22	0.28	0.39	4.40	0.25	0.40	0.31
FeO	9.09	9.11	5.91	7.96	7.44	0.79	13.40	7.60	7.23
Cl	0.00	0.00	0.00	0.02	0.00	0.00	0.00	0.02	0.00
MgO	16.62	16.89	17.14	17.44	15.59	0.03	13.15	16.11	16.56
K_2O	0.01	0.01	0.01	0.01	0.01	0.22	0.01	0.00	0.01
Al_2O_3	2.90	2.61	2.99	2.62	1.97	30.69	0.97	2.85	3.02
MnO	0.15	0.18	0.13	0.16	0.16	0.01	0.24	0.15	0.16
P_2O_5	0.02	0.03	0.00	0.01	0.01	0.00	0.00	0.00	0.01
F	0.00	0.00	0.00	0.02	0.00	0.00	0.02	0.00	0.06
Cr_2O_3	0.63	0.51	1.04	0.63	0.43	0.00	0.04	0.53	0.83
Total	100.23	100.64	99.01	99.24	98.69	101.19	100.01	99.04	99.08

Orthopyroxene

Sample	EQ-19	EQ-19	EQ-19	EQ-19	EQ-19	EQ-19	EQ-20	EQ-20	EQ-20	EQ-20	EQ-20	EQ-14	EQ-14
Grain	1	1	1	1	2	2	1	1	1	2	2	1	1
Location	core	core	core	core	core	core	core	core	rim	core	core	core	core
TiO_2	0.43	0.41	0.42	0.33	0.31	0.33	0.28	0.21	0.26	0.23	0.21	0.34	0.42
SiO_2	54.11	53.49	53.61	52.93	54.47	54.07	54.70	54.35	54.27	54.67	54.69	54.46	54.08
CaO	2.31	2.28	2.52	2.28	2.24	2.20	1.72	1.80	1.55	1.65	1.63	1.23	1.41
Na_2O	0.01	0.04	0.02	0.03	0.04	0.00	0.01	0.02	0.04	0.01	0.00	0.04	0.02
FeO	13.43	13.95	14.05	14.10	12.40	12.73	11.56	11.74	11.66	11.69	11.72	13.74	13.69
Cl	0.01	0.00	0.00	0.00	0.00	0.00	0.00	0.02	0.00	0.00	0.03	0.00	0.00
MgO	28.25	27.75	27.70	27.29	29.07	28.31	30.01	30.09	30.30	29.81	29.71	28.71	28.74
K_2O	0.01	0.02	0.01	0.01	0.02	0.01	0.01	0.01	0.02	0.01	0.01	0.02	0.01
Al_2O_3	1.83	1.74	1.83	1.81	1.92	1.92	1.53	1.46	1.48	1.52	1.45	0.78	0.95
MnO	0.23	0.23	0.23	0.23	0.21	0.22	0.19	0.22	0.20	0.20	0.22	0.25	0.24
P_2O_5	0.00	0.02	0.02	0.00	0.01	0.00	0.02	0.00	0.05	0.00	0.00	0.02	0.00
F	0.00	0.00	0.04	0.00	0.04	0.00	0.00	0.04	0.00	0.00	0.02	0.02	0.01
Cr_2O_3	0.42	0.38	0.46	0.41	0.49	0.46	0.48	0.46	0.52	0.52	0.45	0.08	0.11
Total	101.03	100.31	100.90	99.42	101.20	100.24	100.51	100.37	100.35	100.29	100.12	99.67	99.66

Sample	EQ-14	EQ-14	EQ-14	CR-31	CR-31	CR-31	CR-31	CR-46	CR-46	CR-46	CR-46	CR-46	LJ-6
Grain	1	2	2	1	1	3	3	1	2	2	3	3	2
Location	rim	core	rim	core	rim	core	rim	core	core	rim	core	rim	rim
TiO_2	0.37	0.17	0.05	0.31	0.32	0.40	0.42	0.26	0.30	0.18	0.30	0.35	0.00
SiO_2	54.38	54.88	54.72	54.41	54.62	54.32	54.18	54.12	53.94	54.81	54.37	53.61	57.16
CaO	1.34	1.14	1.07	2.19	2.11	2.15	1.68	2.21	1.39	0.85	2.17	2.12	8.53
Na_2O	0.03	0.03	0.02	0.03	0.04	0.05	0.03	0.06	0.03	0.05	0.02	0.05	6.04
FeO	13.81	14.03	13.95	13.32	14.17	13.86	15.50	12.98	15.47	15.77	13.53	15.21	0.88
Cl	0.00	0.00	0.00	0.00	0.01	0.01	0.01	0.02	0.01	0.00	0.02	0.01	0.03
MgO	28.86	28.81	28.84	28.56	28.33	28.24	27.40	28.14	27.38	28.32	27.96	27.05	0.51
K_2O	0.00	0.00	0.01	0.01	0.00	0.00	0.01	0.01	0.02	0.01	0.01	0.01	0.61
Al_2O_3	0.76	0.55	0.67	1.39	1.46	1.57	0.98	1.44	0.82	1.02	1.41	1.40	26.21
MnO	0.25	0.24	0.27	0.24	0.24	0.26	0.28	0.23	0.29	0.29	0.23	0.25	0.00
P_2O_5	0.03	0.00	0.00	0.00	0.00	0.02	0.00	0.02	0.00	0.01	0.06	0.01	0.02
F	0.02	0.01	0.00	0.00	0.00	0.01	0.00	0.02	0.04	0.00	0.00	0.03	0.00
Cr_2O_3	0.11	0.08	0.15	0.36	0.28	0.30	0.05	0.40	0.09	0.03	0.39	0.35	0.00
Total	99.94	99.93	99.76	100.82	101.58	101.17	100.53	99.91	99.77	101.35	100.46	100.42	99.98

Sample	EQ-13	EQ-13	EQ-13	EQ-13	EQ-6	EQ-6	EQ-6	EQ-6	LJ-24	LJ-24	LJ-24	LJ-24	LJ-24
Grain	2	2	3	3	1	1	3	3	1	1	1	1	3
Location	core	rim	core	rim	core	rim	core	rim	core	rim	core	rim	core
TiO_2	0.30	0.28	0.23	0.36	0.41	0.62	0.40	0.62	0.45	0.42	0.21	0.30	0.22
SiO_2	54.15	55.08	54.51	54.03	52.55	52.46	53.65	53.38	53.58	53.59	54.76	54.05	54.73
CaO	2.13	2.14	3.48	2.08	2.14	2.03	2.08	2.13	1.82	1.85	2.31	2.19	2.28
Na_2O	0.04	0.05	0.10	0.03	0.02	0.04	0.04	0.03	0.05	0.02	0.04	0.04	0.05
FeO	12.78	12.49	12.34	13.48	14.57	17.63	15.00	17.17	18.33	18.83	14.83	18.12	14.28
Cl	0.00	0.01	0.01	0.00	0.01	0.00	0.00	0.02	0.00	0.00	0.00	0.00	0.00
MgO	28.83	29.17	27.85	27.91	27.37	25.44	27.15	25.84	25.65	25.17	27.55	25.35	27.89
K_2O	0.02	0.00	0.02	0.00	0.01	0.01	0.01	0.01	0.00	0.00	0.01	0.01	0.00
Al_2O_3	1.19	1.20	1.09	1.49	1.64	1.46	1.49	1.44	1.17	1.20	1.31	1.26	1.27
MnO	0.24	0.22	0.23	0.27	0.24	0.28	0.24	0.29	0.32	0.33	0.26	0.29	0.21
P_2O_5	0.00	0.00	0.03	0.03	0.04	0.00	0.00	0.02	0.03	0.05	0.00	0.00	0.00
F	0.00	0.00	0.00	0.01	0.00	0.00	0.00	0.01	0.00	0.00	0.00	0.04	0.00
Cr_2O_3	0.29	0.32	0.27	0.26	0.32	0.14	0.26	0.15	0.09	0.09	0.14	0.10	0.15
Total	99.97	100.95	100.15	99.93	99.30	100.10	100.32	101.10	101.49	101.55	101.42	101.72	101.08

Sample	LJ-24	MR-25	MR-25	MR-25	MR-25	MR-25	MR-25	VD-850	VD-850	VD-850	VD-850	VD-850	VD-850
Grain	3	1	1	2	2	3	3	1	1	2	2	3	3
Location	rim	core	rim	core	rim	core	rim	core	rim	core	rim	core	rim
TiO_2	0.30	0.10	0.58	0.18	0.23	0.27	0.30	0.24	0.17	0.13	0.34	0.13	0.51
SiO_2	53.98	54.49	52.13	54.35	52.99	54.28	53.13	54.28	54.22	53.52	54.01	54.16	53.64
CaO	2.22	2.30	1.95	2.05	2.23	2.38	2.27	1.99	2.38	3.15	2.03	1.97	1.67
Na_2O	0.04	0.02	0.03	0.01	0.02	0.02	0.02	0.02	0.06	0.07	0.06	0.03	0.01
FeO	16.80	13.68	20.34	13.94	18.73	13.29	17.76	12.56	12.39	12.59	13.47	13.55	14.64
Cl	0.00	0.00	0.00	0.00	0.01	0.00	0.00	0.00	0.00	0.00	0.01	0.01	0.01
MgO	26.02	27.88	23.29	28.17	24.31	27.94	25.36	29.08	28.69	27.80	28.15	27.99	27.73
K_2O	0.01	0.00	0.01	0.00	0.01	0.01	0.01	0.01	0.01	0.00	0.01	0.01	0.01
Al_2O_3	1.30	0.98	1.16	1.23	1.24	1.37	1.36	1.39	1.33	1.37	1.18	1.31	1.07
MnO	0.28	0.23	0.31	0.25	0.27	0.25	0.26	0.22	0.20	0.21	0.23	0.24	0.23
P_2O_5	0.00	0.00	0.00	0.00	0.00	0.02	0.00	0.00	0.00	0.00	0.00	0.02	0.04
F	0.00	0.00	0.01	0.00	0.00	0.00	0.01	0.00	0.00	0.00	0.00	0.04	0.00
Cr_2O_3	0.13	0.10	0.08	0.18	0.09	0.26	0.10	0.41	0.38	0.40	0.31	0.37	0.23
Total	101.07	99.78	99.89	100.36	100.14	100.09	100.56	100.19	99.83	99.26	99.80	99.82	99.76

Sample	MR-14	MR-14	MR-14	MR-14	MR-14	MR-14	V1-02	V1-02	V1-02	V1-02	VD-724	VD-724	VD-724
Grain	1	1	2	2	3	3	1	1	2	2	1	1	2
Location	rim	rim	core	rim	core	rim	core	rim	core	rim	core	rim	core
TiO_2	0.24	0.47	0.41	0.42	0.25	0.53	0.25	0.25	0.32	0.32	0.13	0.18	0.19
SiO_2	53.93	54.26	53.41	53.74	54.09	53.70	55.30	55.33	54.80	55.51	55.39	55.78	55.11
CaO	2.16	1.90	2.12	2.09	2.21	1.86	2.11	2.06	2.00	2.01	1.65	1.64	1.84
Na_2O	0.05	0.03	0.05	0.02	0.04	0.05	0.02	0.02	0.02	0.04	0.03	0.01	0.03
FeO	13.02	14.69	14.71	14.89	13.76	14.98	9.64	9.71	9.66	9.83	11.00	11.01	11.01
Cl	0.04	0.04	0.01	0.04	0.00	0.00	0.01	0.02	0.00	0.01	0.00	0.03	0.00
MgO	27.90	27.63	27.50	27.54	27.83	27.39	31.14	30.93	31.08	30.95	30.31	30.58	30.35
K_2O	0.02	0.01	0.00	0.01	0.01	0.01	0.02	0.01	0.00	0.01	0.01	0.01	0.00
Al_2O_3	1.48	1.37	1.50	1.48	1.52	1.36	1.49	1.47	1.52	1.50	1.19	1.23	1.63
MnO	0.25	0.28	0.27	0.29	0.26	0.27	0.17	0.17	0.19	0.16	0.19	0.21	0.17
P_2O_5	0.00	0.00	0.00	0.00	0.03	0.00	0.00	0.00	0.03	0.00	0.00	0.00	0.00
F	0.00	0.02	0.02	0.00	0.00	0.00	0.01	0.00	0.00	0.00	0.02	0.00	0.00
Cr_2O_3	0.31	0.19	0.25	0.24	0.31	0.13	0.42	0.41	0.44	0.46	0.39	0.38	0.56
Total	99.38	100.86	100.25	100.75	100.30	100.27	100.57	100.37	100.06	100.81	100.27	101.03	100.89

Sample	VD-724	VD-724	VD-724	V3-03	V3-03	V3-03	V3-03	V3-03	V3-03	V3-03	V3-03	EQ-19	EQ-19
Grain	2	3	3	1	1	2	2	3	3	4	4	1	1
Location	rim	core	rim	core	rim	core	rim	core	rim	core	rim	core	core
TiO_2	0.13	0.22	0.16	0.23	0.24	0.32	0.25	0.09	0.15	0.27	0.31	0.40	0.38
SiO_2	55.01	55.47	55.27	53.53	53.91	53.68	53.17	54.06	53.67	54.08	54.17	54.47	54.03
CaO	1.70	1.93	1.62	2.24	2.26	1.67	1.45	2.59	2.13	2.15	2.01	2.17	2.20
Na_2O	0.03	0.05	0.01	0.05	0.02	0.03	0.01	0.02	0.03	0.05	0.02	0.02	0.02
FeO	11.09	11.01	11.18	11.69	11.58	12.76	12.83	10.37	11.36	11.93	12.45	14.76	14.60
Cl	0.00	0.00	0.00	0.00	0.00	0.00	0.00	0.00	0.00	0.01	0.00	0.00	0.01
MgO	30.47	30.26	30.47	29.48	29.02	28.94	29.00	29.72	29.31	29.06	28.87	27.71	27.52
K_2O	0.01	0.01	0.00	0.01	0.00	0.00	0.00	0.00	0.02	0.01	0.01	0.01	0.01
Al_2O_3	1.52	1.35	1.49	1.35	1.36	1.33	1.28	1.11	1.44	1.36	1.33	1.16	1.33
MnO	0.18	0.19	0.18	0.23	0.20	0.22	0.23	0.18	0.22	0.20	0.22	0.24	0.24
P_2O_5	0.00	0.00	0.00	0.00	0.00	0.00	0.00	0.02	0.00	0.00	0.00	0.05	0.02
F	0.00	0.00	0.00	0.03	0.00	0.00	0.00	0.02	0.00	0.02	0.00	0.03	0.00
Cr_2O_3	0.45	0.45	0.52	0.31	0.32	0.35	0.32	0.40	0.34	0.32	0.30	0.23	0.30
Total	100.59	100.93	100.89	99.13	98.91	99.30	98.53	98.56	98.66	99.45	99.68	101.23	100.65

Sample	EQ-19	EQ-19	EQ-19
Grain	1	1	1
Location	core	rim	core
TiO_2	0.22	0.34	0.42
SiO_2	54.78	54.04	53.95
CaO	2.20	1.20	2.37
Na_2O	0.02	0.05	0.06
FeO	13.40	15.78	13.87
Cl	0.03	0.01	0.02
MgO	28.50	27.58	27.57
K_2O	0.00	0.01	0.01
Al_2O_3	1.09	1.01	1.74
MnO	0.23	0.29	0.22
P_2O_5	0.00	0.02	0.01
F	0.01	0.03	0.02
Cr_2O_3	0.27	0.21	0.42
Total	100.73	100.54	100.67

K-Feldspar

Sample	EQ-14	EQ-14	EQ-14	EQ-14	CR-31	CR-31	LJ-6	LJ-6	LJ-6	LJ-6	EQ-15	EQ-15	EQ-15	EQ-15
Grain	1	1	2	2	1	1	1	1	2	2	1	1	2	2
Location	core	rim	core	rim	core	rim	core	rim	core	rim	core	rim	core	rim
TiO_2	0.12	0.06	0.11	0.12	0.00	0.00	0.02	0.02	0.03	0.07	0.00	0.02	0.02	0.00
SiO_2	63.14	63.32	62.92	62.84	64.92	65.07	64.20	64.32	63.81	63.37	64.43	63.50	64.44	63.75
CaO	1.22	1.18	1.02	1.11	0.46	0.63	0.16	0.10	0.25	0.25	0.10	0.08	0.10	0.10
Na_2O	5.00	4.89	4.84	4.60	3.43	3.22	1.60	1.27	1.85	1.74	1.70	1.22	2.42	1.94
FeO	0.21	0.31	0.14	0.18	0.30	0.19	0.27	0.20	0.28	0.18	0.09	0.80	0.04	0.14
Cl	0.00	0.00	0.00	0.00	0.00	0.05	0.01	0.07	0.00	0.00	0.00	0.00	0.00	0.00
MgO	0.00	0.02	0.00	0.00	0.00	0.01	0.00	0.03	0.01	0.00	0.05	0.55	0.00	0.01
K_2O	7.96	8.12	8.23	8.47	10.93	11.21	13.24	14.02	12.82	12.84	13.49	13.46	12.30	12.96
Al_2O_3	20.42	20.61	20.32	20.34	19.85	20.00	19.03	19.01	19.17	19.14	19.15	19.14	19.31	19.12
MnO	0.00	0.00	0.01	0.00	0.00	0.00	0.00	0.00	0.00	0.01	0.01	0.01	0.00	0.00
P_2O_5	0.02	0.02	0.03	0.01	0.06	0.03	0.03	0.02	0.02	0.00	0.12	0.10	0.06	0.09
F	0.00	0.00	0.00	0.03	0.02	0.04	0.01	0.04	0.00	0.00	0.00	0.02	0.01	0.00
Cr_2O_3	0.01	0.00	0.00	0.00	0.01	0.02	0.00	0.02	0.00	0.00	0.00	0.00	0.00	0.00
Total	98.09	98.54	97.63	97.69	99.97	100.44	98.57	99.06	98.24	97.61	99.13	98.89	98.69	98.11

Sample	EQ-13	EQ-13	EQ-6	EQ-6	EQ-6	EQ-6	MR-25	MR-25	MR-25	MR-25	M-26	M-26	M-26	M-26
Grain	1	1	1	1	2	2	1	1	2	2	1	1	2	2
Location	core	core	core	rim	core	rim	core	rim	core	rim	rim	core	core	core
TiO_2	0.11	0.09	0.02	0.08	0.00	0.00	0.09	0.09	0.06	0.02	0.06	0.07	0.02	0.00
SiO_2	63.97	63.42	64.25	64.07	64.24	64.06	63.68	63.57	63.47	63.34	63.74	62.03	63.51	62.39
CaO	0.95	1.35	0.58	0.55	0.28	0.31	0.26	0.32	0.34	0.36	0.05	0.26	0.19	0.03
Na_2O	4.43	4.64	3.36	3.29	2.32	2.94	1.29	1.26	1.18	0.92	1.06	3.16	2.79	0.24
FeO	0.16	0.35	0.16	0.21	0.34	0.19	0.14	0.14	0.18	0.21	0.07	0.05	0.04	0.09
Cl	0.01	0.00	0.01	0.01	0.01	0.00	0.01	0.02	0.02	0.00	0.03	0.00	0.01	0.07
MgO	0.00	0.01	0.00	0.03	0.69	0.02	0.03	0.00	0.00	0.00	0.04	0.01	0.01	0.00
K_2O	9.00	8.24	11.01	11.11	9.82	11.50	13.33	13.65	13.78	13.55	13.44	10.60	11.91	14.61
Al_2O_3	20.28	20.49	19.65	19.49	19.68	19.32	18.64	18.82	19.26	19.23	18.99	19.28	19.11	19.03
MnO	0.00	0.00	0.00	0.00	0.01	0.00	0.01	0.00	0.00	0.00	0.01	0.00	0.00	0.01
P_2O_5	0.00	0.03	0.03	0.02	0.04	0.04	0.02	0.02	0.04	0.03	0.09	0.13	0.13	0.00
F	0.01	0.05	0.01	0.03	0.00	0.00	0.00	0.00	0.03	0.03	0.00	0.01	0.00	0.00
Cr_2O_3	0.00	0.00	0.00	0.01	0.00	0.01	0.00	0.00	0.00	0.00	0.00	0.00	0.00	0.02
Total	98.92	98.63	99.07	98.87	97.43	98.40	97.49	97.89	98.34	97.67	97.55	95.59	97.72	96.47

Micas (generally biotite)

Sample	EQ-19	EQ-19	EQ-19	EQ-19	EQ-19	EQ-19	EQ-19	EQ-14	EQ-14	EQ-14	EQ-14	CR-31	CR-31	CR-31
Grain	1	1	1	1	2	2	2	1	1	2	2	1	1	2
Location	core	core	core	core	core	core	rim	core	rim	core	rim	core	rim	core
TiO_2	6.54	6.32	6.37	6.25	5.02	4.94	5.47	6.99	6.32	5.59	5.88	5.35	4.06	5.10
SiO_2	37.93	38.74	37.44	36.86	37.81	38.13	38.60	37.72	38.18	38.29	38.06	38.43	38.79	38.33
CaO	0.00	0.00	0.00	0.01	0.00	0.00	0.01	0.03	0.01	0.00	0.00	0.00	0.00	0.02
Na_2O	0.23	0.25	0.32	0.28	0.48	0.46	0.48	0.55	0.50	0.51	0.59	0.60	0.49	0.44
FeO	14.21	14.14	14.07	13.90	13.18	12.78	12.59	7.89	8.95	9.17	9.37	10.82	10.47	10.41
Cl	0.29	0.27	0.29	0.30	0.34	0.32	0.28	0.17	0.16	0.20	0.20	0.16	0.22	0.26
MgO	14.50	15.29	14.46	13.88	16.60	16.36	16.75	17.52	17.99	18.02	17.69	18.26	18.58	17.78
K_2O	8.91	9.13	8.90	9.06	8.73	8.93	8.96	8.85	9.12	8.46	8.88	8.89	8.87	9.05
Al_2O_3	13.30	13.25	14.03	13.93	13.92	13.89	14.01	13.71	13.88	13.35	13.80	14.15	14.49	14.04
MnO	0.03	0.04	0.03	0.04	0.02	0.05	0.02	0.02	0.02	0.01	0.04	0.03	0.02	0.03
P_2O_5	0.03	0.00	0.02	0.01	0.02	0.00	0.02	0.00	0.00	0.01	0.00	0.04	0.02	0.01
F	0.00	0.00	0.00	0.02	0.00	0.00	0.00	0.00	0.07	0.02	0.01	0.03	0.00	0.03
Cr_2O_3	0.11	0.14	0.21	0.17	0.20	0.17	0.13	0.73	0.51	0.33	0.36	0.08	0.04	0.09
Total	96.01	97.50	96.07	94.62	96.23	95.95	97.24	94.13	95.64	93.90	94.83	96.77	96.01	95.50

Sample	CR-31	CR-46	CR-46	CR-46	EQ-15	EQ-15	EQ-15	EQ-15	EQ-6	EQ-6	EQ-6	EQ-6	M-26	M-26
Grain	2	1	1	2	1	1	2	2	1	1	2	2	2	2
Location	rim	core	rim	core					core	rim	core	rim		
TiO_2	3.75	7.26	6.91	5.99	5.29	5.56	2.69	2.63	6.09	6.22	4.41	4.55	3.07	3.19
SiO_2	37.34	37.73	36.56	37.26	36.33	36.52	35.82	35.98	37.26	37.49	38.71	38.33	35.51	35.52
CaO	0.04	0.00	0.00	0.11	0.00	0.00	0.00	0.00	0.00	0.00	0.01	0.01	0.00	0.00
Na_2O	0.36	0.40	0.37	0.31	0.27	0.26	0.11	0.12	0.36	0.32	0.53	0.51	0.38	0.33
FeO	13.02	10.31	14.37	12.42	20.02	19.62	21.41	21.38	14.14	14.00	10.00	10.12	26.82	26.59
Cl	0.58	0.17	0.18	0.27	0.09	0.09	0.05	0.07	0.31	0.27	0.19	0.16	1.02	1.01
MgO	19.41	16.53	17.29	17.46	10.25	10.28	10.59	10.94	14.93	15.02	18.74	18.18	7.84	7.79
K_2O	8.15	9.19	8.70	7.81	8.75	8.65	9.00	8.82	9.02	9.16	8.52	8.64	8.67	8.70
Al_2O_3	13.45	13.92	13.02	13.49	15.47	15.22	16.88	16.25	13.71	13.75	14.33	14.31	14.58	14.49
MnO	0.06	0.03	0.04	0.06	0.06	0.07	0.09	0.11	0.04	0.04	0.01	0.03	0.11	0.10
P_2O_5	0.01	0.02	0.00	0.03	0.00	0.01	0.00	0.07	0.02	0.00	0.00	0.00	0.04	0.00
F	0.00	0.03	0.02	0.04	0.00	0.01	0.00	0.00	0.00	0.00	0.00	0.03	0.00	0.02
Cr_2O_3	0.03	0.42	0.45	0.20	0.20	0.25	0.06	0.05	0.08	0.15	0.16	0.17	0.00	0.00
Total	96.07	95.95	97.87	95.36	96.70	96.52	96.70	96.39	95.89	96.36	95.55	94.99	97.80	97.49

Apatite

Sample	EQ-19	EQ-19	EQ-19	EQ-14	EQ-14	CR-31	CR-46	EQ-13	EQ-13	EQ-6	EQ-6	MR-25	MR-25
Grain	1	1	1	3	3	1	1	1	1	1	1	1	1
Location	core	core	rim	core	rim	core	core	core	rim	core	rim	core	rim
TiO_2	0.00	0.00	1.67	0.00	0.00	0.00	0.00	0.00	0.00	0.00	0.06	0.00	0.00
SiO_2	0.08	0.08	26.25	0.04	0.38	0.06	0.03	0.07	0.08	1.08	53.84	0.03	0.00
CaO	51.92	51.70	12.61	47.42	50.47	51.29	51.22	51.63	51.26	50.29	11.37	52.87	52.43
Na_2O	0.13	0.09	0.19	0.25	0.22	0.14	0.07	0.26	0.25	0.10	5.57	0.02	0.01
FeO	0.30	0.30	19.58	0.29	0.28	0.27	0.36	0.33	0.36	1.12	0.36	0.28	0.27
Cl	3.11	3.23	0.69	2.79	3.13	2.92	2.37	2.65	2.56	2.57	0.10	1.26	1.17
MgO	0.05	0.02	13.28	0.06	0.07	0.13	0.11	0.09	0.08	0.54	0.05	0.07	0.04
K_2O	0.02	0.02	2.47	0.05	0.12	0.01	0.01	0.01	0.02	0.01	0.21	0.03	0.03
Al_2O_3	0.00	0.00	8.81	0.00	0.02	0.01	0.01	0.00	0.00	0.39	28.49	0.00	0.00
MnO	0.02	0.04	0.11	0.03	0.04	0.04	0.03	0.02	0.03	0.04	0.01	0.04	0.04
P_2O_5	41.16	41.16	10.19	39.58	40.31	40.75	41.15	39.78	40.93	40.33	1.08	42.18	42.22
F	3.55	3.60	0.46	3.69	3.36	3.30	3.49	3.44	3.51	3.48	0.09	3.66	3.67
Cr_2O_3	0.00	0.00	0.19	0.00	0.00	0.00	0.01	0.00	0.00	0.00	0.01	0.00	0.00
Total	98.14	98.00	96.15	92.02	96.28	96.86	96.85	96.23	97.01	97.89	101.16	98.60	98.08

APPENDIX C – Geochemical Data Comparison

The following chart details all available geochemical data for the samples from this study. Data from the study of Francis (1994) (DF) is compared to new data from this study (MP). Wherever significant discrepancies exist, the data is highlighted.

Author:	MP	DF	MP	MP		MP	DF	MP	MP
Sample:	VD-724	VD-724	VD-724	VD-724		VD-850	VD-850	VD-850	VD-850
Method:	ICPMS	XRF/INAA	Fusion	IDTIMS		ICPMS	XRF/INAA	Fusion	IDTIMS
SiO2	50.57	50.58				53.62	54.34		
Al2O3	2.59	2.77				4.56	4.51		
Fe2O3	7.58	7.72				12.05	12.92		
MnO	0.14	0.14				0.21	0.22		
MgO	20.97	20.44				24.03	23.46		
CaO	15.78	16.67				4.20	4.42		
Na2O	0.22	0.01				0.50	0.12		
K2O	0.08	0.01				0.34	0.26		
TiO2	0.30	0.31				0.41	0.56		
P2O5	0.10	0.02				0.02	0.03		
LOI	1.29	1.08				0.12	0.01		
Total	99.62	99.65				100.06	100.85		
Sc			44					27	
V	141	138	135			130	138	111	
Cr	5780	5283				2790	2381		
Co	57	81				90	164		
Ni	367	326				519	482		
Cu	43	10				50	15		
Zn	44	25				99	85		
Ga	4					7			
Ge	3					2			
Rb	2	6		1.91		5	8		4.21
Sr	18	20	20	17.44		108	95	108	116.76
Y	5	5	6			5	6	5	
Zr	14	12	10			15	23	15	
Nb	0.4	5.0				0.6	5.0		
Sn									
Sb									
Cs	0.4					0.2			
Ba	23	60	30			101	117	101	
La	1.43					1.64			
Ce	3.46					3.76			
Pr	0.49					0.49			
Nd	2.66			1.65		2.39			2.45
Sm	0.84			0.50		0.69			0.66
Eu	0.27					0.31			
Gd	0.95					0.88			
Tb	0.17					0.15			
Dy	1.04					0.92			
Ho	0.21					0.20			
Er	0.58					0.61			
Tm	0.08					0.09			
Yb	0.48					0.55			
Lu	0.07			0.07		0.08			0.08
Hf	0.40			0.358		0.50			0.416
Ta	0.07					0.04			
Tl	0.06								
Th	0.21					0.25			
U	0.06					0.07			

Author:	MP	DF	MP	MP		MP	DF	MP	MP
Sample:	V3-03	V3-03	V3-03	V3-03		EQ-6	EQ-6	EQ-6	EQ-6
Method:	ICPMS	XRF/INAA	Fusion	IDTIMS		ICPMS	XRF/INAA	Fusion	IDTIMS
SiO2	52.33	52.57				49.05	48.69		
Al2O3	3.73	3.89				14.41	13.25		
Fe2O3	7.68	8.00				8.54	11.91		
MnO	0.17	0.17				0.14	0.16		
MgO	19.70	19.82				14.21	13.14		
CaO	14.21	14.86				9.02	9.63		
Na2O	0.34	0.12				1.48	1.31		
K2O	0.11	0.08				0.55	0.65		
TiO2	0.39	0.41				0.84	1		
P2O5	0.03	0.02				0.07	0.09		
LOI	0.34	0.25				0.41	0.35		
Total	99.02	100.19				98.72	100.18		
Sc	45						25.6	20	
V	167	190	165				204	162	
Cr	4770	3832				750	882		
Co	68					38	119		
Ni	417	379				280	523		
Cu	64					70	147		
Zn	49						66		
Ga	6					13			
Ge	2.1					0.6			
Rb	3	6		2.52		14	16		13.25
Sr	46		46	52.44				249	280.95
Y	7		7			14			
Zr	11		10					56	
Nb	0.4	4				4.1	7		
Sn									
Sb									
Cs	0.2					0.7			
Ba	103	118	100				178	130	
La	1.15					8.18	9.4		
Ce	3.20					18.3	20		
Pr	0.49					2.33			
Nd	2.88			3.26		10.1	11.7		10.64
Sm	0.97			1.13		2.48	2.58		2.54
Eu	0.36					0.89	0.9		
Gd	1.29					2.64			
Tb	0.23					0.42	0.42		
Dy	1.42					2.38			
Ho	0.28					0.46	0.48		
Er	0.82					1.34			
Tm	0.12					0.19			
Yb	0.73					1.16	1.5		
Lu	0.10			0.09		0.16	0.23		0.17
Hf	0.4			0.373		1.7	2.3		1.721
Ta						0.28	0.5		
W									
Tl									
Pb						7	4		
Bi									
Th	0.14					1.43	1.7		
U	0.03					0.39	0.5		

Author:	MP	DF	MP	MP		MP	DF	MP	MP
Sample:	EQ-14	EQ-14	EQ-14	EQ-14		CR-46	CR-46	CR-46	CR-46
Method:	ICPMS	XRF/INAA	Fusion	IDTIMS		ICPMS	XRF/INAA	Fusion	IDTIMS
SiO2	43.69	43.39				45.97			
Al2O3	5.66	7.26				9.00			
Fe2O3	13.09	14.03				13.34			
MnO	0.18	0.18				0.17			
MgO	25.24	22.72				18.65			
CaO	4.75	5.72				7.84			
Na2O	0.67	0.5				1.52			
K2O	0.86	0.46				0.59			
TiO2	1.27	0.81				0.98			
P2O5	0.12	0.08				0.12			
LOI	3.50	4.16				0.59			
Total	99.02	99.31				98.78			
Sc			20			25			
V		175	218			212		204	
Cr	1870	2382				1820			
Co	69	138				87			
Ni	680	1085				702			
Cu	110	136				122			
Zn	70	72				89			
Ga	11					13			
Ge	0.9					1.4			
Rb	24	14		22.61		13			12.53
Sr			134	129.76		161		153	153.03
Y	20					15		15	
Zr			100			72		73	
Nb	7.1	6				4.4			
Sn						2			
Sb									
Cs	1.3					0.8			
Ba		144	192			146		141	
La	12.1					9.41			
Ce	27.4					21.2			
Pr	3.47					2.72			
Nd	14.9			14.98		12.2			14.19
Sm	3.68			3.54		3.02			3.49
Eu	0.99					1.00			
Gd	3.8					3.11			
Tb	0.57					0.52			
Dy	3.35					3.04			
Ho	0.67					0.57			
Er	1.94					1.64			
Tm	0.27					0.24			
Yb	1.64					1.44			
Lu	0.23			0.25		0.20			0.20
Hf	2.7			3.06		2.2			2.084
Ta	0.49					0.32			
W									
Tl	0.08					0.09			
Pb		2							
Bi									
Th	2.41					1.72			
U	0.66					0.42			

Author:	MP	DF	MP	MP		MP	DF	MP	MP
Sample:	LJ-24	LJ-24	LJ-24	LJ-24		MR-14	MR-14	MR-14	MR-14
Method:	ICPMS	XRF/INAA	Fusion	IDTIMS		ICPMS	XRF/INAA	Fusion	IDTIMS
SiO2	49.77					47.91	47.58		
Al2O3	11.50					10.25	11.93		
Fe2O3	10.86					11.91	11.51		
MnO	0.17					0.18	0.18		
MgO	14.08					17.02	16.1		
CaO	11.60					10.22	10.9		
Na2O	1.15					1.03	0.78		
K2O	0.23					0.49	0.42		
TiO2	0.55					0.74	0.74		
P2O5	0.05					0.08	0.07		
LOI	-0.23					0.30	0.12		
Total	99.72					100.13	99.17		
Sc	39					32			
V	209		205			200	492	195	
Cr	1010					1920	127		
Co	66					76	127		
Ni	329					503	492		
Cu	112					146	313		
Zn	60					71	60		
Ga	12					12			
Ge	1.4					1.3			
Rb	6			6.32		13	14		11.29
Sr	130		128	138.99		120		116	110.9
Y	10		11			14		14	
Zr	29		29			53		52	
Nb	1.4					3.0	6		
Sn	1					1			
Sb									
Cs	0.2					0.5			
Ba	75		77			133	156	129	
La	3.77					7.12			
Ce	8.44					15.9			
Pr	1.14					1.98			
Nd	5.28			4.77		9.11			11.66
Sm	1.52			1.3		2.38			3.09
Eu	0.59					0.74			
Gd	1.70					2.44			
Tb	0.31					0.44			
Dy	2.01					2.68			
Ho	0.41					0.54			
Er	1.18					1.59			
Tm	0.18					0.23			
Yb	1.09					1.42			
Lu	0.16			0.16		0.20			0.20
Hf	0.9			0.903		1.6	189		1.533
Ta	0.09					0.22	1752		
W									
Tl	0.06					0.12			
Pb							5		
Bi						0.1			
Th	0.72					1.62			
U	0.18					0.38			

Author:	MP	DF	MP		MP	DF	MP		MP	DF	MP
Sample:	MR-25	MR-25	MR-25		V1-05	V1-05	V1-05		V1-10	V1-10	V1-10
Method:	ICPMS	XRF/INAA	Fusion		ICPMS	XRF/INAA	Fusion		ICPMS	XRF/INAA	Fusion
SiO2	51.25	50.87			33.01	34.4			35.79	36.31	
Al2O3	12.95	13.41			1.89	1.48			0.74	0.84	
Fe2O3	9.60	9.91			16.01	15.53			14.04	14.84	
MnO	0.16	0.17			0.15	0.16			0.11	0.12	
MgO	11.51	11.58			34.40	34.22			36.13	35.27	
CaO	11.87	11.98			0.26	0.27			0.02	0.49	
Na2O	1.48	0.97			-0.01	0.01			-0.01	0.01	
K2O	0.54	0.48			-0.01	0.01			0.05	0.01	
TiO2	0.63	0.65			0.16	0.15			0.08	0.1	
P2O5	0.05	0.04			0.02	0.02			0.02	0.01	
LOI	0.06				12.69	13.27			12.26	12.12	
Total	100.09	100.06			98.38	99.52			99.20	100.12	
Sc	40				8				10		
V	229	199	233		136	123	118		35	70	34
Cr	987	852			>10,000	12110			6300	5542	
Co	54	83			110				165		
Ni	239	244			1,070	1638			1,470	1409	
Cu	90	76			35				23		
Zn	60	57			64				89		
Ga	14				4				2		
Ge	1.3				0.7				1.2		
Rb	10	12				5				5	
Sr	165		165		3		4				1
Y	11		11		1		2		1		2
Zr	35		37		9		9		5		5
Nb	2.0	5			0.5	4			0.2	5	
Sn											
Sb											
Cs	0.3										
Ba	105	136	105		6	17	6		4	14	9
La	4.50				0.68				0.32		
Ce	10.4				1.29				0.74		
Pr	1.33				0.19				0.10		
Nd	6.30				0.85				0.52		
Sm	1.74				0.23				0.16		
Eu	0.70				0.08				0.05		
Gd	1.97				0.23				0.20		
Tb	0.34				0.04				0.03		
Dy	2.10				0.25				0.19		
Ho	0.43				0.05				0.04		
Er	1.26				0.16				0.12		
Tm	0.18				0.02				0.02		
Yb	1.10				0.16				0.12		
Lu	0.16				0.02				0.02		
Hf	1.0				0.2				0.1		
Ta	0.14				0.01						
W											
Tl	0.07										
Pb		4									
Bi											
Th	0.85				0.10				0.05		
U	0.22				0.04				0.06		

Author:	MP	DF	MP		MP	DF	MP		MP	DF	MP
Sample:	V1-02	V1-02	V1-02		V1-01	V1-01	V1-01		SL-42	SL-42	SL-42
Method:	ICPMS	XRF/INAA	Fusion		ICPMS	XRF/INAA	Fusion		ICPMS	XRF/INAA	Fusion
SiO2	46.56	46.28			34.52	34.92			48.14	48.03	
Al2O3	2.86	2.85			1.30	1.36			16.45	16.35	
Fe2O3	8.10	8.63			12.55	12.99			3.55	3.95	
MnO	0.14	0.14			0.13	0.14			0.07	0.08	
MgO	24.41	25.03			36.82	35.88			10.96	11.82	
CaO	12.06	12.11			0.26	0.27			16.17	15.15	
Na2O	0.15	0.01			-0.01	0.01			0.47	0.24	
K2O	0.05	0.01			-0.01	0.01			1.18	1.69	
TiO2	0.25	0.26			0.13	0.14			0.13	0.15	
P2O5	0.02	0.01			0.02	0.02			0.02	0.01	
LOI	4.53	4.63			14.18	14.13			2.34	2.39	
Total	99.13	99.96			99.56	99.87			99.48	99.86	
Sc	44				9				34		
V	134	159	127		61	92	61		133	135	128
Cr	4430	3558			4780	7663			1250	1240	
Co	93				113				28	21	
Ni	604	586			899	1385			194	219	
Cu	31				15					17	
Zn	50				57					10	
Ga	4				3				11		
Ge	2.0				0.8				1.3		
Rb	1	5				5			11	15	
Sr	12		13		2		2		175		177
Y	5		6		2		1		2		2
Zr	6		3		7		11		5		2
Nb	0.3	4			0.5	5				3	
Sn									1		
Sb											
Cs	0.2								0.4		
Ba	5	24	10			13	3		78	144	78
La	0.91				0.65				0.29		
Ce	2.34				1.59				0.84		
Pr	0.36				0.21				0.15		
Nd	2.01				1.01				0.91		
Sm	0.65				0.28				0.34		
Eu	0.24				0.09				0.20		
Gd	0.86				0.28				0.49		
Tb	0.15				0.05				0.09		
Dy	0.96				0.30				0.53		
Ho	0.20				0.06				0.10		
Er	0.58				0.18				0.29		
Tm	0.08				0.03				0.04		
Yb	0.51				0.18				0.24		
Lu	0.07				0.03				0.03		
Hf	0.2				0.2				0.2		
Ta					0.01						
W											
Tl	0.06										
Pb											
Bi											

Author:	MP	DF	MP		MP	DF	MP		MP	DF	MP
Sample:	ES-10	ES-10	ES-10		VD-722	VD-722	VD-722		CR-6	CR-6	CR-6
Method:	ICPMS	XRF/INAA	Fusion		ICPMS	XRF/INAA	Fusion		ICPMS	XRF/INAA	Fusion
SiO2	42.99	42.58			49.72	49.44			41.42	41.03	
Al2O3	2.38	2.46			2.78	2.87			6.89	6.92	
Fe2O3	11.48	12.20			8.29	8.64			11.96	12.46	
MnO	0.17	0.17			0.15	0.16			0.17	0.17	
MgO	26.49	26.86			21.29	21.58			24.81	24.81	
CaO	7.52	7.43			15.11	15.41			7.76	7.36	
Na2O	0.03	0.01			0.16	0.01			0.09	0.21	
K2O	0.04	0.01			0.03	0.01			0.09	0.11	
TiO2	0.32	0.32			0.34	0.35			0.31	0.33	
P2O5	0.03	0.02			0.03	0.02			0.04	0.03	
LOI	8.03	8.21			1.81	1.47			6.27	6.08	
Total	99.45	100.26			99.73	99.96			99.80	99.51	
Sc	34				41				22		
V	154	146	155		130	128	121		112	119	101
Cr	3180	3088			5270	4877			3490	3288	
Co	99	162			68	98			105	142	
Ni	873	969			289	238			1,030	1138	
Cu		10			40	10			66	147	
Zn	41	36			42	29			76	58	
Ga	4				5				7		
Ge	1.5				2.1				1.1		
Rb	2	6			3	6			5	7	
Sr	10		10		22		21		92		86
Y	6		6		6		7		5		5
Zr	17		11		17		14		22		19
Nb	0.5	6			0.6	5			1.1	4	
Sn	1				1				1		
Sb											
Cs	0.2				0.4				0.3		
Ba	7	37	13		42	80	42		89	112	88
La	1.51				1.51				2.17		
Ce	3.92				3.97				5.01		
Pr	0.57				0.58				0.67		
Nd	3.09				2.98				3.20		
Sm	0.96				0.92				0.86		
Eu	0.31				0.35				0.32		
Gd	1.11				1.11				0.92		
Tb	0.20				0.19				0.16		
Dy	1.19				1.20				0.99		
Ho	0.23				0.24				0.19		
Er	0.65				0.69				0.57		
Tm	0.09				0.10				0.09		
Yb	0.57				0.59				0.54		
Lu	0.08				0.09				0.08		
Hf	0.5				0.5				0.6		
Ta	0.02				0.02				0.06		
W											
Tl					0.06				-0.05		
Pb										2	
Bi											
Th	0.23				0.25				0.45		
U	0.06				0.05				0.10		

Author:	MP	DF	MP		MP	DF	MP		MP	DF	MP
Sample:	VD-707	VD-707	VD-707		LJ-6	LJ-6	LJ-6		EQ-20	EQ-20	EQ-20
Method:	ICPMS	XRF/INAA	Fusion		ICPMS	XRF/INAA	Fusion		ICPMS	XRF/INAA	Fusion
SiO2	45.92	46.36			52.95	52.73			48.95	48.48	
Al2O3	1.26	1.35			13.67	14.29			2.24	2.35	
Fe2O3	7.43	7.85			10.55	12.54			8.23	8.59	
MnO	0.14	0.14			0.17	0.17			0.17	0.16	
MgO	25.82	25.61			6.53	6.68			21.13	21.77	
CaO	11.11	11.76			9.76	10.07			15.06	15.18	
Na2O	-0.01	0.01			2.25	1.79			0.18	0.74	
K2O	0.02	0.01			1.14	1.16			0.05	0.01	
TiO2	0.18	0.19			1.70	1.73			0.38	0.39	
P2O5	-0.01	0.01			0.16	0.18			0.02	0.01	
LOI	6.98	7.04				0.01			2.52	2.39	
Total	98.88	100.34			98.75	100.10			98.93	100.07	
Sc	39				31				56		
V	119	112	110		301	317	309		245	253	251
Cr	3790	3953			198	192			4830	4631	
Co	76	98			36	104			65	81	
Ni	596	574			155	78			546	540	
Cu	10	10			127	51			12	71	
Zn		17			69	89			34	10	
Ga	2				18				4		
Ge	1.4				0.8				1.8		
Rb		4			30	31			1	3	
Sr	8		8		270		265		15		13
Y	4		4		25		24		8		8
Zr	5		4		133		136		12		7
Nb		5			8.3	11			0.8	4	
Sn					1						
Sb											
Cs					0.7				0.2		
Ba		24	8		272	299	267		5	31	10
La	0.32				17.5				0.90		
Ce	1.09				38.5				2.84		
Pr	0.20				4.76				0.50		
Nd	1.32				21.2				2.95		
Sm	0.47				5.46				1.06		
Eu	0.18				1.73				0.38		
Gd	0.65				5.27				1.33		
Tb	0.12				0.87				0.25		
Dy	0.74				4.96				1.48		
Ho	0.15				0.94				0.28		
Er	0.44				2.71				0.80		
Tm	0.06				0.38				0.12		
Yb	0.38				2.31				0.72		
Lu	0.06				0.34				0.10		
Hf	0.2				3.8				0.6		
Ta					0.64				-0.01		
W											
Tl					0.18				-0.05		
Pb						6					
Bi	0.1										
Th					3.71				0.11		
U					0.93				0.02		

Author:	MP	DF	MP		MP	DF	MP		MP	DF	MP
Sample:	VD-709	VD-709	VD-709		EQ-15	EQ-15	EQ-15		EQ-19	EQ-19	EQ-19
Method:	ICPMS	XRF/INAA	Fusion		ICPMS	XRF/INAA	Fusion		ICPMS	XRF/INAA	Fusion
SiO2	46.78	47.09			56.18	56.24			49.90	47.77	
Al2O3	1.30	1.48			21.58	21.35			9.64	9.99	
Fe2O3	7.15	7.41			8.17	9.31			10.79	13.59	
MnO	0.12	0.12			0.14	0.16			0.17	0.18	
MgO	25.25	24.75			4.53	4.8			18.12	17.59	
CaO	12.87	13.54			0.63	0.73			7.84	8.14	
Na2O	0.13	0.01			0.99	1.34			1.21	1.04	
K2O		0.01			3.26	3.15			0.24	0.34	
TiO2	0.20	0.21			0.71	0.66			0.67	0.73	
P2O5		0.01			0.06	0.06			0.05	0.06	
LOI	5.64	5.33			2.89	2.68			0.79	0.56	
Total	99.43	99.96			99.13	100.48			99.42	99.99	
Sc	43						11				27
V	135	127	129			142	128			195	178
Cr	4010	4027			130	218			1240	1708	
Co	71	94			18	67			43	131	
Ni	545	593			50	90			380	780	
Cu	11	10			20	164			40	117	
Zn		14			120	148			60	72	
Ga	3				29				10		
Ge	1.9				2.2				0.6		
Rb		4			135	136			7	10	
Sr	9		8				132				155
Y	4		2		18				11		
Zr	5		5				160				36
Nb	0.2	5			11.5	11			2.4	5	
Sn					2						
Sb									0.3		
Cs					9.8				0.4		
Ba		25	2			394	469			120	85
La	0.30				32.4				5.23		
Ce	1.07				64.9				11.6		
Pr	0.20				7.18				1.55		
Nd	1.33				26				6.76		
Sm	0.49				4.84				1.82		
Eu	0.17				0.74				0.65		
Gd	0.63				3.75				1.92		
Tb	0.13				0.57				0.32		
Dy	0.83				2.81				1.83		
Ho	0.16				0.56				0.37		
Er	0.49				1.69				1.08		
Tm	0.07				0.24				0.16		
Yb	0.42				1.5				0.97		
Lu	0.06				0.22				0.13		
Hf	0.2				4.5				1.1		
Ta					1.02				0.17		
W					0.8						
Tl					0.57						
Pb					27	20				2	
Bi					0.2						
Th					12.6				0.81		
U					2.61				0.22		

Author:	MP	DF	MP	MP	DF	MP	MP	DF	MP
Sample:	EQ-13	EQ-13	EQ-13	M-26	M-26	M-26	EQ-22	EQ-22	EQ-22
Method:	ICPMS	XRF/INAA	Fusion	ICPMS	XRF/INAA	Fusion	ICPMS	XRF/INAA	Fusion
SiO2	46.42	44.71		64.95	49.59		44.35	44.22	
Al2O3	7.55	8.18		13.14	18.69		1.45	1.52	
Fe2O3	11.30	14.13		7.99	8.72		7.05	10.03	
MnO	0.17	0.18		0.12	0.13		0.18	0.19	
MgO	22.45	20.43		1.44	9.14		28.83	26.31	
CaO	5.84	6.38		1.99	7.41		8.36	9.24	
Na2O	0.93	1.53		1.37	1.5		0.11	0.68	
K2O	0.56	0.54		5.57	2.94			0.02	
TiO2	1.05	0.98		1.42	0.62		0.25	0.26	
P2O5	0.08	0.09		0.25	0.09			0.01	
LOI	2.66	2.56		1.73	1.72		8.65	7.96	
Total	99.01	99.71		99.96	100.55		99.22	100.34	
Sc		31.2	22		17.5	18			44
V		199	198		127	101		189	189
Cr	1540	2107			203.2		3020	6547	
Co	51	138		9	64		39	104	
Ni	470	978			366		380	2524	
Cu	70	158		20	316			55	
Zn	60	78		240	43			33	
Ga	11			20			2		
Ge	0.6			1.6			0.7		
Rb	17	15		165	79		2	4	
Sr			132			179			9
Y	16			41			6		
Zr			81			254			5
Nb	5.3	6		18.3	5		0.2	3	
Sn				4					
Sb				0.9					
Cs	1			6.3			0.2		
Ba		155	143		454	1176		22	5
La	9.26			42.6	13.4		0.63		
Ce	20.8			85.6	27		1.64		
Pr	2.62			10.1			0.29		
Nd	11.4			38.8	11		1.93		
Sm	2.81			8.65	2.19		0.69		
Eu	0.89			2.24	0.87		0.24		
Gd	2.92			7.99			0.88		
Tb	0.5			1.26	0.36		0.15		
Dy	2.93			7.27			0.94		
Ho	0.57			1.37	0.5		0.19		
Er	1.58			4.07			0.57		
Tm	0.22			0.58			0.08		
Yb	1.39			3.59	1.1		0.45		
Lu	0.20			0.49	0.17		0.07		
Hf	2.3			6.8	1.7		0.3		
Ta	0.37			1.44	0.4		0.02		
W				1.5			5.3		
Tl	0.06			1.34					
Pb		2		64	7				
Bi				1					
Th	1.79			11.2	2.9				
U	0.49			3.2	1				

Author:	MP	DF	MP
Sample:	CR-31	CR-31	CR-31
Method:	ICPMS	XRF/INAA	Fusion
SiO2	47.85	48.99	
Al2O3	9.13	8.97	
Fe2O3	11.57	12.56	
MnO	0.17	0.18	
MgO	18.78	18.82	
CaO	7.44	6.92	
Na2O	1.18	1.23	
K2O	0.74	0.68	
TiO2	0.97	1.02	
P2O5	0.09	0.09	
LOI	1.42	0.91	
Total	99.34	100.37	
Sc			29
V		212	222
Cr	1040	1548	
Co	53	115	
Ni	480	717	
Cu	60	175	
Zn	50	69	
Ga	12		
Ge	1.2		
Rb	15	16	
Sr			135
Y	17		
Zr			69
Nb	4.5	7	
Sn			
Sb			
Cs	0.7		
Ba		167	127
La	8.36		
Ce	18.9		
Pr	2.47		
Nd	10.7		
Sm	2.79		
Eu	0.91		
Gd	3		
Tb	0.5		
Dy	2.98		
Ho	0.58		
Er	1.67		
Tm	0.24		
Yb	1.49		
Lu	0.21		
Hf	2		
Ta	0.3		
W			
Tl	0.06		
Pb			
Bi			
Th	1.68		
U	0.44		

Appendix D – Standard Isotopic Measurements

Nu Plasma
Neodymium **Recognized value 0.512665**
Alfa 200ppb standard

Date	No.	143Nd/144Nd	1SE	2SE	145Nd/144Nd	1SE	2SE
3-Sep-04	168	0.512235	3.89E-06	7.78E-06	0.348410	2.70E-06	5.40E-06
3-Sep-04	169	0.512241	4.66E-06	9.32E-06	0.348422	3.45E-06	6.90E-06
3-Sep-04	170	0.512221	4.15E-06	8.30E-06	0.348413	3.57E-06	7.14E-06
7-Sep-04	171	0.512246	4.37E-06	8.74E-06	0.348429	3.01E-06	6.02E-06
8-Sep-04	172	0.512223	3.58E-06	7.16E-06	0.348396	2.69E-06	5.38E-06
8-Sep-04	173	0.512213	3.91E-06	7.82E-06	0.348399	2.12E-06	4.24E-06
8-Sep-04	174	0.512229	3.21E-06	6.42E-06	0.348417	2.66E-06	5.32E-06
8-Sep-04	175	0.512227	3.84E-06	7.68E-06	0.348411	2.42E-06	4.84E-06
13-Sep-04	176	0.512217	2.94E-06	5.88E-06	0.348406	2.46E-06	4.92E-06
13-Sep-04	177	0.512225	2.57E-06	5.14E-06	0.348414	2.57E-06	5.14E-06
13-Sep-04	178	0.512211	2.37E-06	4.74E-06	0.348414	2.10E-06	4.20E-06
13-Sep-04	179	0.512227	2.52E-06	5.04E-06	0.348422	2.64E-06	5.28E-06
14-Sep-04	180	0.512226	2.62E-06	5.24E-06	0.348398	1.72E-06	3.44E-06
14-Sep-04	181	0.512239	3.06E-06	6.12E-06	0.348418	2.85E-06	5.70E-06
14-Sep-04	182	0.512236	3.07E-06	6.14E-06	0.348418	1.55E-06	3.10E-06
16-Sep-04	183	0.512227	2.68E-06	5.36E-06	0.348411	1.91E-06	3.82E-06
16-Sep-04	184	0.512229	2.40E-06	4.80E-06	0.348415	1.72E-06	3.44E-06
16-Sep-04	185	0.512238	2.36E-06	4.72E-06	0.348415	2.21E-06	4.42E-06
22-Sep-04	186	0.512223	2.50E-06	5.00E-06	0.348411	1.63E-06	3.26E-06
22-Sep-04	187	0.512224	2.09E-06	4.18E-06	0.348409	1.44E-06	2.88E-06
22-Sep-04	188	0.512202	2.43E-06	4.86E-06	0.348414	1.85E-06	3.70E-06
27-Sep-04	189	0.512212	3.24E-06	6.48E-06	0.348406	1.94E-06	3.88E-06
27-Sep-04	190	0.512206	3.11E-06	6.22E-06	0.348399	1.90E-06	3.80E-06
27-Sep-04	191	0.512231	3.29E-06	6.58E-06	0.348417	2.05E-06	4.10E-06
28-Sep-04	192	0.512224	2.90E-06	5.80E-06	0.348416	1.87E-06	3.74E-06
28-Sep-04	193	0.512233	3.11E-06	6.22E-06	0.348419	2.10E-06	4.20E-06
28-Sep-04	194	0.512230	2.72E-06	5.44E-06	0.348417	1.77E-06	3.54E-06
20-Oct-04	195	0.512234	2.44E-06	4.88E-06	0.348412	1.47E-06	2.94E-06
20-Oct-04	196	0.512232	2.57E-06	5.14E-06	0.348416	2.35E-06	4.70E-06
20-Oct-04	197	0.512242	1.64E-06	3.28E-06	0.348419	1.39E-06	2.78E-06
25-Oct-04	198	0.512239	2.50E-06	5.00E-06	0.348418	1.82E-06	3.64E-06
25-Oct-04	199	0.512243	2.02E-06	4.04E-06	0.348421	1.70E-06	3.40E-06
25-Oct-04	200	0.512246	2.40E-06	4.80E-06	0.348420	1.90E-06	3.80E-06
25-Oct-04	201	0.512248	2.74E-06	5.48E-06	0.348422	1.54E-06	3.08E-06
26-Oct-04	202	0.512247	1.69E-06	3.38E-06	0.348412	1.14E-06	2.28E-06
3-Dec-04	203	0.512243	3.54E-06	7.08E-06	0.348392	3.09E-06	6.18E-06
3-Dec-04	204	0.512230	4.22E-06	8.44E-06	0.348405	3.01E-06	6.02E-06
3-Dec-04	205	0.512231	3.74E-06	7.48E-06	0.348406	2.54E-06	5.08E-06
14-Dec-04	206	0.512232	4.46E-06	8.92E-06	0.348407	2.53E-06	5.06E-06
18-Jan-05	207	0.512248	3.67E-06	7.34E-06	0.348427	2.15E-06	4.30E-06
18-Jan-05	208	0.512245	3.86E-06	7.72E-06	0.348423	2.18E-06	4.36E-06
18-Jan-05	209	0.512242	3.34E-06	6.68E-06	0.348415	2.34E-06	4.68E-06
19-Jan-05	210	0.512243	3.30E-06	6.60E-06	0.348418	1.97E-06	3.94E-06
19-Jan-05	211	0.512246	4.12E-06	8.24E-06	0.348420	2.51E-06	5.02E-06
21-Jan-05	212	0.512247	3.84E-06	7.68E-06	0.348428	2.39E-06	4.78E-06
Sept-Jan. 2005							
average		**0.512232**			**0.348414**		
stdev(2s)		**0.000024**			**0.000017**		
PPM (2s)		**46**			**48**		

Nu
Plasma

Strontium
NIST SRM 987
50ppb

Recognized value 0.710245

Date	No.	87/86Sr (Rb corr)	1SE	2SE	84/86Sr	1SE	2SE
7-May-04	1	0.710278	5.48E-06	1.10E-05	0.056362	8.86E-06	0.00001772
10-May-04	2	0.710287	7.25E-06	1.45E-05	0.056329	1.24E-05	0.0000248
10-May-04	3	0.710257	5.67E-06	1.13E-05	0.056371	6.52E-06	0.00001304
10-May-04	4	0.710308	8.66E-06	1.73E-05	0.056485	8.16E-06	0.00001632
10-May-04	5	0.710270	8.27E-06	1.65E-05	0.056373	1.07E-05	0.0000214
1-Jun-04	6	0.710281	2.40E-05	4.80E-05	0.056107	2.43E-05	0.0000486
1-Jun-04	7	0.710273	2.59E-06	5.18E-06	0.056004	2.02E-05	0.0000404
1-Jun-04	8	0.710260	2.85E-05	5.70E-05	0.056468	1.06E-05	0.0000212
1-Jun-04	9	0.710314	4.56E-05	9.12E-05	0.056585	1.88E-05	0.0000376
2-Jun-04	10	0.710217	4.50E-06	9.00E-06	0.056687	5.46E-06	0.00001092
2-Jun-04	11	0.710230	8.18E-06	1.64E-05	0.056760	6.73E-06	0.00001346
2-Jun-04	12	0.710292	6.00E-06	1.20E-05	0.056515	7.05E-06	0.0000141
2-Jun-04	13	0.710258	5.91E-06	1.18E-05	0.056791	1.55E-05	0.000031
3-Jun-04	14	0.710244	5.43E-06	1.09E-05	0.056905	1.10E-05	0.000022
3-Jun-04	15	0.710237	5.43E-06	1.09E-05	0.056911	8.85E-06	0.0000177
3-Jun-04	16	0.710289	6.07E-06	1.21E-05	0.056554	8.80E-06	0.0000176
3-Jun-04	17	0.710298	8.24E-06	1.65E-05	0.056324	2.93E-05	0.0000586
4-Jun-04	18	0.710241	7.16E-06	1.43E-05	0.057021	7.69E-06	0.00001538
4-Jun-04	19	0.710247	9.02E-06	1.80E-05	0.056826	1.07E-05	0.0000214
7-Jun-04	20	0.710281	5.01E-06	1.00E-05	0.056448	6.94E-06	0.00001388
7-Jul-04	21	0.710260	9.24E-06	1.85E-05	0.056582	4.53E-06	0.00000906
7-Jul-04	22	0.710266	5.81E-06	1.16E-05	0.056591	7.71E-06	0.00001542
7-Jul-04	24	0.710271	7.33E-06	1.47E-05	0.05455	2.06E-05	4.12E-05
13-Jan-05	25	0.710285	1.06E-05	2.12E-05	0.05605	1.77E-05	3.54E-05
29-Mar-05	26	0.710316	1.20E-05	2.40E-05	0.05625	1.44E-05	2.88E-05
29-Mar-05	27	0.710268	1.20E-05	2.40E-05		1.46E-05	2.92E-05
30-Mar-05	28	0.710298	1.49E-05	2.98E-05		1.26E-05	2.52E-05
31-Mar-05	29	0.710249	1.26E-05	2.52E-05		3.33E-05	6.66E-05
18-Apr-05	30	0.710237	1.02E-05	2.04E-05	0.05655	7.77E-06	1.55E-05
15-Jun-05	31	0.710318	1.41E-05	2.82E-05	0.05651	1.85E-05	3.70E-05
16-Jun-05	32	0.710291	9.50E-06	1.90E-05	0.05636	9.65E-06	1.93E-05
27-Jun-05	33	0.710268	1.62E-05	3.24E-05	0.05632	1.07E-05	2.14E-05
29-Jun-05	34	0.710254	9.37E-06	1.87E-05	0.05593	1.09E-05	2.18E-05
16-Sep-05	35	0.710277	1.17E-05	2.34E-05	0.05638	8.45E-06	1.69E-05
13-Oct-05	36	0.710260	9.88E-06	1.98E-05	0.05640	1.85E-05	3.70E-05
14-Oct-05	37	0.710253	1.05E-05	2.10E-05	0.05636	1.67E-05	3.34E-05
28-Oct-05	38	0.710258	1.38E-05	2.76E-05	0.05619	1.48E-05	2.96E-05
28-Nov-05	39	0.710223	1.46E-05	2.92E-05	0.05657	1.22E-05	2.44E-05
29-Nov-05	40	0.710224	1.06E-05	2.12E-05	0.05650	5.14E-06	1.03E-05
30-Nov-05	41	0.710250	1.32E-05	2.64E-05	0.05661	1.43E-05	2.86E-05
13-Dec-05	42	0.710238	1.10E-05	2.20E-05	0.05654	7.95E-06	1.59E-05
30-Jan-06	43	0.710209	1.19E-05	2.38E-05	0.05642	1.06E-05	2.12E-05
31-Jan-06	44	0.710223	1.34E-05	2.68E-05	0.05640	2.36E-05	4.72E-05
16-Feb-06	45	0.710256	1.18E-05	2.36E-05	0.05664	6.97E-06	1.39E-05
16-Feb-06	46	0.710218	6.89E-06	1.38E-05	0.05651	9.78E-06	1.96E-05
13-Mar-06	47	0.710225	8.43E-06	1.69E-05	0.05634	1.51E-05	3.02E-05

Continued..

Date	No.	87/86Sr (Rb corr)	1SE	2SE	84/86Sr	1SE	2SE
23-Mar-06	48	0.710214	7.73E-06	1.55E-05	0.05646	6.31E-06	1.26E-05
31-Mar-06	49	0.710206	8.60E-06	1.72E-05	0.05646	6.99E-06	1.40E-05
8-May-06	50	0.710220	9.69E-06	1.94E-05	0.05644	1.32E-05	2.64E-05
29-May-06	51	0.710209	7.75E-06	1.55E-05	0.05648	8.48E-06	1.70E-05
30-May-06	52	0.710206	8.31E-06	1.66E-05	0.05642	1.02E-05	2.04E-05
1-Jun-06	53	0.710202	1.04E-05	2.08E-05	0.05650	9.02E-06	1.80E-05
6-Jun-06	54	0.710227	1.30E-05	2.60E-05	0.05641	6.41E-06	1.28E-05
6-Jun-06	55	0.710215	1.13E-05	2.26E-05	0.05647	1.56E-05	3.12E-05
9-Jun-06	56	0.710237	1.26E-05	2.52E-05	0.05643	3.48E-05	6.96E-05
5-Sep-06	57	0.710250	1.26E-05	2.52E-05	0.05635	1.15E-05	2.30E-05
6-Sep-06	58	0.710267	1.40E-05	2.80E-05	0.05638	1.01E-05	2.02E-05
14-Sep-06	59	0.710217	1.04E-05	2.08E-05	0.05635	2.58E-05	5.16E-05
14-Sep-06	60	0.710210	1.47E-05	2.94E-05	0.05617	8.69E-06	1.74E-05
28-Sep-06	61	0.710239	1.10E-05	2.20E-05	0.05631	1.24E-05	2.48E-05
29-Sep-06	62	0.710217	1.16E-05	2.32E-05	0.05640	9.42E-06	1.88E-05
3-Jan-07	63	0.710235	9.45E-06	1.89E-05	0.05632	1.12E-05	2.24E-05
1-Feb-07	64	0.710214	1.19E-05	2.38E-05	0.05630	5.09E-05	1.02E-04
2-Feb-07	65	0.710215	1.05E-05	2.10E-05	0.05632	1.52E-05	3.04E-05
21-Feb-07	66	0.710222	1.17E-05	2.34E-05	0.05636	8.73E-06	1.75E-05
average		**0.710222**			**0.05639**	1.00E+04	
stdev(2s)		**0.000033**			**0.00016**	1.00E+02	

JMC 475 *accepted $^{176}Hf/^{177}Hf$ ratio of this standard is 0.282195 =+/-0.000015*

Anal. #	Total volts	176Hf/177Hf	1s	178Hf/177Hf	1s	180Hf/177Hf	1s	174Hf/177Hf	Date and Details			
17	3.55	0.282145	0.0000044	1.46724	0.000013	1.88678	0.000029		Oct/16/2003	50 ppb	DSN	asp. Rate= 80 ul/min (verified)
18	3.69	0.282153	0.0000061	1.46726	0.000013	1.88685	0.000030					
19	3.71	0.282153	0.0000064	1.46726	0.000013	1.88686	0.000023					
20	3.34	0.282166	0.0000057	1.46724	0.000011	1.88685	0.000024		Oct/17/2003	50 ppb	DSN	asp. Rate= 80 ul/min (verified)
21	3.69	0.282150	0.0000067	1.46725	0.000011							
22	2.28	0.282154	0.0000055	1.46729	0.000014	1.88666	0.000033		Nov/13/2003	50 ppb	DSN	asp. Rate= 80 ul/min (verified)
23	2.35	0.282160	0.0000070	1.46726	0.000013	1.88661	0.000041					
24	2.24	0.282162	0.0000100	1.46722	0.000019	1.88668	0.000045		Nov/14/2003	50 ppb	DSN	asp. Rate= 80 ul/min (verified)
25	3.74	0.282158	0.0000062	1.46727	0.000010	1.88684	0.000029					
26	4.12	0.282164	0.0000047	1.46729	0.000012	1.88657	0.000031		Nov/17/2003	50 ppb	DSN	asp. Rate= 150 ul/min (verified) -teflon neb.
27	4.20	0.282160	0.0000047	1.46728	0.0000086	1.88660	0.000030					
28	4.24	0.282160	0.0000054	1.46729	0.000010	1.88667	0.000027					
29	2.03	0.282148	0.0000094	1.46732	0.000017	1.88693	0.000037		Dec/17/2003	50 ppb	DSN	asp. Rate= 100 ul/min (verified) -teflon neb.
30	1.94	0.282156	0.0000095	1.46728	0.000023	1.88685	0.000042					
31	3.23	0.282166	0.0000066	1.46728	0.000013	1.88694	0.000022	0.00866	Jan/07/2004	50 ppb	DSN	asp. Rate= 100 ul/min (verified) -teflon neb.
32	2.88	0.282144	0.0000085	1.46733	0.000018	1.88674	0.000045	0.00866	Jan/08/2004	50 ppb	DSN	asp. Rate= 100 ul/min (verified) -teflon neb.
33	2.46	0.282155	0.0000068	1.46735	0.000016	1.88694	0.000036	0.00866	Jan/20/2004	50 ppb	DSN	asp. Rate= 100 ul/min (verified) -teflon neb.
34	3.18	0.282163	0.0000073	1.46733	0.000016	1.88689	0.000048	0.00867	May/28/2004	50 ppb	DSN	asp. Rate= 100 ul/min (verified) -micromist neb
35	0.95	0.282176	0.0000144	1.46718	0.000027	1.88668	0.000128	0.00867	Oct/14/2004	50 ppb	DSN	asp. Rate= 100 ul/min (verified) -micromist neb
36	4.46	0.282166	0.0000047	1.46726	0.000011	1.88689	0.000024	0.00876	Oct/14/2004	50 ppb	DSN	asp. Rate= 100 ul/min (verified) -micromist neb
37	7.16	0.282161	0.0000033	1.46727	0.000008	1.88678	0.000022	0.00865	Oct/15/2004	50 ppb	DSN	asp. Rate= 100 ul/min (verified) -micromist neb
38	5.00	0.282151	0.0000041	1.46726	0.000007	1.88668	0.00002	0.00865	Oct/22/2004	50 ppb	DSN	asp. Rate= 100 ul/min (verified) -micromist neb
39	2.74	0.282163	0.0000062	1.46728	0.000011	1.88677	0.00003	0.00864	Dec/20/2004	50 ppb	DSN	asp. Rate= 100 ul/min (verified) -micromist neb
40	2.67	0.282152	0.0000074	1.46728	0.000023	1.88677	0.000038	0.00866	Jan/11/2005	50 ppb	DSN	asp. Rate= 100 ul/min (verified) -micromist neb
43	3.64	0.282156	0.0000058	1.46730	0.0000085	1.88674	0.0000282	0.00864	Mar/9/2005	50 ppb	DSN	asp. Rate= 100 ul/min (verified) -micromist neb
44	3.53	0.282151	0.0000054	1.46727	0.000013	1.88671	0.00032	0.00864	April/11/2005	50 ppb	DSN	asp. Rate= 100 ul/min (verified) -micromist neb
	AVG=	**0.282157**		**1.467275**		**1.886771**		**0.008663**				
	2STDEV=	**0.000015**		**0.000071**		**0.000220**		**0.000061**				
	STDEV (PPM, 2s)=	**53**		**48**		**117**		**7056**				

Coral Internal Standard
Dec/1/2003

60 um spot size
4 Hz, 70% energy level, ~10 J/cm2
1.00 L/min He
3.19 L/min Ar membrane gas flow

60 sec
ablation
13.0 L/min cooling gas (Ar)
1.0 L/min aux gas (Ar)
Forward power 1300 watts

Analysis #	87Sr/86Sr corr.	error (1s)	84Sr/86Sr	error (1s)	86Sr/88Sr raw	Total Sr (v)
1	0.70925	0.000037	0.056513	0.0000086	0.11619	5.906
2	0.70921	0.000047	0.056540	0.000013	0.11624	4.267
3	0.70928	0.000049	0.056457	0.0000201	0.11615	3.277
4	0.70925	0.000047	0.056394	0.0000162	0.11616	3.952
5	0.70924	0.000041	0.056607	0.0000146	0.11622	3.946
6	0.70914	0.000044	0.056589	0.000011	0.11616	4.211
7	0.70933	0.000043	0.056547	0.000014	0.11614	4.294
8	0.70925	0.000039	0.056413	0.000020	0.11622	4.137
9	0.70929	0.000048	0.056545	0.000014	0.11621	4.137
10	0.70919	0.000058	0.056547	0.000016	0.11613	4.150
11	0.70922	0.000044	0.056404	0.000023	0.11620	3.976
12	0.70925	0.000045	0.056536	0.000013	0.11620	3.963
13	0.70929	0.000045	0.056565	0.000011	0.11612	4.348
14	0.70930	0.000049	0.056445	0.000014	0.11613	4.167
15	0.70926	0.000049	0.056518	0.000015	0.11617	4.102
16	0.70922	0.000041	0.056548	0.000012	0.11612	4.320
17	0.70924	0.000045	0.056412	0.000015	0.11612	4.413
18	0.70926	0.000034	0.056492	0.000015	0.11619	3.971
19	0.70919	0.000048	0.056557	0.000016	0.11617	4.114
20	0.70922	0.000042	0.056457	0.000018	0.11614	4.253
21	0.70922	0.000052	0.056513	0.000013	0.11617	4.061
22	0.70922	0.000041	0.056546	0.000014	0.11610	4.093
23	0.70929	0.000044	0.056455	0.000013	0.11609	4.353
24	0.70932	0.000037	0.056146	0.000020	0.11641	3.372
25	0.70932	0.000032	0.056491	0.000016	0.11608	4.370
Dec/2/2003						
26	0.70922	0.000044	0.056742	0.000013	0.11522	5.657
27	0.70928	0.000045	0.056617	0.000013	0.11519	5.843
28	0.70923	0.000037	0.056402	0.000016	0.11524	5.851
29	0.70921	0.000044	0.056628	0.000014	0.11520	6.170
30	0.70929	0.000039	0.056517	0.000010	0.11517	6.494
31	0.70922	0.000042	0.056518	0.000010	0.11521	6.348
32	0.70932	0.000044	0.056459	0.000011	0.11515	6.422
33	0.70920	0.000044	0.056544	0.000009	0.11519	6.702
34	0.70922	0.000045	0.056588	0.000010	0.11516	6.773
35	0.70924	0.000032	0.056564	0.000008	0.11520	6.500
Jan/24/2005						
36	0.70913	0.000036	0.05647	0.000024	0.11454	3.736
37	0.70926	0.000033	0.05662	0.000018	0.11454	3.393
38	0.70918	0.000045	0.05660	0.000020	0.11455	3.309
39	0.70921	0.000035	0.05650	0.000017	0.11455	3.291
40	0.70908	0.000035	0.05663	0.000016	0.11456	3.479
Jan. Average=	**0.709172**		**0.056562**		**0.114549**	
STDDEV(2s)=	**0.000140**		**0.000149**		**0.000015**	
Overall Average (N=40)=	**0.70924**		**0.05651**		**0.11589**	
STDDEV(2s)=	**0.00011**		**0.00019**		**0.00090**	

Standard	Analysis No.	$^{206}Pb/^{204}Pb$	StdErr 1s	$^{207}Pb/^{204}Pb$	StdErr 1s	$^{207}Pb/^{206}Pb$	StdErr 1s
Broken Hill Pb ore deposit- TIMS							
	Accepted values	**15.97**	**0.02**	**15.35**	**0.021**	**0.9609**	**0.0006**
	Amazonite_IC_1	16.00	0.03	15.41	0.02	0.9634	0.0010
	Amazonite_IC_2	16.07	0.03	15.55	0.03	0.9678	0.0008
	Amazonite_IC_3	16.23	0.04	15.75	0.05	0.9700	0.0010
	Amazonite_IC_4	16.12	0.03	15.60	0.03	0.9679	0.0008
	Amazonite_IC_5	16.12	0.03	15.49	0.03	0.9607	0.0011
	Amazonite_IC_6	16.10	0.04	15.54	0.04	0.9649	0.0009
	Amazonite_IC_7	16.09	0.03	15.55	0.03	0.9662	0.0010
	Amazonite_IC_8	15.89	0.03	15.42	0.03	0.9704	0.0007
	Amazonite_IC_9	16.01	0.03	15.41	0.03	0.9627	0.0011
	Amazonite_IC_10	16.11	0.03	15.41	0.03	0.9566	0.0009
	Amazonite_IC_11	16.15	0.05	15.48	0.04	0.9589	0.0012
	Amazonite_IC_12	16.11	0.04	15.41	0.04	0.9566	0.0012
	Average=	**16.08**		**15.50**		**0.9638**	
	STDEV (2s)=	**0.17**		**0.21**		**0.0097**	
NIST 612							
	Accepted values	**17.094**	**0.0026**	**15.51**	**0.0036**	**0.9073**	**0.0000**
	Analysis#	**206Pb/204Pb**	**error (1s)**	**207Pb/204Pb**	**error (1s)**	**207Pb/206Pb**	**error (1s)**
	1	17.07	0.06	15.44	0.07	0.9037	0.0026
	2	17.24	0.08	15.48	0.07	0.9040	0.0031
	3	17.15	0.07	15.62	0.07	0.9124	0.0029
	4	17.30	0.05	15.74	0.07	0.9078	0.0024
	5	16.95	0.08	15.29	0.06	0.9008	0.0020
	6	16.99	0.08	15.29	0.06	0.8994	0.0025
	7	17.19	0.07	15.43	0.08	0.8991	0.0023
	8	17.40	0.08	15.75	0.09	0.9027	0.0026
	9	17.09	0.09	15.26	0.12	0.8996	0.0026
	10	17.17	0.11	15.47	0.13	0.9042	0.0033
	Average=	**17.16**		**15.48**		**0.9034**	
	STDEV (2s)=	**0.28**		**0.36**		**0.0084**	